

ENGINEERING OF MULTIFUNCTIONAL NANOPARTICLES FOR PRECISION THERANOSTICS OF
GLIOBLASTOMA

By

Meghan Lorene Hill

A DISSERTATION

Submitted to
Michigan State University
in partial fulfillment of the requirements
for the degree of

Biomedical Engineering – Doctor of Philosophy

2024

ABSTRACT

Glioblastoma is one of the most aggressive and invasive types of cancer. Unfortunately, due to the overlapping nature of side-effects with other types of neurological diseases and the difficulty to identify them with diagnostic measures, it is not discovered until stage four. At this point, patients have limited options for care and ultimately end up in palliative care not long after diagnosis. The blood-brain barrier (BBB) has proved to be a difficult boundary for current modern medicines as it prevents adequate accumulation within the brain. As gliomas often form in inoperable parts of the brain, conventional FDA-approved therapies prove to be ineffective. Within the past ten years, targeting strategies using RGD peptides have proven effective at transporting drugs, contrast agents, or nanoparticle delivery vehicles across the barrier, but suffer from off-targeting effects due to expression of the peptide-recognizing integrins on the surface of healthy cells. Extracellular vesicles, particularly exosomes, have shown promising specific targeting effects of cells from which the vesicles originate. They have also shown a remarkable ability to pass through the BBB innately. The focus of this project was the development of a glioblastoma derived-exosome coated Prussian Blue nanoparticle (Exo:PB) that could easily accumulate within glioblastoma tissues and provide enhanced diagnostics as well as localized therapy. Prussian Blue nanoparticles are FDA-approved for scavenging heavy metals present within the body after extreme radiation exposure. Based on their exceptional application to photothermal therapy and ability to be used for photoacoustic imaging and MRI, they are an ideal candidate for glioblastoma theranostics. By investigating the distribution and accumulation patterns of these newly developed Exo:PB nanoparticles within

preclinical mouse models, earlier diagnosis and treatment intervention can be achieved for glioblastoma.

I would like to dedicate this dissertation to my mom, dad, and grandparents for all their support. This has been a long journey and without your support, I would not have made it this far

ACKNOWLEDGEMENTS

I would like to express my appreciation for my PhD advisor, Dr. Taeho Kim. As a mentor, he constantly pushed me to be a better researcher and provided me with the guidance to persevere through my graduate studies. I would not have reached this stage without his instruction and patience.

For my committee members, Dr. Assaf Gilad, Dr. Masamitsu Kanada, and Dr. Xuefei Huang, thank you for your guidance and willingness to talk to me about research and future plans.

Finally, I would like to thank my lab members: Kay Hadrick, Seock-Jin Chung, Hyun-Joo Woo, Praveen Kumar, Leila Mwangi, Md Nafiujjaman, and Chorong Park for their contributions and help through my time at Michigan State University.

TABLE OF CONTENTS

LIST OF ABBREVIATIONS.....	viii
Chapter 1: Introduction.....	1
1.1: Clinical Overview of Glioblastoma	1
1.2: Nanoparticles for Brain Cancer Diagnosis and Therapy	9
1.3: Imaging Modalities for Glioblastoma.....	20
1.4: Therapeutic Strategies for Glioblastoma.....	24
1.5: FDA Approval and Future Clinical Translation to Improve Patient Outcomes	32
Chapter 2: Exosome Coated Prussian Blue Nanoparticles (Exo:PB) for Early Detection and Treatment of Glioblastoma	35
2.1: Introduction	35
2.2: Methods.....	49
2.3: Results/Discussion.....	61
2.4: Conclusions	107
Chapter 3: Anti-inflammation Effects of Exo:PB Particles.....	108
3.1: Introduction	108
3.2: Methods.....	112
3.3: Results/Discussion.....	115
3.4: Conclusions	124
Chapter 4: Targeting of Glioblastoma with RGD peptide	125
4.1: Introduction	125
4.2: Methods.....	128
4.3: Results/Discussion.....	132
4.4: Conclusions	145
Chapter 5: Development of Gadolinium Doped Prussian Blue Nanoparticles for MRI-Guided LITT Treatment	146
5.1: Introduction	146
5.2: Methods.....	149
5.3: Results/Discussion.....	152
5.4: Conclusions	161
Chapter 6: Conclusions and Future Directions.....	162
6.1: Conclusions	162
6.2: Future Directions.....	165
REFERENCES.....	166

APPENDIX 192

LIST OF ABBREVIATIONS

$^1\text{O}_2$ – Singlet Oxygen Species

5-ALA – 5-aminolevulinic Acid

AB – Apoptotic Body

AuNR – Gold Nanorod

BBB – Blood-Brain Barrier

BBTB – Blood-Brain Tumor Barrier

bioTEM – Biological Transmission Electron Microscopy

CAR – Center for Animal Resources

CAT – Catalase

CF – Cerebral Fluid

CT – Computerized Tomography

CTAB – Cetyltrimethylammonium Bromide

DCFDA – 2',7'-dichlorofluorescein diacetate

DDI – Double-Distilled Water

Dil - 1,1'-Dioctadecyl-3,3,3',3'-Tetramethylindocarbocyanine

Dil-Exo:PB - 1,1'-Dioctadecyl-3,3,3',3'-Tetramethylindocarbocyanine stained Exosome Coated Prussian Blue Nanoparticle

DLS – Dynamic Light Scattering

DMPC – 1,2-dimyristoyl-sn-glycero-3-phosphocholine

DMSO – Dimethyl Sulfoxide

DNA – Deoxynucleic Acid

DOTAP – 1,2-dioleoyl-3-trimethylammonium-propane

DOX – Doxorubicin

DPPC – 1,2-dipalmitoyl-sn-glycero-3-phosphocholine

DSPC – 1,2-distearoyl-sn-glycero-3-phosphocholine

EDX – X-ray Spectroscopy

EPR – Enhanced Permeability and Retention Effect

ESI-TOF - Electrospray Ionization Time-of-Flight

EV – Extracellular Vesicle

Exo:PB – Exosome Coated Prussian Blue Nanoparticle

FBS – Fetal Bovine Serum

FCC – Face Centered Cubic

FDA – Food and Drug Administration

FTIR – Fourier Transform Infrared

Gd:PB – Gadolinium Doped Prussian Blue Nanoparticle

GOD – Glucose Oxidase

GPx – Glutathione Peroxidase

GUV – Giant Unilamellar Vesicle

Hb - Deoxyhemoglobin

HbO₂ - Hemoglobin

HbT -Total Hemoglobin Signal

HCl – Hydrochloric Acid

H&E – Hematoxylin and Eosin

HEPES – N-(2-Hydroxyethyl)piperazine-N'-(2-ethanesulfonic acid)

HSA – Human Serum Albumin

IACUC - Institutional Animal Care and Use Committee

ICP – Inductively Coupled Plasma

ICP-MS – Inductively Coupled Plasma Mass Spectrometry

LD50 – Lethal Dose 50

IHC – Immunohistochemistry

ILV – Intraluminal Vesicle

iMRI – Intraoperative Magnetic Resonance Imaging

IONP – Iron Oxide Nanoparticle

IV – Intravenous

LITT – Laser Interstitial Thermal Treatment

LPS – Lipopolysaccharide

LUV – Large Unilamellar Vesicle

MB – Microbubble

MGMT - O6-methylguanine-DNA methyltransferase

MLV – Multilamellar Vesicle

MPE – Maximum Permissible Exposure

MRI – Magnetic Resonance Imaging

mSO₂ – Microvesicle Blood Saturation

MSOT - Multispectral Optoacoustic Tomographic Imaging System

MTT - 3-(4,5-Dimethylthiazol-2-yl)-2,5-diphenyltetrazolium bromide

MV – Microvesicle

MVB – Multivesicular Body

MVV – Multivesicular Vesicle

NAC – N-acetylcysteine

NIR – Near-Infrared

NIR II – Second Near-Infrared

NSAID – Nonsteroidal Anti-Inflammatory Drug

NTA – Nanoparticle Tracking Analyzer

OCT – Optimal Cutting Temperature

PAI – Photoacoustic Imaging

PB – Prussian Blue

PBNP – Prussian Blue Nanoparticle

PBS – Phosphate Buffered Saline

PDI – Polydispersity Index

PEG – Poly-Ethylene Glycol

PEG:PB – Pegylated Prussian Blue Nanoparticle

PEG-PLGA – poly(ethylene glycol)-poly(D, L-lactide-co-glycolide)

PET – Positron Electron Tomography

PET-CT – Positron Electron Tomography with Computerized Tomography

PG – Prussian Green

PFA – Paraformaldehyde

PLGA - Poly(D, L-lactide-co-glycolide)

PLL – Poly-L-Lysine

POD – Peroxidase

PTT – Photothermal Therapy

Purpald – 4-amino-3-hydrazino-5-mercapto-1,2,4-triazole

PVP – Polyvinylpyrrolidone

PVP-PBNP – Polyvinylpyrrolidone Coated Prussian Blue Nanoparticle

PW – Prussian White

PY – Prussian Yellow

r₁ – Longitudinal Relaxation Time Relaxivity

r₂ – Transverse Relaxation Time Relaxivity

R₁ – Longitudinal Relaxation Rate

R₂ – Transverse Relaxation Rate

RGD – Arginine-Glycine-Aspartic Acid

RF – Radiofrequency

RITC – Rhodamine Isothiocyanate

RITC-PEG:PB - Rhodamine Isothiocyanate PEGylated Prussian Blue Nanoparticles

RITC-RGD – Rhodamine Isothiocyanate RGD

RITC-RGD:PB - Rhodamine Isothiocyanate RGD Conjugated Prussian Blue Nanoparticle

RNA – Ribonucleic Acid

ROS – Reactive Oxygen Species

RT – Room Temperature

SERS – Surface-Enhanced Raman Scattering.

SOD – Superoxide Dismutase

SPION – Super Paramagnetic Iron Oxide Nanoparticle

SUV – Small Unilamellar Vesicle

T1 – Longitudinal Relaxation Time

T2 – Transverse Relaxation Time

TEA – Triethylamine

TEM – Transmission Electron Microscopy

TRf – Transferrin Receptor

ULV – Unilamellar Vesicle

USPION – Ultra-Small Iron Oxide Nanoparticle

Chapter 1: Introduction

1.1: Clinical Overview of Glioblastoma

Glioblastoma is a very invasive and deadly form of brain cancer that has a 5-year survival rate of <7%¹. Common symptoms of this cancer include headaches, problems with speech, memory loss, general confusion, and vision problems^{2, 3}. While the most common regions for these tumors to form are in the frontal and temporal lobes, symptoms may not conclude the cause is cancer. Due to the overlapping nature of these symptoms with many other types of neurological disorders, glioblastoma can be very difficult to diagnose without expensive imaging and invasive procedures to properly identify⁴. Typically, an individual would be referred for an MRI and/or a PET-CT to determine if there is a tumor present and then sent to a specialist to perform a biopsy to determine the type of cancer. Not only is this costly but is a very painful process for the patient to go through before starting therapy. Now, once the cancer is diagnosed as glioblastoma, there are few options for the patient in terms of treatment. Chemotherapy, with Temozolomide being the most common drug used, and radiation are common initial treatments^{5, 6}. Unfortunately, due to the impenetrable nature of the blood-brain-barrier many types of chemotherapies used for other types of cancer do not work⁷⁻¹². Once the location of the tumor is identified, if it resides in an area of the brain where removal would cause minimal damage to surrounding brain tissue, resection would be recommended^{13, 14}. As the most invasive procedure that can be done for this type of cancer, the patient risks losing certain bodily functions that can reduce overall quality of life. Finally, if the cancer has progressed to a point where treatment is rendered useless, the patient will be moved to palliative care.

Biology of Glioblastoma: Most cancers are classified by the type of cells that they originate from¹⁵. Glioblastoma is a primarily astrocyte originating cancer that is known for little to no immune disturbance¹⁶. Based on the nature of this cancer, it is known to infiltrate healthy tissue within the surrounding tumor environment. As this cancer can be very heterogeneous and difficult to diagnose, it has been classified to have four subtypes: proneural, neural, classical, and mesenchymal¹⁷.

1. Proneural: Patients are often more resistant to therapy and are more susceptible to death at an early stage. Associated with younger patients. Prominent Cell Type: Oligodendrocyte¹⁸.
2. Neural: Prominent Cell Type: Oligodendrocyte and Astrocyte¹⁸.
3. Classical: Less resistant to therapies in which patients tend to survive longer. Prominent Cell Type: Astrocyte¹⁷.
4. Mesenchymal: The most aggressive subtype. Patients are more responsive to therapies. Patients from this subtype tend to suffer from high amounts of inflammation and necrosis within the tumor area. Prominent Cell Type: Astroglial¹⁹.

These subtypes are determined as through the expression and abnormalities of different genetic markers: PDGFRA, IDH1, EGFR, and NF1. For specific correlation, it was seen that proneural subtypes have a high frequency of mutations within the IDH1 and TP53 genes at 30 and 54%, respectively^{20, 21}. On the other end of the spectrum, the mesenchymal subtype had the highest number of mutations within the NF1 gene at 37%^{21, 22}. This information on specific mutations is helpful, but looking at the bigger picture in terms of alterations in chromosomes and the related gene effected is also of importance. Specifically, amplified events within the

7p11.2, 7q21.2, 7q31.2, 7q34, 4q12, 17q11.2, 10q23, 9p21.3, and 13q14 were quite prominent in patients with the different subtypes of glioblastoma. Neural, classical, and mesenchymal subtypes showed >85% events within 7p11.2, 7q21.2, 7q31.2 and 7q34 regions^{21, 23}. This corresponds to EGFR, CDK6, and MET genes. In comparison, the proneural subtype has <55% of events across all the regions^{21, 24}. This aligns with the fact that proneural subtype patients are more resistant to therapies and tend to have a more sudden onset death from the disease. When patients of the different subtypes are treated with the same chemotherapy/radiotherapy plan, classical and mesenchymal patients tend to respond better. Neural subtype patients showed positive effects but were not statistically different from proneural in which the treatment was not effective^{21, 25}. It is often debated on whether the proneural or mesenchymal subtype is the worst to be diagnosed with. Proneural affects younger patients that are less receptive to treatment while mesenchymal primarily affects older patients that are quite receptive to specific treatment plans. When looking at clinical data, proneural and mesenchymal subtype patients tend to live greater than 40 months with treatment. Though it is seen that ~25% of patients with the mesenchymal subtype and <20% of proneural patients survive the same period²¹. In terms of aggressiveness, it is difficult to quantify. One way to measure it can be based on average survival rate or the karnofsky score (a score given to an individual based on the ability of the patient to care for themselves)²⁶. Another might be O6-methylguanine-DNA methyltransferase (MGMT) gene expression (responsible for DNA repair and is correlated to therapeutic success)²⁷.

In general, it has been shown that there is no statistical correlation between patient subtype and MGMT expression as over half of patients from all subtypes show more tendency to not have methylated MGMT^{28, 29}. The literature often conflicts over this statement as usually less than half of patients diagnosed with glioblastoma have methylated MGMT, but those that do have showed substantial better response to treatment and overall tend to survive longer³⁰. While this is a great first step to identifying a potential biomarker for therapeutic success, it is not a distinguishing marker for any specific subtype^{21, 31}.

The karnofsky score is given to a patient based on their ability to care for themselves. The scale ranges from 0-100, where 0 is definitive that the patient has died and 100 is a healthy patient. For patients diagnosed with glioblastoma, the average karnofsky score is high (usually greater than 80)^{32, 33}. While this seems to indicate that patients would have a good quality of life and disease prognosis, it only gives a quantifiable number to the physical and psychological abilities of the patient. Since glioblastoma is not diagnosed until stage IV, patients often show minor symptoms that don't affect daily tasks. This tends to skew the score upwards as patients come across as "healthy" in the beginning. As a result, the score decreases rapidly over time and the patient starts to deteriorate from the disease³⁴. In comparison to patients diagnosed with pancreatic cancer (another cancer that is normally found late stage and has low prognosis), the karnofsky score is <80³⁵.

Glioblastoma tumors are unique in their origin and have a lot of heterogeneity even between subtypes. From biological mutations to overall clinical prognosis, this type of cancer is difficult to identify and options for the patient are limited. To improve the overall outcome, the

nature of this cancer must be understood and the underlying mechanisms must be studied to bridge the gap between a <7% to 100% survival rate.

Biology of the BBB: As the main obstacle to overcome for most modern-day medicines used for brain related disease, the blood-brain barrier (BBB) is nature's best defense at protecting the brain^{9, 10, 36-38}. In its simplest form, it is a layer of endothelial cells that surround the brain that dictates what is essential for the brain³⁹. In general, the BBB protects the brain from external blood-based pathogens, dysregulated ion concentrations, prevents excess immune cell presence, excessive internal injury, as well as restrict disease progression or infiltration to the brain⁴⁰. The endothelial cell boundary creates tight junctions that provide strict channels of access for any material that is within the blood. Within these tight junctions sit claudin transmembrane proteins that regulate transport. There are currently more than 20 identified claudin proteins^{41, 42}. Some general properties that these proteins mitigate entrance of are size, electrical resistance, ionic charge, surface protein expression, concentration, etc^{38, 43}. The BBB properties of common preclinical models such as mice, rats, zebrafish, and non-human primates in comparison to human BBB has been widely investigated. In general, it was found that expression of claudin proteins, endothelial barrier composition, and permeability to contrast agents are very similar between rodent and human models^{44, 45}. This is a great biological boundary that prevents many external infiltrates that can cause disease or infection, but it also prevents clinical intervention for internal neurological disorders/diseases. In terms of glioblastoma, this greatly limits treatment options and reduces the chance of early diagnosis. To date, there are only 20 FDA approved treatment agents for brain tumors and a handful of diagnostic agents that can help with detection and treatment⁴⁶.

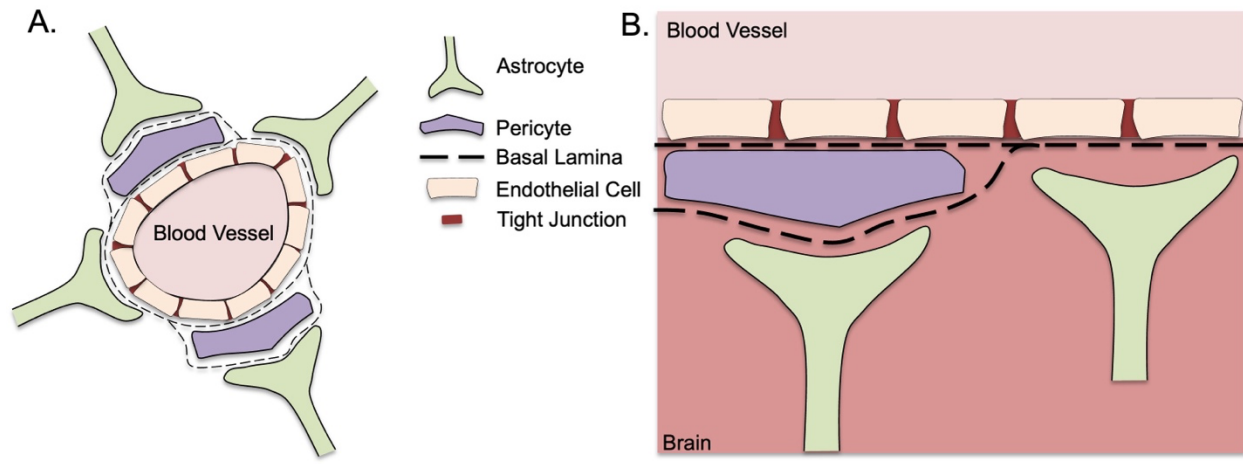


Figure 1: Representative graphic of the blood-brain barrier. (A) Cross section view of a blood vessel that interfaces with the brain. (B) Straight view of the blood brain barrier. Green = astrocyte cells, Purple = pericyte cells, Tan = endothelial cells, Dark Red = Tight Junctions, Cross Hatched Black Line = basal lamina.

The overall structure of the BBB is separated in 4 distinct layers: endothelial cell, basal lamina, pericyte, and astrocyte⁴⁷ (**Figure 1**). The endothelial layer faces the circulating blood outside of the brain while the astrocyte layer interfaces with parenchyma. Within this structure lies two distinct types of transporters: efflux and nutrient^{48, 49}. The main difference between the two being the types of molecules that they process as well as direction of concentration gradient. Efflux are primarily fixated on the outside of the endothelial layer and move molecules using active transport as they move up the concentration gradient⁵⁰. There are many types of efflux transporters that allow a wide variety of substrates/molecules to pass through (Ex: BCRP, Mdr1, and MRPs)⁵¹. Though there is a large diversity of large molecules these transporters can accommodate it prevents traditional small and neutrally charged molecules from passing through. This is one of the greatest hurdles that must be overcome for modern medicines. The other main transporters based in the BBB are nutrient. These transporters act as the gateway for many types of essential nutrients that are needed for a healthy brain. Specifically done as transport down the concentration gradient as typically no energy is needed for this process. There are a wide variety of nutrient transporters, but what is unique about this class is the singularity of substrates that they work with. Whether it be solute or receptor-mediated each protein system allows for a specific type of substrate to pass through. The most common examples being slc2a1 (glut1) for glucose, transferrin for transferrin and iron, lipoprotein (LRP1/LRP8) for transport of lipoproteins, etc^{52, 53}. As these are the most passive and easiest pathway to exploit for entrance into the brain, many researchers are looked into modification of receptors or cloaking mechanisms for targeted drug delivery⁵⁴.

There are three primary ways of entry for a drug to enter the brain and efficiently accumulate in the region of interest. These include carrier-mediated transport, passive diffusion, and vesicular trafficking⁵⁴. The most popular route of entry for essential bigger molecules is through carrier-mediated transport. These wide variety of transporters include both efflux (active) and nutrient (passive) and as mentioned before are easiest to exploit for new drugs/ diagnostic agents. This is because once a certain confirmation of substrate is determined for a specific protein transport, therapeutics or therapeutic carriers can be modified to trick the transporters into allowing them to pass. While this seems to be an efficient way to discover and manufacture more agents for brain-related disease, the process to develop these agents is slow and directly competes with the molecules that already use those transporters which make it inefficient.

1.2: Nanoparticles for Brain Cancer Diagnosis and Therapy

Imaging modalities such as MRI, CT, PET, etc. can help clinicians accurately diagnose patients.

For surface-based cancers, these methods can easily distinguish tumor tissue from normal.

Unfortunately, for hard to detect or metastasized tumors these imaging techniques prove to be difficult without proper contrast agents⁵⁵. There are many types with different structures such as organic or inorganic molecules, nanoparticles, protein-based structures, etc⁵⁶. Based on the surface transporters of the BBB, molecular and protein-based structures have a difficult time entering the brain due to poor receptor-specific binding or the inability to interact properly with passive transporters to pass innately. Nanoparticles can easily be manufactured and modified to allow for increased access to the brain^{36, 37, 57-63}. To date, there is only one nanoparticle that has been FDA approved for enhanced MRI contrast of brain cancers: iron oxide nanoparticles (IONPs), but research has been done on many other formulations⁶⁴.

Iron Oxide: The most common inorganic nanoparticle used in the clinic for glioblastoma (**Figure 2A**). It can act as either a longitudinal relaxation time (T1) or transverse relaxation time (T2) MRI contrast agent to help diagnose brain cancers or other solid based tumors. Now it can act as either T1 or T2 based on the size of the particle⁶⁵. As iron oxide exists in Fe_2O_3 and Fe_3O_4 chemical forms, the patient would be injected with one or the other depending on initial MRI or PET-CT results. Within the past 10 years in particular these particles have become very popular for enhanced imaging contrast as they are dramatically less toxic than the gadolinium-based agents that had been the standard within the clinic⁶⁶. Iron oxide nanoparticles (IONPs) typically range in size from 15nm to $3\mu\text{m}$ (hydrodynamic diameter) with a polymeric coating on the surface for clinical application⁶⁷. The application in which the particles are used for typically

dictates the size. In general, the bigger the particle the higher magnetic to dead zone ratio there is, but beyond 30nm the ratio becomes negligible in comparison to size⁶⁶. This is important as this shifts the particle dynamic from superparamagnetic to paramagnetic, which is what determines whether it will provide the necessary contrast needed. As iron is typically excreted through the digestive system, IONPs are normally used as a contrast agent for the gastrointestinal tract, with special emphasis on the liver. Due to the great ability they have to accumulate in areas of increased blood supply, their use in tumor identification is unparalleled. As early diagnosis of brain cancers has become more of a focus recently, IONPs have been utilized within the clinic to help determine tumor boundaries and help clinicians figure out if surgical resection is an option for the patient^{68, 69}. Unfortunately, with the BBB preventing sufficient accumulation within the tumor the results are not always accurate. Glioblastoma can cause disruption of the BBB depending on the location which can allow for increased penetration of the particles, but this is not a common enough occurrence to be sufficient. The most common ways to circumvent this problem are extra surface conjugation of targeting moieties to the surface of IONPs or carrying cloaking mechanisms. While preclinical research has seemed promising, these modifications can be expensive and therefore hard to translate into the clinic.

Liposomes and Microbubbles: Synthetic lipid-based vesicle structures are the gold standard for drug delivery systems in the clinic⁷⁰. Liposomes have changed the field for effective treatment of solid tumors through encapsulation and release of hydrophobic drugs⁷¹. As the basis for most lipid particle research, microbubbles, nanobubbles, nanovesicles, etc. have been created and modified for a wide variety of uses in medicine. For use against glioblastoma, liposomes and

microbubbles have both been investigated^{72, 73}. Typically, the two particles are used for different objectives in brain tumor targeting and treatment. The different uses are primarily due to the difference in structure. Liposomes contain a membrane-based structure that consists of an internal aqueous core while microbubbles are a single lipid layer with a gas core^{74, 75}. Therefore, liposomes are traditionally used more for surface modification and sustained drug delivery while microbubbles are used for cellular disruption and detection using ultrasound.

Liposomes: Mostly known for their role in the commonly used cancer drug Doxil (doxorubicin HCl loaded liposomes) (**Figure 2B**). Liposomes are popular as they can be easily manufactured at high concentrations and modified based on the overall purpose they need to serve.

Liposomes fall into 2 distinct categories based on their structure: large unilamellar vesicles (LUV) and unilamellar vesicles (ULV)⁷⁶. The main difference between the two is size and multi-membrane presence. For both LUVs and ULVs there are two subtypes. For LUVs, there are small unilamellar vesicles (SUV) and giant unilamellar vesicles (GUV), and for ULVs there are multilamellar vesicles (MLV) and multivesicular vesicles (MVV). For the purposes of clinical use, SUVs are the most common as their size is ~100nm⁷⁷. Traditionally, SUVs are made in two different ways: thin film or injection^{76, 77}. Thin film is based on suspending a mixture of lipids and/or drugs in highly volatile solvents, such as chloroform, and drying is evenly to make a film. This film is then resuspended in water or buffer and sonicated to create liposomes. Injection formation is done by adding either ethanol/lipid or ether/lipid mixture is added to water and then the organic part is dried off over time⁷⁸. The injection method works slight differently in which the lipids are dissolved in a solvent such as ethanol or ether and then injected into a

stirring aqueous solution. During the injection time, the liposome structures self-assemble within the emulsion bubbles formed⁷⁹. Both methods can be scaled easily and are reproducible. Liposomes traditionally consist mostly of a base short chain lipid such as 1,2-dimyristoyl-sn-glycero-3-phosphocholine (DMPC), 1,2-dipalmitoyl-sn-glycero-3-phosphocholine (DPPC), or 1,2-distearoyl-sn-glycero-3-phosphocholine (DSPC) which range from 14-18 carbon chain lengths. The remaining ~10-20% of the structure is consisted of PEG, cholesterol, charged lipids such as 1,2-dioleoyl-3-trimethylammonium-propane (DOTAP), targeting moieties etc. As the structures are formed, chemotherapeutics or genetic therapies can be loaded into either the aqueous core or into the self-formed lipid bilayer. This makes liposomes a highly variable, highly manipulative structures as a delivery platform for diverse therapeutic applications. For glioblastoma treatment, many studies have utilized liposomes as carrier vehicles for hydrophobic drugs. Many articles have reported the use of temozolomide loaded liposomes for glioblastoma treatment through ultrasound disruption^{80, 81}. While liposomes are very useful in the clinic, they are expensive to manufacture and can also be unstable long term. Most recent studies have shown that repeated doses of liposomes can cause adverse reactions in individuals due to the immune system recognizing the agents as foreign⁸².

Microbubbles: Microbubbles (MBs) are simply micro-sized bubbles that have been used for a wide variety of purposes (**Figure 2B**). These particles consist of a single monolayer of lipids with a gaseous core⁷⁵. This makes them particularly useful as ultrasound contrast agents. When they are exposed to different ultrasound frequencies, they can create small bursts of energy which can indicate areas of blood flow in which the MBs are present or can create cavitations in tissue to allow for increased permeability (such as the BBB)^{7, 83, 84}. In terms of targeted drug delivery,

MBs are loaded with either drug or genetic therapeutic material and when they reach their targeted location within the body they are exposed to external ultrasound waves which cause the bubbles to pop and localize the delivery⁸⁵. The general mechanism in which this happens is once the ultrasound is applied, they undergo a gradual diffusion in which the lipid layer forms minor fractures in the surface due to the increase in pressure. This causes an outward force of bursting that then forms many smaller bubbles⁸⁶. The smaller bubbles can be detected using ultrasound imaging, while the outward burst causes a cavitation effect in nearby tissue⁸⁷⁻⁸⁹. The downside of MBs is their instability and difficulty to modify. As they are easy to pop, even the slightest modification to the surface can cause a decrease in yield.

Extracellular Vesicles: The newest type of delivery/contrast agent to be introduced into the literature are extracellular vesicles (**Figure 2C**). As biological based vesicles that are produced by every cell within the body, they have been investigated as therapeutic cargo carriers as well as specific diagnostic markers for cancers⁹⁰. They are separated into three categories based on size and surface markers:

1. Apoptotic Bodies (AB)
2. Microvesicle (MV)
3. Exosomes

Apoptotic Bodies: These vesicles are released from apoptotic cells during separation of the cell membrane during decay⁹¹. Typically, they have sizes greater than $1\mu\text{m}$ ⁹². Unlike their microvesicle and exosome counterparts, ABs are not popular for therapeutic or diagnostic use as their structures are less stable, have size limitations, many overlapping surface markers to that of the originating cell, as well as the distinct problem of being a cellular messenger for

programmed cell death⁹³. There are recent studies that have investigated using ABs as therapeutic vehicles to promote phagocytosis in area of interest⁹². Their diagnostic application now is limited to identification of apoptotic cells.

Microvesicles: Formed by outer budding of the cell membrane, MVs have been widely investigated due to their size (~100nm - 1 μ m), surface marker expression, and targeting ability of specific cells⁹⁴. Clinical studies have shown MVs can provide great diagnostic information about the aggressiveness of glioblastoma based on mRNA and protein expression through a simple blood test⁹⁵. MVs have been investigated as cellular communication vesicles, with particular emphasis on long range communication⁹⁶. In terms of diagnosis, this can be very helpful as they could potentially help identify areas of metastasis. Due to their size, MVs haven't been widely studied as delivery vehicles for brain cancers. It has also been noted that their mechanism of transport across the BBB, which is believed to be by membrane fusion, cannot be easily facilitated due to surface markers (mostly from the originating plasma membrane or cytoskeleton) that are present⁹⁷.

Exosomes: The most widely investigated extracellular vesicle for brain targeting. The main difference of origin of exosomes in comparison to MVs is the location where they are formed. Exosomes are found within multivesicular bodies (MVBs) which are formed by inward budding of the plasma membrane⁹⁸. Specifically, lysosomes will undergo microautophagy within the cell that starts the process for debris removal from the cell. During this process, late endosomes are formed. As exosomes are formed from the internal budding of the endosomal membrane, MVBs are created⁹⁹. When MVBs are formed, they are responsible for sorting/recycling proteins within the cell^{100, 101}. During the process in which late endosomes become MVBs,

intraluminal vesicles (ILVs, early exosomes) are formed from proteins captured during the endosomal process. As the MVB starts to interact with other organelles and vesicles, the ILVs morph into exosomes based on their surface markers and internal cargo. Finally, when MVBs are ready to release the internal contents, they will fuse with the plasma membrane and release cell debris, exosomes, etc. through exocytosis¹⁰². Exosome size (30-120nm) works great for high accumulation and easy detection of tumors due to their capability to fit within angiogenic formed blood vessels. The expression of CD63, CD81, CD9, and Flotillin-1 markers on their surface make them ideal for brain cancer detection and therapy based on their ability to cross the BBB innately^{12, 58, 59, 98, 103-108}. Coincidentally, MVBs also allow for exosomes to pass through the BBB through receptor-mediated phagocytosis⁹⁸. Since the exosomes are viewed as natural, they are not discarded by lysosomes and are allowed to proceed to the brain¹⁰⁹. Many studies have shown that based on the origin of the exosome, they can be used for specific brain tumor targeting indicating they can pass through both the BBB and the blood-brain tumor barrier with minimal loss¹¹⁰. Unfortunately, there are a few reasons why exosomes are not used clinically. The first being that exosomes can be difficult to detect using traditional imaging methods. As exosomes can only be tagged fluorescently, depth penetration becomes an issue. The second is that like many soft, lipid-based materials they are unstable and can lose therapeutic cargo over short periods of time¹⁰¹. Then finally, there are off-target concerns as the full role of exosomes within the human body is not fully understood. While these vesicles have a high affinity for cancerous tissue, there have been reports that exosomes can cause increased proliferation⁹⁸. As exosomes are used for cellular communication, the internal cargo as well as surface markers from those expelled from cancer cells can possibly cause tumorigenic

effects. It has been seen that gliomas that exist in hypoxic environments will secrete exosomes that can promote a M2 macrophage shift and increase tumor proliferation¹¹¹. While this could be problematic for the clinical translation of exosomes, further engineering of either surface markers or internal cargo has led to a decrease in tumorigenesis in many types of cancer¹¹².

Proteins and Peptides: It is a known fact that most nanoparticles without further surface modification have faster clearance, poor targeting ability, and aggregation issues^{113, 114}. For passive targeting of tumors, polymeric coatings such as poly-ethylene glycol (PEG) or poly-L-lysine (PLL), are common to increase circulation times but still rely on the Enhanced Retention and Permeability effect (EPR) for sufficient accumulation^{115, 116}. This unfortunately is not enough for use in identification and therapy of brain tumors as these coatings still prevent crossing of the BBB. This is why research has pivoted to the use of peptides, proteins, and more biomimetic structures to trick the transport proteins into allowing the particle to pass.

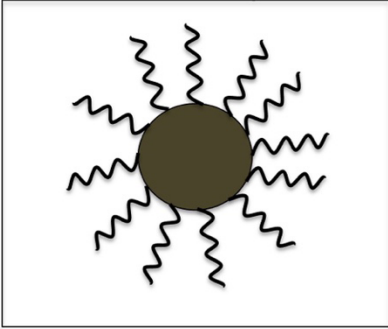
Proteins: Protein based nanoparticles have become of interest to researchers as they don't cause an illicit immune response and are easy to modify based on many different exposed end groups¹¹⁷⁻¹¹⁹ (**Figure 2D**). This can be shown in Gregory et al. where they engineered a synthetic protein consisted of Human Serum Albumin (HSA) and iRGD peptide that after IV injection was able to cross the BBB and deliver STAT3 inhibiting siRNA¹²⁰. Another example is the work done by Xu et al. in which they created cationic bovine serum albumin nanoparticles by conjugating PEG-PLGA to the surface. These particles showed efficient uptake within brain tissue¹²¹. While protein platforms have shown promising results, the main problem that must be addressed is targeting of the brain tumor itself. This is where peptides have been introduced.

Peptides: Peptides are short sequences of amino acids that can form proteins when chained together¹²² (**Figure 2D**). Based on their high binding affinity to specific surface receptors, they can be used to help identify tumors as well as be used as therapeutic agents¹²³. Certain peptides such as RGD, CooP, ACooPK, AP, T12, iNGR, cyclicRGD, Cilengitide, C6, UNO, tLyP-1, PL3, and others have been used for glioblastoma targeting and therapy^{124, 125}. All have different surface protein targets. A couple of the most common include T12 (Transferring receptor – TRf), RGD ($\alpha v \beta 3$, $\alpha v \beta 5$, and $\alpha v \beta 1$ integrins), C6 (MMP2/MMP9), and PL3 (Tenascin-C)¹²⁴. Many have been conjugated to nanoparticles for more effective delivery to the brain. Ruan et al. presented work on RGD modified micelles that were able to pass through both the BBB and BBTB and effectively deliver paclitaxel to orthotopic brain tumor bearing mice¹²⁵. Another study done by Lingasamy et al. conjugated PL3 peptide to both iron oxide nanoworms and silver nanoparticles to target and treat glioblastoma and prostate cancers. They were able to see high accumulation within subcutaneous tumors for both, but saw a reduced amount within their orthotopic glioblastoma model based on *ex vivo* results. Though in comparison to non-conjugated particles, there was a significant amount that accumulated within the brain region¹²³. Even though peptides can be very effective theranostic agents, they are expensive to manufacture and have short-term stability which makes clinical translation difficult¹²⁶. Overall, there are many types of surface modifications that can be done to increase delivery and therapeutic effect for brain tumors^{126, 127}. Protein and peptide delivery systems have been some of the most promising technologies.

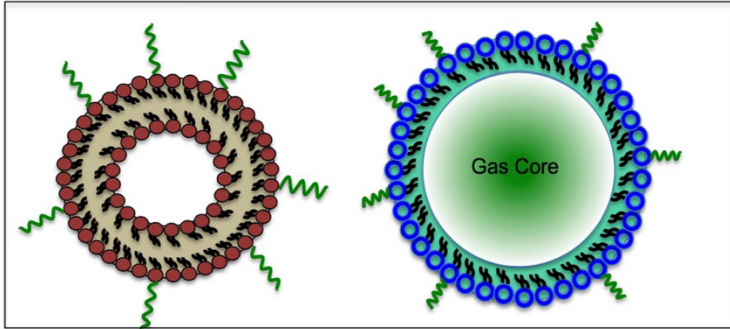
Overall, there are a few types of nanoparticles that stand out for glioblastoma theranostics. Ranging from inorganic nanoparticles such as iron oxide to biological structures

such as proteins and extracellular vesicles. They all have advantages and disadvantages, which is why there is a need to develop new nanomaterials that can build upon the foundation already laid by the clinically approved particles. The goal is to improve patient outcomes for glioblastoma and help increase overall quality of life.

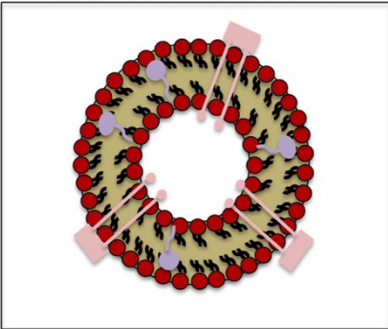
A. Iron Oxide Nanoparticles



B. Liposomes and Microbubbles



C. Extracellular Vesicles



D. Peptides and Proteins

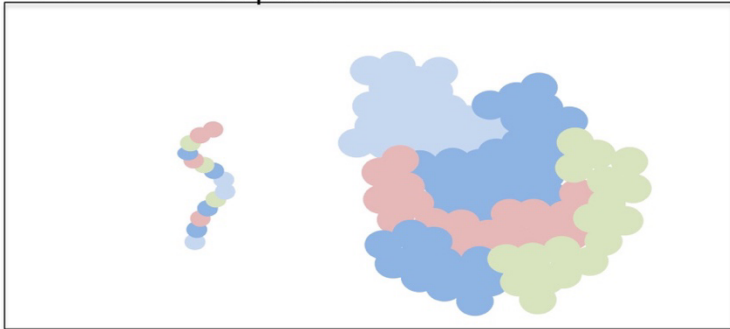


Figure 2: Representative graphic of nano-based technologies used for brain cancer diagnosis and therapy. (A) Iron oxide Nanoparticles with a PEG coating. (B) Liposome and microbubble structures. (C) Extracellular vesicle general illustration. (D) General peptide and protein illustration.

1.3: Imaging Modalities for Glioblastoma

The first step that any patient with potential glioblastoma symptoms will take is a diagnostic procedure. This can range from a simple x-ray to a Magnetic Resonance Imaging (MRI) depending on the density/location of the tumor. The main types of imaging used for diagnosing glioblastoma are MRI, Computerized Tomography (CT), Positron Electron Tomography (PET) and Photoacoustic Imaging (PAI)^{68, 128}. These methods serve different areas as they represent differences in cost, depth, sensitivity, spatial resolution, etc. So, it is important for a wide variety of imaging techniques be available to clinicians to help diagnose patients early.

Magnetic Resonance Imaging: The most common imaging technique used to diagnose glioblastoma^{116, 129-132}. When a patient is inserted into an MRI machine, an external magnetic field is applied which aligns all the H⁺ ions within the exposed area of the body along the z-axis. This creates a nominal amount of energy that can be transferred into an MRI image. As the amount of energy can only give one sort of contrast in an image, radiofrequency (RF) coils/pulses are implemented to shift the direction of alignment to along the x-y axis. The RF pulse is considered a B1 pulse as it shifts the paradigm from B0 (z-axis) to B1 (x-y axis). This transverse magnetization that is formed is picked up by an external coil (the RF coil) and corresponds to a direct correlation to the number of H⁺ ions in a given tissue. Now, there are two main types of relaxation times that come from these signals: T1 and T2. T1 is the time for vertical magnetization to return to the normal spin state, while T2 is the time for the transverse magnetization to return to the normal spin state. Tissues with more water presence (higher H⁺) have higher T1 contrast as less energy is needed to shift from the normal spin state to the vertical magnetization (z-axis)¹³³. As the magnetic field is applied to an individual inside of an

MRI, certain areas experience differences in magnetic frequency to obtain a distinguishable image of a specific organ. Specifically, the spin resonant frequency coupled with the pulsed frequency from the coils helps to identify different types of tissue in a single image. Proton density, T1/T2 relaxation time, spin resonant frequency, and the pulsed frequency directly influence the quality of the image¹³⁴. Clinically used contrast agents such as gadolinium chelating agents, iron oxide nanoparticles, etc. help increase contrast for either T1 or T2 imaging¹⁴.

As neurosurgeries have become a more common within recent years for a wide variety of neurological disorders, MRI has evolved to help enhance these methods¹³¹. For traditional MRI, a pre-operative set of images of the brain would be taken and referenced during the surgery to ensure the location (for tumor resection, electrode placement, epileptic lesion removal, etc.) is accurate¹³. The surgery would then be performed, and a post-operative image would be taken to determine if, for example, a tumor has been removed completely. Unfortunately, once a hole is made into the skull, there can be a shift in placement in the brain due to cerebral fluid (CF) loss, tissue retraction due to fluid loss, as well as small discrepancies between when the pre-operative image was taken and the surgery¹³⁵. Intraoperative MRI (iMRI) works by taking real-time images of the brain during the surgical procedure¹³⁶. A small-based MRI machine with a 3T magnet is used when all metal objects are moved outside of a certain boundary. At different points throughout the surgery, the iMRI will be wheeled to the patient and an image will be taken. After the image is taken and the iMRI is wheeled away, all metal surgical tools can move back to the patient and then the surgeon continues with the procedure. This system is very convenient for doctors to accurately be able to tell if the entirety

of a tumor/lesion has been removed in real-time without having to subject the patient to a surgery later¹³³.

PET: Positron electron tomography (PET) is one of the newest editions to imaging. Based on the signal of radio-nucleotides that are injected as contrast agents, this imaging modality has little depth penetration issues^{137, 138}. Specifically, it looks at the metabolic and biochemical interactions within the body. After a tracer is injected into the patient, it will start to emit single positron that will interact with nearby tissue. This produces a set of photons that are picked by scintillation crystals within the surrounding PET cameras that are then converted into an image¹³⁷. The primary benefit of PET imaging is that it has no depth penetration limitations. This allows for a virtually perfect signal to be obtained. Unfortunately, PET gives no information of the anatomical structure within the body so it can be hard to distinguish where exactly the signal is coming from. As a result, it is commonly paired with either MRI or CT. For brain tumor detection, it is common to use the tracers to overlay PET and MRI to determine areas of blood flow that can help properly identify tumor boundaries^{139, 140}.

Computerized Tomography/X-ray: Computerized tomography (CT) and X-ray are two very similar imaging techniques used within the clinical setting. The primary difference between the two is the delivery of the x-ray beams to the patient. For a traditional x-ray, a single beam is directed at the patient that stands between the source and the detector. Since x-ray beams interact with higher density materials within the body, a shadow-based image is formed by the detector. While this procedure is very straightforward and fast, the patient must be oriented many ways to get a full spectrum of images to see the uniformity of the area being investigated¹⁴¹. This is why CT was developed. CT machines allows for x-ray beams to rotate

around the patient as the patient slowly moves through the tube. This allows for more robust 3D images to be produced that can accurately help the physician determine what the issue may be¹⁴². While X-ray and CT cannot provide accurate information of tumors within the brain due to the density of the skull, it can help determine areas of metastasis as well as how to proceed for certain types of treatment.

Photoacoustic Imaging: Photoacoustic imaging (PAI) is one of the newest additions to the diagnostic field for brain related diseases. Combining both optical and acoustic imaging techniques, it has revolutionized the field due to its unique capabilities. PAI works based on a “light in, sound out” approach¹¹⁷. Pulsed laser light is used to excite the exposed tissue through thermoelastic expansion¹¹⁶. This expansion allows for minute acoustic waves to form that can be picked up by an external transducer. The signal is typically overlaid with traditional ultrasound for anatomical structure^{116, 143}. For certain signals such as hemoglobin, deoxyhemoglobin, or mSO₂, a contrast agent is not needed as the substances themselves convert the light energy. This is helpful as these signals can help determine tumors, areas with lack of blood flow (hypoxia), inflammatory regions, etc¹⁴⁴. With photoacoustic imaging, regions that present high levels of deoxyhemoglobin are typically associated with hypoxia or high inflammation as these conditions rely on environments with low oxygen levels. As hemoglobin and deoxyhemoglobin are endogenous contrast agents, they can be observed with photoacoustic imaging, but cannot deduce what the exact disease or condition is in the region without further testing. These signals while helpful, alone they can’t accurately distinguish the border regions of tumors or inflammatory regions. As a result, a wide variety of contrast agents have been developed for *in vivo* imaging of many different diseases using mouse models.

Unfortunately, very few can be translated to larger animal models due to depth penetration limits as well as toxicity problems. As PAI is still based on an optical setup, translation to the clinic has been difficult. There are preliminary studies for use in breast cancer detection, but full FDA approval is still in progress. For brain diseases, there are studies that have looked at stroke, epilepsy, tumors, etc. based on the combination of deep penetration of ultrasound imaging and high image resolution from optical signatures^{37, 116, 145-147}. These studies have shown that PAI is highly accurate in determining these areas of injury or disease^{130, 148}.

1.4: Therapeutic Strategies for Glioblastoma

Once a brain cancer is properly diagnosed, a patient is given a few options for therapy to push towards remission. These usually include surgical resection (if possible) coupled with chemotherapy and radiation. As gliomas are invasive cancers that usually form within the frontal and temporal lobes, only certain tumors can be removed without making quality of life for the patient worse¹⁴². Newer therapies introduced through Medtronic with their Visualase™ MRI-guided laser ablation system, have given clinicians a different option for patients with chemo-resistant or inoperable tumors¹³¹.

Surgical Resection: For glioblastoma, surgical resection is one of the most utilized techniques to reduce overall tumor size and extend the patient's life^{13, 14, 136}. Once the tumor is identified through MRI and surgical biopsy, the removal is planned based on the location of the tumor. Once determined, the patient will either be kept awake during the surgery or kept under anesthesia. Instances in which the patient would be kept awake include if the tumor is located near the motor functioning cortex, Broca's area for speech, or presses against the occipital lobe that affects vision. During this time, the surgeon will ask the patient questions to determine if

there has been any irreparable damage done while removing the tumor. In instances of glioblastoma, this is particularly important as the cells infiltrate healthy tissue and thus can be difficult to remove without affecting surrounding astrocytic and neuronal cells.

There are two common methods for tumor removal: fluorescence-guided surgery and neuronavigation. Fluorescence-guided surgery is done typically by systemically injecting 5-aminolevulinic acid (5-ALA) that can be metabolized by tumor cells to allow them to be detectable under UV-light^{149, 150}. During the surgery, blue light will be illuminated onto the exposed tissue region to show the tumor region as a bright red color. This allows the doctor to remove as much of the tumor as possible with a much safer approach. The second, neuronavigation, is based on orienting the patient's head within a stereotaxic device and doing intermittent intraoperative MRI (iMRI) imaging during the surgery. This helps to determine exactly the site of the tumor based on changes in the tissue packing after the incision is made.

Radiation: Radiation is one of the two most common treatment methods used for cancer treatments due to deep depth penetration. A highly ionized beam is pointed at the general location of the tumor which allows ionized atoms to form around the tissue that causes DNA damage¹⁴¹. This prevents cell division and promotes cell death within the exposed region. The problem with radiation therapies is that healthy and cancer cells alike can experience cell death if exposed to the beam. For tumors that are deeper within the body, this can harm major organs and increase the chance of cancer forming in other parts of the body.

For patients diagnosed with glioblastoma, there are two types of radiation treatment that can be done: whole-brain radiation therapy and stereotaxic radiosurgery^{151, 152}. For smaller tumors that are difficult to see under MRI, whole-brain radiation therapy is done. This is where

the entire brain of the patient is exposed to the radiation beam at a much lower intensity. Due to the breadth coverage, there are many side-effects that can occur. These typically include memory loss, cataracts, and a small chance of motor impairment¹⁵³. The other type of radiation therapy, stereotaxic radiosurgery, is more involved but tends to be more effective. This therapy involves a high energy beam directed at exactly the tumor site. To perform this type of treatment, the exact location of the tumor must be known. This is done through an initial MRI scan which helps determine the depth as well as the location to vital parts of the brain. While this can limit the number of side-effects, the high ionization can still cause local inflammation within the brain which can lead to other problems.

Chemotherapy: The primary treatment method used for patients diagnosed with cancer is often chemotherapy. The drugs that are approved work through many different mechanisms such as DNA destruction, prevention of catalytic activity in the cell, reduction of cell metabolism, RNA interference, impede protein formation, etc^{27, 46}. Chemotherapeutics typically rely on passive targeting of the tumor site. In specific, once the drug is intravenously injected a portion will accumulate within the cancerous site due to an increased independent blood supply that the tumor forms. This is inefficient and typically causes many side-effects as the drugs are toxic to cancerous and healthy cells alike¹⁵⁴. There has been research done to improve circulation time as well as improved accumulation with carrier-based vehicles such as liposomes. There have been successful liposome-drug formulations. such as Doxil[®] or Lipusu[®], that have been FDA-approved and beneficial to the clinic. Unfortunately, due to the instable nature of liposomes, they can have premature release and can be difficult to manipulate for

active targeting⁷⁶. This is why there is still a great need for a better drug delivery platform for patients with cancer.

In the realm of glioblastoma treatment methods, there are limited drugs within the clinic that can be used due to the impenetrable nature of the BBB. For all of the drugs FDA approved in the US. There are currently only 20 drugs that are FDA approved for treatment of brain tumors. Out of the 20, five are used for glioblastoma, three for astrocytoma, and 2 for neuroblastoma⁴⁶. Those for glioblastoma are listed in **Table 1**. There are other types of chemotherapeutics that are used in combination for treatment of gliomas that are not listed due to the inability to work as a single agent.

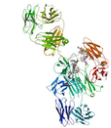
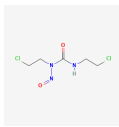
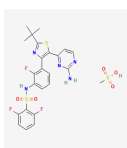
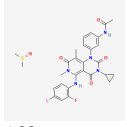
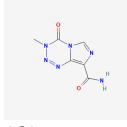
Name of Drug	US Brand Name	Type of Drug	Mechanism of Action	Chemical Structure	Primary Use	Can pass through BBB?
Bevacizumab	Alymsys, Avastin, Mvasi, Zirabev	Antibody	Binds to circulating Vascular endothelial growth factor (VEGF) ¹⁵⁵ .	 156	Patients that have a reoccurring brain tumor	Yes, but limited
Carmustine	BiCNU	Drug	Prevents cross-linking in DNA.	 157	Adjuvant drug to help reduce size of primary tumor	yes
Dabrafenib Mesylate	Tafinlar	Drug	Acts as a reversible ATP-competitive kinase inhibitor to prevent catalytic activity within the cell ¹⁵⁸ .	 159	Low grade gliomas diagnosed in children >1 year who require systemic therapy.	no
Trametinib Dimethyl Sulfoxide	Mekinist	Drug	Acts as an inhibitor for MEK1 and MEK2 to prevent catalytic activity within the cell.	 160	Low grade gliomas diagnosed in children >1 year who require systemic therapy.	Yes, but limited
Temozolomide	Temodar	Drug	Binds to DNA to prevent cell division ⁶ .	 161	Used in partner with radiation therapy.	yes

Table 1: Overview of Current Chemotherapeutics used within the Clinic for Gliomas. Mechanism of action, ability to cross the BBB, structure, and clinically used name are listed.

As gliomas are the most common type of brain cancer, it is not surprising that 25% of the FDA approved drugs for brain cancers are used for treatment of it. With such a limited number available, there is an extreme need for new therapeutics to be developed. Unfortunately, there are a wide variety of other drugs that could be effective, but due to poor blood transportation they cannot be used for brain cancers. If a new type of carrier can be developed, this can be overcome and open the door for enhanced chemo and dual therapies.

Photothermal and Photodynamic Therapies: These are the newest type of minimally invasive therapies to be introduced in the fight against cancer^{62, 162-164}. The general mechanism behind both photothermal and photodynamic therapy is relatively the same, but the method by which they reduce tumor size is different. A continuous laser light is used to excite a material within the body that will then cause a response in terms of elevated temperature (photothermal) or formation of radical species within the environment (photodynamic). Both methods are non-invasive and targeted therapies. The laser used is not harmful to the patient, which allows only the areas in which the laser and the excited material contact each other to experience a therapeutic effect. Overall, these methods provide a minimally invasive option to surgical resection to reduce tumor size and extend patient lifespan with the potential to be provided in an out-patient setting^{114, 131, 162, 165}.

Photothermal Therapy: Photothermal therapy is based off the principle that if tumor cells are heated beyond a certain temperature, apoptosis will occur. A photoactive material is injected into the patient either locally or intravenously and then the region of interest is exposed to a laser. Typically, these lasers range from ~600-1000nm as that is the primary penetration range for the biological transparency window. When the material is exposed to the laser energy, the

surface atoms of the material will become excited and start to vibrate. This vibrational energy will start to generate local heat with the local region that will slowly start to heat the space that can cause cellular apoptosis at 50°C^{166, 167}. As this type of therapy is relatively localized, it is effective in only killing the cells of interest. While the therapy is highly effective in this manner, it has the disadvantage of inducing local inflammation and burning within the region¹⁶⁸. This causes discomfort and pain for the patient. In respect for use in the brain, this type of therapy is very difficult to implement due to penetration of the laser through the skull. As the skull is made of dense bone material, majority if not all of light exposed will be either absorbed or refracted¹¹⁶. This prevents any therapeutic effect from happening and thus can be difficult for translational use. Within the past ~5 years this has been investigated and rectified with the innovation of Laser Interstitial Thermal Treatment (LITT) systems. These systems work by drilling a small bur hole into the skull and inserting a laser-based line into the tumor site using MRI guidance. This basic operation would allow for the patient to be in and out of the hospital in one day with minimal off target side-effects¹³¹. The laser used is high energy and high wavelength (800-1064nm) with the aim for tumor ablation without the use of an amplifying agent. There are at least two FDA-approved systems: Visualase[®] and NeuroBlate[®] which is promising for this field. Unfortunately, due to the uncommonness of this type of therapy in the clinic many patients are not given the option. Therefore, the efficacy in comparison to other common practices is relatively unknown at this time.

Photodynamic Therapy: The main difference between photodynamic therapy and photothermal therapy is the type of photoactive material used and the mechanism in which apoptosis is initiated. In general, when the photosensitizer material is excited by laser light, reactive oxygen

species (ROS) are generated. Specifically, when the photosensitizer absorbs light, it transfers the excess energy in the form of electrons to surrounding molecular oxygen species. When the photosensitizer reaches its unstable excited state, it will normally transfer a portion of its energy to molecular oxygen which will then produce singlet oxygen species ($^1\text{O}_2$)¹⁶⁶. This is known as a type one reaction. The second type of reaction that can occur is when the electron transfer happens with a solid substrate. This can be a cell membrane, surface protein, molecules, etc. When this phenomenon happens, ROS species such as: O_2^- , H_2O_2 , or OH^- , can be formed. Whether produced by a type one reaction or type two reaction, these species will cause cell death due to oxidative stress that is promoted within the cell¹⁶⁹. While photodynamic therapy can prove to be effective on a small scale, it has had problems translating into the clinic. This is primarily because the therapy is not completely successful at eradicating tumors by itself. The photosensitizer materials can also have solubility and aggregation issues which prevent clinical translation.

Light-based therapies have shown to be successful in certain aspects of solid tumor treatment. For tumors that are close to the surface of the skin, both photothermal and photodynamic therapies can provide enough energy to reduce size of the mass. While there have been new technologies developed to deliver laser power internally with minimally invasive techniques, this is limited to photothermal therapy. More research must be done to determine the effectiveness of these therapies in comparison to commonly used procedures. If proven to be better for a wide variety of cancers, it is possible that these types of therapies will become more used.

1.5: FDA Approval and Future Clinical Translation to Improve Patient Outcomes

The U.S. Food and Drug Administration (FDA) is the primary department in the United States designated in approving medical technologies and methods. While they are not in charge of what gets approved for use in other countries, they are one of the most stringent organizations when allowing new technologies to reach the clinic. As thousands of technologies are submitted to the FDA each year, only a handful make it to the patient. This is due to the class system in which the FDA uses to test the submitted technologies and determine which will be safe to use. There are five steps total: 1. Discovery and Development, 2. Preclinical Research, 3. Clinical Research, 4. FDA Review, and 5. FDA Post-Market Safety Monitoring. With glioblastoma being one of the hardest diseases to combat with modern FDA-approved technologies, there are many new drug combinations, systems, and diagnostic agents that go through this process. With only five approved drug agents for use against glioblastoma, it can be said that most preclinically investigated substances fail at one of the many stages or phases during approval.

Stage one represents research done in the laboratory setting. Once a promising agent (therapeutic, diagnostic, etc...) is determined, further research is done on the *in vivo* level to determine the biodistribution, off-target, and metabolic effects. Way of administration, dosage, interaction with other drugs, and effectiveness on different types of people is also looked at. This is the stage in which most agents that are aimed to be used for glioblastoma seem the most promising. Usually research is done in subcutaneous or orthotopic mouse models, which give valuable information but can skew the expectations of translation to bigger *in vivo* models. To investigate this primary problem, the technology is moved to stage two. Bigger animal models such as rats, dogs, or primates are used to validate distribution patterns as well as

toxicity and optimal dosage. These are the most accurate models for glioblastoma as some of these models can have naturally occurring brain tumors that can test the feasibility for clinical use.

Once the agent is determined to be promising for clinical translation, it is filed for stage three approval. This is the stage in which most technologies are rejected by the FDA. While the first two stages are done at the laboratory setting while following proper FDA guidelines, stage 3 requires full FDA oversight. The clinical phase research is split into three different trials in which the candidate material must pass in order to move on to the next stage. All clinical study numbers come from clinicaltrials.gov¹⁷⁰. It should be noted that not all clinical trials are taking place in the United States. For phase one studies, ~70% of test candidates will pass. As of January 2024, there are 69 early Phase 1 studies occurring for glioblastoma, with 23 currently looking for patients and 19 completed. Besides this, there are 795 ongoing Phase 1 studies taking place. 140 are looking for patients and 385 have been completed. Moving to phase two, only 33% will pass to phase 3. There currently has been more success for drugs aimed at glioblastoma treatment as there are 865 ongoing Phase 2 studies. 127 are recruiting and 405 have completed. The number doesn't match the estimated percentage drop in drugs that pass but indicates that the quality and success has gone up those meant for glioblastoma. For phase 3, ~20-30% of candidates will pass. The amount of studies drops dramatically down to 104 ongoing Phase 3 studies with 15 recruiting and 44 completed. This is very close to the number estimated to pass. This indicates that when tested in a larger population, results were inconclusive or provided data that the drug has too many adverse effects that can be life-threatening. Finally, for stage four there are currently 6 ongoing studies with 3 recruiting and 1

completed. With a total of 1,839 studies going on through all four phases, only 0.3% exist within the last stage. Based on this information and similar results from previous years, there is a less than one percent chance that an agent aimed for glioblastoma treatment or diagnosis will be used long-term within the clinic.

The last two stages, four and five, determine if the candidate material has shown potential to be widely distributed as a clinically used agent. This is the point in which an official application for a new therapeutic and/or diagnostic modality is submitted to the FDA for review. The selected committee will then meticulously review all the gathered information from both laboratory and clinical stages. Once approved the drug is manufactured on a large scale.

For glioblastoma diagnosis and treatment agents there are very limited agents that have made it through stage 4 of FDA approval. This includes 5 drugs used for treatment and a handful of diagnostic agents that are commonly used for general enhanced contrast imaging. The biggest obstacle that researchers have when trying to get a candidate approved for use in patients with glioblastoma is that the candidate must be able to pass through the BBB and it must not interfere with major parts of the brain. Most of the proposed materials fail both criteria and therefore fail at the first stage of approval. The overall loops back to why glioblastoma is so deadly and quality of life for patients is low. With limited options for early diagnosis and effective treatment, it is critical that a new theranostic agent be developed to bridge the gap between palliative care and remission.

Chapter 2: Exosome Coated Prussian Blue Nanoparticles (Exo:PB) for Early Detection and Treatment of Glioblastoma

The work presented in this chapter is readapted from Hill, M. L. et al. Exosome-Coated Prussian Blue Nanoparticles for Specific Targeting and Treatment of Glioblastoma. *ACS Applied Materials & Interfaces*. **2024**, 16 (16), 20286-20301. DOI: 10.1021/acsami.4c02364¹⁷¹.

2.1: Introduction

Chemical Synthesis: Prussian Blue nanoparticles (PBNPs) are an FDA-approved agent for use in removal of heavy metal toxins within the body due to radiation poisoning¹⁷². Based on their FCC lattice structure, PBNPs can easily absorb certain heavy metals such as thallium and cesium¹⁷³. The outer matrix consists of a Fe^{3+} -CN- Fe^{2+} repeating sections that when formed creates pockets within the inside of the structure that can hold positively charged ions. With PBNPs having a surface charge of around -40mV with the number of cyanide groups present, large positively charged ions within the surrounding environment are easily taken up to help try and balance the overall charge of the particle^{8, 116, 174}.

The synthesis of PBNPs is quite straightforward and cheap process. There are a few different chemicals that have been used, but the most traditional reaction is a co-precipitation between potassium ferrocyanide ($\text{K}_4[\text{Fe}(\text{CN})_6]$) and iron (III) chloride (FeCl_3) in the presence of a surfactant^{8, 116, 175-177}. The type of surfactant used must be able to form a complex with the iron chloride that doesn't hinder the reaction with the potassium ferrocyanide. These are typically carboxylic end group dominant structures such as citric acid or poly-L-lysine (PLL)^{116, 148, 168, 176, 178}. Typically, the electron configuration of iron ($1s^12s^22p^63s^23p^64s^23d^6$) would only allow for 3 bonds to form with the single electrons within the third d orbital. Iron can exist in other ion

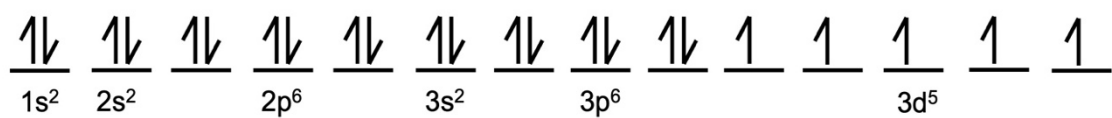
states such as Fe^{2+} , Fe^{3+} , Fe^{4+} , and Fe^{6+} based on the elements ability to donate excess electrons. As Fe^{2+} and Fe^{3+} are the most favorable states for iron to exist in, it is not surprising that these are the two ions that are based within the PBNP structure (**Figure 3**).

Citric acid coated PBNPs are the most commonly used within the literature^{116, 179}. This is due to cheap and easy fabrication with an emphasis on monodisperse particle population and good size control^{8, 175}. The first step in synthesizing the particles is mixing FeCl_3 and citric acid within a DDI water solution. FeCl_3 exists as an ion solution as free suspended Fe^{3+} and Cl^- ions. Once citric acid is introduced into the solution, the carboxylic end groups are hydrolyzed to form carbonyl end groups that can then bond to the free form Fe^{3+} ions to form an iron-citrate complex. Each Fe^{3+} ion can bond with 3 citric acid molecules as two CO groups covalently attach to one portion of the iron. Traditionally, Fe^{3+} would only be able to form 5 bonds based on its electron configuration, but in certain conditions is can for 6 based on the ability to rearrange its outer electrons into different orbitals¹⁸⁰. In the case of iron-citrate, the citric acid acts as a ligand in order to form a coordination complex with the iron. Each CO group that bonds with the central iron wants to donate its extra electron to become a stable structure. To create an even coordination complex, three citric acid molecules will bond with the central iron in which the last CO group will donate an electron to give the overall complex a -1 charge (**Figure 4A**). The outer electrons for the Fe^{3+} are rearranged to accommodate the extra electron by adding the 4s orbital ($1s^2 2s^2 2p^6 3s^2 3p^6 4s^1 3d^5$). After the iron-citrate complex is formed, $\text{K}_4[\text{Fe}(\text{CN})_6]$ is added dropwise at 60°C . As it is added the color will shift from a slight yellow (iron-citrate) to a dark blue color. This is indicative of the co-precipitation between the iron-citrate and the potassium ferrocyanide, in which the Fe^{2+} and Fe^{3+} ions are connected by cyanide bridges. The

iron-citrate complex will lose one of the citric acid molecules and form a coordination bond with the one of the nitrogen atoms within the potassium ferrocyanide structure. This allows for each Fe^{2+} ion to continue to make six bonds and each Fe^{3+} ion to make five. Overall an FCC lattice structure is formed with alternating Fe^{2+} and Fe^{3+} with citric acid attached to the outer surface^{176, 181}. This structure allows for the great NIR absorption by intervalence charge-transfer on the $\text{Fe}^{2+}/\text{Fe}^{3+}$ and easy modification of the surface due to the exposed OH groups^{8, 115, 116, 177, 181, 182} (**Figure 4B**).

Electron Configuration of Fe ions within PBNP Structure

Fe^{3+}



Fe^{2+}

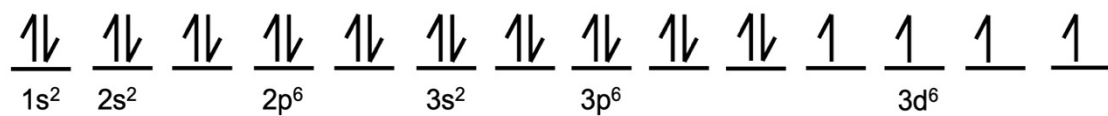


Figure 3: Electron configuration of Fe^{2+} and Fe^{3+} present within the PBNP Structure. Arrows indicate electron spin within s, p, or d orbitals.

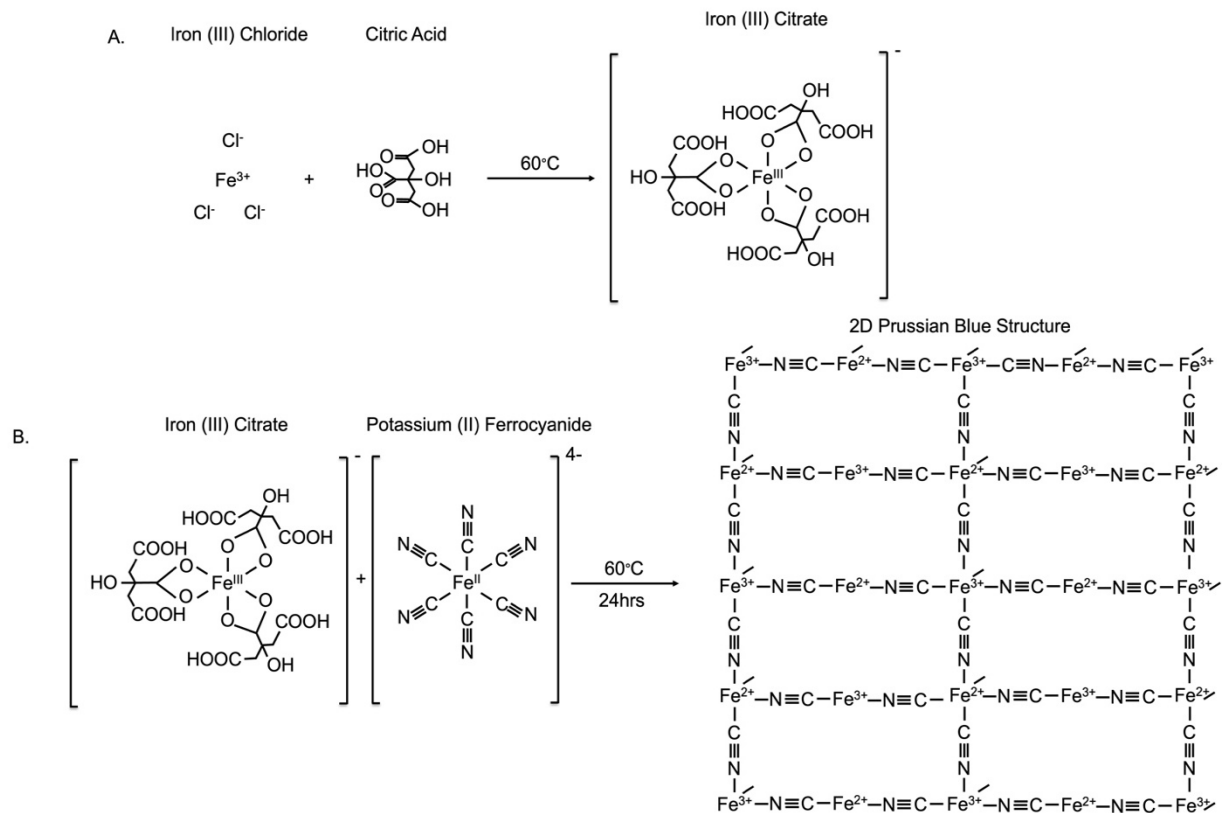


Figure 4: Reaction mechanism for Prussian blue nanoparticles. (A) Formation of iron citrate complex. (B) Reaction to obtain PBNP particles based on the co-precipitation between iron (III) citrate and potassium (II) ferrocyanide.

PBNP History and Transition into the Clinical Setting: Compared to other FDA-approved drugs, Prussian Blue has a unique history. In 1706, it is stated that it was first discovered when an artist was trying to create a red paint by combining potash, pyrite, and what was assumed to be animal blood¹⁸³. Due to the iron composition within the different types of rock and blood, a Prussian blue complex was formed which turned the pigment a dark blue color. Over time, the general components to make Prussian blue were changed to an oxidation process to maximize the amount of iron ions within the solution¹⁸⁴. Most commonly known as the Milori process, named for the company that the process originated from, a large vat of copperas (iron sulfate), ammonium sulfate, sodium sulfate, and sulfuric acid are mixed at 80-90°F. Sodium ferrocyanide is added slowly, which starts to form a white precipitate known as Prussian white. This is heated to 167°F and more sulfuric acid is added. To start the oxidation process, sodium chlorate is added to the vat which will slowly produce the blue pigment^{184, 185}. There are two types of intermediate materials that can be made. One previously mentioned is Prussian white, which is the insoluble version¹⁸⁶. The other is Prussian green, which is a partially oxidized complex that forms between Prussian white and Prussian blue¹⁸⁷. While this method is very effective at creating mass quantities, the size control is very poor (micrometer sized particles), making them useful for only industrial and artistic applications¹⁸⁴.

Transition into the medical clinic started when researchers saw that PBNPs can effectively take up radioactive compounds within the surrounding environment of the particle. Throughout the 1980s and early 2000s there have been many radioactive accidents that have resulted in hundreds of individuals obtaining radiation poisoning. Starting with the Chernobyl disaster that occurred in Pripyat, Ukraine in 1986, PBNPs were used widespread as an antidote

to improve patient outcomes^{188, 189}. While they had been previously used within the clinic with a minimal number of patients, it was the aftermath of the Chernobyl disaster that allowed Prussian Blue to be tested on a large population and eventually gained FDA-approval within the United States in 2003¹⁷². Based on the FCC lattice structure that PBNPs exist in, large heavy metal ions present within the body are absorbed into the open portions that potassium ions typically compete for¹⁷⁹. This happens based on an ion exchange that occurs within the gastrointestinal or liver regions of the body as PBNPs are taken as an oral agent. When the particles encounter high amounts of large radius ions, they perform an ion exchange with the potassium ions present within the structure¹⁹⁰. Naturally, as the number of thallium or cesium increases within the environment of the particles, they will slowly replace the potassium within the structure. Since the radioactive ions have larger ionic radii, they get stuck in the empty spaces of PBNPs and are safely excreted from the body through the gastrointestinal tract^{173, 191}. Results have shown that Prussian Blue can result in a decreased excretion time for cesium from 110 days to 30 days and decrease the elimination rate of thallium from 8 days, down to 2 days¹⁹².

Applications in Cancer: After their FDA-approval as a radiation exposure antidote, PBNPs were widely researched for other medical applications. With a peak absorbance between 700-750nm and the ability to easily manipulate the structure, many scientists explored their application for cancer^{8, 129, 168, 175, 182, 193-198}. Many studies have looked at using the particles for photothermal therapy, sustained drug release for targeted drug delivery, anti-inflammation effects, high-intensity focused ultrasound, photodynamic therapy, and use as contrast agents for MRI, photoacoustic, CT, surface-enhanced raman scattering (SERS), fluorescence, PET, and

ultrasound. Since the structure can easily be modified, all these different types of therapies and diagnostic methods can be enhanced. For just PBNPs, they have an innate ability for photothermal therapy, MRI, anti-inflammation, sustained drug release, and photoacoustic imaging without any extreme change to the particle.

Photothermal Therapy and Targeted Drug Delivery: The most popular therapeutic strategy for PBNPs is photothermal therapy. This is because of the high light absorbance profile within the biological transparency window and high photo-stability^{8, 148, 182, 195}. They are the ideal substitute for often used gold nanorods (AuNRs) which suffer from photodegradation¹⁹⁹⁻²⁰¹. Xie et al. showed promising effects of PBNPs intratumorally and intravenously injected into 4T1 xenograft bearing mice and exposed to an 808nm laser for up to 10 minutes. Results showed that IT showed the highest temperature gain at ~60°C, in comparison to IV with a maximum temperature of 45°C, there was still tumor size reduction in both groups with no statistical difference¹⁶⁸. In another study, Fu et al. used iron oxide nanoparticles coated with a Prussian blue nanoshell to enhance magnetic targeting, MRI imaging contrast, and photothermal therapeutic effect in a U-87 subcutaneous tumor model. They were able to see almost full remission of the tumor after 18 days of intravenous treatment while also being able to gain great tumor contrast using MRI after injection²⁰². While photothermal therapy can be an effective independent therapy, cancer cells can become less responsive to it over time²⁰³. It can also cause extreme amount of necrotic tissue to form which can be uncomfortable and painful for the patient²⁰⁴. This had led researchers to try a variety of combination therapies. Lu et al. looked at using hollowed out Prussian blue nanoparticle structures to passively load doxorubicin (DOX) into and allow for a sustained release over time once within the tumor area

and combine this with photothermal therapy to increase the efficacy against tumor cells. Based on the structure of the particle, they were able to show that when exposed to an 808nm laser, DOX would be released. When not exposed to the laser, DOX would remain within the structure, thus allowing for an advanced delivery tool that minimizes off-target chemotherapeutic effects. When xenograft HeLa bearing mice were injected with these particles, the DOX loaded particles were shown to have a greater effect at reducing tumor size than the non-DOX loaded PBNPs over the same 14 days treatment period²⁰⁵. This is promising as it shows that base Prussian blue nanoparticles can be improved with changes to their structure. Whether that be inclusion of a drug, another type of nanoparticle, or another metallic ion to enhance imaging capabilities. With it being a highly manipulative structure, PBNPs have great potential within the clinical setting for a wide variety of application.

When PBNPs are synthesized, they are solid structures. This can be changed when exposed to a solution of hydrochloric acid (HCl) that will slowly start to etch the foundation. During this process, HCl reacts with the potassium ferrocyanide to produce ferric ferrocyanide²⁰⁶. This causes pockets within the lattice to form and create a mesoporous formation. Hydrophobic drugs such as doxorubicin or paclitaxel, can easily be loaded by mixing with the particles¹⁹⁵. Quantification of the loading capacity is done by centrifuging the particles and measuring the amount of drug within the supernatant. Jing et al. showed that PBNPs could be loaded with 10-hydroxycamptothecin and injected into HeLa bearing subcutaneous mice. They were able to show that through a combination therapy of photothermal and directed chemodrug, there was no tumor reoccurrence 18 days after treatment¹⁸². This is promising information as single treatment types often show limited results and high rates of the cancer

reappearing in the future. Now because of PBNPs innate ability for energy transfer from light to heat, majority of the literature presented for use in cancer has combined targeted drug delivery with PTT to enhance local effects. Unfortunately, the preparation of hollow or mesoporous based PBNPs can be dangerous as cyanide gas is a direct product of the etching process²⁰⁷. This can make scaling efforts difficult and dangerous, which could prove clinical translation problematic. Xu et al. investigated this and tested a wide variety of reaction conditions to yield monodisperse particles with consistent porosity. They found that by increasing the amount of HCl present within the solution increases the overall size of the particles, but by matching with the proper concentration of surfactant were able to get uniform spherical particles of ~69.05nm. To test their application for biological systems, PAI and T₁/T₂ MRI imaging was done and showed linear correlation with concentration and in vivo detection within 4T1 subcutaneous bearing mice¹⁹⁸. There have been many studies that have shown that hollow or mesoporous based PBNPs structures can enhance their imaging capabilities. For PAI and MRI, there are more exposed atoms for either H⁺ or the laser to interact with. This indicates that there is an area in which hollow/mesoporous PBNPs could be used within the clinic for a wide variety of reasons.

Magnetic Resonance Imaging: Iron based nanoparticles have been a staple in MRI contrast agents for the past 30 years because of the strong spin interaction they have with tissue in their environment^{66, 208}. Super paramagnetic iron oxide nanoparticles (SPIONs) have a strong T₂ contrast due to their small size and ability to develop a strong induced magnetic field²⁰⁹. In comparison, PBNPs are also able to develop their own magnetic field to produce areas of dark within an MRI image by disturbing local spin of H⁺ ions. Due to the typical size range of PBNPs

(50-100nm), they are not super effective agents without extra modification¹⁷⁶. This is due to the magnetic:dead ratio that occurs with bigger particles as well as the increased presence of Fe³⁺ ions within the structure. As Fe³⁺ has 5 unpaired electrons (compared to 4 for Fe²⁺), it can interact with more surrounding water molecules and shorten the T₁ relaxation time, thus increasing the T₁ contrast. The most common modification is heavy metal doping. Due to the alternating iron surface valence on the PBNP surface, either Fe²⁺ or Fe³⁺ ions can be replaced by gadolinium or manganese ions. As gadolinium and manganese are already commonly used metals for MRI imaging, they easily improve the generated magnetic field by the particles^{115, 129}. Wang et al. synthesized gadolinium doped PBNPs using a standard procedure for application in photodynamic therapy, chemotherapy, MRI imaging, and enhanced catalase activity. They were able to show great accumulation and contrast for both T₁ and T₂ MRI after IV injection in a 4T1 subcutaneous mouse model¹⁹⁷. In a different study by Dumont et al. gadolinium ions were incorporated into the lattice pockets instead of replacing Fe³⁺ ions. They showed that the Gd:PB particles have higher r₁ and r₂ values (~38.5 and ~44.7) in comparison to PBNP (~4.7 and ~7.3). This indicates that the doped particles give a much higher MRI contrast even if the gadolinium ions are not directly on the surface of the particle¹⁷⁴. Now, there has been a shift in the clinic from using gadolinium-based contrast agents due to high toxicity levels. This had led researchers to look at doping Prussian blue with other types of metals that can still allow for high MRI contrast. Manganese is one of the most popular alternatives. Zhu et al. presented evidence that Mn doped PBNPs did increase overall T₁ contrast but has minimal increase in r₁ values (PBNPs: 5.73, Mn PBNP: 7.64 mM⁻¹s⁻¹). In vivo imaging with 4T1 subcutaneous bearing mice, showed great contrast within the tumor area, but there was little signal that came from

the tumor area using PAI²¹⁰. This gives evidence that while manganese doped particles can enhance MRI contrast, it is not as good as gadolinium. One other issue that arose with manganese-based contrast agents is that multiple uses can lead to manganism (manganese poisoning), which is a detrimental neurodegenerative disorder²¹¹. Due to toxicity problems with doped particles, many have failed during the FDA-approval process. This leaves an extreme need to find alternatives that will minimally change the overall structure of Prussian Blue but increase MRI contrast abilities.

Photoacoustic Imaging: Like PTT, PBNPs are often used as photoacoustic imaging contrast agents based on their high absorbance within the biological transparency window and high light conversion properties^{116, 212}. There have been many studies that have utilized PBNPs to detect cancerous tumors as well as many other disease models *in vivo*. First reported in 2013 by Liang et al. from Peking University, Beijing, PBNPs were able to show good PAI signal within a phantom model with varying thicknesses of chicken breast covering the particles. They were able to show up to 4.3cm, PAI signal for 80ug/mL and 100ug/mL was still visible²¹². Like MRI imaging, when PBNPs are doped with other metals such as gadolinium or manganese the overall absorbance peak shifts closer to the second near-infrared (NIR II) window²¹³. This means that a stronger independent particle signal can be obtained as there is less overlap with hemoglobin and deoxyhemoglobin. Tao et al. demonstrated this by synthesizing manganese doped PBNPs and intravenously injecting them into SKOV-3 subcutaneous tumor bearing mice. They were able to see a linear correlation between concentration and PAI signal when particles were embedded within agarose gel. It was also seen that 12hrs post injection, the highest accumulation of PBNPs occurred within the tumor region. They compared this with MRI signal

intensity from the particles and saw a similar trend. T₁ imaging showed highest accumulation at 12hrs post injection and had distinctive image contrast¹⁹⁶. This shows that PBNPs are very versatile tools that can be used for combination imaging using the same particle. This can not only allow for more accurate detection of early-stage tumors but provide exact tumor boundary information for surgical resection.

Cell-Membrane Coated Nanoparticle Technology: Lipid coated nanoparticles have been of great interest to the scientific community since the start of liposomal delivery strategies for targeted drug delivery. It was seen that the additional coating not only allowed for extended circulation within the body but reduced overall immune response. More recently, researchers have investigated using more biological derived materials for coating to increase targeting and accumulation effects for a wide variety of diseases^{62, 214-218}. Starting in 2011, Liangfang Zhang's laboratory from the University of California, San Diego started research into using cell membranes as a camouflaging method for nanoparticles. This started with their paper on the use of red blood cell derived cell membranes as a coating for PLGA nanoparticles to investigate the biodistribution properties within an in vivo mouse model. What they saw is a much higher retention of the particles within the blood up to 72hrs after intravenous injection²¹⁶. This basis led to therapeutic applications of camouflaged nanoparticles in bioremediation, anti-inflammation, and for use as agents against infection^{217, 219, 220}. One of the biggest contributions they had to the field was by Zhang et al. which investigated the effects of neutrophil cell membrane coated PLGA nanoparticles on synovial inflammation within arthritic joints. They presented novel data which showed increased targeting of the neutrophil coated nanoparticles for inflammatory tissue without specific identification of inflammation factors before

treatment²¹⁸. Now cell membrane coatings for nanoparticles have proven useful for a wide variety of *in vivo* disease models but have a disadvantage for brain targeting. Cell membrane coated nanoparticles tend to have great targeting effects, but must be very specific to the disease²²¹. They also tend to suffer from instability and ineffective cellular internalization²²². To circumvent this problem, scientists have modified the membrane structures with targeting peptides such as RGD, cyclic-RGD, C6, PL3, etc. While this can be successful, it requires extra time and cost²²³. As more research is done into extracellular vesicles, researchers have looked to using them as coating for nanoparticles due to their innate ability to pass through the BBB. In one such study, Kutchy et al. created astrocyte derived extracellular vesicle coated ultra-small iron oxide nanoparticles (USPIONs). Through MRI, they were able to see great accumulation within the brain up to 4 hours after intravenous injection²²⁴. Overall, these provide great promise in biomimetic materials for use within clinical practices for the brain. While extracellular vesicles are still highly debated as whether they are safe to use within the clinic, they could be used in phase one clinical studies to measure the effects against end-of-life patients to see if there is potential for translation for healthier individuals.

The basis of this project is to investigate the effects of exosome coated Prussian blue nanoparticles for early detection and treatment of glioblastoma. We have been able to show precision targeting using an orthotopic mouse model through *in vivo* photoacoustic imaging and *ex vivo* analysis including bioTEM, fluorescence imaging, and ICP. Effective therapeutic effect using PTT was seen in a U-87 subcutaneous model following intravenous injection. Overall, the data presented here shows a novel noninvasive method of utilizing PBNPs for glioblastoma theranostics.

2.2: Methods

Prussian Blue Nanoparticle (PBNPS) Synthesis

PBNPs were synthesized using a co-precipitation reaction between iron (III) chloride and potassium (II) ferrocyanide in the presence of citric acid. Initially, two separate 10mM solutions of FeCl_3 and $\text{K}_4[\text{Fe}(\text{CN})_6]$ are prepared in DDI water. Each solution is diluted to 1mM and 1g of citric is added to the FeCl_3 solution. The new citric acid- FeCl_3 solution is stirred at 60°C until everything is dissolved. $\text{K}_4[\text{Fe}(\text{CN})_6]$ is then added at a rapid dropwise rate to the stirring solution. During this step, the solution will change from a slight yellow to a deep blue color. The solution is stirred overnight at 60°C . The next day, the reaction mixture is washed with equal parts DDI water and acetone at 10,000rpm for 20min (x3). The final particle mixture is suspended in DDI water.

PEGylated Prussian Blue Nanoparticle (PEG:PB) Synthesis

PEG:PB particles were prepared using a two-step synthesis with some modifications¹⁷⁸. Using the same PBNP synthesis conditions, 1mM of FeCl_3 containing 1g of polyvinylpyrrolidone (PVP) and 1mM of $\text{K}_4[\text{Fe}(\text{CN})_6]$ were mixed and left to stir at 60°C overnight. The next day, the particles were washed with equal parts water and acetone at 12,000rpm for 20min (x3). The final suspension of the PVP-PBNPs were suspended in water. To PEGylate the particles a surfactant exchange was performed. 2mg/mL of PVP-PBNPs and poly bis(amine) were stirred at RT for 24hrs. The next day, the PEG:PB particles were washed with DDI water at 12,000rpm for 20min (x3). The final PEG:PB solution was stored in DDI water at 4°C . Conjugation to the surface of the particles was done using a PerkinElmer Spectrum 2 FTIR using a drop cast method.

Isolation of U-87 Derived Exosomes

U-87 cells were plated in 100cm³ cell cultures dishes in EMEM media with 10% Fetal Bovine Serum (FBS) and left to incubate at 5% humidity and 37°C for 24 hours. The next day, the cells were washed with PBS and replaced with EV-depleted EMEM. The cells were then left for another 24hrs to incubate at 5% humidity and 37°C. The last day, the media was taken from each cell culture dish and placed in 50mL conical tubes. The tubes were then centrifuged at 600xg for 10min to remove any cells within the solution. The supernatant was removed and transferred to a new set of tubes where they were centrifuged at 2000xg for 30min to remove apoptotic bodies, 20,000xg for 60min to remove microvesicles, and 100,000xg for 60min to isolate the exosomes. The final exosome solutions was stored in PBS at -80°C until used.

Preparation of Exosome Coated Prussian Blue Nanoparticles (Exo:PB)

The Exo:PB particles were prepared using a physical extrusion method. Initially, 1×10^9 exosomes are mixed with 1.5mg/mL PBNPs and then extruded using an Avanti Polar Lipids Mini Extruder. The mixture is passed through 200nm PC membranes for 11 passes which results in a pale blue color. Following extrusion, the particles are centrifuged at 12,000rpm for 20min and then resuspended in 1mL of DDI water. For fluorescent labeling of the Exo:PB particles, 1mg/mL of 1,1'-Diiododecyl-3,3,3',3'-Tetramethylindocarbocyanine (DiI) is added and incubated at 37°C for 1hr. The DiI-Exo:PB particles are then washed DDI water at 12,000rpm for 20min (x2). The final DiI-Exo:PB solutions are suspended in DDI water and stored at 4°C.

Nanoparticle Tracking Analysis

Concentration and initial size distributions of nanoparticles/exosomes were determined using Nanoparticle Tracking Analyzer (NTA, ZetaView). Each set of particles were diluted differently to

fall within proper scanning parameters of the instrument. Parameters used: trace: 10, minisize: 5/6, MTR: 30, nm/class: 5, sensitivity: 85, shutter: 250.

Dynamic Light Scattering

Size distributions and zeta potentials of higher concentrations of nanoparticles/exosomes were done using Dynamic Light Scattering (DLS, Zeta Sizer Nano, Malvern Instruments). 1mL of particles was added into a plastic cuvette and measured three times to obtain an average size and polydispersity index (PDI). For zeta potential values, 500uL – 1mL of solution was added to a folded capillary zeta cell cuvette and measured three times. Parameters used: material (PBNP) refractive index: 1.440, dispersant (water) refractive index: 1.330, temperature: 25°C, equilibration time: 60 seconds, measurement angle: 173° backscatter.

Transmission Electron Microscopy

Size and morphology of all particles was measured using a 220FS Transmission Electron Microscopy (TEM, JEOL) with energy-dispersive X-ray Spectroscopy (EDX) capabilities. For preparation and imaging of exosomes and Exo:PB particles a uranyl-acetate staining method was used. Samples were mixed with equal volume of 2% paraformaldehyde (PFA), added to a 300-mesh copper grid and left to dry for 20 minutes within a fume hood. The grids are then washed with PBS and 1% glutaraldehyde is added and left for 5 minutes. Samples then go through a wash process with DDI water (x8). Finally, 1% uranyl acetate is added to the grid and left to sit for 1 minute.

Gold Nanorod Synthesis

Gold nanorods (AuNRs) were synthesized using a seed-mediated growth method using a previously established protocol with some modifications²²⁵. First, a prepared seed solution

containing 2.5mL of 0.1M gold (III) chloride, 5mL of 2mM cetyltrimethylammonium bromide (CTAB), 600uL of 10mM sodium borohydride, and 2.5mL of DDI water. Next, a growth solution is prepared in which 460uL of 100mM silver nitrate, 5.1mL of 87mM ascorbic acid, and 1.8mL seed solution are added to 740mL of 2mM CTAB. The combined solution is left overnight to react. The following day, the reaction mixture is washed at 10,000rpm for 10min with DDI water (x3). The final solution is stored in water.

Photothermal Capabilities of Particles

To determine overall changes in temperature, 1mL of PBNPs at 0, 1, 2, 4, 8, and 16mg/mL were exposed to an 808nm laser ($2\text{W}/\text{cm}^2$) for 10 minutes. Each sample was placed 1 inch from the laser output and the temperature of the solution was monitored every minute using a handheld laser Cx Series FLIR camera. To determine the photothermal stability of PBNP, Exo:PB, PEG:PB, and U-87 exosomes, 1mg/mL (1mL) of each was exposed to an 808nm laser at $2\text{W}/\text{cm}^2$ for 10 minutes. After 10 minutes, the particles were allotted a 10-minute cooling period in which the laser was turned off. The comparison photothermal stability study done between AuNRs (0.5mg/mL) and PBNPs (0.5mg/mL) was done using the same setup, but particles were exposed to the laser for 10-minute increments (x3) followed by a 5-minute cooling period. For comparison of size before and after laser exposure for Exo:PB, PEG:PB, and U-87 exosomes, the particles were exposed to an 808nm ($2\text{W}/\text{cm}^2$) for 1 minute where DLS was taken before and after exposure.

Photothermal Conversion Efficiency

The photothermal conversion efficiency (η) of Exo:PB, PEG:PB, PBNP, and AuNRs were determined from **Figure 15A** and **Figure 15B**. For the first photothermal cycle, the cooling cycle

(highlighted in blue) was used to find θ utilizing equation (1). T ($^{\circ}\text{C}$) = temperature at any time point within the cooling cycle, T_{surr} ($^{\circ}\text{C}$) = temperature of the solvent, T_{max} ($^{\circ}\text{C}$) = maximum temperature reached within the cooling cycle. T_{surr} was found using a vial of water under the same conditions.

$$\theta = \frac{T - T_{surr}}{T_{max} - T_{surr}} \quad (1)$$

After θ is calculated for each temperature within the cooling cycle, a τ (s) constant is found by graphing the inverse relationship between time and $-\ln(\theta)$. τ is the slope of the linear correlation as seen in equation (2). t (s) = any given time during the cooling period.

$$t = \tau \ln(\theta) \quad (2)$$

Once τ is determined for each particle, hs ($\text{J}/\text{s}^{\circ}\text{C}$) can be calculated from equation (3). hs is represented by the heat transfer coefficient (h) and total surface area of the solution (s). m (g) = mass of the solution, C ($\text{J}/\text{g}^{\circ}\text{C}$) = specific heat capacity of the solution.

$$hs = \frac{mC}{\tau} \quad (3)$$

The photothermal conversion efficiency can then be calculated using equation (4). Q_{surr} (J/s) is determined from a vial of water exposed to the same conditions. I (W) = laser power, A_{808} = absorbance of the particle solution at 808nm.

$$\eta = \frac{hs(T_{max} - T_{surr}) - Q_{surr}}{I(1 - 10^{-A_{808}})} \quad (4)$$

Cellular Uptake

U-87 cells were seeded at 10,000 cells/well in a 4-slide chamber and left overnight in a cell incubator at 37°C and 5% humidity. The following day, each well was treated with either 0.1mg/mL of Dil-Exo:PB, Dil stained U-87 exosomes, or rhodamine isothiocyanate pegylated Prussian Blue nanoparticles (RITC-PEG:PB) and left overnight at 37°C and 5% humidity. On the final day, the cells were washed with PBS and stained with Calcein AM (1uM) and mounted using Prolong Gold reagent with DAPI. Images were taken using THUNDER microscopy (Leica Microscopy).

Timed Cellular Uptake

U-87 cells were seeded at 10,000 cells per well in a 96-well plate and left to incubate overnight at 37°C and 5% humidity. The next day, all wells were treated with 1.5mg/mL Dil-Exo:PB or RITC-PEG:PB. The particle fluorescence was measured each hour for 12 hours and then at 12 and 24 hours (Dil: Ex: 550nm, Em: 564nm, RITC: Ex: 570nm, Em: 595nm). Each fluorescence value was then compared to a concentration curve for Dil-Exo:PB and RITC-PEG:PB.

In vitro BBB Passage

U-87 cells were seeded at 20,000 cells per well in CytoSelect™ 24-well Cell Migration and Cell Invasion plates with 8um well inserts and left to incubate overnight at 37°C and 5% humidity. After 24 hours, 0.1mg/mL Dil-Exo:PB or RITC-PEG:PB was added to the upper portion of the well inserts. On the third day, the well inserts were removed, and the U-87 cells were stained with 1uM Calcein AM and DAPI. Cells were imaged using Keyence microscopy.

In vitro Tumorigenesis Model

U-87 cells were seeded at 10,000 cells/well in a 96-well plate and left to incubate overnight at 37°C and 5% humidity. The next day, cells were treated with 0.1mg/mL Exo:PB, PEG:PB, or nothing and left for another 24 hours at 37°C and 5% humidity. At 24 and 48 hours post treatment, cells were washed with PBS and stained with 1uM Calcein AM. Immediately after staining, fluorescent measurements were taken (Ex: 494nm, Em: 517nm).

Cellular Viability

To start, U-87 cells were seeded in a 96-well plate at 10,000 cells/well and left overnight at 37°C and 5% humidity. The following day, wells were treated with 0, 0.03125, 0.0625, or 0.25mg/mL of Exo:PB, PEG:PB, PBNPs, or U-87 exosomes and then incubated for another 24 hours at 37°C and 5% humidity. On the final day, the supernatant was removed and 5mg/mL of a 3-(4,5-Dimethylthiazol-2-yl)-2,5-diphenyltetrazolium bromide (MTT) solution and left to incubate for 4 hours. Finally, the MTT solution is removed to expose the formed formazan crystals and resuspended in dimethyl sulfoxide (DMSO). The absorbance is measured using a SoftMax Pro plate reader (Molecular Devices, CA) at 570nm. For laser-based effects *in vitro*, on the last day the cells were exposed to an 808nm laser (1.5W/cm²) for 1 minute and then the MTT assay was performed.

Live and Dead Cell Assay

U-87 cells were seeded at 30,000 cell/well in a 24-well plate and left to incubate overnight at 37°C and 5% humidity. The next day, cell were treated with 0.1mg/mL of Exo:PB, PBNP, PEG:PB, U-87 exosomes or nothing and left to incubate for 1 hour. The cells were then exposed to an 808nm laser (2W/cm²) for 1 minute and left overnight at 37°C and 5% humidity. On the last

day, the cells were washed with PBS and stained with Calcein AM (1 μ M) and Propidium Iodide (2 μ M). Images were taken using Keyence microscopy.

Calculated Maximum Temperature at Cellular Level

U-87 cells were seeded in a 24-well plate at 20,000 cells/well and left to incubate overnight at 37°C and 5% humidity. On the second day, the cells were treated with PBNP, Exo:PB, or PEG:PB at 1.5mg/mL and left to incubate overnight at 37°C and 5% humidity for another 24 hours. On the third day, U-87 cells were detached using 0.05% trypsin and centrifuged at 1000rpm for 10 minutes to obtain a cell pellet. Each cell pellet (N=3 for each treatment condition) was then resuspended in 100 μ L of EMEM media and exposed to a 2W/cm² 808nm laser for 1 minute with the temperature measured before and after 1 minute. The concentration of the particles within the cells were back calculated based on concentration vs change in temperature standard curve for PBNP, PEG:PB, or Exo:PB. As the particles had a consistent concentration of 0.1mg/mL within the cell pellets, a secondary curve of volume vs change in temperature standard was determined and used to back calculate the maximum temperature within a U-87 cell.

$V=4.6875 \times 10^{-5} \text{ mm}^3$ was determined using **Figure 10**.

Animal Usage and Treatment

All animal studies performed were approved by the Institutional Animal Care and Use Committee (IACUC) at Michigan State University. Animal wellbeing and care throughout all studies were maintained by the Center for Animal Resources (CAR) and Michigan State University. All animal experiments were done with at least an N=3. Mice were anesthetized with an isoflurane/oxygen mixture during all procedures. All mice used were male NuJ immunodeficient.

U-87 *in vivo* Subcutaneous Tumor Model Development

Luciferase expressing U-87 cells were prepared with Sleeping Beauty transposon²²⁶. 500,000 cells/tumor of luciferase expressing U-87 cells were mixed 1:1 volumetric ratio with Matrigel. Approximately 100uL of cells and Matrigel mixture were injected into the flank region of the mouse. All tumors were visible about 1 week after inducement.

In vivo Photothermal Treatment with Intertumoral Injection

After subcutaneous tumors were visible, 1mg of Exo:PB or PEG:PB was injected intratumorally on days 0 and 7. Directly after injection, the tumors are exposed to an 808nm laser ($2\text{W}/\text{cm}^2$) for 1 minute. Tumor size was monitored every day throughout the experiment using a vernier caliper. Physical sizes were compared with luciferase signals obtained using IVIS imaging (PerkinElmer Inc., Waltham, MA).

In vivo Photothermal Treatment with Intravenous Injection

After subcutaneous tumors were visible, 1mg of Exo:PB or PEG:PB was injected intravenously on days 0, 3, and 6. Three hours after the injection, the tumors were exposed to an 808nm laser ($2\text{W}/\text{cm}^2$) for 10 minutes. Physical tumor size and body weight of mice were measured every two days with a vernier caliper and standard open benchtop scale.

Photoacoustic MSOT Imaging

A InVision 512-echo preclinical multispectral photoacoustic tomographic (MSOT) imaging system (iThera Medical, Germany) was used for all photoacoustic imaging studies. Anesthesia was disposed as a 2% isoflurane/oxygen mixture during all imaging. Mice were applied with ultrasound gel and wrapped in a thin polyethylene membrane and then submerged in a water tank while in a horizontal position. 1mg of particle was injected into mice intravenously and

images were taken pre-injection, 0, 1, 2, 3, 6, 12, and 24 hours afterward. Imaging was done in 0.2mm increments with an average of 10 illumination wavelengths (680, 700, 730, 760, 800, and 850nm). Hemoglobin (HbO₂), deoxyhemoglobin (Hb), and Total hemoglobin (HbT) were measured using these wavelengths. Acquisition times were less than 10 minutes and image analysis was done using ViewMSOT software.

U-87 *in vivo* Orthotopic Brain Tumor Model Development

The mouse was initially anesthetized using a 2% isoflurane/oxygen mixture. Meloxicam (1mg) is administered through an intraperitoneal injection to help alleviate pain. The mouse is then transferred to a stereotaxic device and the head is sterilized with iodine. An incision is made on anterior side of the skull where a 10uL needle is adjusted to 2mm x and 1.5mm y from the bregma. The skull is punctured in the designated area with a small gauge needle and the 10uL needle is lowered into the hole down to 2.5mm. U-87 luciferase expressing cells (3uL, 3×10^5 cells) are injected at 0.5uL/min and then left to sit for 5 minutes post injection. The needle is removed 1mm/min and then the mouse is removed, and the incision is sutured. Bioluminescent signal within the brain region is checked 1-2 weeks after the surgery to identify tumor size.

Particle Accumulation in *in vivo* Orthotopic Brain Tumor Model

Once the mice were anesthetized using a 2% isoflurane/oxygen mixture, 2mg of RITC-PEG:PB or Dil-Exo:PB was intravenously injected. Photoacoustic images were taken 3 hours post injection.

Ex vivo Histological Analysis

After *in vivo* studies were finished, the mice were sacrificed, and the tumors or brains were removed and sectioned using a cryostat. First the optimal cutting temperature (OCT) compound layer was removed to expose the bare tissue. Each slide was then stained with hematoxylin for

45 seconds and washed multiple times with water. The tissue is then stained with eosin for 30 seconds and washed multiple times with ethanol. The final stained slide is fixed using xylene glue and imaged using Keyence microscopy.

Ex vivo Immunohistology

Immunofluorescent staining was done using an anti-cleaved caspase-3 antibody as an apoptosis marker and an anti-Ki67 antibody as a tumor marker. The antibodies were incubated with the tissue samples at 4°C overnight. The next day, the tissue was washed with PBS and an Alexa 488 conjugated secondary antibody was incubated for 1 hour at RT. The slides were then mounted using a Prolong Gold reagent with DAPI. Images were taken using THUNDER microscopy (Leica Microsystems, Germany).

BioTEM Sample Preparation and Imaging

After glioblastoma orthotopic tumor bearing mice were sacrificed, the brains were excised and placed in 4% PFA for fixation and preservation. A small portion of the brain would then be cut out and resuspended in 0.1M cacodylate buffer containing 2.5% glutaraldehyde and left overnight within a fume hood. The following day, all the tissue samples were washed with 0.1M cacodylate buffer for 10 minutes (x3) and then fixed with 1% osmium tetra oxide in 0.1M cacodylate buffer for 2 hours. The samples were then washed again with 0.1M cacodylate buffer for 10 minutes (x3). Each tissue is then dehydrated with acetone in temperatures ranging from 50°C to 100°C. Finally, a spur resin is applied to infiltrate the samples while simultaneously reducing the amount of acetone used every 2-3 hours. The amount of acetone used is inversely proportional to the amount of spur resin used at any given time point. Once there is 100% spur resin used the blocks are left in an oven for 24 hours and then sectioned using an RMC MYX

ultramicrotome (Boeckeler Instruments). Final TEM images were obtained using a 1400 Flash (JEOL, Japan).

Fluorescence Bio-Distribution

Mice were intravenously injected with 1mg of Exo:PB or PEG:PB particles and then sacrificed 24 hours after. The brain, heart, lungs, kidneys, spleen, liver, and leg muscle were taken and placed within different wells of a 24 wells plate. Fluorescence intensity was measured using IVIS imaging.

Inductively Coupled Plasma Mass Spectrometry (ICP-MS) Sample Preparation and

Quantification

Mice were intravenously injected with 1mg of Exo:PB or PEG:PB particles and then sacrificed 24 hours after. The brain was excised and cut into two portions: the tumor hemisphere and the contra lateral hemisphere. The tissue was digested in highly concentrated nitric acid using a CEM Mars6 Microwave Digestion System and then run through an Agilent 8900 QQQ-ICP-MS. All samples were compared to a freshly prepared iron standard curve prepared at the same time.

Statistical Analysis

All in vitro experiments were done with at least an n=6 and performed within a sterile environment. All in vivo experiments were performed with at least an n=3 and done with proper animal handling techniques. Statistical analysis was done with Graphpad Prism or Excel for one and two-tailed t-test analysis. $P < 0.05$ was considered significant.

2.3: Results/Discussion

Characterization of PBNP, Exo:PB, and PEG:PB Nanoparticles

Prussian Blue Nanoparticles (PBNPs) were synthesized using a co-precipitation between FeCl_3 and $\text{K}_4[\text{Fe}(\text{CN})_6]$ in the presence of citric acid or polyvinylpyrrolidone (PVP). This resulted in uniform particle size of $\sim 70\text{nm}$ and zeta potential of -42.1mV as determined through dynamic light scattering (DLS) and nanoparticle tracking analyzer (NTA) in **Figure 5A, 5D and 5E**. The reaction size was scalable up to 0.15g of nanoparticles after washing and quantified through lyophilization. Overall size, uniformity, and morphology of nanoparticles was determined using transmission electron microscopy (TEM) and was found to be cubic and well-dispersed (**Figure 6A**). Traditionally, when PBNPs are synthesized without a surfactant (ex: citric acid or PVP) they will still be dispersed and of similar size but suffer from long term instability as the particles will start to aggregate. As iron chloride solutions can easily form coordination complexes with the proper type of ligands, often compounds such as citric acid, PVP, or poly-L-lysine (PLL) are chosen as the exposed hydroxyl end groups make it a preferable complex to be formed. Since these types of surfactants are not common within the body, particles with these types of coatings can get excreted quickly and can aggregate in various pH environments found within the body. To increase circulation within our *in vivo* models as well as create a proper standard in which Exo:PB could be compared against, we chose to do a surfactant substitution to switch PVP with a $\text{NH}_2\text{-PEG-NH}_2$ coating. PEG is known to increase circulation time as well as improve overall passive targeting in tumors due to angiogenic formed blood vessels. The initial PVP coating allows for a passive conjugation of $\text{NH}_2\text{-PEG-NH}_2$ from a basic hydrolysis reaction in ethanol. PVP will detach from the Fe^{3+} ions which allows for the $\text{NH}_2\text{-PEG-NH}_2$ to attach as there

is no longer OH⁻ ions to compete with. The conjugation was validated using FTIR (**Figure 7**). Using DLS and NTA, the size and zeta potential were shown to be ~100nm and -9.54mV after PEGylation (**Figure 5B, 5D and 5E**). TEM validated size and monodispersity as well as consistency in cubic morphology (**Figure 6A**).

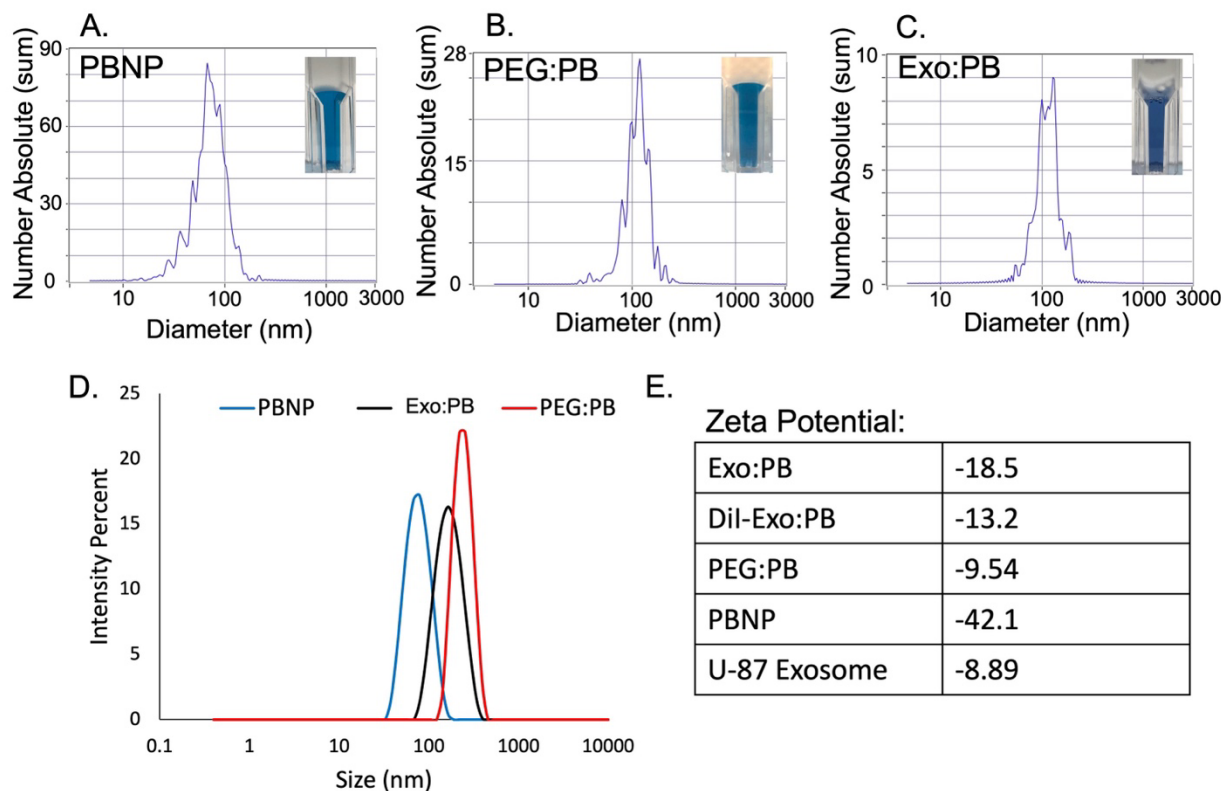


Figure 5: Particle Size and Zeta Potential. Nanoparticle Tracking Analyzer (NTA) graphed results for (A) PBNP (average size: 70.2nm), (B) PEG:PB (average size: 111.8nm), and (C) Exo:PB (average size: 111.6nm). Inserted Images are respective nanoparticle solutions. (D) Dynamic Light Scattering (DLS) results for PBNP (blue, average size: 71.81nm), Exo:PB (black, average size: 151.8nm), and PEG:PB (red, average size: 123nm). (E) Zeta potential values determined from DLS for Exo:PB, Dil-Exo:PB, PEG:PB, PBNP, and U-87 exosomes. Readapted with permission from reference¹⁷¹, Copyright 2024, American Chemical Society.

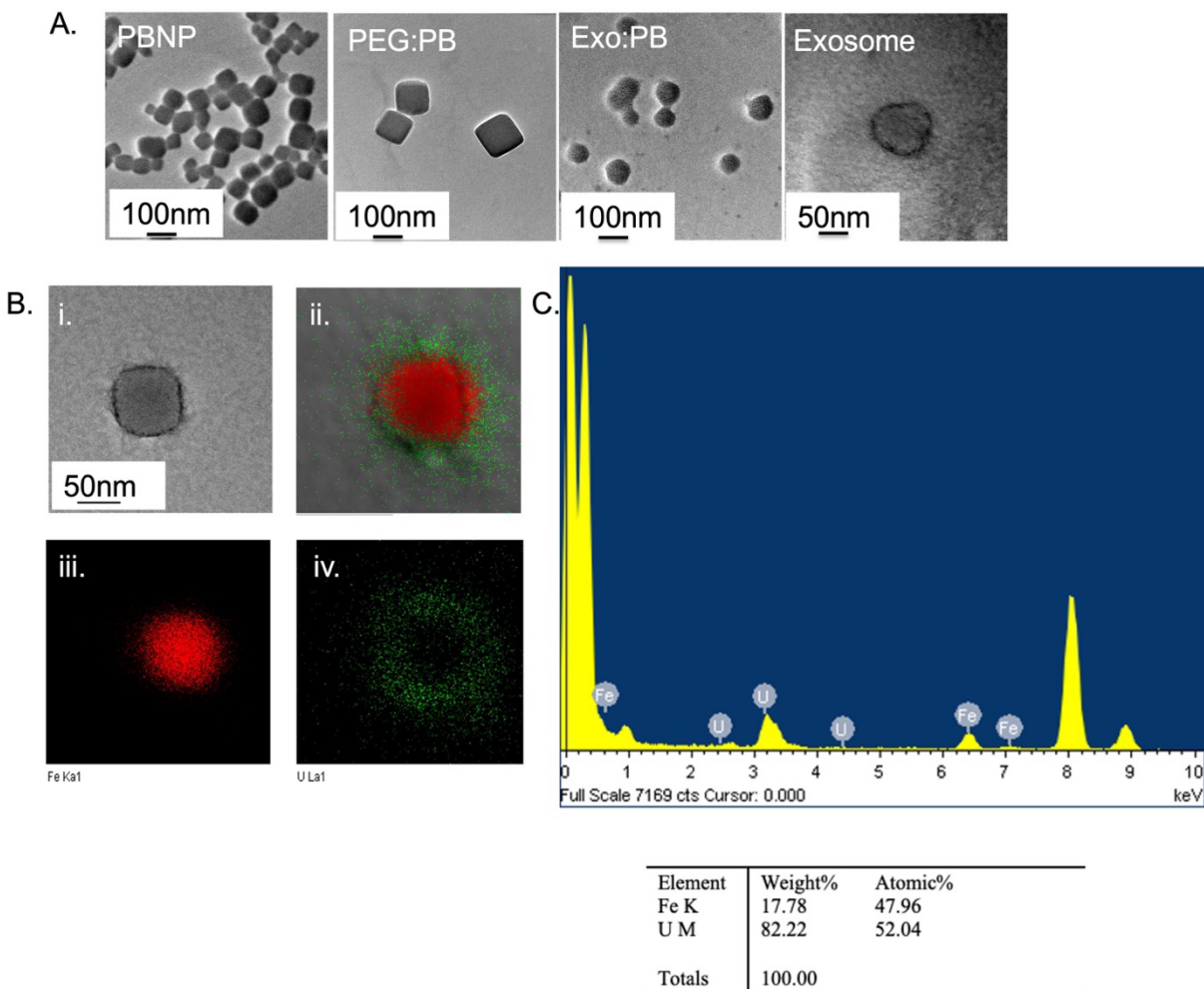


Figure 6: Transmission Electron Microscopy of Nanoparticles. (A) TEM images of PBNP, PEG:PB, Exo:PB, and U-87 derived exosomes. Scale bar is 100nm for PBNP, PEG:PB, and Exo:PB. Scale bar is 50nm for U-87 derived exosomes. (B) Electron mapping results for uranyl acetate stained Exo:PB. (i) brightfield image of stained Exo:PB. (ii) Electron mapping overlay of stained Exo:PB particle. Green = uranium, Red = Iron. (iii) Iron mapping signal of the PBNP core. (iv) Uranium mapping of the exosome stained coating. Readapted with permission from reference¹⁷¹, Copyright 2024, American Chemical Society.

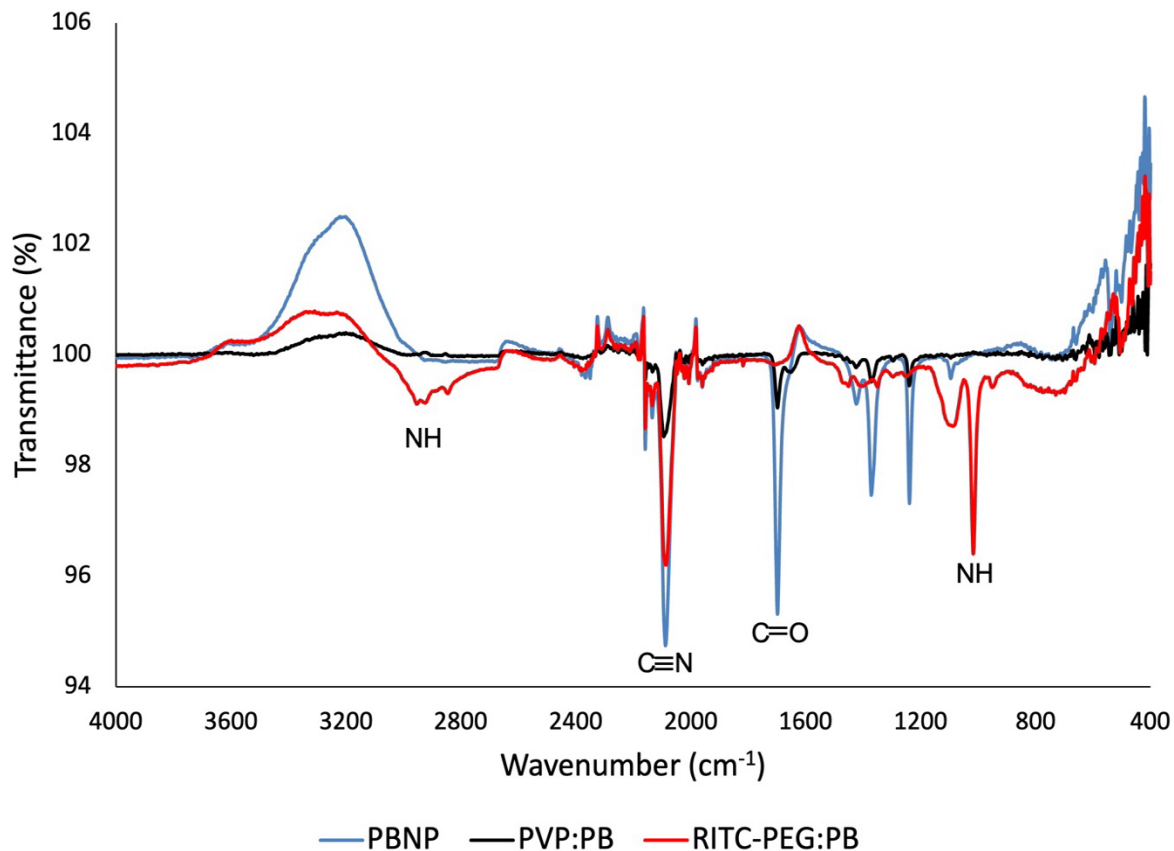


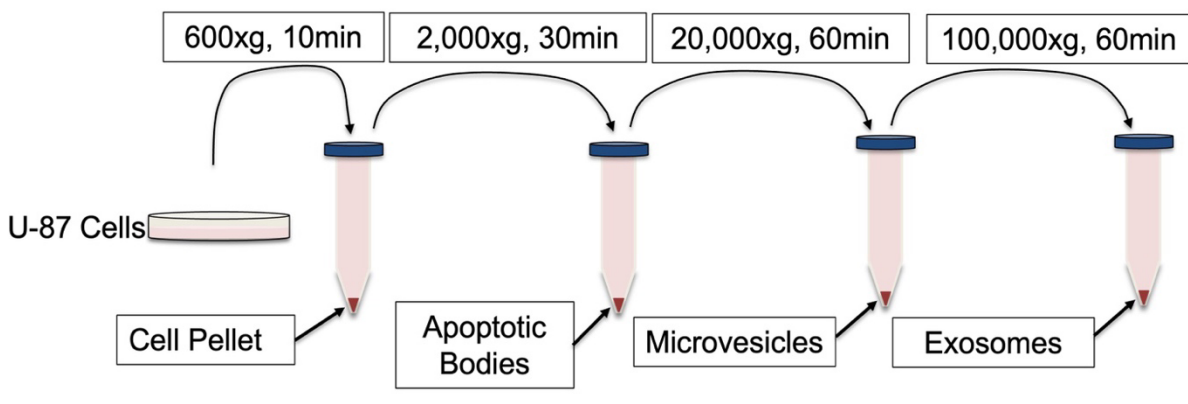
Figure 7: Fourier Transform Infrared (FTIR) for PBNP (blue), PVP:PB (black), and RITC-PEG:PB (red). CN and CO are markers for PBNP and PVP:PB, NH is the marker for RITC-PEG:PB. Thanks to Praveen Kumar for running the sample. Readapted with permission from reference¹⁷¹, Copyright 2024, American Chemical Society.

To create exosome coated PBNPs (Exo:PB), a physical extrusion method was used. Initially, U-87 derived exosomes were isolated using a differential centrifugation method (**Figure 8**). After isolation, all exosomes were stored at -80°C to prevent early onset degradation. When Exo:PB particles were formed, U-87 exosomes would be taken from the -80°C freezer and thawed on ice until they were fully liquid. A solution of citric acid coated PBNPs is then mixed with 1mL of thawed exosomes and extruded through a 200nm membrane at room temperature for 11 passes (**Figure 8**). After the first couple of passes, the color will start to shift from a transparent light blue color to a darker opaque blue color, which indicates that PBNPs are being coated successfully (**Figure 5**). After extrusion is performed, DLS and NTA were performed to check size distributions as well as zeta potential. It is found that the PBNP particles shift from $\sim 70\text{nm}$ to $\sim 120\text{nm}$ and become more positively charged at -18.5mV (**Figures 5C, 5D, and 5E**). As U-87 derived exosomes have a zeta potential of -8.89mV , the change in surface charge for Exo:PB indicates the coating was successful (**Figure 5E**). While all these indirect methods were good signs that the exosomes were attaching to the surface of the PBNPs, without direct measurement it cannot be fully decided if the extrusion method is effective. TEM images showed that the Exo:PB particles had a more rounded appearance (**Figure 6A**). This was promising data, but further staining was needed to validate that the coating covered the entirety of the particle and not a just the portion seen on the TEM grid. Exo:PB particles were stained using an uranyl acetate method in which the particles were fixed using paraformaldehyde (PFA) and glutaraldehyde and then stained with uranyl acetate. As uranyl acetate only interacts with lipid-based materials, it would only stain the exosome layer, allowing for us to distinguish between the PBNP core and exosome coating. Electron mapping

was performed and validated that there was a uranium-stained layer on the outside of the iron-based particle core (**Figure 6B and 6C**). Finally, western blot analysis was done to check that traditional protein markers present on the surface of the exosomes were not stripped during the extrusion process. It was seen that Flotillin-1 was present in the cell lysate, Exo:PB, and U-87 exosomes. β -actin was absent from both Exo:PB and U-87 exosomes which presents that the PBNPs were coated with exosomes and not the cell membrane (**Figure 9A**). After particle validation was done, it was seen that Exo:PB were stable at 4°C for up to nine months, which is promising for clinical translation (**Figure 9B**). In comparison, U-87 exosomes progressively become larger over a one week period at 4°C (**Figure 9C**). While PBNPs are known to have great stability for long periods of time, membrane coated particles tend to have early dissociation due to hydrolysis and lipid instability^{116, 215}. Since our particles show that there is no evidence of membrane stripping and the size and PDI are constant, our particles would be ideal for use within the clinic. There have been previous studies looking at the used of extracellular vesicle containing iron oxide nanoparticles prepared through electroporation, incubation, extrusion, or chemical conjugation methods. However, these particles suffer from instability and degradation of the EV layer over time^{113, 227}. These are things we have not seen with our particles up to this point.

A.

EV Isolation Process



B.

Exosome:Prussian Blue Formation

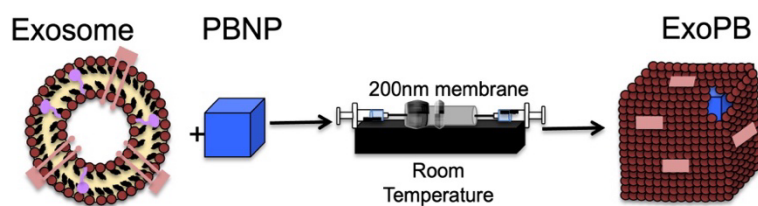


Figure 8: Exosome isolation and Exo:PB formation process. (A) Extracellular vesicles isolation process, where U-87 exosomes are the final product. (B) Extrusion process of PBNPs and U-87 derived exosomes to form Exo:PB. Reproduced with permission from reference¹⁷¹, Copyright 2024, American Chemical Society.

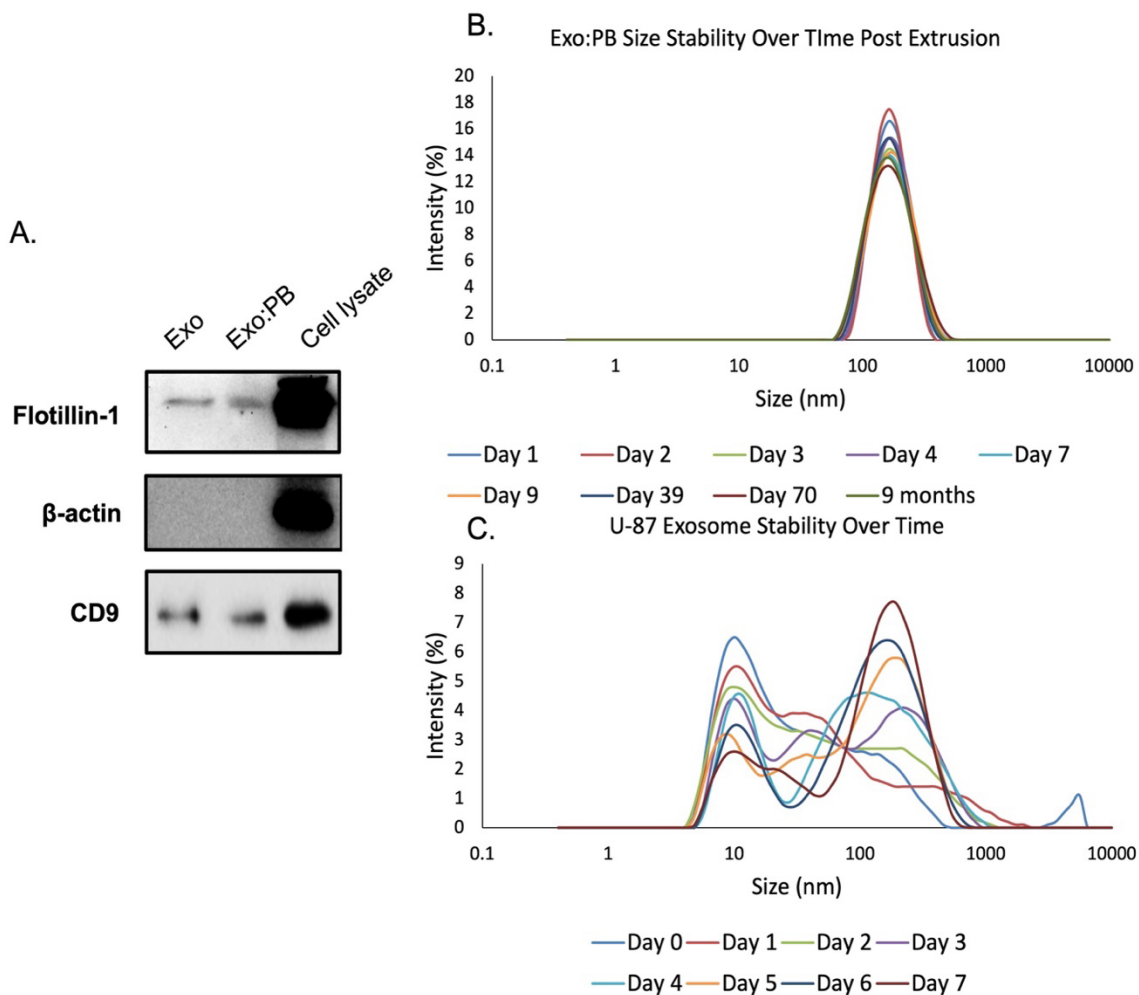


Figure 9: Further Exo:PB particle characterization. (A) Western blot results for U-87 derived exosomes, Exo:PB, and U-87 cell lysate for Flotillin-1 (exosome), CD9 (exosome), and β -actin (cell membrane) markers. (B) Long term stability of Exo:PB particles after storage at 4°C. (C) Stability of U-87 exosomes for 1 week at 4°C. Readapted with permission from reference¹⁷¹, Copyright 2024, American Chemical Society.

The main mechanism needed for glioblastoma diagnosis and treatment is the ability to pass through the blood-brain barrier. Our particles rely on the innate ability of exosomes to succeed in this area. As a result, we needed to validate the cellular uptake patterns of Exo:PB to see how they compare to U-87 exosomes. Two different *in vitro* experiments were done: a basic cellular uptake with U-87 cells and a basement membrane-based BBB uptake. When Dil-Exo:PB, RITC-PEG:PB, and Dil-U-87 derived exosomes were incubated with U-87 cells for 24 hours, it was seen that the cellular uptake patterns for the exosomes and Exo:PB were similar as the intracellular fluorescence level from both were similar. In comparison, the RITC-PEG:PB had a much lower fluorescence intensity that was detected, which indicates that the Exo:PB has a much higher cellular internalization through endocytosis, receptor mediated uptake, and membrane fusion²²⁸ (**Figure 10**). This is further seen through a time-based cell-based uptake in which it is seen that the Dil-Exo:PB had peak uptake between 7 and 8 hours at ~1.3mg/mL and continues to have a detectable signal within cells for up to 48 hours (**Figure 11**). As a result, the Exo:PB particles are more readily taken up into cells which is beneficial for targeted diagnostics and precision therapeutics. Once the general uptake patterns were observed, Dil-Exo:PB and RITC-PEG:PB particles were exposed to an *in vitro* BBB setup in which one set of wells contain an insert with a normal 200nm polycarbonate membrane (control) and the other contains a basement membrane that mimics the basal lamina of the BBB (experimental). While this not as representative as a model that contains an endothelial cell layer to mimic the tight junctions of the BBB, the model does prevent some passage of particles to the bottom layer. U-87 cells were plated onto the bottom of the plate and the particles were added into a trans well insert and allowed to incubate for 24 hours (**Figure 12A**). After 24 hours, the inserts were removed, and

cells were imaged to see the targeting effects of the particles. It was seen that for the control setup, all of the particles were able to pass through and target the U-87 cells without issue. In comparison, the experimental wells showed that the Dil-Exo:PB particles were present within the U-87 cells, but to a much lesser efficiency. The RITC-PEG-PB particles were unable to pass through as there was no signal detected (**Figure 12B**). Particles were also evaluated to see if tumorigenesis would be a problem. It was seen that there was no difference in cell growth up to 48 hours after incubation which follows the typical doubling time of U-87 cells (**Figure 13**).

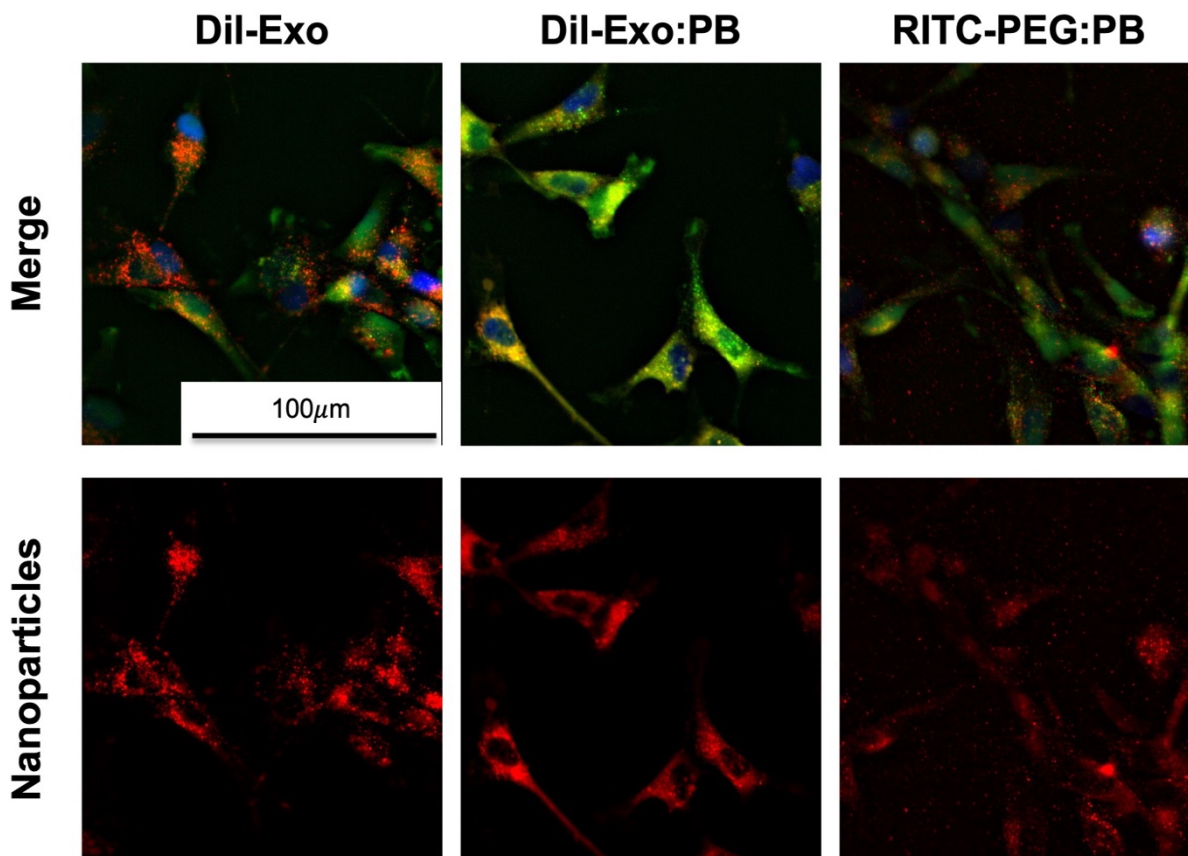


Figure 10: Cellular uptake patterns of Dil-exosomes, Dil-Exo:PB, and RITC-PEG:PB within U-87 cells. Red = nanoparticle signal, Green = calcein AM, Blue = cell nucleus. Scale bar = 100µm. Readapted with permission from reference¹⁷¹, Copyright 2024, American Chemical Society.

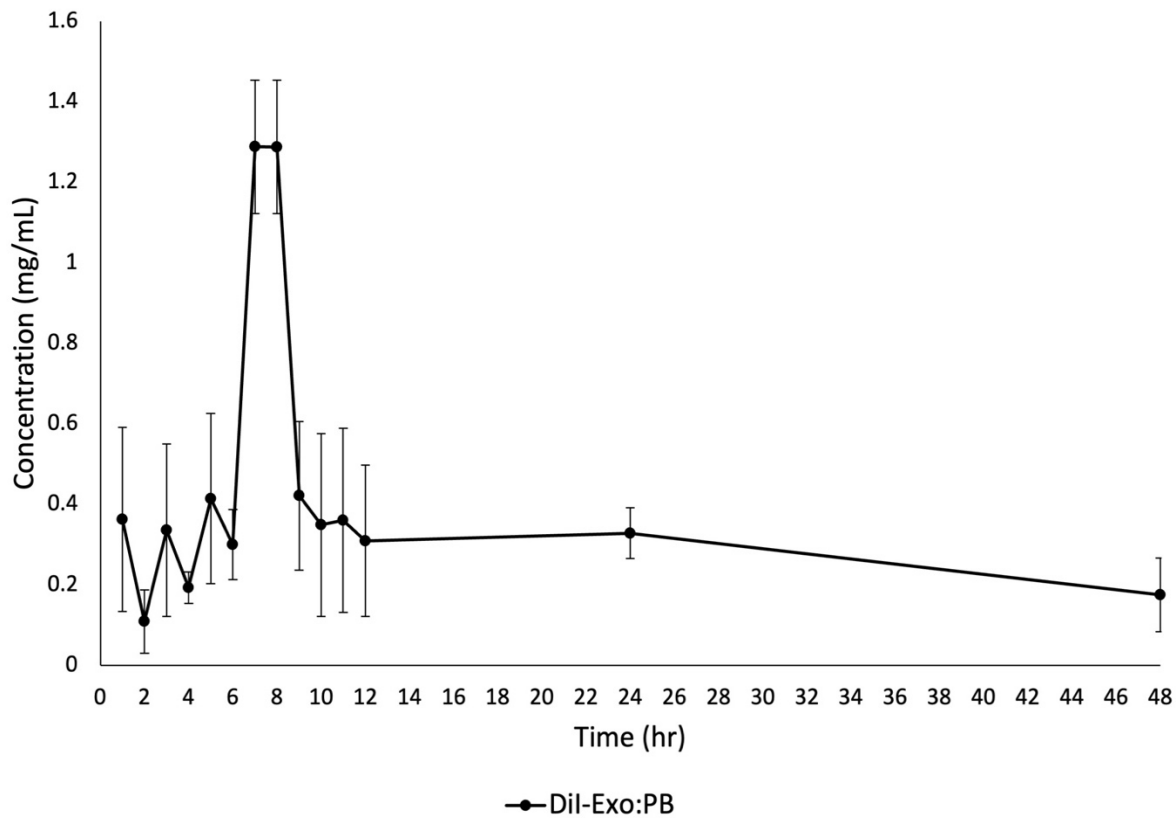


Figure 11: Timed cellular uptake quantified signal for Dil-Exo:PB within U-87 cells. Signal was quantified every hour for 1-12 hours and at 24/48 hours. N=6. Reproduced with permission from reference¹⁷¹, Copyright 2024, American Chemical Society.

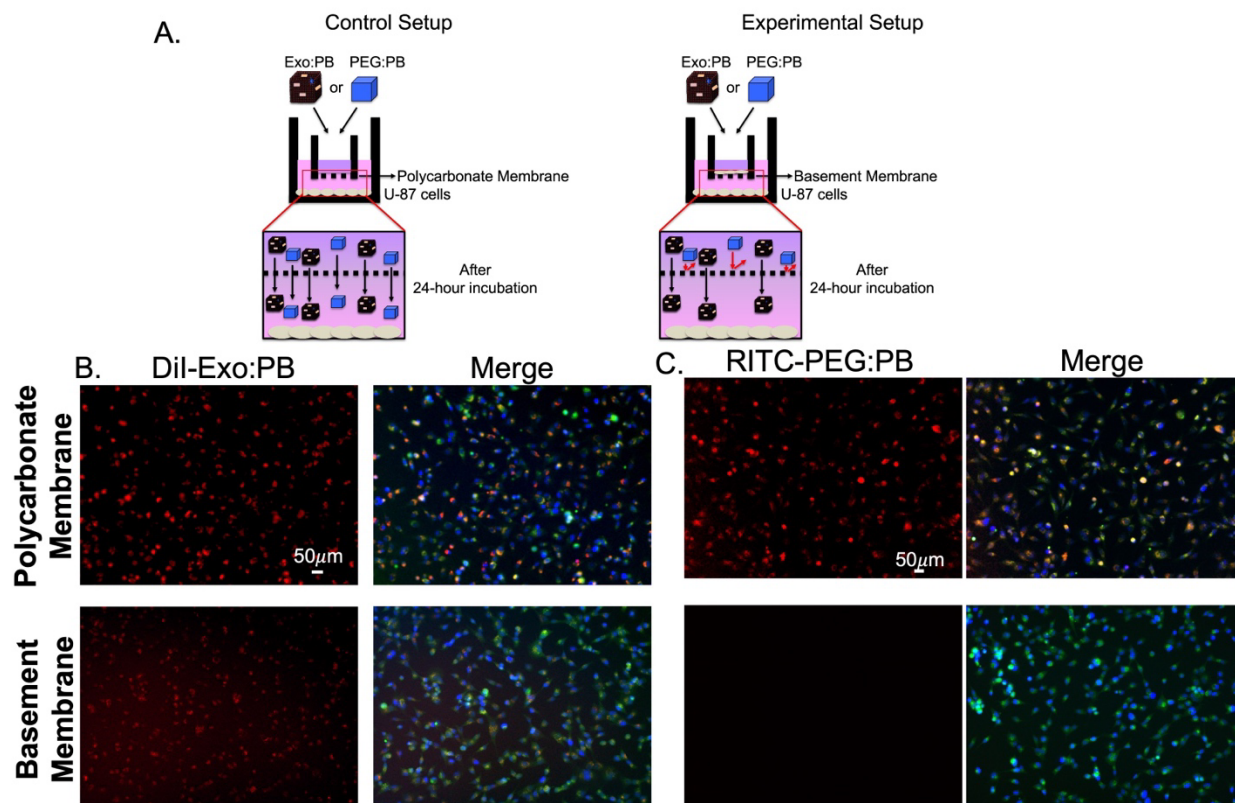


Figure 12: *In vitro* BBB experimental design and results. (A) Graphical representation of experimental setup using polycarbonate membranes as a control and basement membranes as the experimental condition. (B) U-87 cellular results for Dil-Exo:PB particles treated in both setups. Red = Dil-Exo:PB, Green = calcein AM, Blue = cell nucleus. Scale bar = 50µm. (C) U-87 cellular results for RITC-PEG:PB particles treated in both setups. Red = RITC-PEG:PB, Green = calcein AM, Blue = cell nucleus. Scale bar = 50µm. Readapted with permission from reference¹⁷¹, Copyright 2024, American Chemical Society.

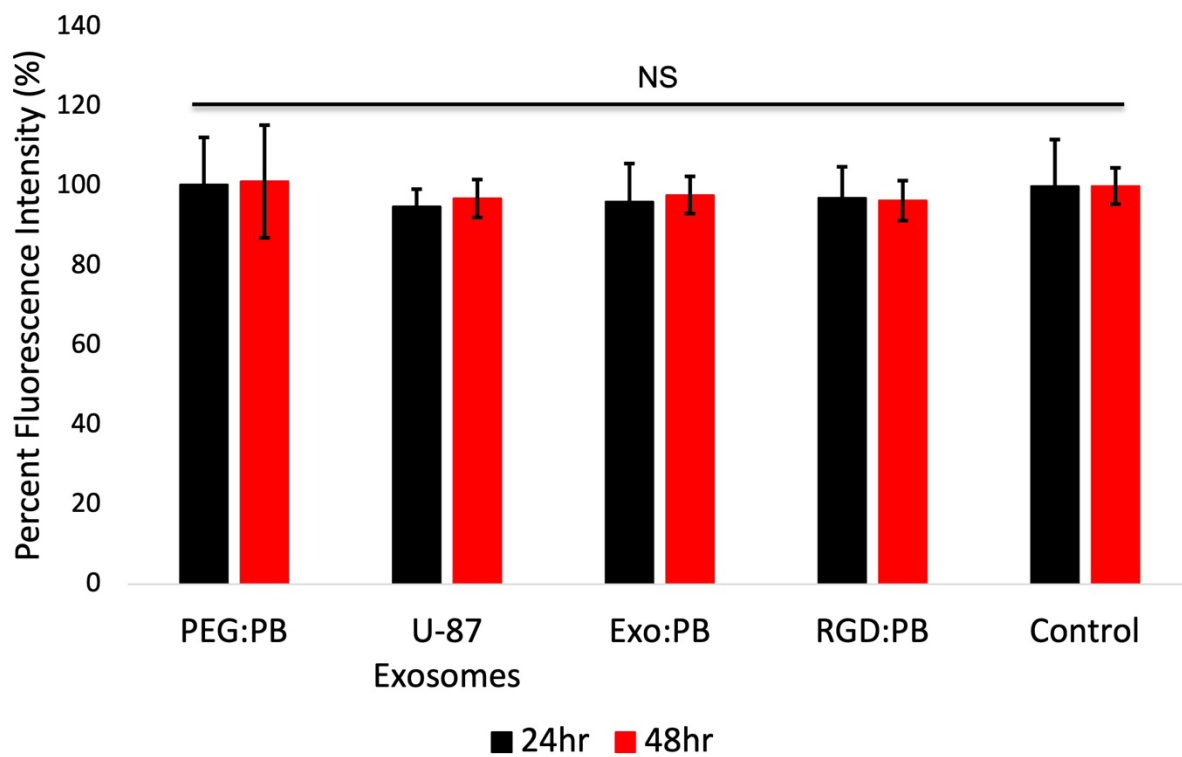


Figure 13: Tumorigenesis *in vitro* results for U-87 exosomes, Exo:PB, PEG:PB, RGD:PB, and control (nothing added). NS = No significance. Reproduced with permission from reference¹⁷¹, Copyright 2024, American Chemical Society.

Photothermal Conversion Abilities

PBNPs are of particular interest for photoconversion applications due to their high absorbance at 700-750nm (**Figure 14**). Since this falls within the biological transparency window (700-950nm), the material is allowed to absorb more of the light vs other tissues and blood in the same region. Based on their ability to absorb the light energy and convert it into localized heat energy, they can be used in photothermal therapy. The primary agent used for photothermal therapy are gold nanorods (AuNRs) due to their high initial photothermal conversion efficiency and biocompatibility. Unfortunately, when AuNRs are exposed to laser energy over multiple cycles, they will start to deform and decrease their photothermal conversion abilities (**Figure 15**). PBNPs have become a popular substitute as they have similar conversion efficiencies as well as show no direct morphological change due to laser exposure. To validate the effects of citric coated PBNPs as well as Exo:PB, PEG:PB, and U-87 derived exosomes, 1mg of each was exposed to an 808nm ($2\text{W}/\text{cm}^2$) laser for 10 minutes, followed by a 10 minute cooling period. The PBNP particles were shown to have the highest heat generation with a maximum temperature of 45.3°C , in comparison to that of PEG:PB and Exo:PB ($\sim 41.8^\circ\text{C}$ and 42.8°C) (**Figures 16A and 17**). The difference in the maximum temperature reached for the PBNPs vs PEG:PB and Exo:PB is likely due to the extra coatings on the surface. As the exosome and PEG surface will absorb a fraction of the light energy that each particle is exposed to, it is less energy that reaches the PBNP surface. As shown in **Figure 18**, when Exo:PB, PEG:PB, and U-87 exosomes are exposed to the 808nm laser ($2\text{W}/\text{cm}^2$) for 1 minute and then have their size measured, the U-87 exosomes have a drastic change in size compared to the Exo:PB and PEG:PB particle which show no change. This is due to the energy absorbed, which causes

instability in the exosome structure due to production of radical groups such as CO, CH₃, and COO. This promotes agglomeration as the lipids will undergo a rapid hydrolysis/oxidation process in which they will fracture and reform new larger amphiphilic particles. While Exo:PB and PEG:PB show no difference in size distribution, it can be theorized that the electrostatic energy holding the exosome coating to the catalytically active surface of the PBNP stabilizes the structure. Finally, the photothermal conversion efficiency (η) is calculated for each particle from the cooling period of **Figure 16B**. Overall, it is seen that PBNP and PEG:PB have similar efficiencies at 54.0 and 53.1%. The Exo:PB value was slightly reduced at 49.4% (**Figure 16B**). This further shows that the exosome layer absorbs a fraction of the light energy than that of the PEG or citric acid. Based on the catalytically active surface of the PBNPs, it is possible that the physical process of the coating provides a basis for strong membrane stability^{229, 230}.

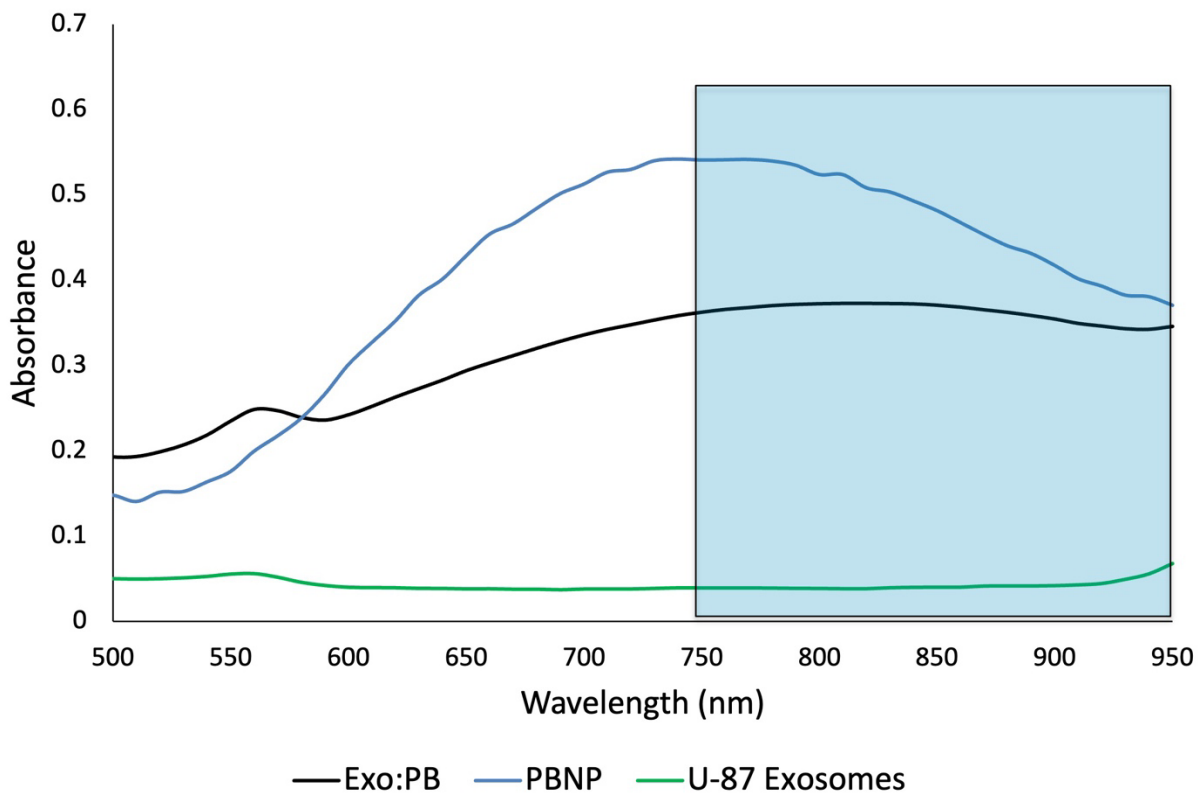


Figure 14: Absorbance curves for Exo:PB (black), PBNP (blue), and U-87 exosomes (green). Blue square represents biological transparency window. Readapted with permission from reference¹⁷¹, Copyright 2024, American Chemical Society.

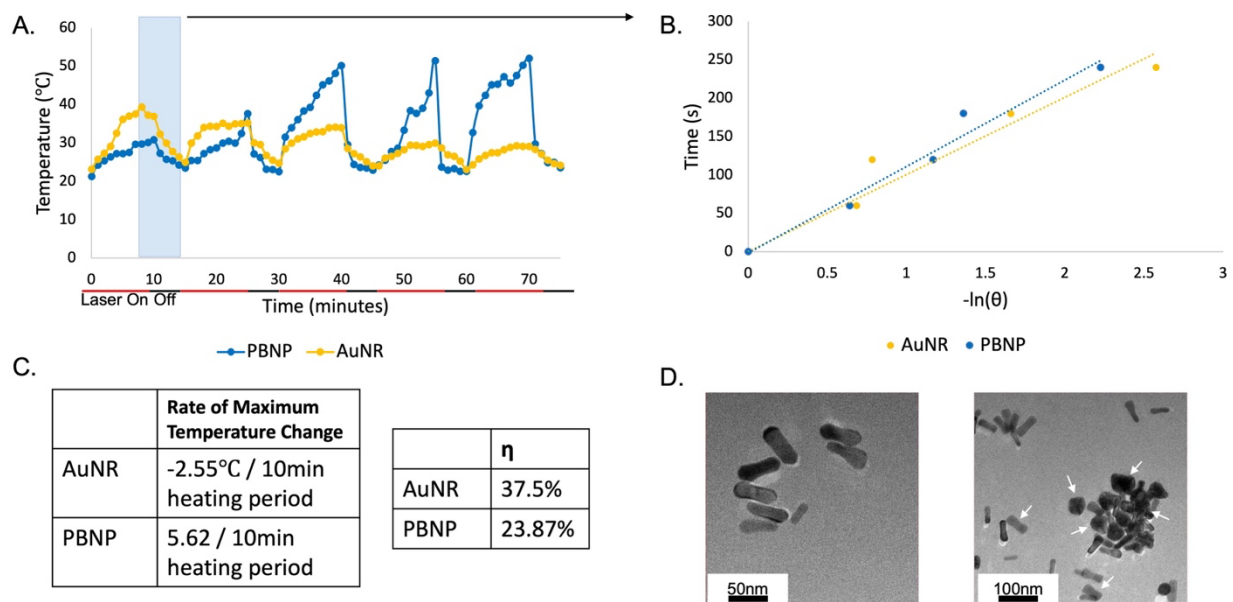


Figure 15: Photothermal results for PBNP and AuNR. (A) Photothermal stability for PBNP (blue) and AuNR (yellow). (B) Logarithmic linear correlation from the first cooling period highlighted in blue from (A). PBNP = blue, AuNR = yellow. (C) Calculated photothermal conversion efficiencies and rate of temperature change for PBNP and AuNR. (D) TEM images of the morphological change of AuNRs after laser exposure. Scale bars = 50nm and 100nm. Reproduced with permission from reference¹⁷¹, Copyright 2024, American Chemical Society.

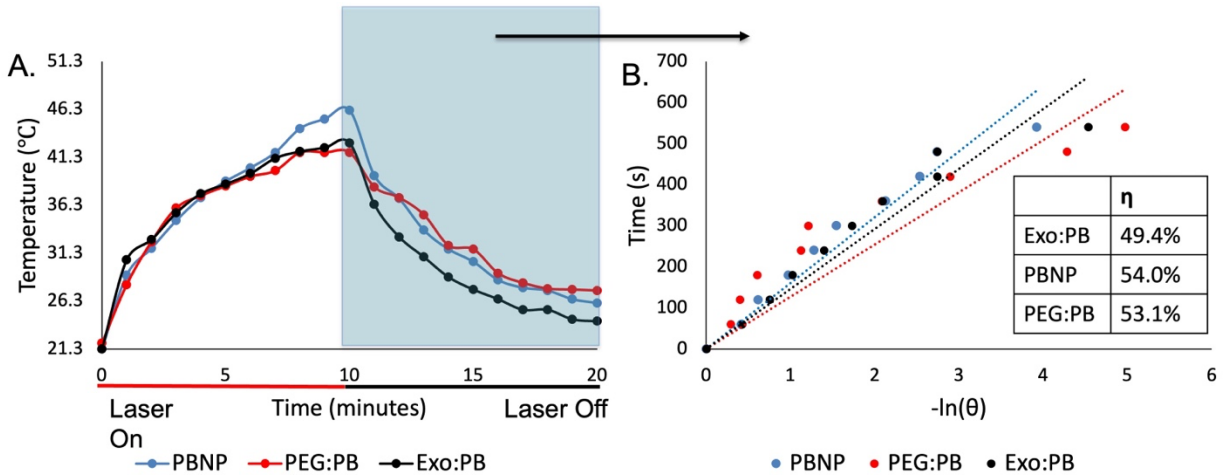


Figure 16: Temperature profile for PBNP, PEG:PB, and Exo:PB. (A) Heating and cooling curve of PBNP (blue), PEG:PB (red), and Exo:PB (black) after exposure to an 808nm laser. (B) Linear logarithmic curve as determined from the blue highlighted region in A). PBNP = blue, PEG:PB = red, Exo:PB = black. Insert is calculated photothermal conversion efficiencies (η). Readapted with permission from reference¹⁷¹, Copyright 2024, American Chemical Society.

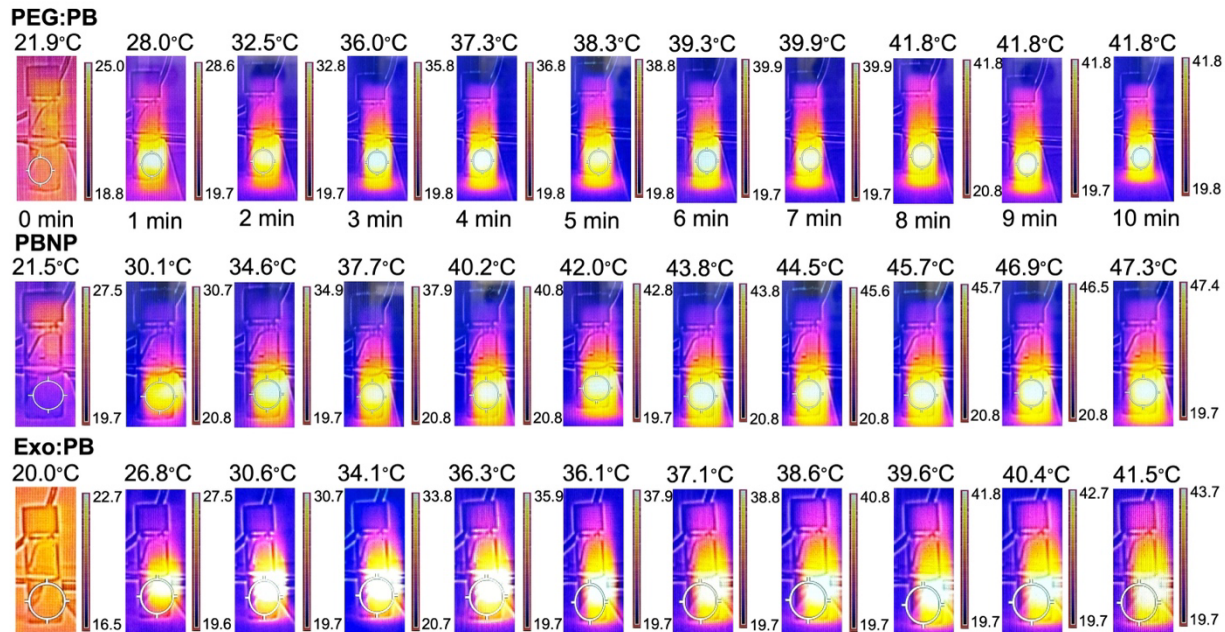


Figure 17: Photothermal profile for PEG:PB, PBNP, and Exo:PB after a 10 minute heating period with an 808nm laser. Images were taken every minute for 10 minutes using a thermal camera. Reproduced with permission from reference¹⁷¹, Copyright 2024, American Chemical Society.

To measure the photothermal therapy capabilities of the PBNP containing particles *in vitro*, two different assays were performed: an MTT assay and a live and dead assay. For the MTT assay, U-87 cells were plated in a 96-well plate and treated with varying concentrations of U-87 exosomes, PBNPs, Exo:PB, or PEG:PB and left to incubate for 24 hours. Up to 0.25mg/mL of all the particles, there is no toxicity seen. When exposed to an 808nm ($2\text{W}/\text{cm}^2$) laser for 1 minute, cell viability reduces by ~50% (**Figure 19**). This indicates that the particles could be administered with no cytotoxic effects, but when exposed to a laser will promote cell death. Now, this was convincing data for overall treatment, but lacked evidence for localized effect. The live and dead assay was done to provide this information. U-87 cells were plated and treated with 0.1mg/mL of PBNP, PEG:PB, Exo:PB, or U-87 exosomes. Each well was then treated for 1 minute with an 808nm ($2\text{W}/\text{cm}^2$) laser and then cells were stained with calcein AM and propidium iodide. When imaged, it was seen that the PBNP, PEG:PB, and Exo:PB particles all showed localized photothermal effects with a distinct area of red (dead cells) within the laser exposed region and a green (healthy cells) region located outside of the exposed region. Furthermore, wells treated with just laser or U-87 exosomes showed no apoptotic nature (**Figure 20**). To determine the temperature reached to cause photothermal effects, the maximum temperature at the cellular level was back calculated using two different standard curves. It was estimated PBNP cause a maximum temperature of 55.67°C , PEG:PB (52.73°C), and Exo:PB (53.30°C) with a concentration of 0.1mg/mL within the cell (**Figure 21**).

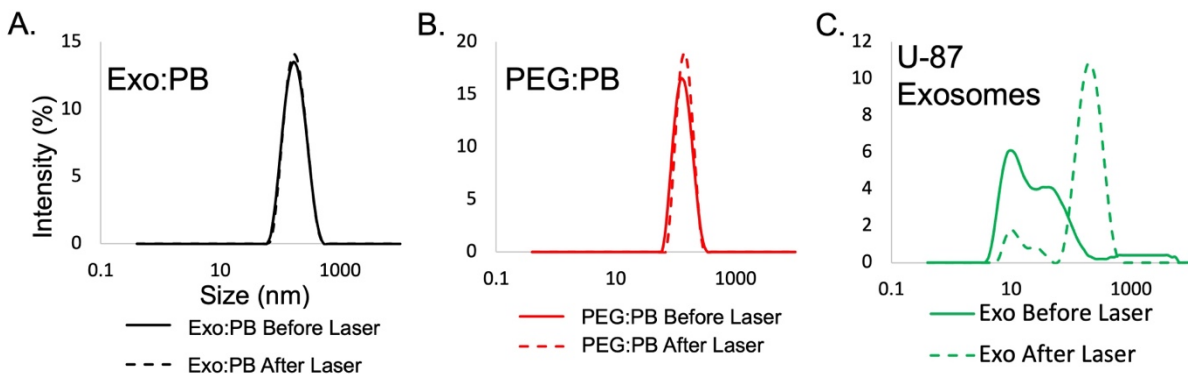


Figure 18: Photothermal size stability of (A) Exo:PB, (B) PEG:PB, and (C) U-87 derived exosomes. Solid line = before laser exposure, Cross Hatched Line = after 1 minute laser exposure. Readapted with permission from reference¹⁷¹, Copyright 2024, American Chemical Society.

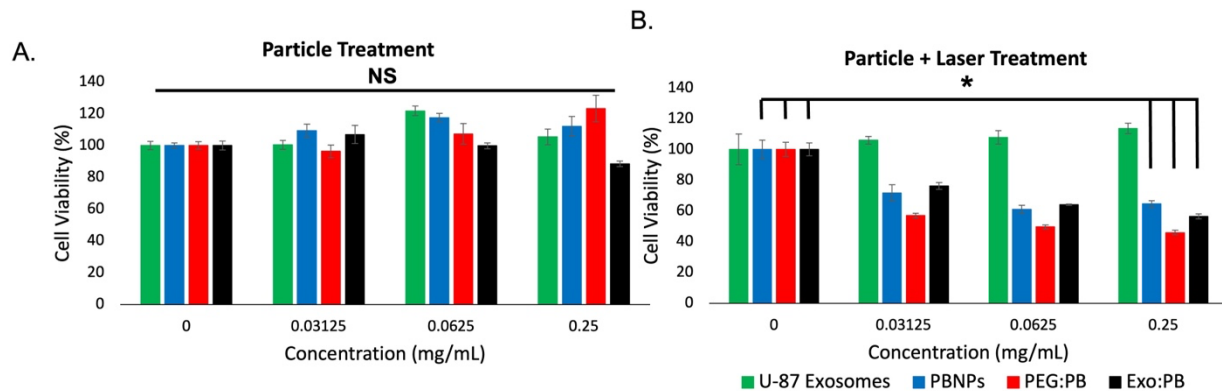


Figure 19: MTT assay results. (A) 24 hours after incubation with different concentrations of U-87 exosomes (green), PBNP (blue), PEG:PB (red), and Exo:PB (black). NS = no significance. N=6. (B) 24 hours after incubation with particles and exposure to an 808nm laser for 1 minute. U-87 exosomes (green), PBNP (blue), PEG:PB (red), and Exo:PB (black). * $p < 0.05$. N=6. Readapted with permission from reference¹⁷¹, Copyright 2024, American Chemical Society.

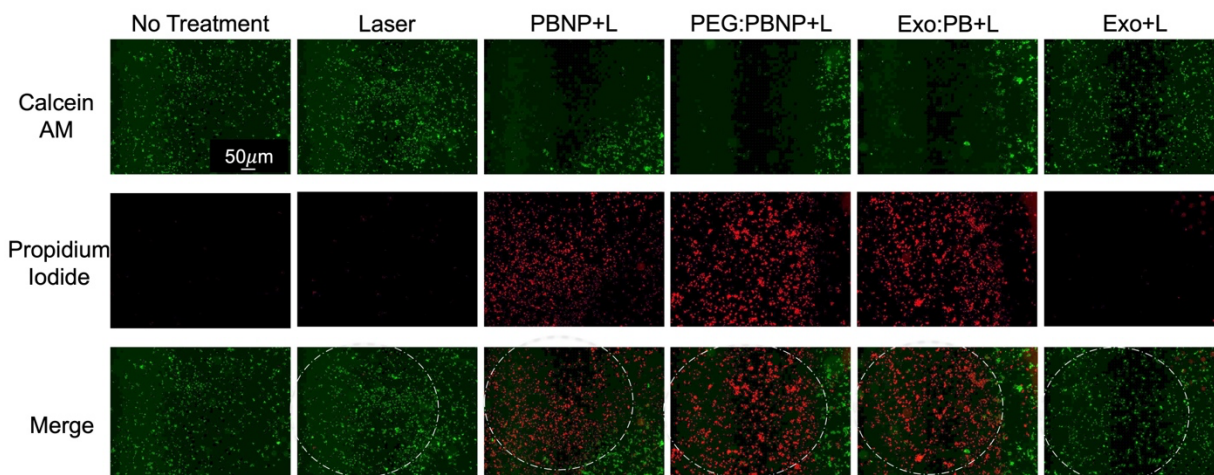
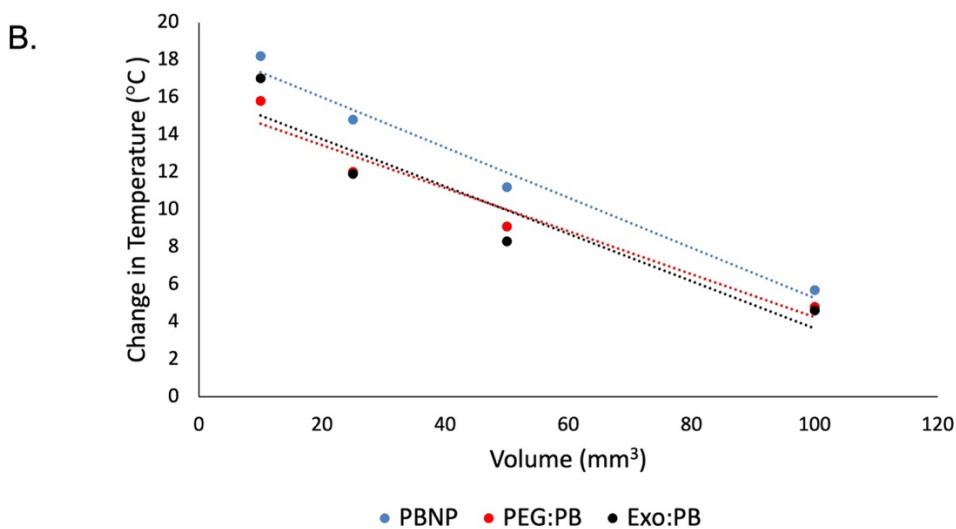
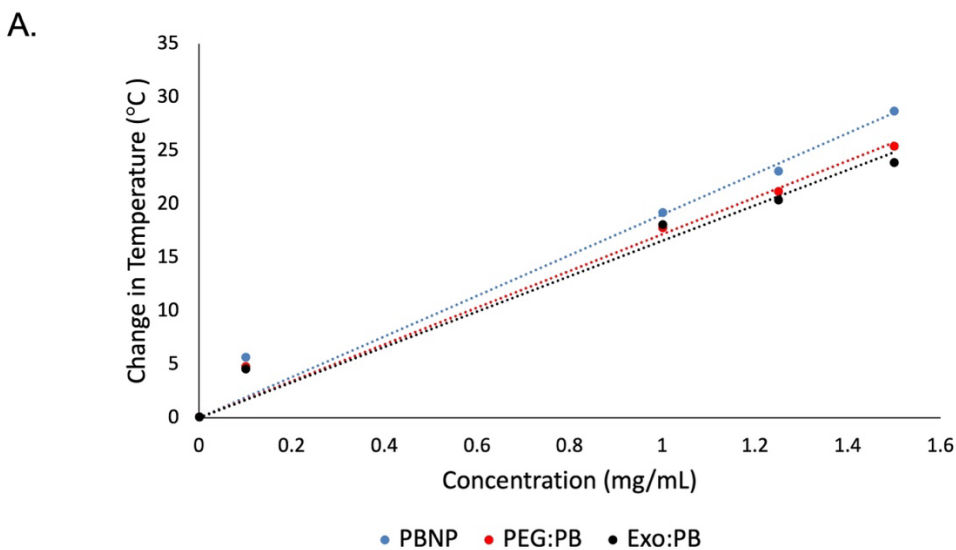


Figure 20: Live and dead assay results after treatment with PBNP plus laser exposure, PEG:PB plus laser exposure, Exo:PB plus laser exposure, U-87 derived exosomes plus laser exposure, laser plus no particles, or no treatment of particle or laser. Green = alive cells (calcein AM), Red = dead cells (propidium iodide). Scale bar = 50µm. Readapted with permission from reference¹⁷¹, Copyright 2024, American Chemical Society.



C.

	Concentration in Cell Pellet (mg/mL)	Calculated Temperature (°C) Reached within Cells
PBNP	0.105 ± 0.0190	55.67
PEG:PB	0.103 ± 0.0034	52.73
Exo:PB	0.122 ± 0.0251	53.30

Figure 21: Estimated particle temperature reached within U-87 cells. (A) Standard curve for concentration vs change in temperature for PBNP (blue), PEG:PB (red), and Exo:PB (black). (B) Standard curve for volume vs change in temperature for PBNP (blue), PEG:PB (red), and Exo:PB (black). (C) Back calculated nanoparticle concentrations and estimated temperature reached within U-87 cells. Reproduced with permission from reference¹⁷¹, Copyright 2024, American Chemical Society.

In vivo U-87 Subcutaneous Tumor Targeting and Treatment

To investigate the *in vivo* targeting effects of Exo:PB in comparison to traditional PBNPs, a U-87 subcutaneous tumor model was utilized. Initially, U-87 cells were mixed with a Matrigel solution and implanted into the flank side of nude male mice (N=6). After ~1-2 weeks, tumors were visible and mice were randomly split into two groups: Exo:PB and PEG:PB. Particles were injected intravenously and particle signal within the tumor area was monitored using photoacoustic imaging (PAI). 2 hours post injection, a strong signal was seen for Exo:PB particles within the tumor region. In comparison, the PEG:PB particles had just started to penetrate the tumor area (**Figures 22A and 23**). This is seen further after quantification of PBNP PAI signal, that there is statistically significantly more Exo:PB that reaches the tumor site than PEG:PB within the same time period (**Figure 22B**). Total blood signal was also quantified and showed that the blood supply to the tumors for both groups was statistically the same, indicating that through passive targeting the particles would have had the same opportunity to reach the source (**Figure 22C**). Immune evasion due to the exosome layer allows for the Exo:PB particles to stay in circulation longer and thus have a higher targeting change in tumor tissues in comparison to the PEG:PB control. The Exo:PB particles also have higher retention capabilities as there is a consistently higher signal PAI signal seen even up to 24 hours post injection. This not only matches with *in vitro* results but provides evidence that the exosome coating allows for increased cellular uptake in specific tissues without fear of off-targeting effects. H&E stained tissue images of the liver, brain, heart, lungs, spleen, kidney, and muscle shows that there is no cytotoxic effects of Exo:PB and PEG:PB particles in comparison to PBS (**Figure 24**).

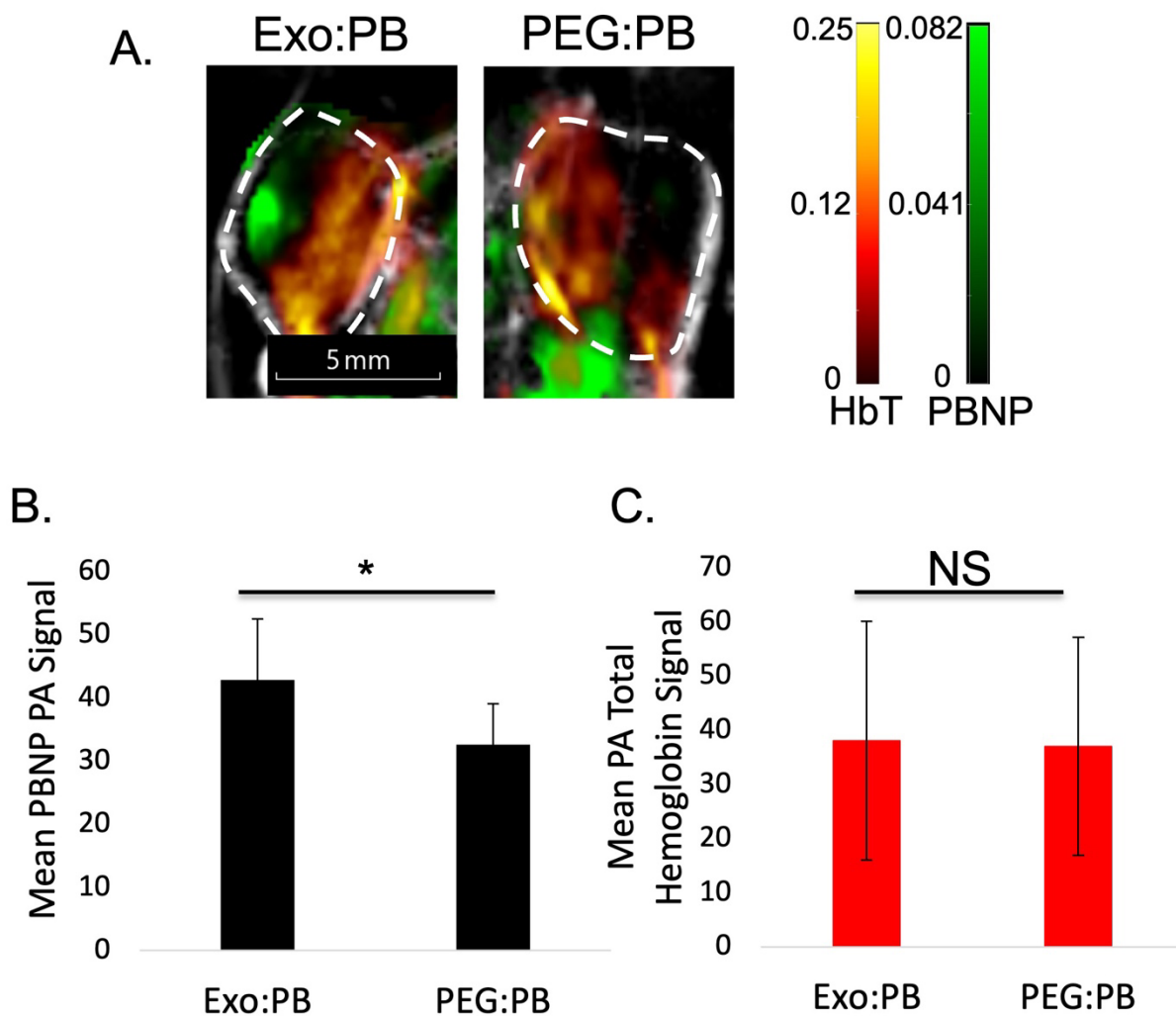


Figure 22: *In vivo* U-87 subcutaneous particle accumulation. (A) Photoacoustic images of subcutaneous tumors 2 hours post intravenous injection. Gray = ultrasound, Red = total hemoglobin signal (HbT), Green = Exo:PB or PEG:PB. Scale bar = 5mm. (B) Average photoacoustic signal intensity within tumors 2 hours after intravenous injection of Exo:PB or PEG:PB. * $p < 0.05$. $N = 4$. (C) Average total hemoglobin signal determined from photoacoustic images of tumors. NS = no significance. $N = 4$. Readapted with permission from reference¹⁷¹, Copyright 2024, American Chemical Society.

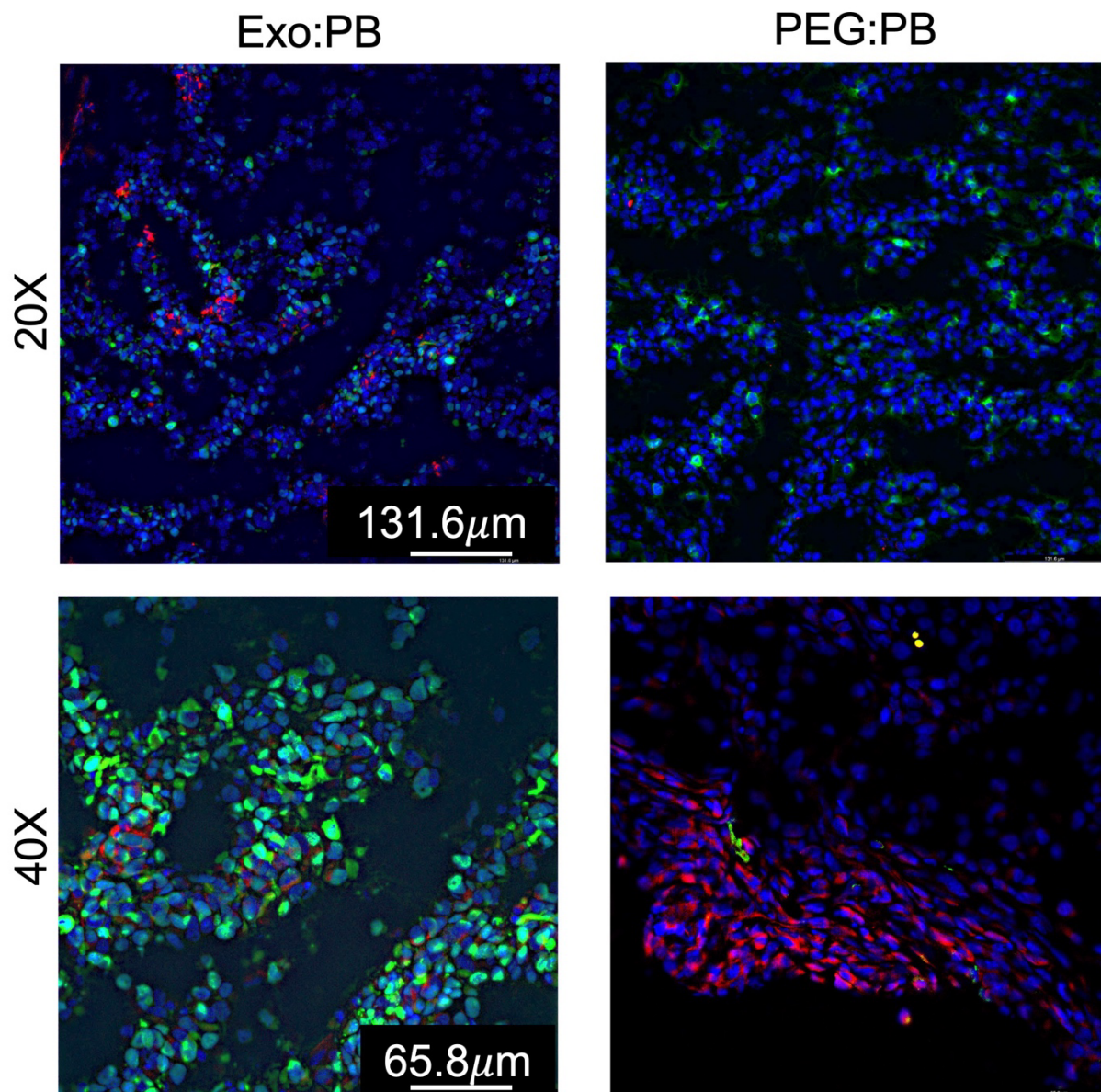


Figure 23: Immunofluorescence images of excised subcutaneous tumor tissue 24 hours after intravenous injection of Dil-Exo:PB or RITC-PEG:PB. Green = Ki67, Blue = cell nucleus, Red = Dil-Exo:PB or RITC-PEG:PB. Scale bar = 131.6 μ m for 20X images and 65.8 μ m for 40X images. Readapted with permission from reference¹⁷¹, Copyright 2024, American Chemical Society.

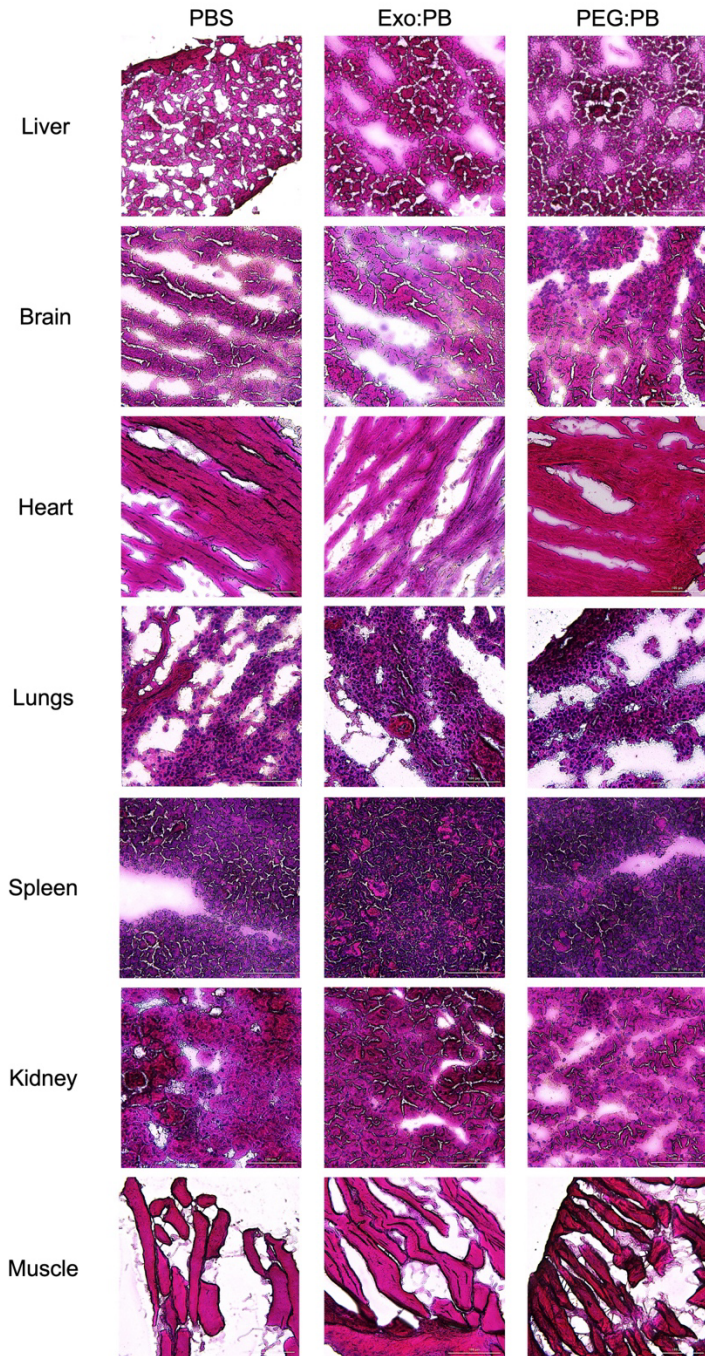


Figure 24: H&E stained images 24 hours after intravenous injection of Exo:PB, PEG:PB, or PEB into subcutaneous glioblastoma bearing mice. Scale bar = 100 μ m. Reproduced with permission from reference¹⁷¹, Copyright 2024, American Chemical Society.

To measure the *in vivo* therapeutic potential of Exo:PB, the Exo:PB, PEG:PB, or PBS was intravenously injected into U-87 subcutaneous tumor bearing mice and then 3 hours post injection, tumors were exposed to an 808nm ($2\text{W}/\text{cm}^2$) for 10 minutes. The tumors were treated with particles and laser every 3 days over an 8-day period, with tumor size being measured every 2 days. It was seen that after the first treatment, PEG:PB and PBS tumor size continued to grow while Exo:PB treated tumors showed only a slight increase in size. This slight increase in size is likely due to an increase of local inflammation within the area as this is one of the primary side-effects of photothermal therapy. Treatment was stopped after 8 days as the size of Exo:PB tumors were no longer visible. PEG:PB tumors stayed at relatively the same size ($\sim 300\text{mm}^3$) throughout the treatment, indicating that the particles were effective at preventing growth, but not at full eradication (**Figure 25A**). PBS treated tumors continued to grow without any issue (**Figure 26A**). Throughout the entire treatment period, all mice were monitored through body weight measurements to make sure they were healthy (**Figures 25B and 26B**). The better therapeutic effect seen by the Exo:PB particles is likely due to the better targeting and accumulation effects as seen in **Figure 22A**. On average more particles would be present and therefore allow for a higher photothermal conversion rate. To ensure the safety of the mice throughout the treatment, a separate set of mice were injected with Exo:PB or PBS intratumorally and monitored to investigate the cytotoxic effects of the laser itself. Tumors were treated with an 808nm ($2\text{W}/\text{cm}^2$) laser for 1 minute. Mice were monitored for 11 days over which the Exo:PB treated tumors showed complete reduction, but the PBS tumors continued to grow up to $\sim 1400\text{mm}^3$ (**Figures 27A and 27B**). There was no evidence of necrosis, skin irritation or excessive inflammation which for the PBS group so it was deduced that the

laser did not cause any harmful effects. After treatment, mice were sacrificed, and tumor tissue was excised. Sectioned tissue was stained with Ki67 (intravenous injection) or cleaved caspase-3 (intertumoral injection) antibodies as well as DAPI²³¹. DiI-Exo:PB particles showed direct overlay with both Ki67 and cleaved caspase-3 markers indicating that it effectively accumulated within the tumor region (**Figures 23 and 27C**) and was the direct cause of cell death once exposed to the laser (**Figure 27C**). Intravenously injected RITC-PEG:PB tumors were sectioned and stained with Ki67 and showed that there was very little accumulation within the tumor area at that time point which supports the imaging data presented in **Figure 23**.

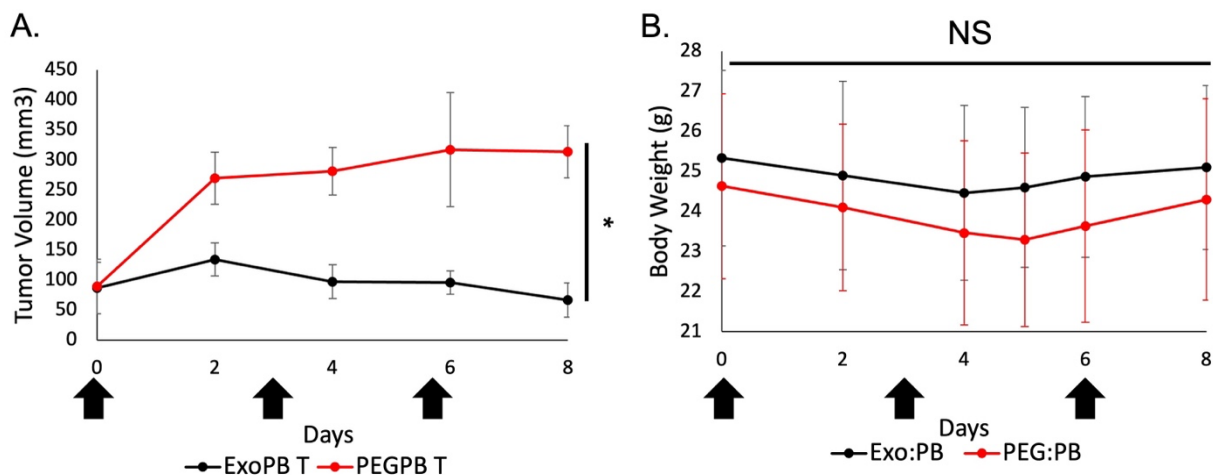


Figure 25: Intravenous In vivo photothermal therapy. (A) Tumor volume after treatment of particle and laser. Black arrows indicate days in which particles were injected and tumors were treated with laser 2 hours after. * $p < 0.05$. $N = 3$. (B) Body weight of mice throughout treatment period. Black arrows indicate days in which particles were injected and tumors were treated with laser 2 hours after. NS = no significance. $N = 3$. Readapted with permission from reference¹⁷¹, Copyright 2024, American Chemical Society.

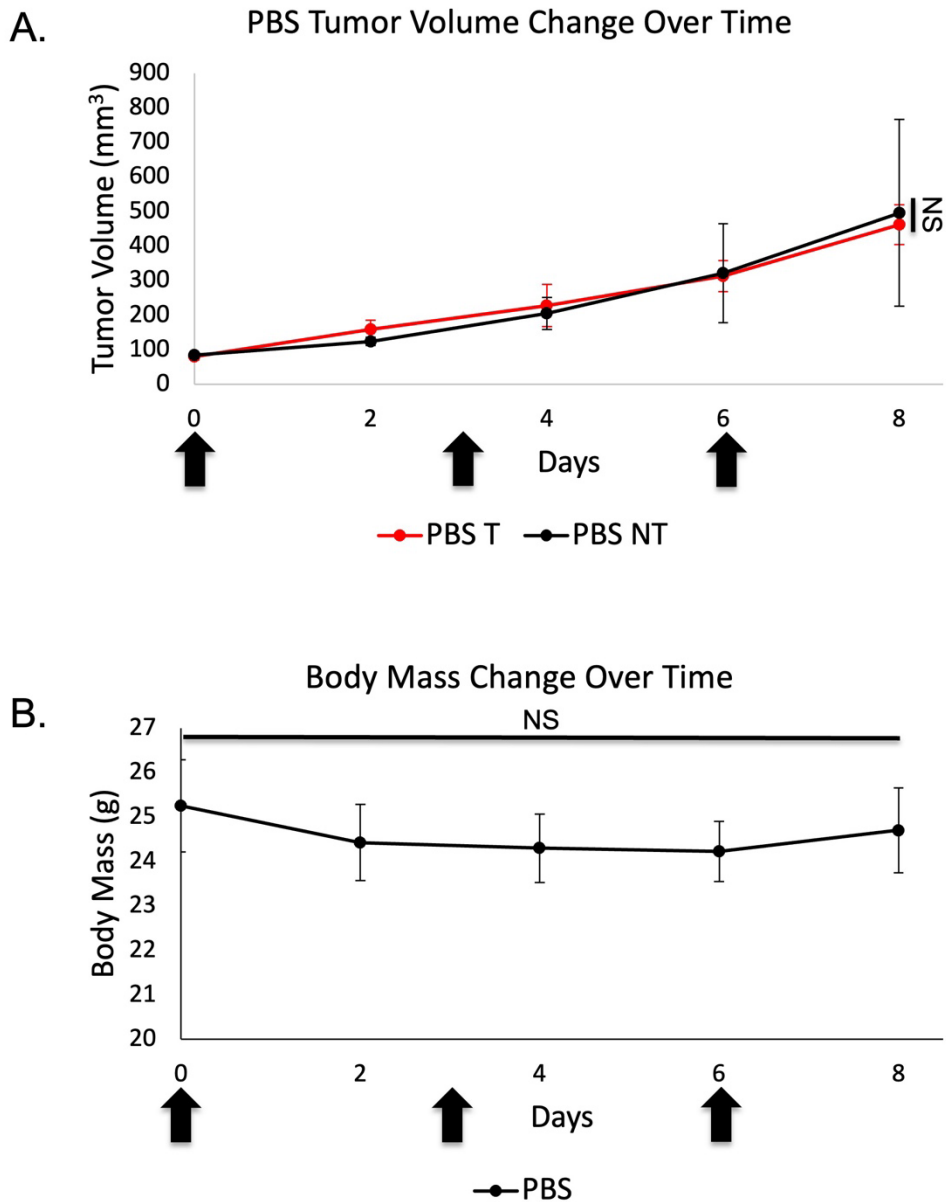


Figure 26: Control intravenous photothermal therapy using PBS. (A) Tumor volume as monitored throughout the treatment period. Black arrows indicate days in which particles were injected and tumors were treated with laser 2 hours after. NS = no significance. N=3.(B) Body weight of mice throughout treatment period. Black arrows indicate days in which particles were injected and tumors were treated with laser 2 hours after. NS = no significance. N=3. Reproduced with permission from reference¹⁷¹, Copyright 2024, American Chemical Society.

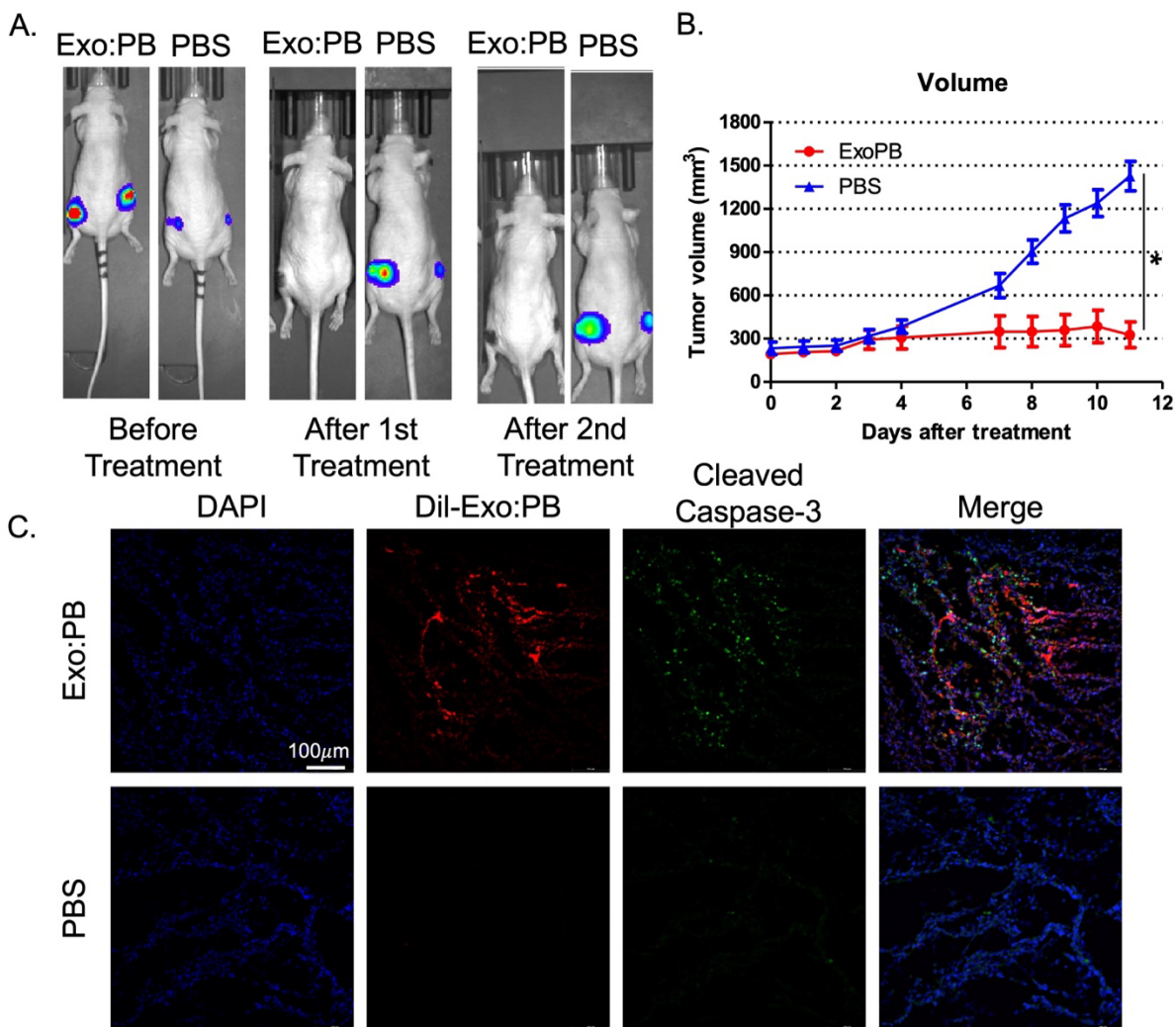
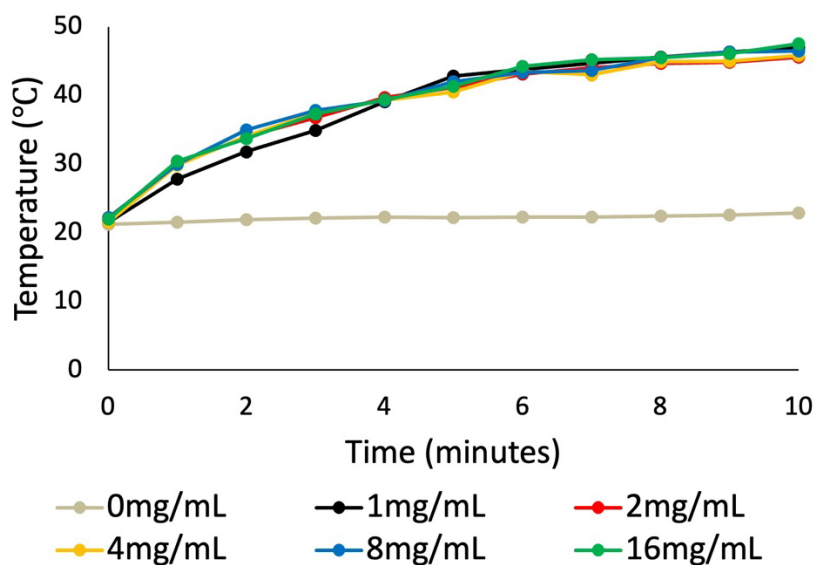


Figure 27: Intratumoral photothermal treatment of subcutaneous tumors. (A) Bioluminescence images of mice before and after treatment with Exo:PB or PBS. (B) Tumor volume throughout treatment period. * $p < 0.05$. $N = 3$. (C) Immunofluorescence images of tumor tissue. Blue = cell nucleus, Red = Dil-Exo:PB, Green = cleaved caspase-3. Scale bar = 100 μ m. Thanks to Seock-Jin Chung for imaging assistance. Reproduced with permission from reference¹⁷¹, Copyright 2024, American Chemical Society.

Laser intensity for therapeutic use was determined from an *in vitro* MTT assay in which U-87 cells were exposed to 808nm intensities ranging from 1.5-5W/cm². It was shown that there was not a statistical difference in cell viability over the entire range, so 2W/cm² was chosen as it is consistent with what has been reported in the literature and showed consistent therapeutic effect *in vitro* (**Figure 28**). Particle dosage was determined by exposing PBNPs at concentrations from 0-16mg/mL to an 808nm laser (2W/cm²) for 10 minutes to determine the maximum temperature that could be reached. It was found that all concentrations from 1-16mg/mL had similar heating photoconversion rates. 1mg/mL was chosen for further experiments as this is similar to the clinical dosage given to patients for radiation exposure. Now, it should be noted that the calculated maximum permissible exposure (MPE) for an 808nm laser in the clinical setting is 0.33W/cm² ^{194, 232}. While this is much lower than the dosage that was used, 2W/cm² is consistent with the literature at this preclinical stage. When our particles are tested with an FDA-approved laser interstitial thermal treatment (LITT) system, the laser intensity and time allotted for treatment will be adjusted to match clinical guidelines.

A.



B.

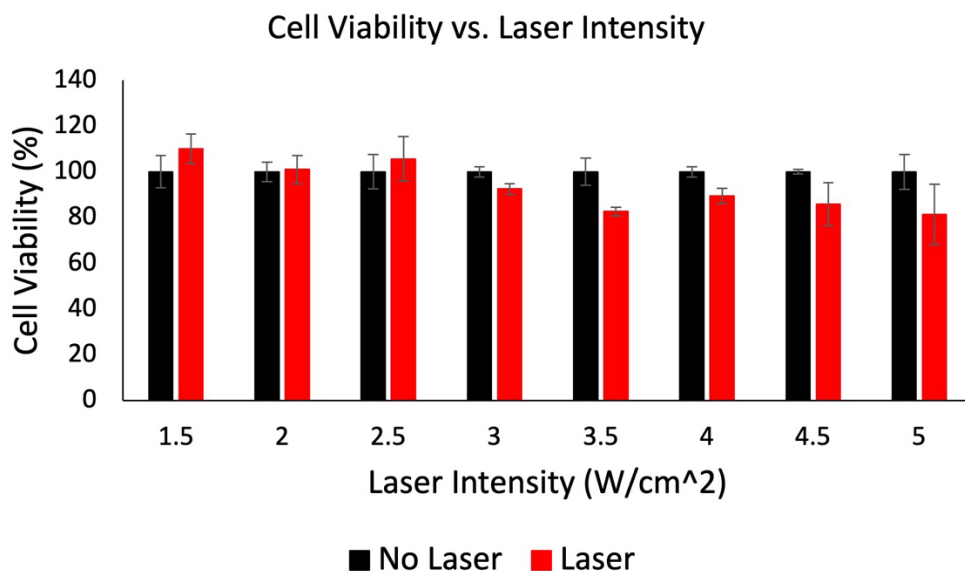


Figure 28: Particle and laser-based effects for use in *in vivo* models. (A) Temperature profile of PBNPs at different concentrations measured over a 10-minute period. (B) MTT assay results of U-87 cells exposed to an 808nm laser of different laser intensities. N=3. Reproduced with permission from reference¹⁷¹, Copyright 2024, American Chemical Society.

In vivo Orthotopic Brain Tumor Diagnostics

Using a previously established method by Baumann et al., we established an orthotopic glioblastoma model using stereotaxic injection²³³. In general, a suspension of luciferase expressing U-87 cells would be injected into the right hemisphere of anesthetized mice placed in a stereotaxic device. Approximately 2-4 weeks post-surgery, luciferase signals within the brain region would be checked using IVIS imaging (**Figure 29A**). Once tumors were of appropriate size, mice were split into two groups: Exo:PB and PEG:PB. About one week after bioluminescence signal is checked, either Exo:PB or PEG:PB was injected intravenously and particle accumulation within the tumor hemisphere of the brain was monitored using PAI. 3 hours post-injection there was a strong signal PBNP signal intensity from the Exo:PB particles (**Figure 29B**). As the signal overlays with the total hemoglobin (Hb+HbO₂) blood signals within the same region, it indicates that Exo:PB is not only able to cross the BBB but intracerebral delivery occurs through the circulatory system. Accumulation patterns were observed through PAI with images taken pre, 1, 3, and 24 hours post injection. All signals were quantified and averaged for the tumor hemisphere and contra lateral hemisphere to determine overall effectiveness of targeting. It can be seen in **Figure 30A**, that the highest accumulation occurs at 3 hours but only decreases by a small amount at 24 hours. This indicates that the Exo:PB particles are retained well in the tissue, specifically within the tumor region. *Ex vivo* analysis of H&E-stained whole brain tissue shows that the histological region for the tumor directly correlates with the region of accumulation within PAI (**Figure 29C**). Further validation was done with inductively coupled plasma mass spectrometry (ICP-MS) to quantify the amount of iron in each hemisphere after 24 hours. It was seen that the amount of iron present within the tumor

hemisphere was statistically higher than that of the contra lateral hemisphere, which indicates that there effective accumulation of Exo:PB within the correct tissue (**Figure 30B**), which is consistent with PAI quantification. Immunofluorescence of excised tissue was performed and showed a great overlap between Dil-Exo:PB and Ki67, indicating that the particles did accumulate within the tumor region (**Figure 31A**). Further *ex vivo* staining with hematoxylin and eosin (H&E) showed a distinct layer between normal brain tissue and tumorous tissue, with direct overlay of the Dil-Exo:PB particles in the tumor region (**Figure 31B**). To validate that the hybrid particles were making it into the tumor site instead of a stained exosomes that had been stripped from the PBNPs after injection, BioTEM was performed. At high magnification, the cubic shape of PBNPs can easily be distinguished within the perinuclear area of the cells (**Figure 32**). Further analysis of the heavy metal stained tissue showed that the Exo:PB particles can accurately help distinguish the tumor origin, tumor boundary, and areas of tumor infiltration. This is exciting as it means that these particles could be used as specific diagnostic markers in the clinic (**Figure 33**)²³⁴. Finally, a biodistribution study was done *in vivo* to quantify the overall amount of PBNPs reaching the brain in comparison to other major organs. As PBNPs are known to cause acute liver toxicity in high concentrations, it was a concern that if targeting wasn't successful other problems could arise. It was seen that ~4% of total particle injection made it to the brain, while majority of particle ended up in the liver (**Figure 34**). Though as these particles are administered through intravenous injection (compared to the oral administration in the clinic), serum indexes in the liver easily reach back to normal levels relatively quickly after exposure²³⁵. This indicates that there would be minimal effects from our particles based on the administration route. Compared to the PEG:PB particles, there was low PAI signal detected at

all time points indicating an inability to pass through the BBB. As the method used to induce the orthotopic glioblastoma model disrupts the BBB, it was of concern that particles may naturally be able to pass into the brain without issue. As we see little evidence from PAI, fluorescence, and BioTEM, the PEG:PB particles were unable to penetrate the brain region successfully. Thus the *in vivo* model was given enough time to heal post-surgery to prevent skewed results. Due to the necrotic nature of glioblastoma, there are instances in which the BBB can be disrupted by the cancer itself and allow for passage of external contents into the brain. Traditional chemotherapies tend to work better in these cases as there is a higher likelihood of passive accumulation within the tumor site without transportation across the BBB. This would allow for the Exo:PB particles to target/accumulate in greater concentrations, but even without disruption of the BBB there is still high quantity that is present within the tumor. Necrosis and hypoxic environments can also cause an influx of macrophages within the tumor microenvironment. While there is a possibility that macrophages could uptake Exo:PB in the blood stream and deliver the particles to the tumor site, based on the little presence of PEG:PB particles within the brain this is likely not the case. As the PEG:PB particles would undergo the same cellular uptake and transportation to the brain, they provide as a good control to show this phenomenon is not the cause for transportation to the tumor site.

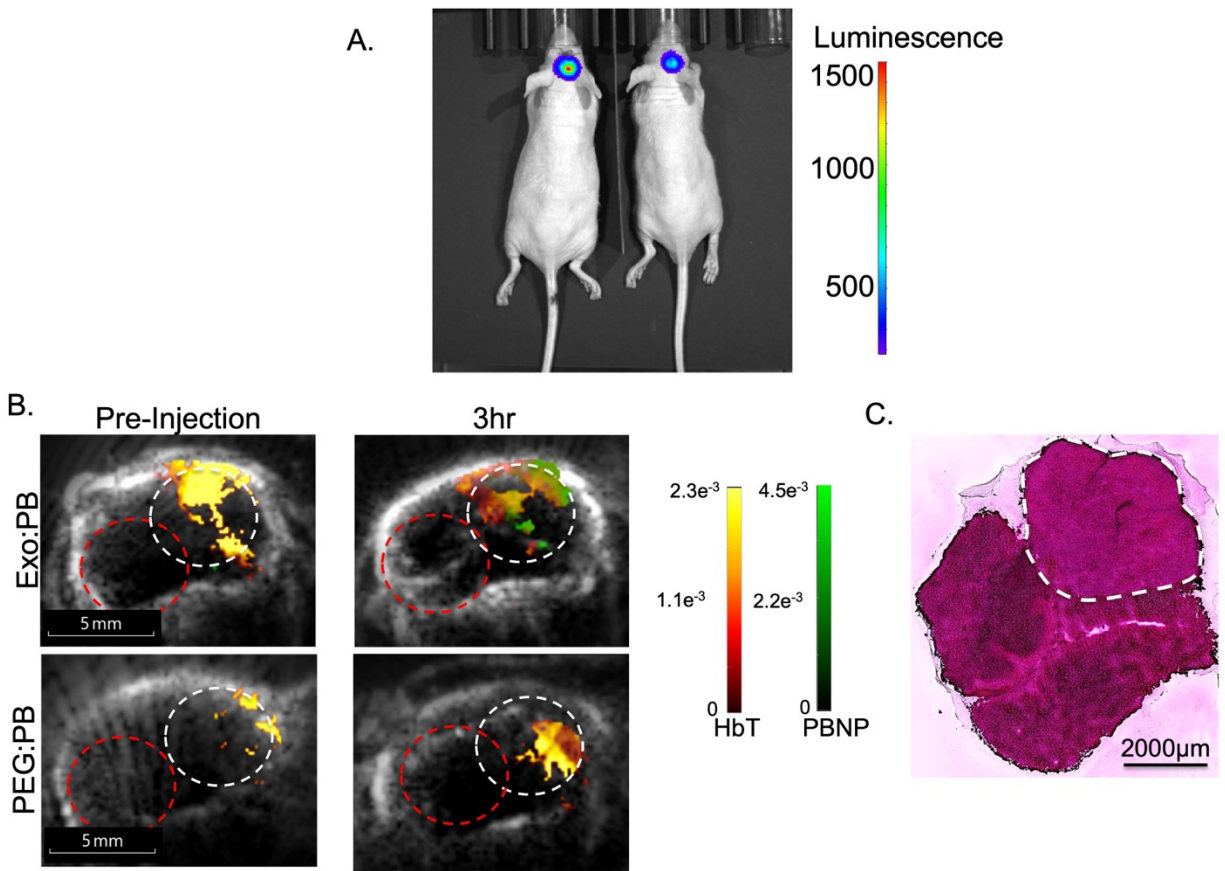


Figure 29: Orthotopic glioblastoma *in vivo* imaging. (A) Bioluminescence imaging of mice before injection to validate tumor size. (B) Photoacoustic images of the brain before and after intravenous injection of Exo:PB and PEG:PB. Gray = ultrasound, Red = total hemoglobin signal (HbT), and Green = Exo:PB or PEG:PB. White circle = tumor hemisphere, Red circle = contra lateral hemisphere. Scale bar = 5mm. (C) H&E stained whole brain with glioblastoma tumor image. White circle = tumor. Scale bar = 2000µm. Readapted with permission from reference¹⁷¹, Copyright 2024, American Chemical Society.

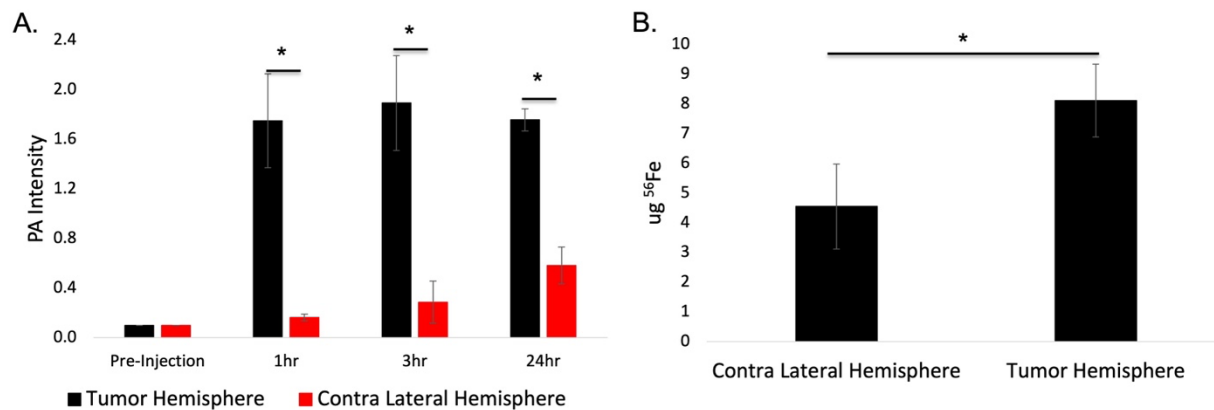


Figure 30: Particle quantification within brain tumor and contra lateral hemispheres. (A) Photoacoustic signal quantification of Exo:PB within the tumor (black) and contra lateral (red) hemispheres pre-injection and 1, 3, and 24 hours post intravenous injection. * $p < 0.05$. $N = 3$. (B) ICP quantification of ^{56}Fe within the tumor and contra lateral hemispheres 24 hours post intravenous injection. * $p < 0.05$. $N = 3$. Readapted with permission from reference¹⁷¹, Copyright 2024, American Chemical Society.

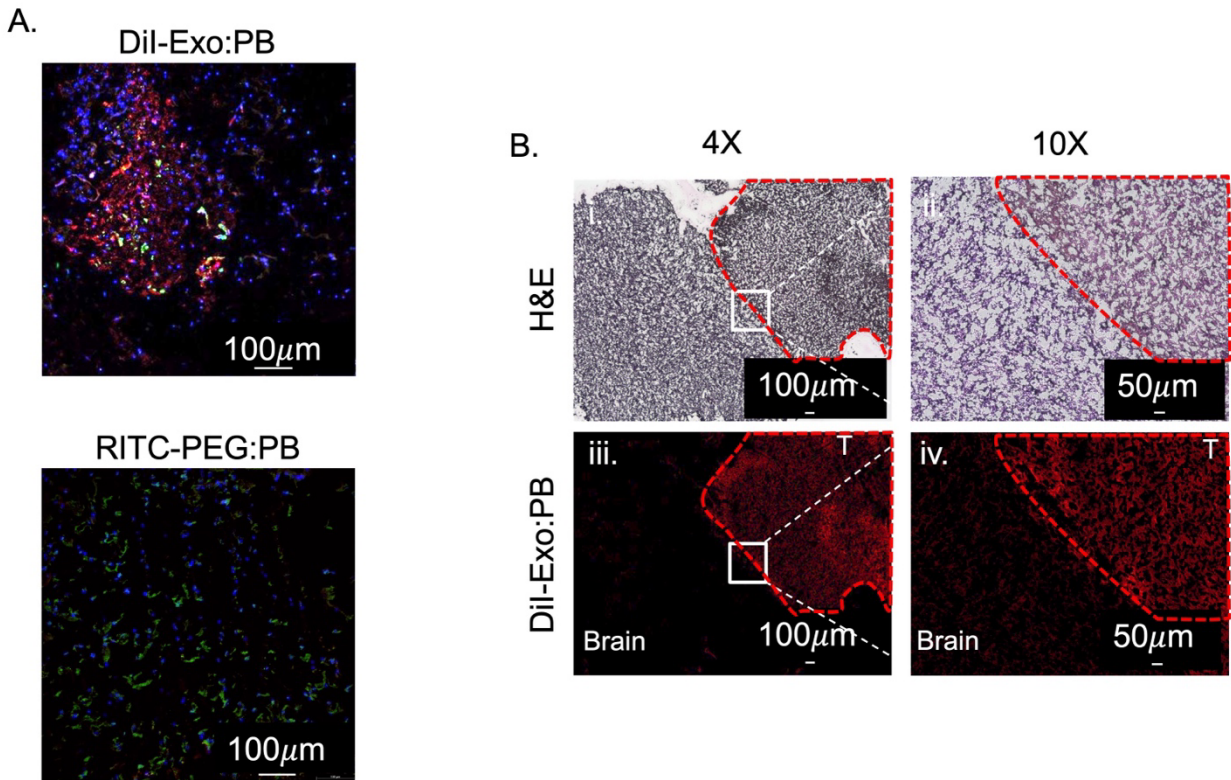


Figure 31: *Ex vivo* tissue staining of brain tumor region. (A) Immunofluorescence staining 24 hours after intravenous injection of Dil-Exo:PB or RITC-PEG:PB. Blue = cell nucleus, Green = Ki67, Red = Dil-Exo:PB or RITC-PEG:PB. Scale bar = 100µm. (B) Hematoxylin and eosin (H&E) staining and overlay fluorescence of brain tissue 24 hours after intravenous injection of Dil-Exo:PB. Scale bar = 100µm for 4X images and 50µm for 10X images. T = tumor. Readapted with permission from reference¹⁷¹, Copyright 2024, American Chemical Society.

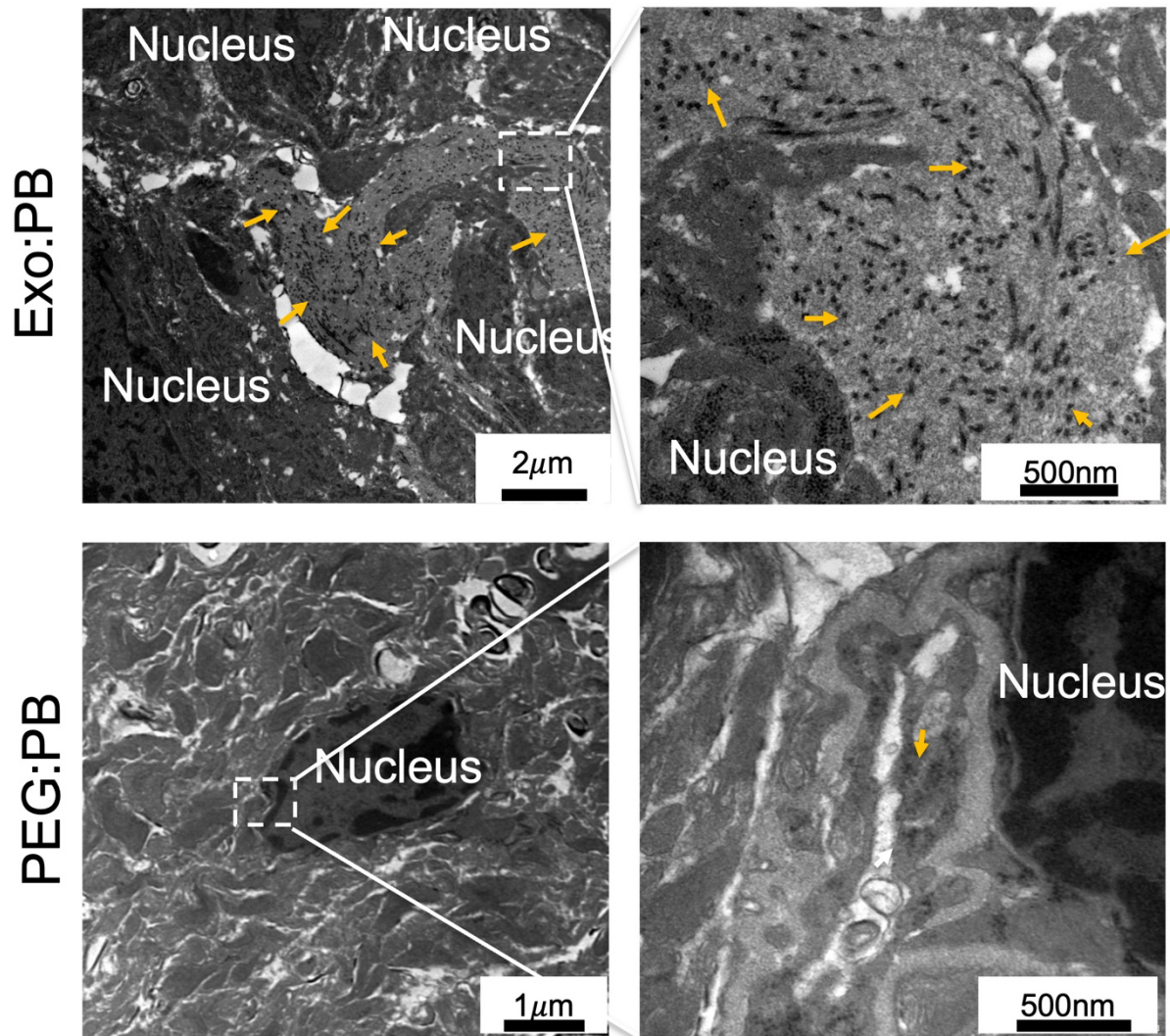


Figure 32: BioTEM images of brain tumor tissue excised 24 hours after intravenous injection of Exo:PB or PEG:PB. Yellow arrows indicate PBNP nanoparticles. Scale bar = 2µm (Exo:PB) and 1µm for 4000X images and 500nm for 12,000X images. Readapted with permission from reference¹⁷¹, Copyright 2024, American Chemical Society.

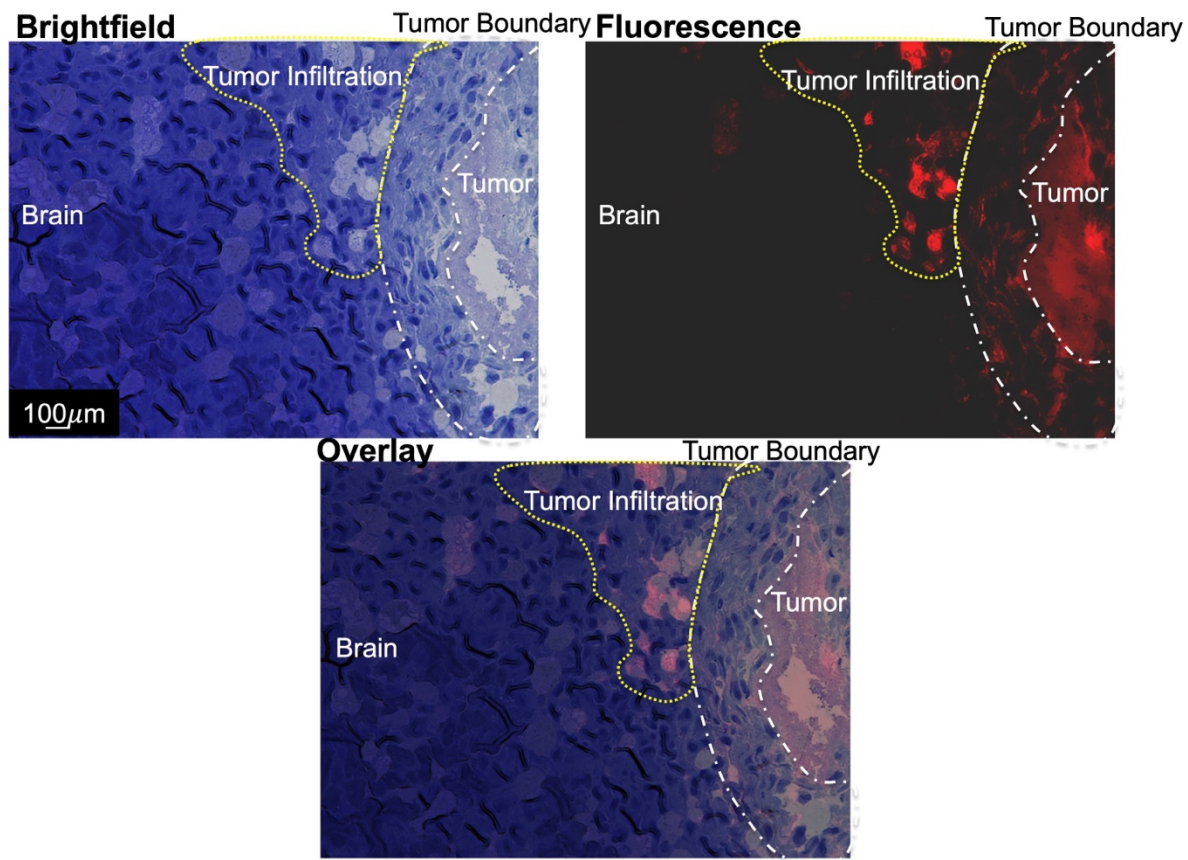


Figure 33: Heavy metal-stained brain tumor tissue and overlay fluorescence. White Dashed Line = tumor boundary, Yellow Dashed Line = tumor infiltration. Scale bar = 100µm. Reproduced with permission from reference¹⁷¹, Copyright 2024, American Chemical Society.

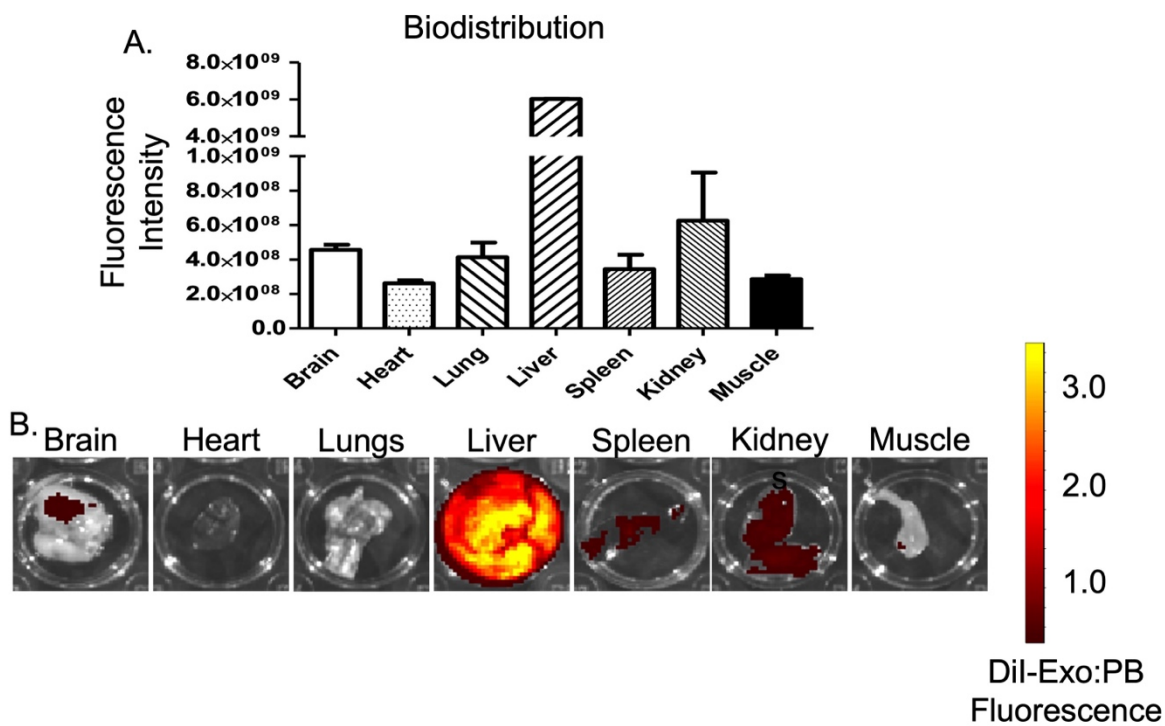


Figure 34: Biodistribution patterns of Exo:PB. (A) Quantified fluorescence signal from DiI-Exo:PB in different organs 24 hours after intravenous injection. N=3. (B) Representative fluorescence image of excised organs. Readapted with permission from reference¹⁷¹, Copyright 2024, American Chemical Society.

2.4: Conclusions

The overall data presented in this chapter provides evidence that PBNPs can easily be coated with U-87 derived exosomes with high reproducibility and high quantities as shown with DLS, NTA, and TEM. Once the particles are prepared, they can easily be stored at 4°C for multiple months and contain innate abilities from both PBNPs and exosomes. After laser exposure (808nm, 2W/cm²), the particles show effective photothermal therapy effects both *in vitro* and *in vivo*. After Exo:PB was injected intravenously into an orthotopic glioblastoma mouse model, the particles were shown to have specific targeting and could identify specific boundaries within the tumor. Since these particles are a hybrid between FDA-approved PBNPs and biologically derived exosomes, their translation into the clinic has a high probability. It would be able to easily act as a dual diagnostic and therapeutic agent with many avenues open for multi-imaging diagnostics, drug delivery, and use in anti-inflammation.

Chapter 3: Anti-inflammation Effects of Exo:PB Particles

3.1: Introduction

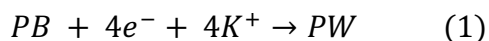
The work presented in this chapter is readapted from Hill, M. L. et al. Exosome-Coated Prussian Blue Nanoparticles for Specific Targeting and Treatment of Glioblastoma. *ACS Applied Materials & Interfaces*. **2024**, 16 (16), 20286-20301. DOI: 10.1021/acsami.4c02364¹⁷¹.

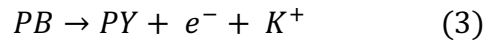
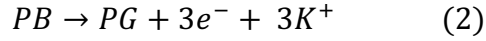
Enzymatic Activity

Many inorganic nanoparticles have become of interest to act as mimetic enzymes due to difference in surface valence of a specific ion on the surface of the particle²³⁶. Structures containing iron, gadolinium, zinc, copper, cerium, etc., have been researched due to their catalytic properties²³⁷. Specifically, many of these nanoparticles showed the ability to mimic biological enzymes such as catalase (CAT), peroxidase (POD), superoxide dismutase (SOD), glutathione peroxidase (GPx), glucose oxidase (GOD), etc.. Huo et al. presented a novel single iron atom nanoparticle that presented both CAT and POD effects while simultaneously reducing 4T1 subcutaneous tumor size by combined ferroptosis and peroxide scavenging²³⁸. In another study by Xu et al., dendritic mesoporous silica nanoparticles doped with Fe²⁺ and Mn²⁺ were synthesized and presented CAT/POD effects that helped regulate macrophage polarization and reduce CT26 inflammation in an *in vivo* subcutaneous model²³⁹. As both studies show, the presence of a metallic ion that can easily initiate oxidation and redox reaction conditions to reduce reactive oxygen species (ROS) within the tumor microenvironment. While these can be effective, the presence of only one ion charge on the surface of the particle limits the overall capabilities as an enzyme. Kalashnikova et al., shows this as they synthesized albumin carrying cerium oxide nanoparticles with Ce³⁺ and Ce⁴⁺ valence sites which allows them to cycle

between a CAT of POD nanozyme while simultaneously having SOD abilities. They were able to show that through local injection of their particles into an *in vivo* arthritis model, that the nanoparticles helped reduce inflammation on the same level as methotrexate (a commonly used anti-inflammation drug used in the clinic)¹¹⁷. This is like similar to the PBNP catalytic mechanism, as they have alternating Fe²⁺/Fe³⁺ valence states on the surface of their structure¹⁷⁶.

Starting in 2016, with a paper published by Zhang et al., PBNPs were first investigated for their multi-enzymatic effects within a biological setting¹⁷⁷. This was done by investigating the reduction/oxidation reactions that occur to transform Prussian blue (PB) to Prussian white (PW), Prussian green (PG), or Prussian Yellow (PY). They found that PBNPs transform between the four structures to work as CAT, POD, and SOD enzymes as the overall surface valences change between each based on reaction conditions and pH¹⁷⁷. When PBNPs encounter hydrogen peroxide, the Fe²⁺ ions on the surface will donate two electrons to produce O₂, 2H⁺, and 2e⁻ within the surrounding environment. These electrons are then immediately involved in the decomposition of more hydrogen peroxide where water is then produced as the final product. This creates an endless cycle of ROS scavenging that reduces overall stress within the inflammatory environment by reducing activation of NFκB and stimulation of pro-inflammatory macrophages due to the release of high mobility group 1 protein²⁴⁰. Overall, PBNPs act as both an oxidizing agent (Fe²⁺) and reducing agent (Fe³⁺) for hydrogen peroxide. This all happens as Prussian blue transforms its structure based on its state of oxidation. In general, there are three reactions that PBNPs follow during its oxidation and reduction process²⁴¹:





What this shows is depending on how many electrons are received or donated at any given redox potential, the overall structure of PBNPs can change¹⁷⁷.

Anti-Inflammation in Cancer

As PBNPs are popular choices for use in photothermal therapy of cancer due to their high photoconversion abilities, they have been investigated to reduce inflammatory side-effects within tumor sites^{177, 197, 241}. The presence of ROS species within tumors can be good and bad. At low levels, there is a debate on whether cell proliferation and angiogenic properties of the cancer cells increase or the depravation can improve already used treatments. There have been studies to show that certain antioxidants have increased tumor growth patterns^{242, 243}. In comparison, high ROS levels can induce apoptotic behavior. Though depending on the region in which the cancer originates, this can be problematic. For some parts of the body such as the brain or heart, it can cause detrimental effects such as heart failure or decline in cognitive function^{244, 245}. This poses an interesting area for use of anti-inflammatory drugs in individuals with brain cancers. Many studies have shown that the used of nonsteroidal anti-inflammatory drugs (NSAIDs) have shown great preliminary results in prevention of glioblastoma^{246, 247}. Due to high ROS levels produced during photothermal therapy, PBNPs can serve a unique role in being both the therapeutic and anti-inflammatory agent^{154, 168, 177, 236, 248, 249}. The particles would immediately be able to respond to the increase in local ROS species produced by pro-inflammatory macrophages and this limit local inflammation.

Hypoxia Reduction

Tumor hypoxia is a unique function of solid tumors in which the tumor outgrows the current blood supply and therefore has parts that are deprived of oxygen^{144, 166}. While these conditions usually induce apoptosis within normal and cancerous tissues, if the cells become accustomed to the conditions, they can become resistant to even other types of treatment⁶⁰. The brain normally has ~4.6% oxygen within the tissue, while brain cancers are known to have less than half of that (1.7%)²⁵⁰. Therefore, introducing a nanozyme that can decrease ROS species and simultaneously introduce oxygen into the region would greatly reduce hypoxic effects. As introduced before, when PBNPs promote the decomposition of hydrogen peroxide through oxidation, an equal amount of oxygen units is produced. To promote oxygen production within these parts of the tumor, can improve treatment methods and patient outcomes. Specifically for glioblastoma, extreme hypoxia is one of the primary components that decreases the survival rate in patients^{251, 252}. The lack of oxygen promotes invasion into healthy tissue and a resistance to chemo and radiation therapies. This proves very difficult for clinicians as spreading can make surgical resection more difficult and resistance to therapy lowers the long-term survival chance of the patient. Photoacoustic has become a very popular tool for visualizing hypoxic areas based on the ability to read blood flow signals. Based on the absorbance patterns of hemoglobin and deoxyhemoglobin, general tumor hypoxic conditions can be determined. Part of the evolution of the photoacoustic imaging technology can introduced an mSO₂ function which allows for an estimated blood map to be shown in respect to the tissue^{144, 253}.

3.2: Methods

Catalase Assay

The catalase activity of Exo:PB and PBNP particles was determined using a Cayman Chemical Catalase Assay Kit. Particles at 0, 0.0625, 0.125, 0.25, 0.5, and 1mg/mL were measured and compared to a catalase control. All samples were compared to a newly prepared standard curve.

OxiVision Peroxidase Assay

To determine peroxidase activity, 1mg/mL Exo:PB or PBNP particles were added to 5uM OxiVision Green Dye and 10mM Hydrogen Peroxide. The solutions were left to react for 20 minutes at RT. Fluorescence values were obtained with a SoftMax Pro plate reader (Molecular Devices, CA) with an excitation of 490nm and emission of 525nm.

DCFDA Assay

Raw 264.7 cells were seeded in a 24-well plate at 30,000 cells/well and left to incubate overnight at 37°C and 5% humidity. The following day, wells were treated with lipopolysaccharide (LPS, 1ug/mL) and Exo:PB or PBNP (1mg/mL) and left to incubate overnight. On the last day, the cells were washed with PBS and N-acetylcysteine (NAC, 30mM) was added to the LPS+NAC group and left to incubate for 30 minutes. 2', 7'-dichlorodihydrofluorescein diacetate (DCFDA) was then added to each well and left to incubate for another 30 minutes. Fluorescence values were obtained using a SoftMax Pro plate reader (Molecular Devices, CA) with an excitation of 485nm and emission of 535nm. Images were obtained using Keyence microscopy.

Photoacoustic MSOT Imaging

A InVision 512-echo preclinical multispectral optoacoustic tomographic (MSOT) imaging system (iThera Medical, Germany) was used for all photoacoustic imaging studies. Anesthesia was disposed as a 2% isoflurane/oxygen mixture during all imaging. Mice were applied with ultrasound gel and wrapped in a thin polyethylene membrane and then submerged in a water tank while in a horizontal position. 1mg of particle was injected into mice intravenously and images were taken pre-injection, 0, 1, 2, 3, 6, 12, and 24 hours afterward. Imaging was done in 0.2mm increments with an average of 10 illumination wavelengths (680, 700, 730, 760, 800, and 850nm). Hemoglobin (HbO₂), deoxyhemoglobin (Hb), and Total hemoglobin (HbT) were measured using these wavelengths. Acquisition times were less than 10 minutes and image analysis was done using ViewMSOT software.

U-87 *in vivo* Subcutaneous Tumor Model Development

Luciferase expressing U-87 cells were prepared with Sleeping Beauty transposon²²⁶. 500,000 cells/tumor of luciferase expressing U-87 cells were mixed 1:1 volumetric ratio with Matrigel. Approximately 100uL of cells and Matrigel mixture were injected into the flank region of the mouse. All tumors were visible about 1 week after inducement.

Subcutaneous Tumor PAI Blood Oxygen Monitoring

After subcutaneous tumors were visible, 1mg of Exo:PB was injected intratumorally on day 0. Directly after injection, the tumors are exposed to an 808nm laser (2W/cm²) for 1 minute. PA images were taken pre, 0, and 7 days post-injection and laser treatment.

U-87 *in vivo* Orthotopic Brain Tumor Model Development

The mouse was initially anesthetized using a 2% isoflurane/oxygen mixture. Meloxicam (1mg) is administered through an intraperitoneal injection to help alleviate pain. The mouse is then transferred to a stereotaxic device and the head is sterilized with iodine. An incision is made on anterior side of the skull where a 10uL needle is adjusted to 2mm x and 1.5mm y from the bregma. The skull is punctured in the designated area with a small gauge needle and the 10uL needle is lowered into the hole down to 2.5mm. U-87 luciferase expressing cells (3uL, 3×10^5 cells) are injected at 0.5uL/min and then left to sit for 5 minutes post injection. The needle is removed 1mm/min and then the mouse is removed, and the incision is sutured. Bioluminescent signal within the brain region is checked 1-2 weeks after the surgery to identify tumor size.

3.3: Results/Discussion

Particle-Based and *in vitro* Catalytic Activity

To determine the catalytic abilities of PBNPs and Exo:PB, they were first subjected to both catalase and peroxidase assays. For catalase capabilities, PBNPs and Exo:PB were exposed at different concentrations to methanol and hydrogen peroxide in the presence of water.

Hydrogen peroxide is hydrolyzed by the catalyst (PB or Exo:PB) to form 2H^+ , O_2 , and 2e^- .

Methanol then reacts with the free oxygen molecules release to form an unstable methoxy intermediate. One of the three hydrogens is donated to form excess water as a byproduct and a double bond is formed to the single oxygen to stabilize the structure^{254, 255}. The final product formed is formaldehyde which is reacted with 4-amino-3-hydrazino-5-mercapto-1,2,4-triazole (purpald) to produce a purple color that is used to calculate the catalase activity of the particle.

When purpald is first added to the solution there is no color change. Over a 10-minute incubation, each formaldehyde compound will interact with the open NH_2 groups within the purpald structure causing a hydroxyl group to form in place of the double bonded oxygen. The methyl groups that are formed within the combined formaldehyde-purpald complex interact with surrounding water to form an unstable formaldehyde-purpald intermediate. In the presence of oxygen the intermediate then forms a stable formaldehyde-purpald compound which exhibits a purple color²⁵⁶ (**Figure 35A**). Overall, 0, 0.0625, 0.0125, 0.25, 0.5, and 1mg/mL of PBNP or Exo:PB were tested under the same concentrations of methanol and hydrogen peroxide. The amount of formaldehyde production was then indirectly quantified by the absorbance of purpald to back calculate the catalase activity based on a 1.0nmol of formaldehyde being produced per minute at 25°C. The activity measured at 1mg/mL for both

PBNPs and Exo:PB were very similar to the positive catalase control in which a bovine liver catalase was used (**Figure 35B**). This indicates that the particles show similar ROS degradation effects as traditional catalase. It also presents information that the exosome coating does not inhibit the ability for hydrogen peroxide to interact with the Fe^{2+} ions on the surface of PBNPs. The second catalytic study that was performed was to test the peroxidase activities of the PBNP and Exo:PB particles. OxiVision is a hydrogen peroxide specific marker. When more hydrogen peroxide is present within the environment, the OxiVision compound will fluoresce a brighter green color. In general, PBNP, Exo:PB, or N-(2-Hydroxyethyl)piperazine-N'-(2-ethanesulfonic acid) (HEPES) buffer were added to a well with OxiVision and then hydrogen peroxide was added. During the incubation period, fluorescence will start to develop with the well with HEPES added as the positive control. What was seen is that Exo:PB particles actually show greater peroxidase activity than PBNPs. This is interesting data, as the exosome coating seems to enhance the catalytic effects which is probably due to some complex present within the coating that also contributes to hydrogen peroxide degradation (**Figure 36**).

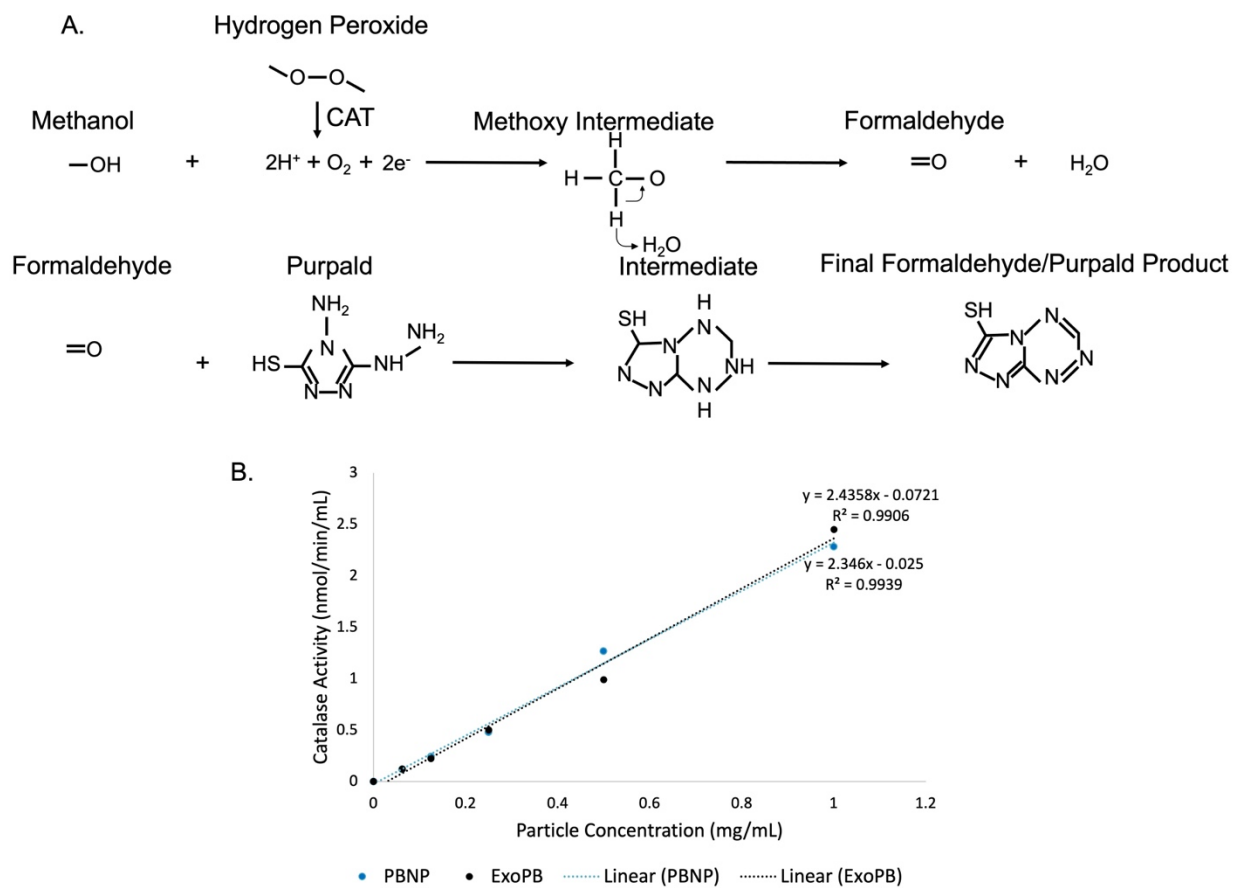


Figure 35: Catalase assay mechanism and results. (A) Mechanism for indirect measurement of catalase activity. (B) Catalase assay results for PBNP (blue) and Exo:PB (black) at different concentrations. Readapted with permission from reference¹⁷¹, Copyright 2024, American Chemical Society.

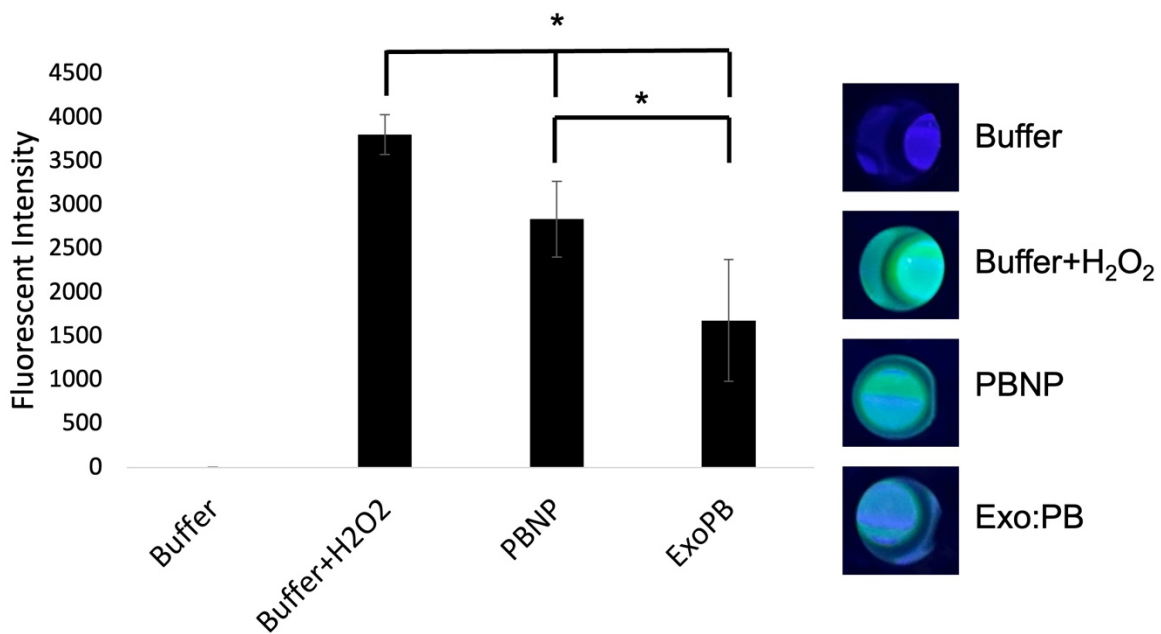


Figure 36: Hydrogen peroxide degradation assay results with insert fluorescent images of representative wells. * $p < 0.05$. $N = 3$. Readapted with permission from reference¹⁷¹, Copyright 2024, American Chemical Society.

The final evaluation for the enzymatic activity is to test the particles within a high ROS producing cellular environment. Using Raw 264.7 stimulated towards pro-inflammatory M1, PBNPs, Exo:PB, and NAC were used to see if general ROS signal could be decreased. A 2',7'-dichlorofluorescein diacetate (DCFDA) compound is utilized as when it diffuses through the cell membrane it will be deacetylated and then oxidized in the presence of ROS species. The more ROS species present, the higher the fluorescence intensity. NAC is used as an intermediate measurement molecule as it has medium levels of anti-ROS activity. Fluorescence quantification and image analysis was used for each of the LPS, non-treatment, LPS+NAC, PBNP, and Exo:PB groups. Overall, PBNPs showed ~40% decrease and Exo:PB showed ~20% decrease in fluorescence intensity vs the LPS control (**Figure 37**). This indicates that the particles have some ROS scavenging capabilities which could be beneficial for reducing inflammation or hypoxia *in vivo*.

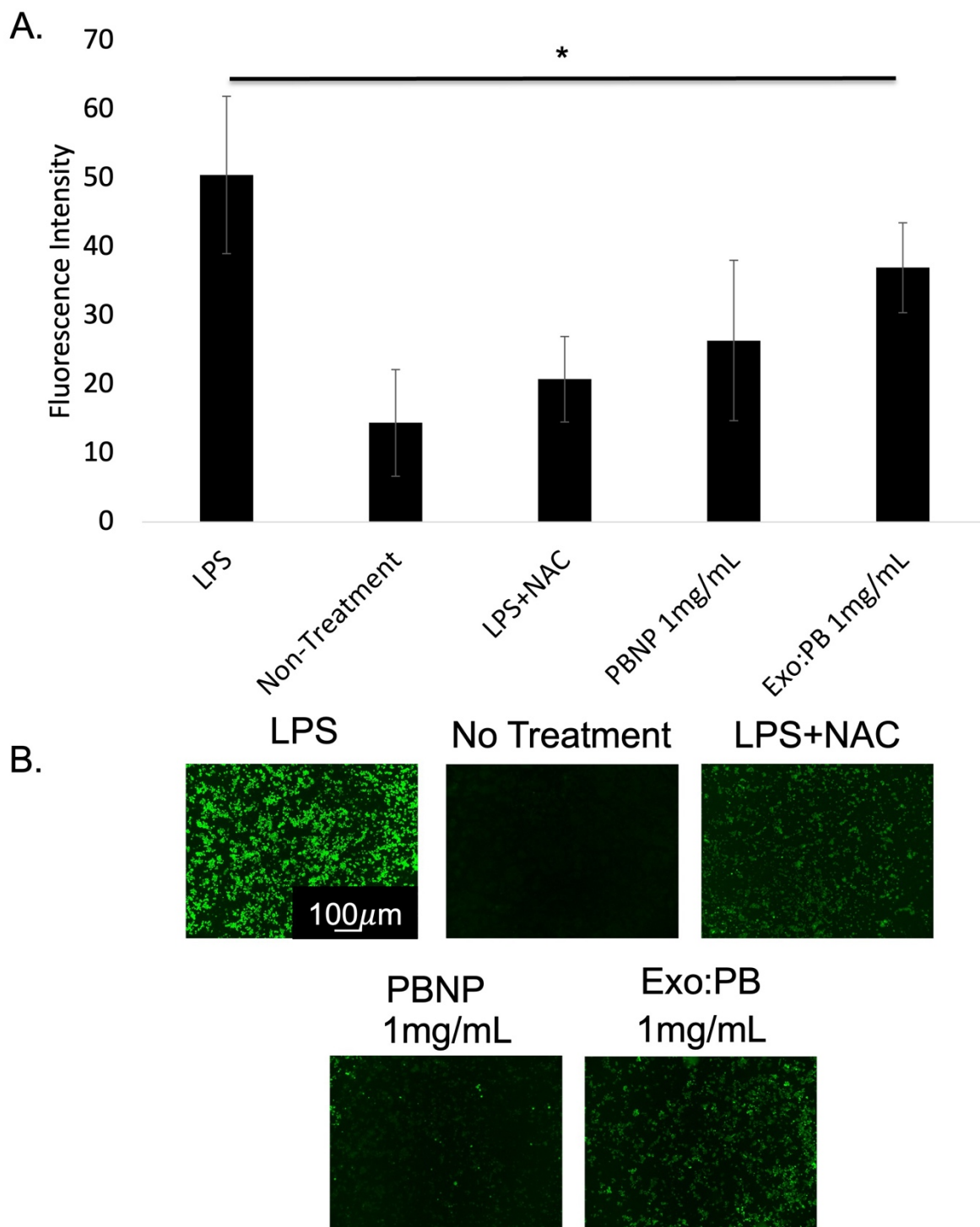


Figure 37: DCFDA assay results. (A) Quantification of fluorescence signal. * $p < 0.05$. $N = 3$. (B) Representative fluorescence images. Scale bar = 100 μ m. Reproduced with permission from reference¹⁷¹, Copyright 2024, American Chemical Society.

In Vivo Hypoxia Reduction

One of the most useful functions apart of photoacoustic imaging, is the ability to measure blood signals within an *in vivo* system. Older versions of PAI allowed the user to only visualize hemoglobin or deoxyhemoglobin based on the absorbance patterns for each. Later versions allowed these signals to be combined to visualize total hemoglobin signal (HbT) or microvesicle blood saturation (mSO₂). These functions are very useful as they allow total distributed blood signals to determine areas of angiogenesis, hypoxia, inflammation, etc. To study the *in vivo* hypoxia reduction capabilities of Exo:PB particles, two animals models were used: a U-87 subcutaneous tumor model and a U-87 orthotopic tumor brain model. After Exo:PB was intratumorally injected into subcutaneous tumors, an 808nm laser (2W/cm²) was applied for 1 minute. Photoacoustic images were taken pre-injection, 24 hours, and 7 days post-injection (**Figure 38**). Signal overlay was restricted to hemoglobin and deoxyhemoglobin to identify areas of hypoxia. It was seen that before injection, that there was some blood supply to the tumor, which is expected, but some areas around the edges of the tumor that showed no signs of signal. These areas with no signal or high deoxyhemoglobin are examples of tumor heterogeneity with hypoxia. Twenty-four hours post-injection showed a slight increase in overall hemoglobin presence within the tumor. This indicates that the particles are starting to scavenge ROS species present and produce oxygen within the local area. After 7 days, there is a large blood supply present within the tumor. This means that a good portion of ROS species have been broken down to produce high levels of oxygen (**Figure 38**). As photothermal therapy can often cause necrotic tissues that contain low levels of oxygen, having a tool that can both

act as the photothermal agent as well as help reduce the primary side-effect of the therapy would make Exo:PB a highly sought after clinical drug.

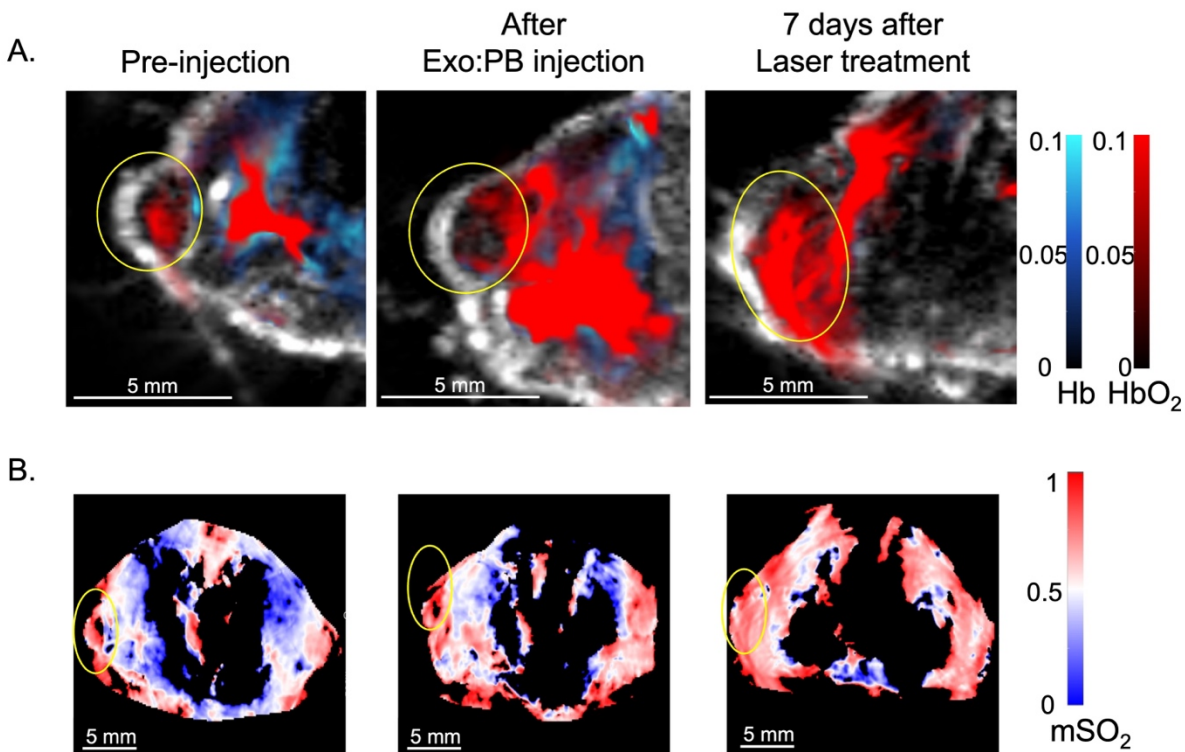


Figure 38: Subcutaneous tumor hypoxia monitoring after photothermal treatment. (A) Hemoglobin (HbO₂, red) and deoxyhemoglobin (Hb, blue) signal within subcutaneous tumors pre-injection, immediately after injection, and 7 days post treatment. Scale bar = 5mm. (B) Corresponding saturated oxygen (mSO₂) images. Scale bar = 5mm. Reproduced with permission from reference¹⁷¹, Copyright 2024, American Chemical Society.

3.4: Conclusions

This chapter discusses the applications of Exo:PB nanoparticles for use as anti-inflammatory and hypoxia reduction agents. It was found that PBNPs contain innate abilities to act as both inorganic peroxidase and catalase enzymes based on the alternating $\text{Fe}^{2+}/\text{Fe}^{3+}$ valence state on the surface of the particle. When tested *in vitro* in the presence of M1 macrophages, general ROS signal was decreased with PBNPs showing more effectiveness than Exo:PB particles. Due to the preferential targeting potential of Exo:PB in *in vivo* glioblastoma models, blood distribution was looked at after intravenous injection to determine if hypoxia could be alleviated. In a subcutaneous model after laser treatment, overall hemoglobin presence was increased within the tumor region after 7 days. This poses a unique opportunity for these particles to both serve as a therapeutic agent and help alleviate the main side-effect of the treatment simultaneously. Overall, this is promising preliminary data for more involved animal studies to determine the clinical potential as an anti-inflammatory drug.

Chapter 4: Targeting of Glioblastoma with RGD peptide

4.1: Introduction

The work presented in this chapter is readapted with permission from Hill, M. L. et al. Exosome-Coated Prussian Blue Nanoparticles for Specific Targeting and Treatment of Glioblastoma. *ACS Applied Materials & Interfaces*. **2024**, 16 (16), 20286-20301. DOI: 10.1021/acsami.4c02364¹⁷¹.

RGD Peptide Use as a Cancer Targeting Agent

Starting in the early 2000s, researchers started looking into the use of RGD peptides for active targeting of cancer cells²⁵⁷. While peptide delivery has a number of advantages including low production cost and reduced immune reaction, there is much room for improvement as they typically have poor stability and uptake within cells²⁵⁸. One of the primary tools to enhance these delivery tools is conjugation to a particle based material to increase overall circulation within the body and increase the probability of being endocytosed from cells²⁵⁹. RGD peptides are popular tools to target cancer cells as many overexpress RGD-recognizing integrins²⁶⁰. These RGD-recognizing integrins such as $\alpha v \beta 1$, $\alpha v \beta 3$, $\alpha v \beta 5$, $\alpha v \beta 6$, $\alpha v \beta 8$, $\alpha 5 \beta 1$, $\alpha 8 \beta 1$, and $\alpha I I b \beta 3$, when overexpressed allow for tumor cells to readily invade healthy tissue as well as promote angiogenesis²⁶¹⁻²⁶³. Naturally, when conjugated to the surface of a delivery vehicle such as a nanoparticle or protein, the RGD sequence would be recognized by the cell and allow for the entire structure to be endocytosed. This is valuable as it would allow for more precise drug release, decrease off-target effects, and increase stability of the peptide. As valuable as this can be for enhancing therapeutics, since many of the integrins that recognize RGD are present on the surface of healthy cells (**Table 2**), there will always be a portion that will not end up in the

target site²⁶⁴⁻²⁶⁶. This is a problem that must be addressed for more precise therapeutics and diagnostics.

Integrin	Healthy Cells That Express	References
$\alpha v \beta 1$	Fibroblasts, non-mesenchymal stem cells, Endothelial	264, 265
$\alpha v \beta 3$	Osteoclasts, Endothelial, Smooth Muscle, Megakaryocytes, Macrophages,	267
$\alpha v \beta 5$	Endothelial, Stromal, Keratinocytes,	260, 268
$\alpha v \beta 6$	Epithelial	269-271
$\alpha v \beta 8$	Intestinal Dendritic, Epithelial	271, 272
$\alpha 5 \beta 1$	Monocytes	273
$\alpha 8 \beta 1$	Mesenchymal Stem Cells, Smooth Muscle, Alveolar Interstitial	274-276
$\alpha IIb \beta 3$	Megakaryocyte	277, 278

Table 2: List of RGD recognizing integrins and which cells typically express normally.

With the expression of $\alpha v \beta 1$, $\alpha v \beta 3$ and $\alpha v \beta 5$ on endothelial cells that help to line the blood-brain barrier (BBB), RGD peptides can easily pass through by passive diffusion. When conjugated to a nanoparticle surface, this allows the particle structure to be transported through the BBB without any issues as well²⁷⁹. Now depending on the overall size, surface charge, and composition of the nanoparticle, transportation could be through different methods. If the particles are small or positively charged, they will likely pass through by passive diffusion which is the same as regular RGD peptide. Bigger particles will likely transport by receptor-mediated transcytosis as the peptide sequence will be recognized and allow the particles to be taken up by endocytosis and transferred across through vesicles. Overall,

peptide conjugation provides a better strategy to pass through the BBB and allow for therapeutics or diagnostics to reach the tumor site.

Application for Glioblastoma

Glioblastoma cells have shown a tendency to overexpress $\alpha v\beta 1$, $\alpha v\beta 3$, $\alpha v\beta 5$, $\alpha v\beta 8$, and $\alpha 8\beta 1$ integrins. The data was gathered from a large sample of patients diagnosed with glioblastoma (n=224, n=274). Immunohistochemistry (IHC) staining was used to validate these findings based on tissue samples taken from patients. What was found is that $\alpha v\beta 5$ is expressed by both glioblastoma endothelial cells and tumor cells, which is a problem for specific targeting using RGD peptide. Though what is promising is that $\alpha v\beta 3$ and $\alpha v\beta 8$ are expressed in the separate populations with $\alpha v\beta 3$ found in the endothelial cells and $\alpha v\beta 8$ found in tumor cells²⁸⁰. When these specific integrins were compared to the four subtypes of glioblastoma: pro-neural, neural, mesenchymal, and classical, it was found that expression varies. Mesenchymal glioblastoma, often referred to as the most aggressive type, overexpressed $\alpha v\beta 1$, $\alpha v\beta 3$, $\alpha v\beta 5$, and $\alpha 5\beta 1$ higher than the other subtypes. In comparison, pro-neural subtype patients under expressed all the same integrins except for $\alpha v\beta 3$. What is interesting, is that $\alpha v\beta 8$ is overexpressed in classical subtypes²⁸¹.

4.2: Methods

Prussian Blue Nanoparticle (PBNP) Synthesis

PBNPs were synthesized using a co-precipitation reaction between iron (III) chloride and potassium (II) ferrocyanide in the presence of citric acid. Initially, two separate 10mM solutions of FeCl_3 and $\text{K}_4[\text{Fe}(\text{CN})_6]$ are prepared in DDI water. Each solution is diluted to 1mM and 1g of citric is added to the FeCl_3 solution. The new citric acid- FeCl_3 solution is stirred at 60°C until everything is dissolved. $\text{K}_4[\text{Fe}(\text{CN})_6]$ is then added at a rapid dropwise rate to the stirring solution. During this step, the solution will change from a slight yellow to a deep blue color. The solution is stirred overnight at 60°C . The next day, the reaction mixture is washed with equal parts DDI water and acetone at 10,000rpm for 20min (x3). The final particle mixture is suspended in DDI water.

RITC-RGD Conjugation

Initially, 2mg of RGD peptide was added to a single 2mL vial and was resuspended in 500uL of DMSO. 20uL of triethylamine (TEA) was then added to the solution. In a separate 2mL vial, 3mg of RITC was also resuspended in 500uL of DMSO. The two vials are then combined into one and mixed at RT for 24 hours. The following day, the RITC-RGD conjugate was purified. Cold diethyl ether was added to create a separation layer. The ether layer was removed and then 100uL of 0.1M HCl was added to precipitate out the sample. To this, 10mL of ethyl acetate was added in which a separation layer would start to form. Finally, to remove the DMSO, 15mL of methanol was added and rotovaped. This was done 2-3x until there is a thin layer of RITC-RGD left in the flask. The sample is resuspended in an acetone/hexane mixture and then left to dry overnight in a fume hood to produce a powder. The final RITC-RGD product is suspended in water.

Preparation of RITC-RGD Prussian Blue Nanoparticles (RITC-RGD:PB)

Using a 1: 200 (peptide: nanoparticle) ratio previously reported citric acid coated Prussian blue nanoparticles (10mg) was mixed with RITC-RGD peptide (50ug) in 4mM borate buffer²⁸². The mixture was left to mix at RT for 24 hours. The conjugated RITC-RGD:PB particles are washed at 12,000rpm for 30 minutes (x2). Final product was suspended in water. Conjugation to the surface of the particles was done using a PerkinElmer Spectrum 2 FTIR using a drop cast method.

Mass Spectrometry

0.2mg of RITC-RGD was validated using a Waters G2-XS-Q-ToF mass spectrometer with a Waters Acquity UPLC. The following conditions were used: 0.2mL/min in 1 water to 9 methanol + 0.1% formic acid.

In vitro BBB Passage

U-87 cells were seeded at 20,000 cells per well in CytoSelect™ 24-well Cell Migration and Cell Invasion plates with 8um well inserts and left to incubate overnight at 37°C and 5% humidity. After 24 hours, 0.1mg/mL Dil-Exo:PB or RITC-PEG:PB was added to the upper portion of the well inserts. On the third day, the well inserts were removed, and the U-87 cells were stained with 1uM Calcein AM and DAPI. Cells were imaged using Keyence microscopy.

Photoacoustic MSOT Imaging

An iVision 512-echo preclinical multispectral photoacoustic tomographic (MSOT) imaging system (iThera Medical, Germany) was used for all photoacoustic imaging studies. Anesthesia was disposed as a 2% isoflurane/oxygen mixture during all imaging. Mice were applied with ultrasound gel and wrapped in a thin polyethylene membrane and then submerged in a water

tank while in a horizontal position. 1mg of particle was injected into mice intravenously and images were taken pre-injection, 0, 1, 2, 3, 6, 12, and 24 hours afterward. Imaging was done in 0.2mm increments with an average of 10 illumination wavelengths (680, 700, 730, 760, 800, and 850nm). Hemoglobin (HbO₂), deoxyhemoglobin (Hb), and Total hemoglobin (HbT) were measured using these wavelengths. Acquisition times were less than 10 minutes and image analysis was done using ViewMSOT software.

U-87 *in vivo* Subcutaneous Tumor Model Development

Luciferase expressing U-87 cells were prepared with Sleeping Beauty transposon²²⁶. 500,000 cells/tumor of luciferase expressing U-87 cells were mixed 1:1 volumetric ratio with Matrigel. Approximately 100uL of cells and Matrigel mixture were injected into the flank region of the mouse. All tumors were visible about 1 week after inducement.

Particle Accumulation in *in vivo* Subcutaneous Tumor Model

RITC-RGD:PB particles were intravenously injected and photoacoustic images were taken pre-injection, 0hr, 2hr, 6hr, and 24hrs post-injection.

U-87 *in vivo* Orthotopic Brain Tumor Model Development

The mouse was initially anesthetized using a 2% isoflurane/oxygen mixture. Meloxicam (1mg) is administered through an intraperitoneal injection to help alleviate pain. The mouse is then transferred to a stereotaxic device and the head is sterilized with iodine. An incision is made on anterior side of the skull where a 10uL needle is adjusted to 2mm x and 1.5mm y from the bregma. The skull is punctured in the designated area with a small gauge needle and the 10uL needle is lowered into the hole down to 2.5mm. U-87 luciferase expressing cells (3uL, 3 x 10⁵ cells) are injected at 0.5uL/min and then left to sit for 5 minutes post injection. The needle is

removed 1mm/min and then the mouse is removed, and the incision is sutured. Bioluminescent signal within the brain region is checked 1-2 weeks after the surgery to identify tumor size.

Particle Accumulation in in vivo Orthotopic Brain Tumor Model

Once the mice were anesthetized using a 2% isoflurane/oxygen mixture, 2mg of RITC-RGD:PB was intravenously injected. Photoacoustic images were taken 3 hours post injection.

Ex vivo Histological Analysis

After in vivo studies were finished, the mice were sacrificed, and the tumors or brains were removed and sectioned using a cryostat. First the optimal cutting temperature (OCT) compound layer was removed to expose the bare tissue. Each slide was then stained with hematoxylin for 45 seconds and washed multiple times with water. The tissue is then stained with eosin for 30 seconds and washed multiple times with ethanol. The final stained slide is fixed using xylene glue and imaged using Keyence microscopy.

Ex vivo Immunohistology

Immunofluorescent staining was done using an anti-Ki67 antibody as a tumor marker. The antibodies were incubated with the tissue samples at 4°C overnight. The next day, the tissue was washed with PBS and an Alexa 488 conjugated secondary antibody was incubated for 1 hour at RT. The slides were then mounted using a Prolong Gold reagent with DAPI. Images were taken using THUNDER microscopy (Leica Microsystems, Germany).

4.3: Results/Discussion

Particle Characterization and *In Vitro* Analysis

Once the RITC-RGD conjugate was validated via mass spectrometry (**Figure 39**), it was mixed with Prussian Blue nanoparticles to create rhodamine isothiocyanate RGD conjugated Prussian Blue nanoparticles (RITC-RGD:PB) which was validated using FTIR with primary peaks for PBNP, RGD, and RITC seen within the spectrum (**Figure 40**). The final particles were characterized using TEM, DLS, and basic absorbance. It was found that particles are larger than native PBNPs with a hydrodynamic diameter of ~170nm (**Figure 41B**). In comparison, size as seen through TEM is smaller at ~80nm (**Figure 41A**). Due to the favorable conjugation conditions between the PBNPs and RITC (NH₂ to Fe interaction), the overall color of the particle solution turns from a blue to blue-pink color. After washing, the pellet appears as fluorescent with an absorbance peak at ~710nm (**Figure 41B**). The amount of RGD conjugated onto the surface was determined to be 0.3mg/mL (**Figure 41D**).

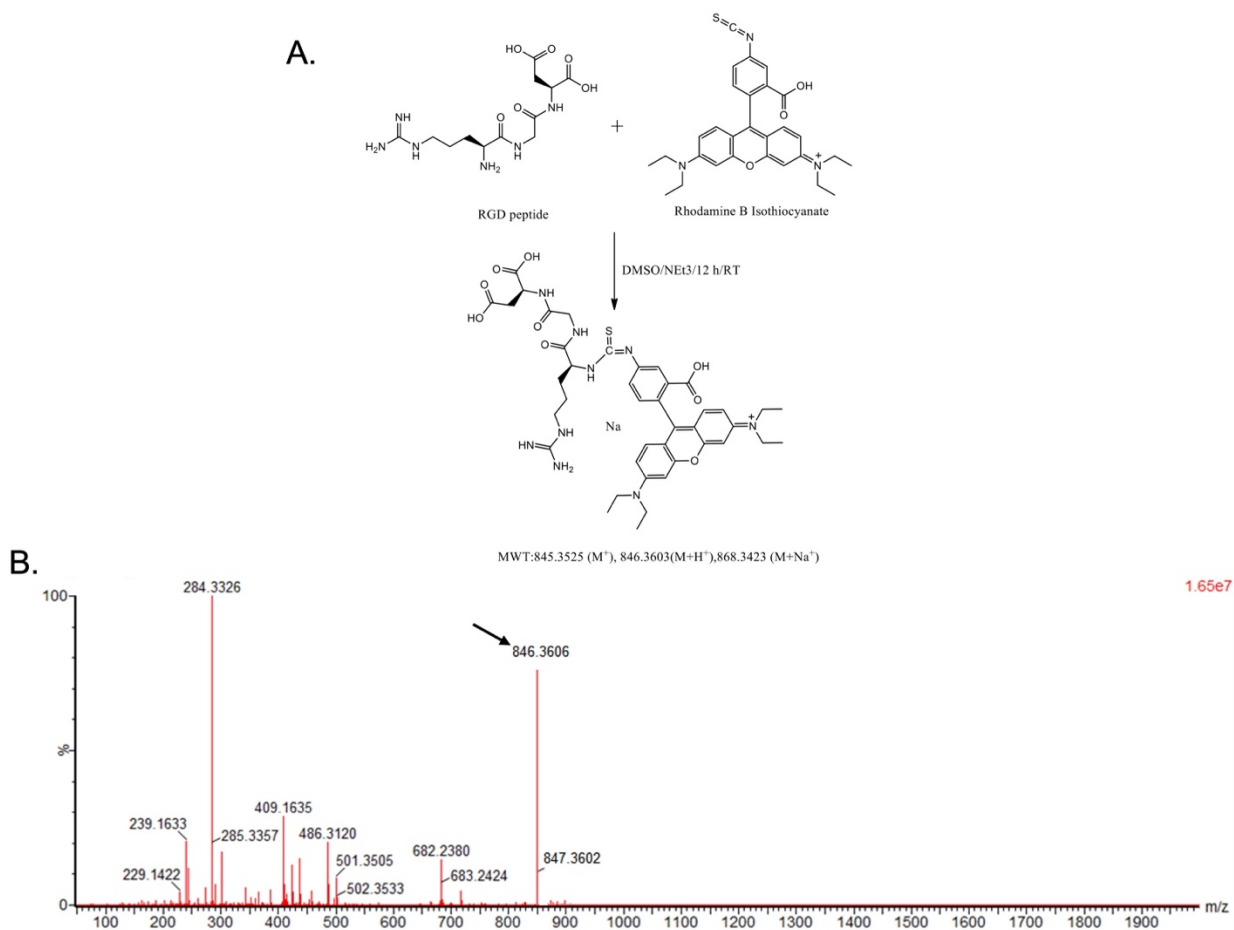


Figure 39: Reaction scheme and validation of RITC-RGD structure. (A) Thiol urea reaction scheme for the formation of RITC-RGD. (B) Mass spectrometry results of purified compound with experimental molecular weight indicated by the black arrow at 846.3606g/mol. Reproduced with permission from reference¹⁷¹, Copyright 2024, American Chemical Society.

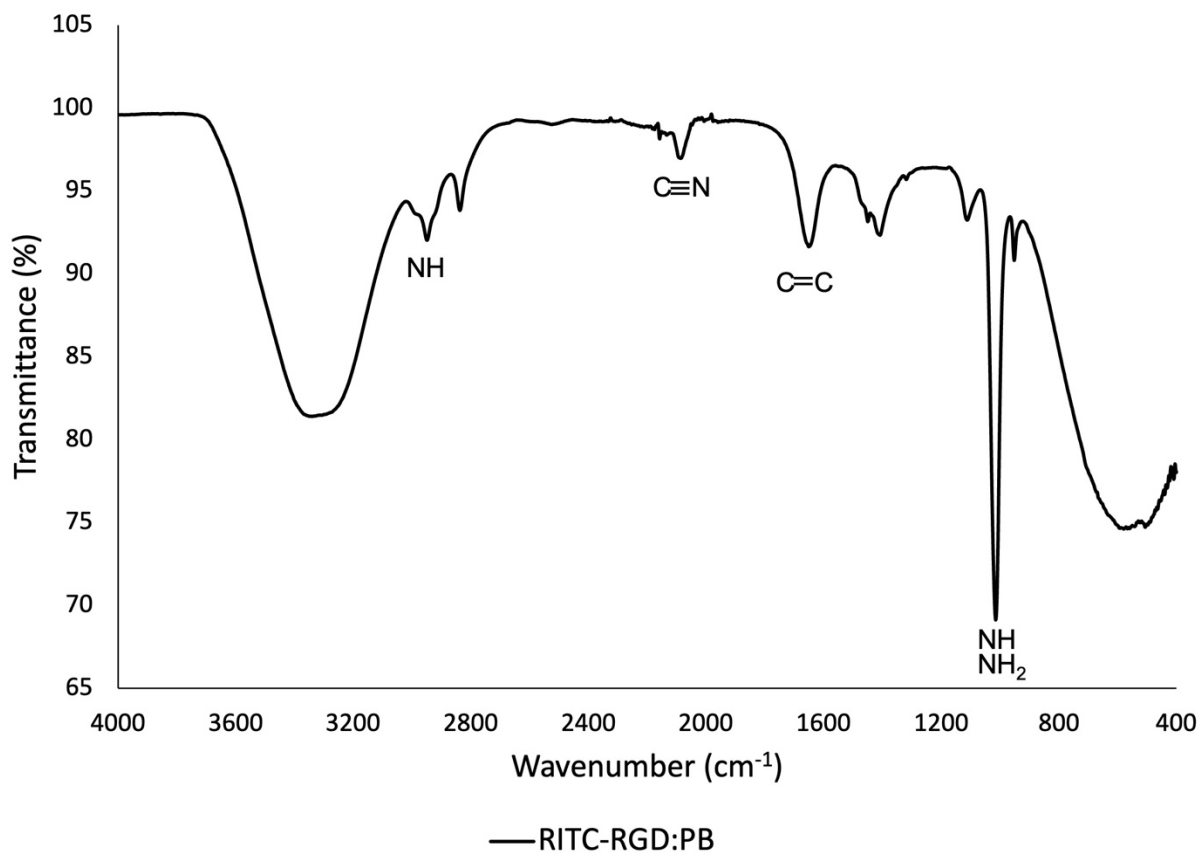


Figure 40: FTIR results for RITC-RGD:PB where CN is the marker for PBNP, NH is the marker for RGD, and CC is the marker for RGD. Thanks to Praveen Kumar for running the sample. Readapted with permission from reference¹⁷¹, Copyright 2024, American Chemical Society.

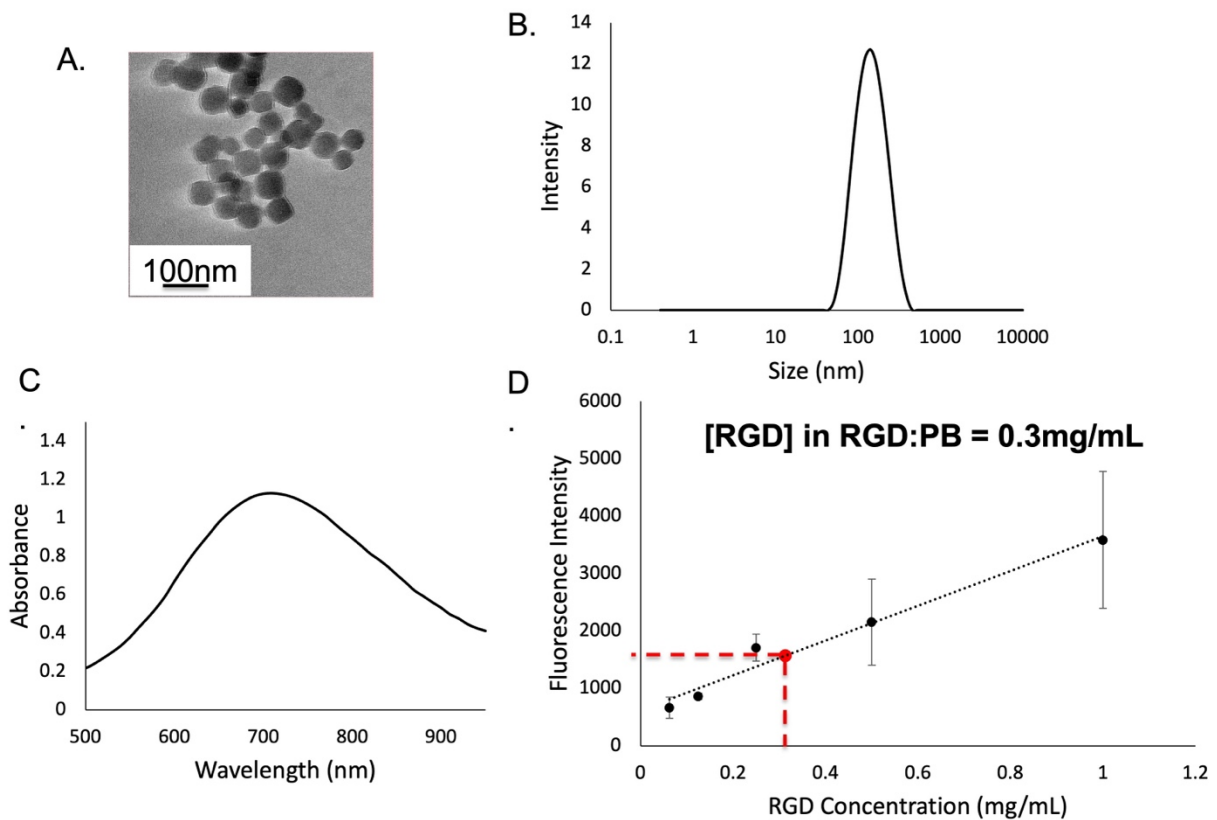


Figure 41: RGD:PB particle characterization. (A) TEM image. Scale bar = 100nm. (B) DLS size distribution. (C) Absorbance curve for RGD:PB particles. (D) Quantification of RGD on the surface of the PBNP particles using a fluorescamine assay. Reproduced with permission from reference¹⁷¹, Copyright 2024, American Chemical Society.

As RGD-PB was used as a positive control group to pass through the BBB and actively target glioblastoma cells, they were tested in an *in vitro* BBB setup using U-87 cells. With the same setup used for both PEG:PB and Exo:PB particles, RGD:PB was treated in wells that either contained a polycarbonate porous membrane or a basement membrane matrix that mimics the BBB. Particles were given 24 hours to pass through each membrane and be endocytosed by U-87 cells on the bottom on the well. The results are comparable to what was seen with Exo:PB. There is a high RITC signal seen in the control wells where a polycarbonate membrane was used, which showed similar intensity to both PEG:PB and Exo:PB. The experimental wells where the basement membrane matrix was used, showed a reduction in signal but was still very high (same pattern as Exo:PB) (**Figure 42**).

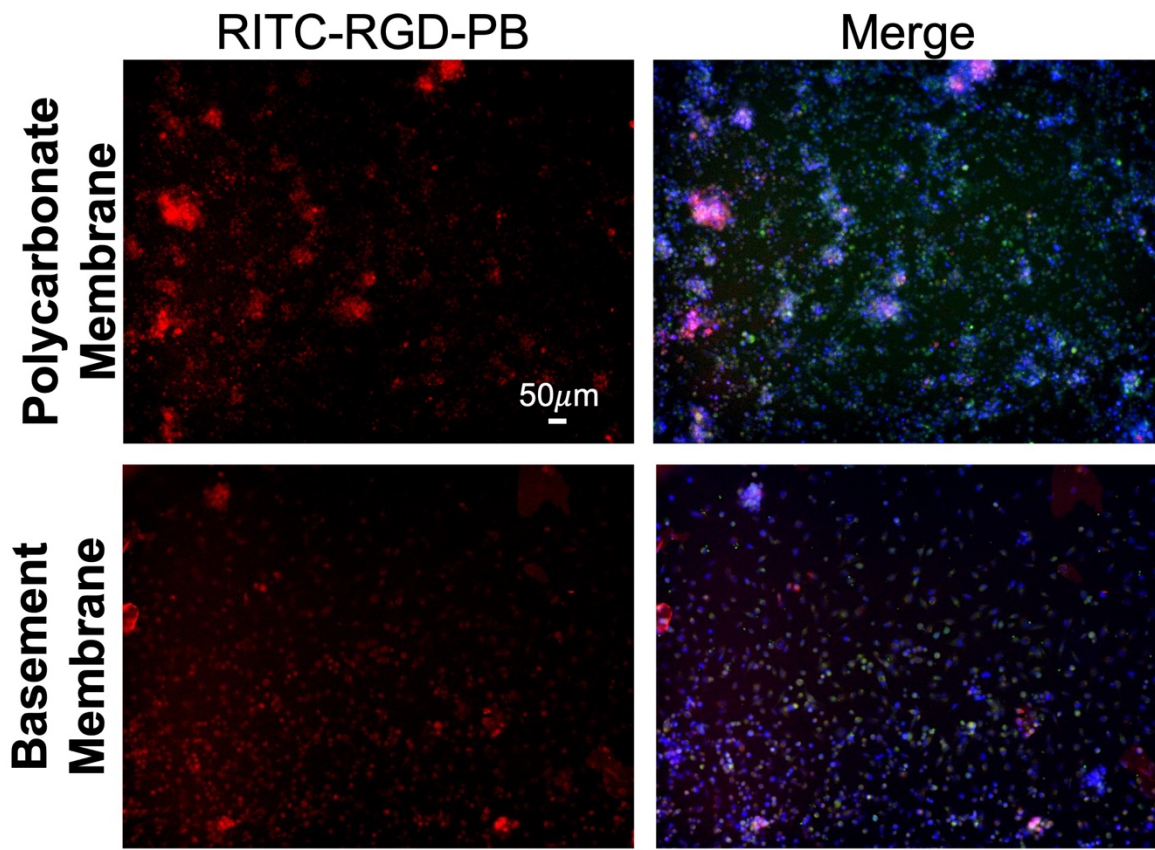


Figure 42: *In vitro* BBB results for RITC-RGD:PB particles after 24 hours of incubation. Green = calcein AM, Blue = cell nucleus, Red = RITC-RGD:PB. Scale bar = 50μm. Readapted with permission from reference¹⁷¹, Copyright 2024, American Chemical Society.

In Vivo Targeting Effects in U-87 Subcutaneous and Orthotopic Models

To investigate the active targeting effects of the RGD:PB particles in comparison to the Exo:PB particles, a U-87 subcutaneous and U-87 orthotopic brain model were used. As is was previously established in chapter 2, Exo:PB has superior targeting effects to PEG:PB particles under the same conditions. This is attributed to the exosome layer present that allows for specific targeting and uptake within glioblastoma cells. As RGD peptide targeting is the standard marker used for advanced clinical studies for cancer identification, it was run under the same conditions to determine if Exo:PB works in the same capacity and therefore would have a chance for clinical advancement.

Once subcutaneous tumors were visible, RITC-RGD:PB particles were injected intravenously and accumulation within the tumor site was monitored using photoacoustic imaging. 2 hours after injection, PA signal intensity was similar to that of Exo:PB while statistically different from PEG:PB (**Figure 43A**). This is based on particle signal within the tumor site as both Exo:PB and RGD:PB show increased accumulation directly in the tumor while PEG:PB is just breaching the tumor site at the same time point (**Figures 43B and 44**). With no difference in average blood supply for PEG:PB, Exo:PB, and RGD:PB tumors, all particles had an equal opportunity to reach the tumor site (**Figure 43C**). Thus, active targeting is what allowed for Exo:PB and RGD:PB to reach their tumors in a higher concentration in a shorter period of time.

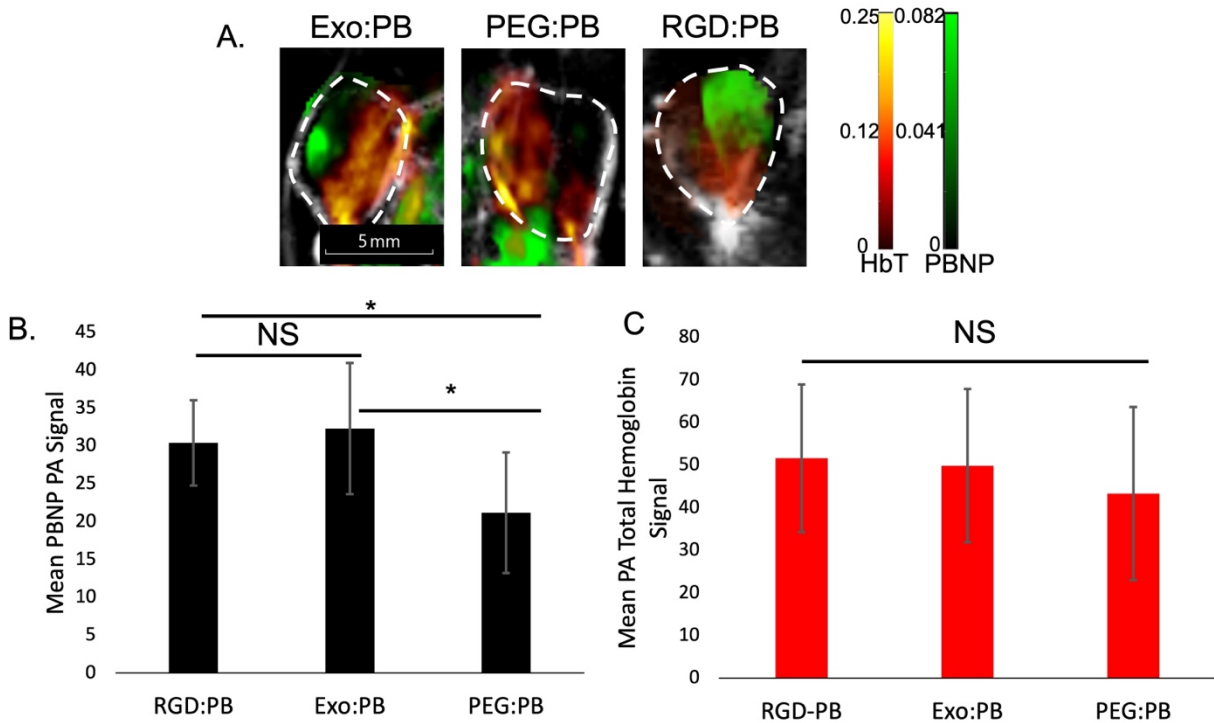


Figure 43: U-87 subcutaneous tumor accumulation patterns. (A) Photoacoustic images of Exo:PB, PEG:PB, and RGD:PB 2 hours post intravenous injection. Gray = ultrasound, Red = total hemoglobin signal (HbT), Green = PBNP. (B) Average photoacoustic PBNP signal quantification. * $p < 0.05$, NS = no significance. N=3. (C) Average total hemoglobin signal. NS = no significance. N=3. Readapted with permission from reference¹⁷¹, Copyright 2024, American Chemical Society.

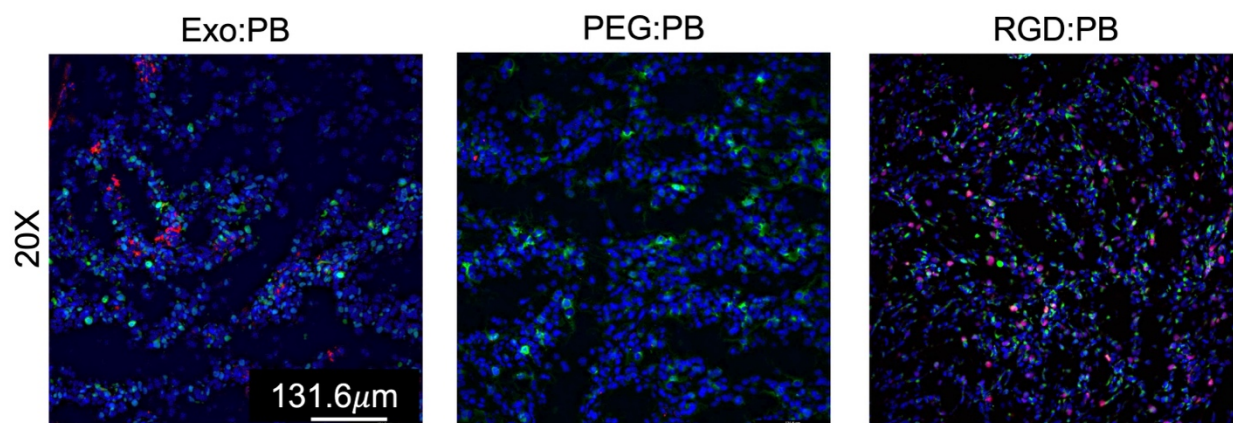


Figure 44: Immunofluorescence staining of subcutaneous tumor tissue. Blue = cell nucleus, Green = Ki67, Red = DiI-Exo:PB, RITC-PEG:PB, or RITC-RGD:PB. Scale bar = 131.6 μ m for 20X image and 65.8 μ m for 40X image. Readapted with permission from reference¹⁷¹, Copyright 2024, American Chemical Society.

To validate the ability for RGD:PB particles to cross the BBB and target glioblastoma tissue, RGD:PB particles were intravenously injected into a U-87 orthotopic brain model and monitored using photoacoustic imaging. Images were taken pre-injection, 1hr, 3hr, and 24hrs post-injection. At the 3hr time point, it can be seen there is a strong signal of RGD:PB throughout both tumor and contra lateral hemispheres. In comparison, the Exo:PB particles show a more localized targeting effect (**Figure 45**). This is consistent with 1-hour and 24-hour time points (**Figure 46**). What is interesting that statistically there seems to be no difference between Exo:PB and RGD:PB within the tumor region. At the 24 hour time point, there is also no difference between RGD:PB signal in the tumor hemisphere vs the contra lateral hemisphere, indicating that the peptide has off-targeting effects (**Figures 46 and 47**). As many RGD recognizing integrins are expressed in other cells, it is not surprising there is such a high off target effect within the brain region. In general, the RGD:PB signal increases as time progresses, but becomes less specific to the tumor area. Both contra lateral signal increases as well as the associated standard deviation, showing that the particles spread with no particular target.

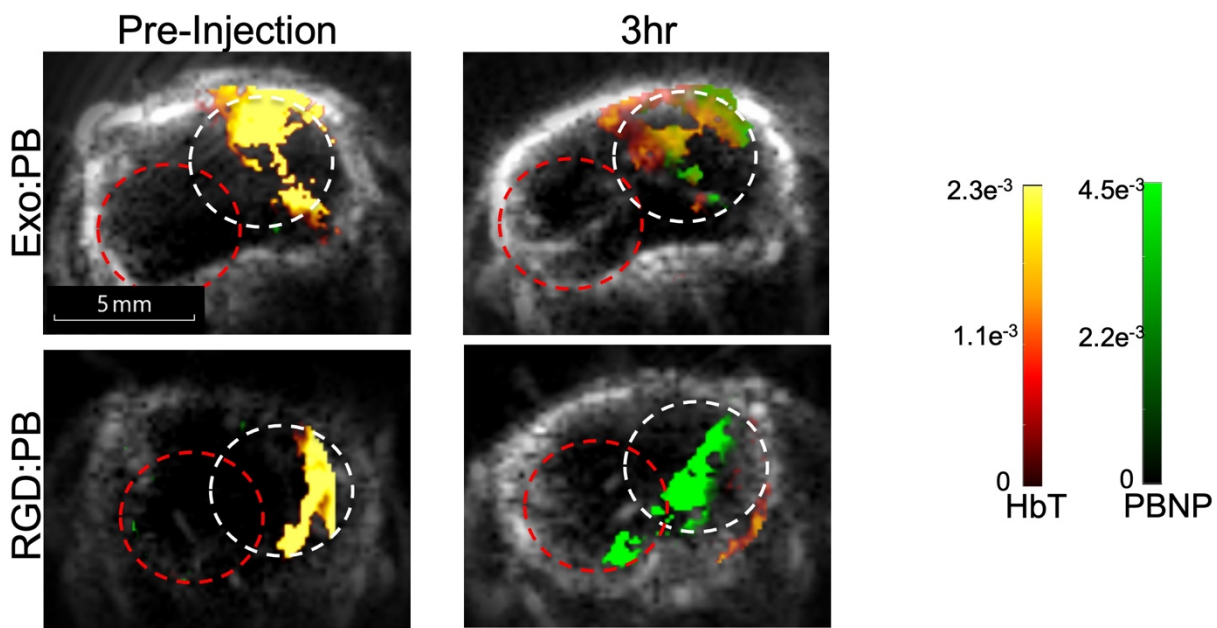


Figure 45: Photoacoustic images of mouse brain 3 hours after intravenous injection of either Exo:PB or RGD:PB. Gray = ultrasound, Red = total hemoglobin signal (HbT), Green = PBNP. Readapted with permission from reference¹⁷¹, Copyright 2024, American Chemical Society.

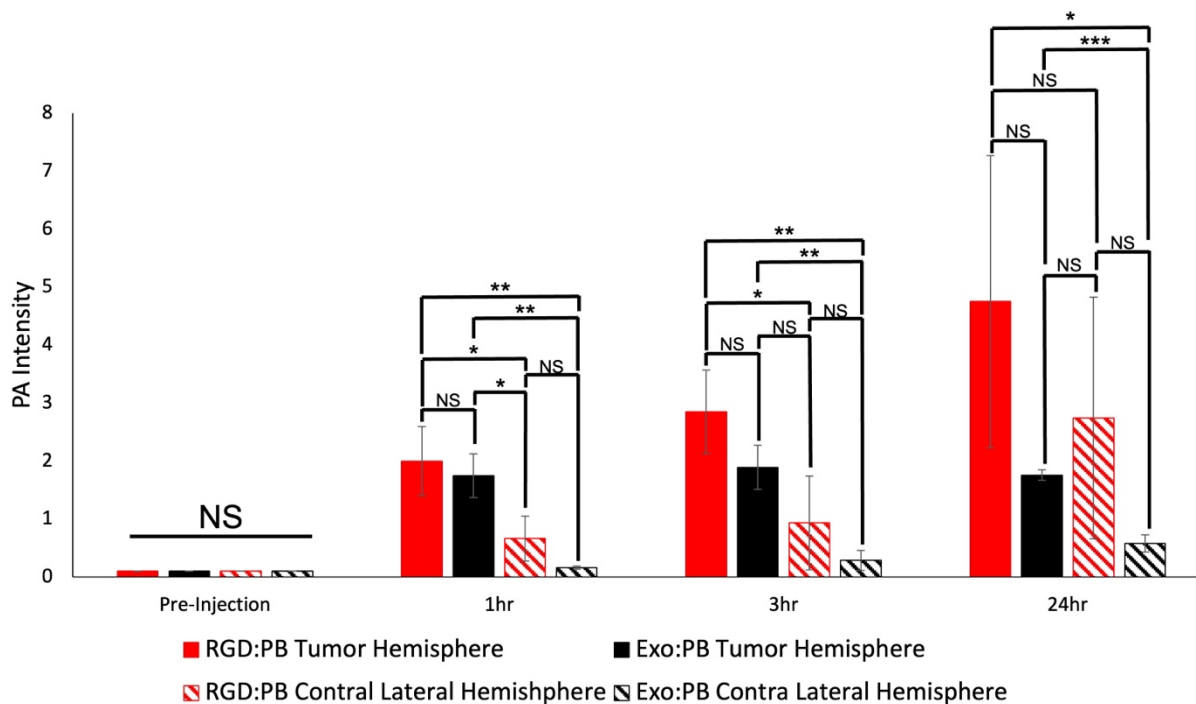


Figure 46: Quantified photoacoustic signal within the tumor hemisphere and contra lateral hemisphere of the brain 3 hours post intravenous injection of RGD:PB or Exo:PB. Solid Red = tumor hemisphere for RGD:PB, Cross Hatched Red = contra lateral hemisphere for RGD:PB, Solid Black = tumor hemisphere for Exo:PB, Cross Hatched Black = contra lateral hemisphere for Exo:PB. * $p < 0.05$, ** $p < 0.01$, *** $p < 0.001$, NS = no significance. N=3. Readapted with permission from reference¹⁷¹, Copyright 2024, American Chemical Society.

Dil-Exo:PB

RITC-RGD:PB

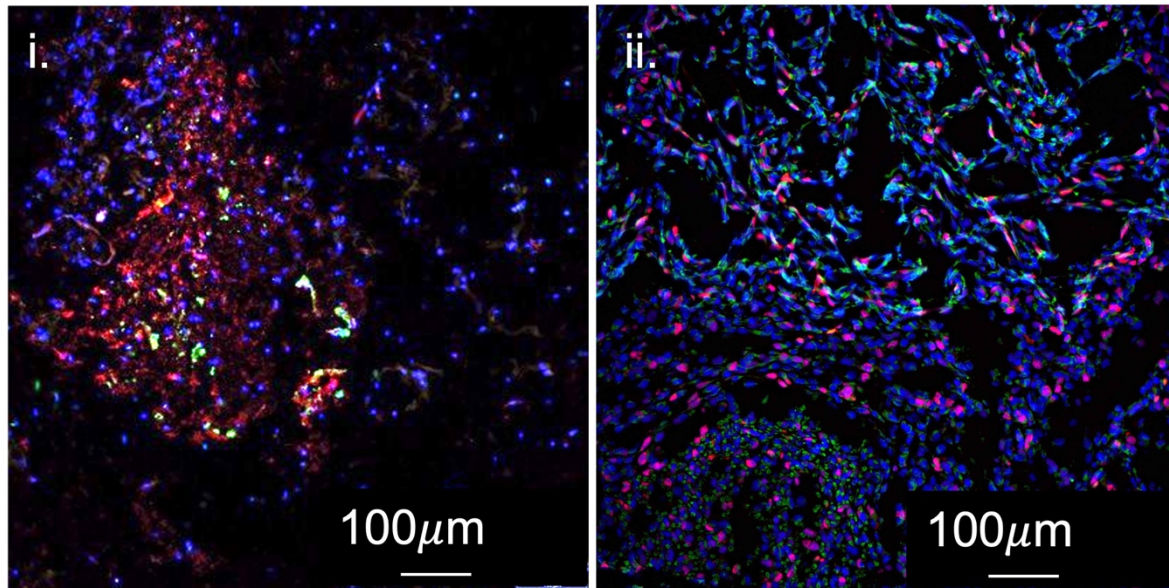


Figure 47: Immunofluorescence staining of brain tumor tissue 24 hours after intravenous injection of Dil-Exo:PB or RITC-RGD:PB. Blue = cell nucleus, Green = Ki67, Red = Dil-Exo:PB or RITC-RGD:PB. Scale bar = 100µm. Readapted with permission from reference¹⁷¹, Copyright 2024, American Chemical Society.

4.4: Conclusions

The data presented in this chapter covers the preparation, characterization, *in vitro*, and *in vivo* testing of RGD:PB particles. The particles showed a slightly bigger size than PBNP, Exo:PB, and PEG:PB particles, but behaved similarly with no obvious toxicity effects. While the initial hypothesis is that the RGD:PB particles would show higher accumulation within glioblastoma cells, it was seen that in our orthotopic brain model that this is not the case. At all levels of testing the RGD:PB particles show no statistical difference from Exo:PB particles. It was seen that RGD:PB particles proved to have less specific targeting of tumors with spread out signal across tumor and contra lateral hemispheres at all time points. This poses a problem for sensitive therapeutics and diagnostics as clinicians would not accurately be able to tell where the tumor boundaries fall. As this is one of the most crucial parts before surgical resection of the tumor, Exo:PB particles would be an ideal substitute as they allow for precise theranostics.

Chapter 5: Development of Gadolinium Doped Prussian Blue Nanoparticles for MRI-Guided LITT Treatment

The part of the work presented in this chapter is readapted with permission from Hill, M. L. et al. Exosome-Coated Prussian Blue Nanoparticles for Specific Targeting and Treatment of Glioblastoma. *ACS Applied Materials & Interfaces*. **2024**, 16 (16), 20286-20301. DOI: 10.1021/acsami.4c02364¹⁷¹.

5.1: Introduction

As photothermal therapy is newer to the clinical setting, there are many hurdles that must be overcome before it can be used as a standard treatment method^{283, 284}. One of the biggest problems tends to be penetration depth of the laser through human tissue. Since there are many types of lasers used within the clinic for a variety of applications, wavelength matters greatly depending on the depth wanting to be reached²⁸⁵. Based on the biological transparency window where general hemoglobin, deoxyhemoglobin, and lipid based absorbances are shown dictates the general wavelengths used for photothermal therapy. Typically, ~600-1000nm is the primary range in which materials are prepared to absorb in if they are to be used for this application²⁸⁶. This includes nanomaterials including gold nanorods, Prussian Blue nanoparticles, carbon nanotubes, ICG-based particles, etc. When it comes to photothermal therapy within the brain, the skull and the materials ability to cross through the BBB are the main obstacles. Laser interstitial Thermal Treatment (LITT) has solved one of these problems as the laser is inserted through a small burr hole made within the skull¹³¹.

As LITT lasers must be inserted under MRI guidance, having a nanoparticle that can act as both a photothermal and cancer identification agent is valuable^{68, 69, 165, 287}. To date, there are no

approved agents for LITT as the instrument itself acts as a photoablation system¹⁶⁵. This can be effective for certain types of superficial tumors but requires a higher laser intensity and longer therapy times. As glioblastoma is an invasive cancer that is often difficult to treat due to its overlapping nature with healthy brain tissue, the laser might be placed in the most identifiable region but many tumor cells are left behind. High laser intensity therapies can also cause extreme amounts of inflammation which can heighten hypoxic effects within the tumor²⁸⁸. The presence of a nanomaterial that could convert low amounts of light energy to heat would lower the laser intensity needed as well as help the clinician determine tumoral boundaries as the laser is being placed into the brain²¹³. Most recently, agents such as gold nanoparticles, magnetic iron oxide, magnesium nanoparticles, and inorganic liposome hybrids have been used for LITT application. The incorporation of these particles has allowed for more specific treatment of tumors within the brain and has reduced off target effects. The downside of these particles is they must be injected into the tumor area after a burr hole has already been made and they can suffer from thermal degradation^{165, 289}. Implementing Prussian Blue nanoparticles as a new nanoparticle agent for LITT is promising since they have great photothermal stability and when modified with the exosome surface (Exo:PB), can be injected systemically with great targeting. The implementation of LITT on a widened scale would reduce the use of chemotherapies that cause extreme off-target side-effects and possibly open the door for precision medicine.

Prussian Blue nanoparticles are known to have weak innate MRI signal. Based on the alternating $\text{Fe}^{2+}/\text{Fe}^{3+}$ valence states on the surface of the particle, one of the ions could be substituted with a heavy metal ion with better MRI response. Many studies have been done to

show that metals such as gadolinium, manganese, zinc, copper, etc. have been successfully incorporated into the structure and enhance imaging contrast capabilities²⁹⁰. The primary reason that these particle formulations have not translated into the clinic is due to toxicity concerns²⁹¹. While Prussian Blue nanoparticles are bioinert, heavy metal doping can cause leaching overtime. These metals ions interact with cell DNA and proteins that cause conformation changes or degradation which can lead to cancer, cell death, or necrosis²⁹².

5.2: Methods

Gadolinium Doped Prussian Blue Nanoparticle (Gd:PB) Synthesis

To synthesize gadolinium doped Prussian Blue nanoparticles (Gd:PB), to one vial 31mg gadolinium (III) chloride (GdCl_3) and 315mg of citric acid is added. To a separate vial, 32mg of potassium (III) ferricyanide ($\text{K}_3[\text{Fe}(\text{CN})_6]$) and 100mg of polyvinylpyrrolidone (PVP) is added. 10mL of 0.1M HCl is added to each vial and stirred at RT to fully dissolve. The vial containing GdCl_3 and citric acid is added to the vial containing $\text{K}_3[\text{Fe}(\text{CN})_6]$ and PVP dropwise. Stir for 2 hours at RT and then stir overnight at 60°C . During the overnight stir period, the solution will turn from clear to a dark blue color. The next day, particle are washed with water at 12,000rpm for 40 minutes. Final particle suspension is stored in water.

Particle Characterization

Gd:PB particles were drop casted onto 300-mesh carbon-based TEM grids and then imaged using a 220FS Transmission Electron Microscopy (TEM, JEOL) with energy-dispersive X-ray Spectroscopy (EDX) capabilities to determine size, morphology, and general composition. Hydrodynamic diameter and zeta potential was measured using DLS. Particle absorbance spectra was gathered using a SoftMax Pro plate reader (Molecular Devices, CA).

In Vitro Cytotoxicity

To start, U251 cells were seeded in a 96-well plate at 10,000 cells/well and left overnight at 37°C and 5% humidity. The following day, wells were treated with 0, 0.015625, 0.03125, 0.0625, 0.125, 0.25, 0.5 or 1mg/mL of either 80nm or 120nm Gd:PB and then incubated for another 24 hours at 37°C and 5% humidity. On the final day, the supernatant was removed and 5mg/mL of a 3-(4,5-Dimethylthiazol-2-yl)-2,5-diphenyltetrazolium bromide (MTT) solution and

left to incubate for 4 hours. Finally, the MTT solution is removed to expose the formed formazan crystals and resuspended in dimethyl sulfoxide (DMSO). The absorbance is measured using a SoftMax Pro plate reader (Molecular Devices, CA) at 570nm.

Laser Based *In Vitro* Cytotoxicity

To start, U251 cells were seeded in a 96-well plate at 10,000 cells/well and left overnight at 37°C and 5% humidity. The following day, wells were treated with 0, 0.015625, 0.03125, 0.0625, 0.125, 0.25, 0.5 or 1mg/mL of 80nm Gd:PB and then incubated for another 24 hours at 37°C and 5% humidity. On the final day, the supernatant was removed, and cells were treated with either a 2W/cm² 808nm or 1W/cm² 980nm laser for 1 minute. Then, 5mg/mL of a 3-(4,5-Dimethylthiazol-2-yl)-2,5-diphenyltetrazolium bromide (MTT) solution and left to incubate for 4 hours. Finally, the MTT solution is removed to expose the formed formazan crystals and resuspended in dimethyl sulfoxide (DMSO). The absorbance is measured using a SoftMax Pro plate reader (Molecular Devices, CA) at 570nm.

Live and Dead Cell Assay

U251 cells were seeded at 30,000 cell/well in a 24-well plate and left to incubate overnight at 37°C and 5% humidity. The next day, cells were treated with 0.25mg/mL of 80nm Gd:PB and left to incubate for 1 hour. The cells were then exposed to an 808nm laser (2W/cm²) for 1 minute and left overnight at 37°C and 5% humidity. On the last day, the cells were washed with PBS and stained with Calcein AM (1uM) and Propidium Iodide (2uM). Images were taken using Keyence microscopy.

Magnetic Resonance Imaging

Gd:PB particles were diluted to 0, 0.625, 1.25, 2.5, 5, and 10mM concentrations with a final volume of 150uL. Particle solutions were then run through a 7T Bruker BioSpec 70/30 MRI.

5.3: Results/Discussion

Nanoparticle Formulation and Characterization

Gd:PBs were synthesized similar to PBNPs. The main difference is the presence of PVP and substitution of GdCl_3 for FeCl_3 . The Gd^{3+} ions act the same as Fe^{3+} ions from FeCl_3 and form an initial gadolinium (III) citrate complex. This is probably the most important step for reducing the overall size of the Gd:PBs as the citric acid allows for a stabilizing complex to be formed which the PVP can build upon. PVP is added to the solution containing potassium ferricyanide, to allow for the gadolinium (III) citrate complex to form separately without direct competition from the PVP to from the coordination complex. Now, not all the Fe^{3+} ions are replaced by Gd^{3+} within the structure. Depending on reaction times and concentrations of reagents used, the maximum amount of incorporated gadolinium can vary. When HCl is mixed with $\text{K}_3[\text{Fe}(\text{CN})_6]$ some of the Fe^{3+} will be reduced to Fe^{2+} will allow for the Prussian Blue complex to form. When the GdCl_3/HCl solution is added, the HCl will act as an etching agent prompting for the substitution of Gd^{3+} in the structure. As this process occurs relatively slowly, the total reaction is about 24 hours longer than that of traditional PBNP. Once synthesized, the particles were characterized by DLS, TEM, and optical absorbance (**Figure 48**). Overall peak absorbance was shifted from $\sim 700\text{nm}$ to 800nm , which is good for translational efforts as they can be used with lasers with longer wavelengths (**Figure 48C**). Size was shown to be $\sim 90\text{nm}$ through DLS measurements, with a low PDI indicating good dispersion (**Figure 48D**). Finally, morphology and true size were checked using TEM and particles were shown to be $\sim 80\text{nm}$ with the natural cubic shape and good dispersity (**Figures 48A and 48B**).

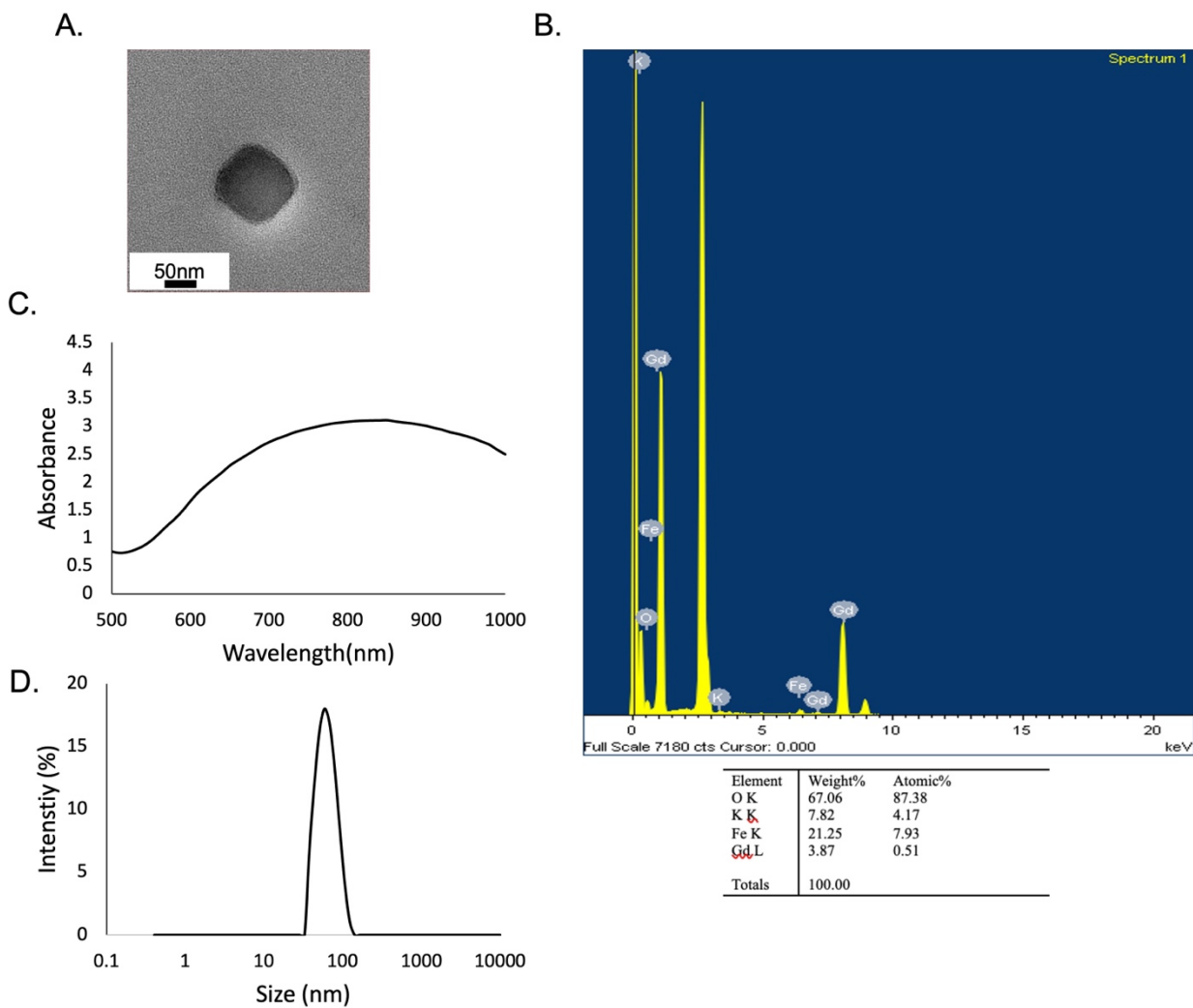


Figure 48: Gd:PB particle characterization. (A) TEM image. Scale bar = 50nm. (B) Corresponding EDS spectrum for TEM image in (A). (C) Gd:PB absorbance curve. (D) DLS size distribution graph. Reproduced with permission from reference¹⁷¹, Copyright 2024, American Chemical Society.

In Vitro Cytotoxicity

Gadolinium containing compounds are known for their extreme toxicity within biological organisms. As a result, by adding gadolinium into the FCC lattice structure of PBNPs the particles will lose their biocompatibility. Size is also a large factor in toxicity as the larger the particle, more gadolinium will be present. An MTT assay was run to evaluate the lethal dose 50 (LD50) of 80 and 120nm Gd:PBs. What was seen is that the 120nm particles start to show immediate toxic effects at 0.015625mg/mL with cell viability reduced down to $63\pm 4.45\%$. In comparison, the 80nm nanoparticles do not show statistical significance until 0.5mg/mL with a cell viability reduced to $76\pm 11.9\%$. Estimated LD50 values based on graphed results are 0.125mg/mL (120nm) and >1mg/mL (80nm) (**Figure 49**). Since the application for these particles is to be used as a dual theranostic agent for LITT with MRI guidance, the 80nm particles were tested with two different laser wavelengths to determine particle efficiency. LITT technologies operate with higher wavelength (>900nm) for clinical applications as these lasers have the least amount of dermatological effect on the patient. These particles were exposed either to an 808nm laser ($2\text{W}/\text{cm}^2$) or 980nm laser ($1\text{W}/\text{cm}^2$). The 808nm was used as a direct comparison to previous studies done with PBNP, PEG:PB, and Exo:PB particles. A downward trend was seen for both lasers as concentration of Gd:PB increased (**Figure 50**). Both showed statistically similar cell viability effects indicating that these particles show the same effect when exposed to a higher wavelength laser as a lower power intensity. This is ideal for clinical translation as it could be directly used with preexisting setups. To reach LD50 effects, these particles would have to be used at a concentration of 0.25mg/mL which is still in the tolerable toxicity range (**Figure 51**). To see the range of laser intensities that could be used for the Gd:PB

exposed to both the 808nm and 980nm lasers, a live and dead assay was performed. The chosen 0.25mg/mL concentration chosen based on the LD50 from U251 cells incubated with particle were exposed to either 0.1W or 1W laser at 980nm. The results are distinctive for the 980nm laser as down to 0.1W there is localized cell death. The 808nm is less effective as the treated region for the 1W shows less cell death in comparison to the 980nm and shows no effect at 0.1W. This is promising as the particles could be used with lower intensity lasers, which can reduce patient side-effects from the laser itself.

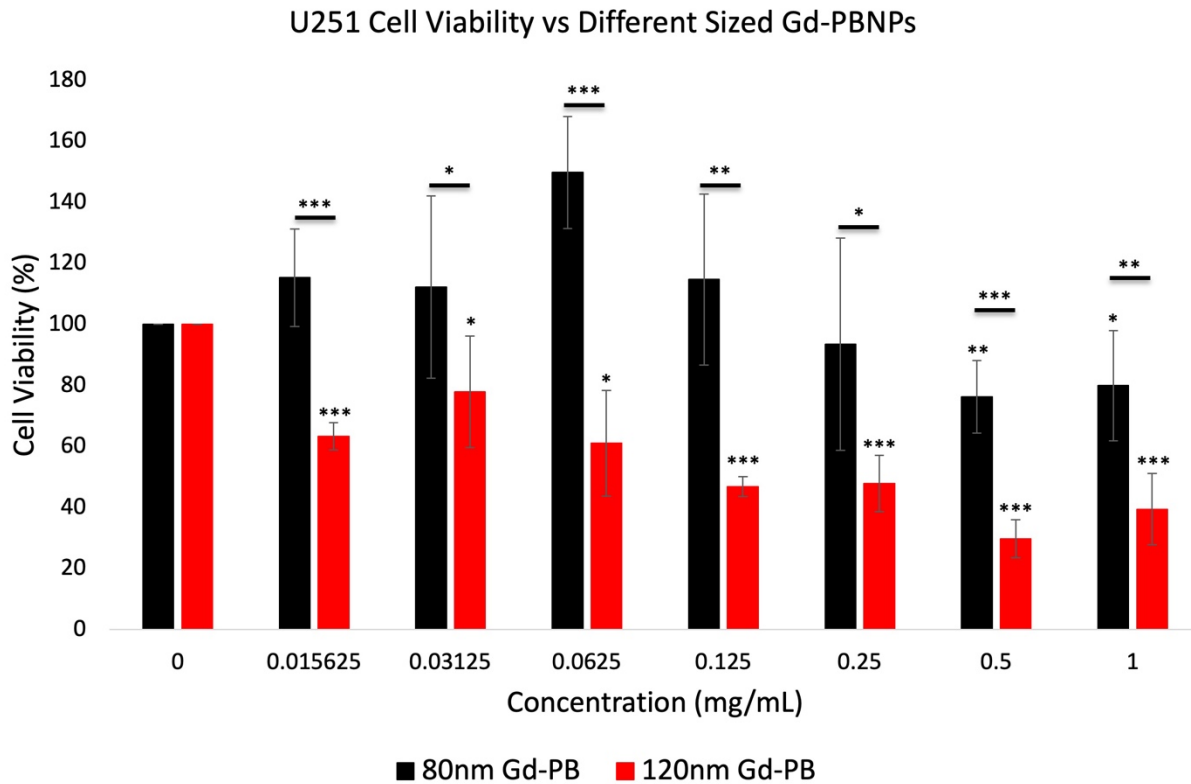


Figure 49: MTT assay results for different concentration of 80nm and 120nm Gd:PB treated U251 cells. Black = 80nm, Red = 120nm. * $p < 0.05$, ** $p < 0.01$, *** $p < 0.001$. $N = 6$. 0.0625mg/mL for the 80nm Gd:PB is an outlier group with excess cell growth as it is statistically different from the 0mg/mL control.

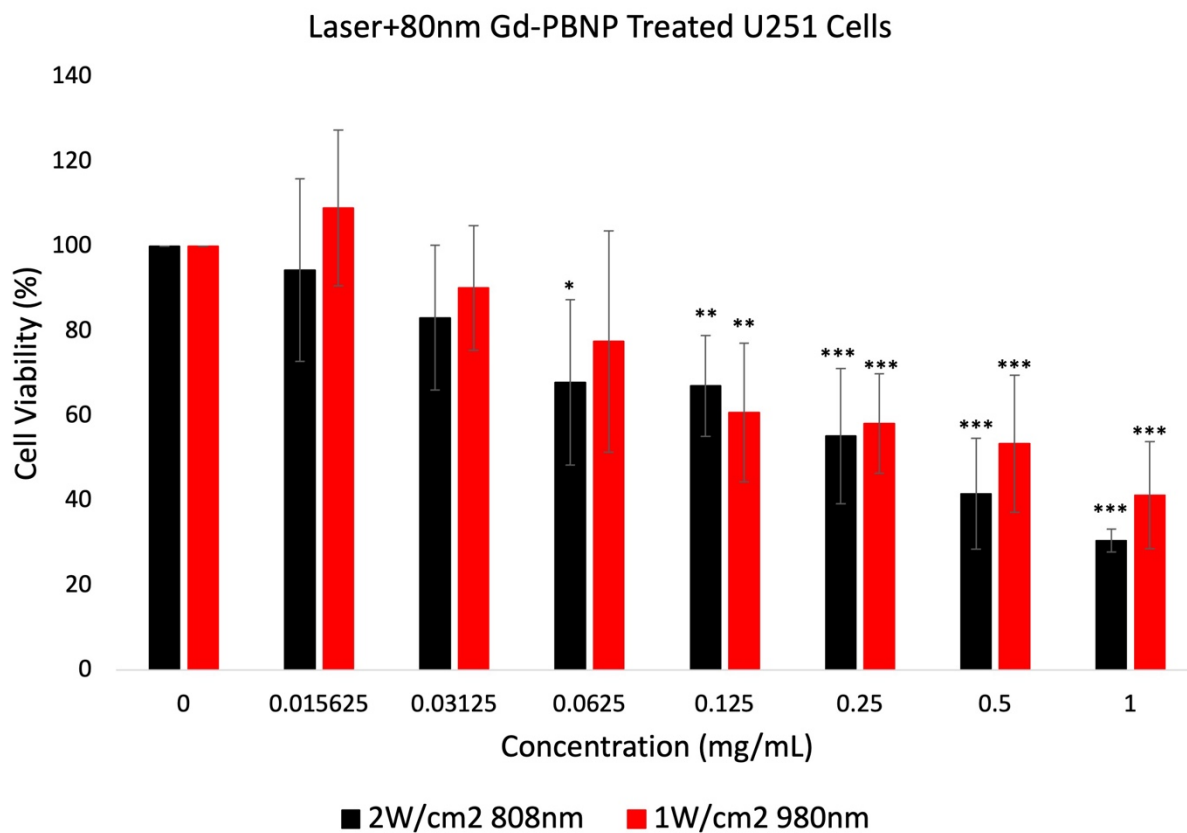


Figure 50: MTT assay results for 80nm Gd:PB at different concentrations treated with a 2W/cm² 808nm (black) and 1W/cm² 980nm laser (red). *p<0.05, **p<0.01, ***p<0.001. N=6.

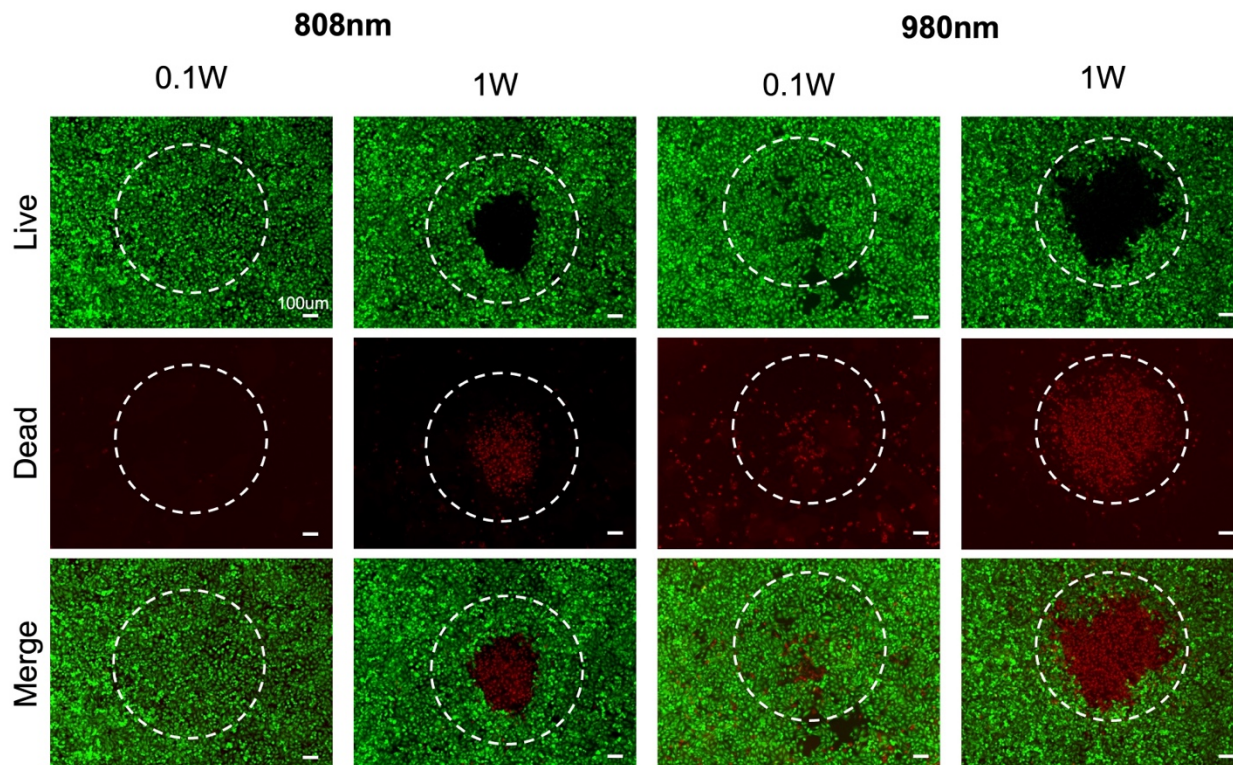


Figure 51: Live and dead assay results for U251 cells incubated with 80nm Gd:PB and exposed to 0.1W or 1W 808nm or 980nm laser. Green = alive cells, Red = dead cells. Scale bar = 100µm.

Magnetic Resonance Imaging

As a preliminary study to measure the MRI signal intensity of the 80nm Gd:PB nanoparticles, a simple T1 MRI study was done. Concentrations of 0, 0.625, 1.25, 2.5, 5, and 10mM of Gd:PB and clinical standard agent Dotarem were run through a 7T MRI and images were used to quantify longitudinal relaxation time relaxivity (r_1) values. T1-weighted images were taken at T1 = 769, 1193, 1727, 2047, 2309, and 2770ms for Gd:PB and the longitudinal relaxation rate (R1) is calculated as $1/T_1$. The relaxivity is then determined to be the slope of R1-R0 vs the concentration which was $0.1\text{mmol}^{-1}\text{s}^{-1}$ for Gd:PB. Now this value is consistent with those found within the literature for PBNPs without metal doping²¹³. While the absorbance pattern as well as ICP results for these particles indicates gadolinium incorporation, it is possible that positioning within the lattice structure doesn't allow for proper interaction with surrounding water molecules allow for the shift in normal spin. As the first substitution made during heavy metal incorporation is to push internal potassium ions out from inside the lattice into the environment before replacing iron, the gadolinium is probably not expressed on the surface to allow for enhanced MRI contrast²¹³. For Dotarem, T1 was evaluated as 63, 112, 211, 388, and 3073ms. Relaxivity was determined to be $3.1\text{mmol}^{-1}\text{s}^{-1}$. This is consistent with what is seen in the literature for the compound²⁹³ (**Figure 52**).

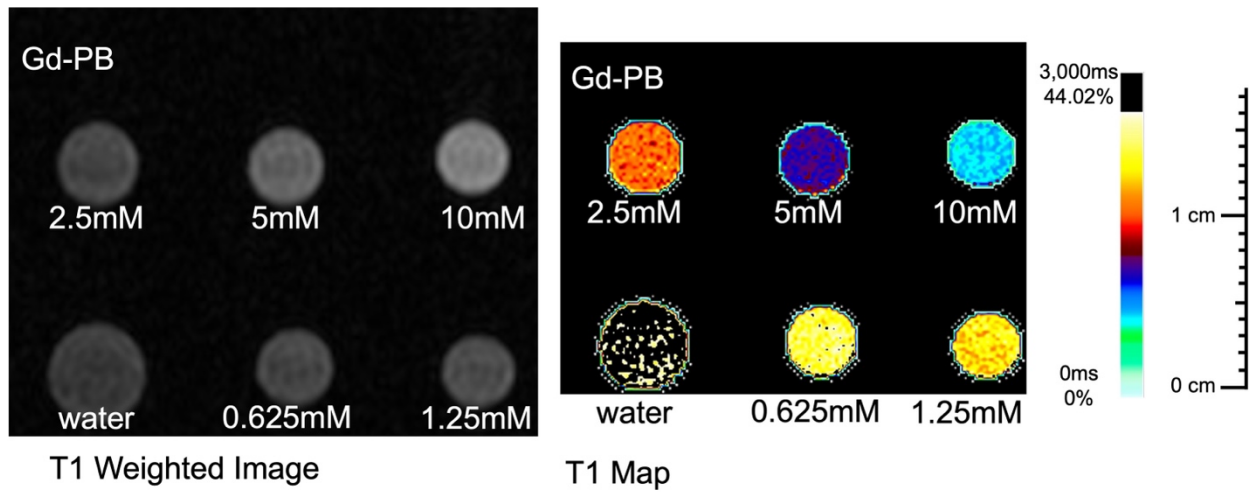


Figure 52: T_1 weighted and mapped MRI images of different concentrations of Gd:PB.

5.4: Conclusions

The contents discussed in this chapter revolve around the development of a gadolinium doped Prussian blue nanoparticle (Gd:PB) and the application it can have for MRI-guided LITT. Particles can be synthesized with uniform size and shifted absorbance with repeatable conditions. Once the particles are treated in U251 cells, it was seen that size greatly impacts toxicity as 120nm showed immediate reduction in cell viability vs the 80nm counterparts. With the 80nm Gd:PB particles, additional *in vitro* experiments were performed to test their efficacy for photothermal therapy with lasers of different wavelengths and power. Results showed that the exposure to a 980nm laser at $0.1\text{W}/\text{cm}^2$ showed similar effects to exposure to an 808nm laser at $2\text{W}/\text{cm}^2$. Finally, preliminary MRI studies were done and showed a consistent r_1 value with PBNPs. Overall, this work provides a solid foundation for expansion of the Exo:PB work for use as an LITT agent. If the MRI signal is improved, once the particles are coated, they could act as a dual diagnostic agent through photoacoustic imaging and MRI and well as enhance photothermal effects for glioblastoma tumors.

Chapter 6: Conclusions and Future Directions

6.1: Conclusions

The work presented in this dissertation is sectioned into four parts:

1. Formation of exosome coated Prussian Blue nanoparticles (Exo:PB) for early detection and treatment of glioblastoma.
2. Use of Exo:PB particles as an anti-inflammatory agent for photothermal therapy side-effects.
3. Comparison of Exo:PB particles to a RGD Prussian Blue conjugate (RGD:PB) to determine clinical efficacy.
4. Synthesis of a gadolinium doped Prussian Blue nanoparticle (Gd:PB) for translation to a clinical laser interstitial thermal treatment (LITT) setting.

An Exo:PB formulation was created that contains the innate properties of U-87 derived exosomes and Prussian Blue nanoparticles. The particles were created from a basic extrusion method and the full coating was validated using DLS, NTA, and TEM. Exosome markers were validated using western blot analysis. Similarities to U-87 exosome cellular behavior was observed using a cell uptake assay with U-87 cells and particles. Photothermal therapeutic effects were evaluated in both *in vitro* and *in vivo* models. Within the *in vivo* subcutaneous local injection model, tumor reduction was seen immediately after laser exposure. In comparison, when Exo:PB and PEG:PB were injected systemically the photothermal effect was less dramatic. Though full tumor reduction was seen after the 8-day treatment period for the Exo:PB particles as there was higher accumulation seen at the time point used for treatment. To determine the use of these particles for glioblastoma diagnosis and treatment, the particles were evaluated using an *in vitro* blood-brain barrier setup as well as an *in vivo* orthotopic brain tumor model.

Exo:PB particles were easily able to pass through the mimicked BBB *in vitro* setup and accumulate within U-87 cells in comparison to the PEG:PB control. High accumulation patterns were seen within orthotopic tumors after intravenous injection for the Exo:PB particles. Distinct tumor targeting was seen through photoacoustic imaging and validated through *ex vivo* analysis. The particles allowed for visualization of the blood brain tumor barrier and tumor infiltration to be possible. As glioblastoma is a very infiltrative cancer that is almost impossible for surgeons to fully remove, this is a big step in increasing patient survival and quality of life.

Exo:PB particles were also evaluated for use as a possible anti-inflammatory agent for heightened ROS species generation during photothermal therapy. Catalase and peroxidase enzymatic scavenging abilities were observed in particle-based assays. When Exo:PB was added to pro-inflammatory M1 macrophage cells, an overall decrease in ROS production was seen. Hypoxia reduction abilities were also measured in *in vivo* U-87 subcutaneous and orthotopic brain tumor models. After intravenous injection overall blood supply increased in both tumor models 1-3 hours post injection. This proves as a great starting point for further evaluation of ROS scavenging effects and their effects during and after photothermal therapy.

As RGD peptide use is the golden standard for glioblastoma targeting due to their remarkable ability to pass through the BBB, RGD conjugated Prussian Blue nanoparticles (RGD:PB) were synthesized as a positive control for Exo:PB. RGD is known to have high accumulation within tumors due to overexpression of RGD-recognizing integrins on the surface of malignant cells. When tested in an *in vitro* BBB setup, RGD:PB particles were easily able to pass through and accumulate within U-87 cells with similar efficacy to that of Exo:PB. Once systemically injected into a U-87 subcutaneous model, after 2 hours it was seen that

accumulation patterns were similar to that of Exo:PB. After the particles were exposed to the U-87 orthotopic model, there was a lot of off-targeting effects seen within the brain. Unlike the Exo:PB, PA signal for RGD:PB was spread out around of the brain and less accurate to the tumor site. This is promising for Exo:PB translation into the clinic as it would prove to be a more accurate marker for glioblastoma allowing for earlier diagnosis and more precise treatment.

Finally, Gd:PB particles were synthesized and tested to investigate potential use in an LITT setup. Exo:PB particles have great targeting effects of glioblastoma, but lack the photothermal conversion efficiency when exposed to longer wavelength lasers and have poor MRI contrast. Doping with gadolinium increased peak absorbance and well as *in vitro* photothermal effects as exposure to an 980nm laser at lower intensity showed better efficacy than exposure to an 808nm laser. When particles were measured using MRI, there was low T1 contrast comparable to that of PBNPs. As LITT technologies utilize lasers >900nm, this is promising data for clinical translation once the particles are coated with an exosome layer to allow for specific targeting of glioblastoma tissue.

6.2: Future Directions

There are many ways in which the ideas presented in this dissertation could be built upon. In terms of the data already presented, the next logical step would be to enhance the MRI image contrast of the Gd:PB particles and then to coat with exosomes and use within an LITT animal model setup. This work is in progress with Henry Ford Hospital System in Detroit, MI where they have developed a U251 orthotopic glioblastoma brain model as well as a patient derived glioblastoma animal model that is compatible with a Visualase™ LITT system. Our particles would be able to enhance the selectivity, effectiveness, and safety of LITT. Further investigation of the anti-inflammatory properties of PBNP or Exo:PB particles for use as a post-treatment drug is another option that is related to the previous topic. For use as a dual therapeutic agent, the PBNPs could be hollowed out using an HCl etching method and loaded with hydrophobic chemotherapeutics for a targeted drug approach coupled with photothermal therapy. Exo:PB particles with coating from different derived exosomes could also be investigated for their targeting efficacy of other types of hard to diagnose tumors (ex: pancreatic cancer)^{294, 295}. Furthermore, the use of immune cell coatings might be able to enhance immune response to cancers.

REFERENCES

- (1) Tamimi, A. F.; Juweid, M. Epidemiology and Outcome of Glioblastoma. In *Glioblastoma*, Codon Publications, 2017; pp 143-154.
- (2) Ijzerman-Korevaar, M.; Snijders, T. J.; de Graeff, A.; Teunissen, S. C. C. M.; de Vos, F. Y. F. Prevalence of Symptoms in glioma patients throughout the disease trajectory: a systematic review. *Journal of Neuroscience-Oncology* **2018**, *140*, 485-496.
- (3) Rasmussen, B. K.; Hansen, S.; Laursen, R. J.; Kosteljanetz, M.; Schultz, H.; Norgard, B. M.; Guldborg, R.; Gradel, K. O. Epidemiology of glioma: clinical characteristics, symptoms, and predictors of glioma patients grade I-IV in the Danish Neuro-Oncology Registry. *Journal of Neuro-Oncology* **2017**, *135*, 571-579.
- (4) Leo, R. J.; Friday, J. N.; Ruggieri, M. L. Subtle neuropsychiatric symptoms of glioblastoma multiforme misdiagnosed as depression. *BMJ Case Reports* **2020**, *13* (3), 1-6.
- (5) Parisi, S.; Corsa, P.; Raguso, A.; Perrone, A.; Cossa, S.; Munafo, T.; Sanpaolo, G.; Donna, E.; Clemente, M. A.; Piombino, M.; et al. Temozolomide and Radiotherapy versus Radiotherapy Alone in High Grade Gliomas: A Very Long Term Comparative Study and Literature Review. *BioMed Research International* **2015**, *2015*, 1-7.
- (6) Stupp, R.; Mason, W. P.; van den Bent, M. J.; Weller, M.; Fisher, B.; Taphoorn, M. J. B.; Belanger, K.; Brandes, A. A.; Marosi, C.; Bogdahn, U.; et al. Radiotherapy plus Concomitant and Adjuvant Temozolomide for Glioblastoma. *New England Journal of Medicine* **2005**, *352*, 987-996.
- (7) Aryal, M.; Arvanitis, C. D.; Alexander, P. M.; McDannold, N. Ultrasound-mediated blood-brain barrier disruption for targeted drug delivery in the central nervous system. *Adv Drug Deliv Rev* **2014**, *72*, 94-109. DOI: 10.1016/j.addr.2014.01.008 From NLM.
- (8) Bonan, N. F.; Ledezma, D. K.; Tovar, M. A.; Balakrishnan, P. B.; Fernandes, R. Anti-Fn14-Conjugated Prussian Blue Nanoparticles as a Targeted Photothermal Therapy Agent for Glioblastoma. *Nanomaterials (Basel)* **2022**, *12* (15), 2645. From NLM.
- (9) Lombardo, S. M.; Schneider, M.; Tureli, A. E.; Tureli, N. G. Crossing the BBB with Nanoparticles: the rational design. *Beilstein Journal of Nanotechnology* **2020**, *11*, 866-883. DOI: <https://doi.org/10.3762/bjnano.11.72>.
- (10) Tang, W.; Fan, W.; Lau, J.; Deng, L.; Shen, Z.; Chen, X. Emerging Blood-Brain-Barrier-Crossing Nanotechnology for Brain Cancer Theranostics. *Chemical Society Reviews* **2019**, (11). DOI: DOI<https://doi.org/10.1039/C8CS00805A>.

- (11) Teleanu, D. M.; Chircov, C.; Grumezescu, A. M.; Volceanov, A.; Teleanu, R. I. Blood-Brain Delivery Methods Using Nanotechnology. *Pharmaceutics* **2018**, *10* (4), 269. DOI: 10.3390/pharmaceutics10040269.
- (12) Yang, T.; Martin, P.; Fogarty, B.; Brown, A.; Schurman, K.; Phipps, R.; Yin, V. P.; Lockman, P.; Bai, S. Exosome delivered anticancer drugs across the blood-brain barrier for brain cancer therapy in Danio rerio. **2015**, *32*, 2003-2014. DOI: <https://doi.org/10.1007/s11095-014-1593-y>.
- (13) Manrique-Guzman, S.; Herrada-Pineda, T.; Revilla-Pacheco, F. *Chapter 12 Surgical Management of Glioblastoma*; Codon Publications, 2017.
- (14) Muller, D. M.; De Swart, M. E.; Ardon, H.; Barkhof, F.; Bello, L.; Berger, M. S.; Bouwknecht, W.; Van den Brink, W.; Nilbali, M. C.; Eijgelaar, R. S.; et al. Timing of glioblastoma surgery and patient outcomes: a multi center cohort study. *Neuro-Oncology Advances* **2021**, *3* (1), 1-10.
- (15) Rycaj, K.; Tang, D. G. Cell-of-Origin of Cancer versus Cancer Stem Cells: Assays and Interpretations. *Cancer Research* **2015**, *75* (19), 4003-4011.
- (16) Antunes, A. R. P.; Scheyltjens, I.; Duerinck, J.; Neyns, B.; Movahedi, K.; Van Ginderachter, J. A. Understanding the glioblastoma immune microenvironment as basis for the development of new immunotherapeutic strategies. *eLife* **2020**, *9*, 1-16.
- (17) Zhang, P.; Xia, Q.; Liu, L.; Li, S.; Dong, L. Current Opinion on Molecular Characterization for GBM Classification in Guiding Clinical Diagnosis, Prognosis, and Therapy. *Frontiers in Molecular Biosciences* **2020**, *7*, 1-13.
- (18) Zong, H.; Verhaak, R. G. W.; Canoll, P. The cellular origin for malignant glioma and prospects for clinical advancements. *Expert Review of Molecular Diagnostics* **2012**, *12* (4), 383-394.
- (19) Ah-Pine, F.; Khettab, M.; Bedoui, Y.; Slama, Y.; Daniel, M.; Doray, B.; Gasque, P. On the origin and development of glioblastoma: multifaceted role of perivascular mesenchymal stromal cells. *Acta Neuropathologica Communications* **2023**, *11* (104), 1-15.
- (20) Cohen, A.; Holmen, S.; Colman, H. IDH1 and IDH2 Mutations in Gliomas. *Current Neurology and Neuroscience Reports* **2013**, *13* (345), 1-7.
- (21) Verhaak, R. G. W.; Hoadley, K. A.; Purdom, E.; Wang, V.; Qi, Y.; Wilkerson, M. D.; Miller, C. R.; Ding, L.; Golub, T.; Mesirov, J. P.; et al. Integrated Genomic Analysis Identifies Clinically Relevant Subtypes of Glioblastoma Characterized by Abnormalities in PDGFRA, IDH1, EGFR, and NF1. *Cancer Cell* **2010**, *17* (1), 98-110.
- (22) Chen, R.; Smith-Cohn, M.; Cohen, A. L.; Colman, H. Glioma Subclassifications and Their Clinical Significance. *14* **2017**, 284-297.

- (23) Gonzalez-Tablas, M.; Crespo, I.; Vital, A. L.; Otero, A.; Nieto, A. B.; Sousa, P.; Patino-Alonso, M. C.; Corchete, L. A.; Tao, H.; Rebelo, O.; et al. Prognostic stratification of adult primary glioblastoma multiforme patients based on their tumor gene amplification profiles. *Oncotarget* **2018**, *9* (46), 28083-28102.
- (24) Franceschi, S.; Citiva, P.; Pasqualetti, F.; Lessi, F.; Modena, M.; Barachini, S.; Morelli, M.; Santonocito, O.; Vannozzi, R.; Pilkington, G. J.; et al. Multiregional Sequencing of IDH-WT Glioblastoma Reveals High Genetic Heterogeneity and a Dynamic Evolutionary History. *Cancers* **2021**, *13* (9), 1-21.
- (25) Murat, A.; Migliavacca, E.; Gorlia, T.; Lambiv, W. L.; Shay, T.; Hamou, M.-F.; de Tribolet, N.; Regli, L.; Wick, W.; Kouwenhoven, M. C. M.; et al. Stem Cell-Related "Self-Renewal" Signature and High Epidermal Growth Factor Receptor Expression Associated With Resistance to Concomitant Chemoradiotherapy in Glioblastoma. *Journal of Clinical Oncology* **2008**, *26*, 3015-3024.
- (26) Phuong, C. P.; Nam, V. L.; Schild, E. S.; Rades, D.; Khoa, T. M. A Survival Score Based on Symptoms and Performance Status for Patients with High-grade Gliomas Receiving Radiochemotherapy. *In Vivo* **2017**, *31* (4), 689-693.
- (27) Rivera, A. L.; Pelloski, C. E.; Gilbert, M. R.; Colman, H.; De La Cruz, C.; Sulman, E. P.; Bekele, B. N.; Aldape, K. D. MGMT promoter methylation is predictive of response to radiotherapy and prognostic in the absence of adjuvant alkylating chemotherapy for glioblastoma. *Neuro-Oncology* **2010**, *12* (2), 116-121.
- (28) White, K.; Connor, K.; Meylan, M.; Sautes-Fridman, C.; Fridman, W. H.; Byrne, A. T. Identification, validation and biological characterisation of novel glioblastoma tumour microenvironment subtypes: implications for precision immunotherapy. *Annals of Oncology* **2023**, *34* (3), 300-314.
- (29) Lakis, N. S.; Brodsky, A. S.; Karashchuk, G.; Audesse, A. J.; Yang, D.; Sturtevant, A.; Lombardo, K.; Wong, I. Y.; Webb, A. E.; Anthony, D. C. Stem cell phenotype predicts therapeutic response in glioblastomas with MGMT promoter methylation. *Acta Neuropathologica Communications* **2022**, *10* (159), 1-15.
- (30) He, Z.-C.; Ping, Y.-F.; Xu, S.-L.; Lin, Y.; Yu, S.-C.; Kung, H.-F.; Bian, X.-W. Lower MGMT expression predicts better prognosis in proneural-like glioblastoma. *International Journal of Clinical and Experimental Medicine* **2015**, *8* (11), 20287-20294.
- (31) Szyłberg, M.; Sokal, P.; Sledzinska, P.; Bebyn, M.; Krajewski, S.; Szyłberg, L.; Szyłberg, A.; Szyłberg, T.; Krystkiewicz, K.; Birski, M.; et al. MGMT Promoter Methylation as a Prognostic Factor in Primary Glioblastoma: A Single-Institution Observational Study. *Biomedicines* **2022**, *10* (8), 1-14.

- (32) Liu, J.; Li, C.; Wang, Y.; Ji, P.; Guo, S.; Zhai, Y.; Wang, N.; Lou, M.; Xu, M.; Chao, M.; et al. Prognostic and Predictive Factors in Elderly Patients With Glioblastoma: A Single-Center Retrospective Study. *Frontiers in Aging Neuroscience* **2022**, *13*.
- (33) Lee, J.; Park, S. H.; Kim, Y. Z. Prognostic Evaluation of Neurological Assessment of the Near-Oncology Scale in Glioblastoma Patients. *Brain Tumor Research and Treatment* **2018**, *6* (1), 22-30.
- (34) Barz, M.; Gerhardt, J.; Bette, S.; Aftahy, A. K.; Huber, T.; Combs, S. E.; Ryang, Y.-M.; Wiestler, B.; Skardelly, M.; Gepfner-Tuma, I.; et al. Prognostic value of tumour volume in patients with a poor Karnofsky performance status scale - a biocentric retrospective study. *BMC Neurology* **2021**, *21*, 1-10.
- (35) Boeck, S.; Hinke, A.; Wilkowski, R.; Heinemann, V. Importance of performance status for treatment outcome in advanced pancreatic cancer. *World Journal of Gastroenterology* **2007**, *13* (2), 224-227.
- (36) Teleanu, D. M.; Chircov, C.; Grumezescu, A. M.; Volceanov, A.; Teleanu, R. I. Blood-Brain Delivery Methods Using Nanotechnology. *Pharmaceutics* **2018**, *10*. DOI: 10.3390/pharmaceutics10040269.
- (37) Liu, X.; Duan, Y.; Liu, B. Nanoparticles as contrast agents for photoacoustic brain imaging. *Aggregate* **2021**, *2* (1), 4-19.
- (38) Betzer O; Shilo M; Opoichinsky R; Barnoy E; Motiei M; Okun E; Yadid G; R., P. The effect of nanoparticle size on the ability to cross the blood-brain barrier: an in vivo study. *Nanomedicine (Lond)* **2017**, *12*, 1533-1546. DOI: 10.2217/nnm-2017-0022.
- (39) Redzic, Z. Molecular biology of the blood-brain and the blood-cerebrospinal fluid barriers: similarities and differences. *Fluids and Barriers of the CNS* **2011**, *8* (3), 1-25.
- (40) Daneman, R.; Prat, A. The Blood-Brain Barrier. *Cold Spring Harbor Perspectives in Biology* **2015**, *7* (1), 1-23.
- (41) Stamatovic, S. V.; Johnson, A. M.; Keep, R. F.; Andjelkovic, A. V. Junctional proteins of the blood-brain barrier: New insights into function and dysfunction. *Tissue Barriers* **2016**, *4* (1), 1-12.
- (42) Singh, A. B.; Sharma, A.; Dhawan, P. Claudin Family of Proteins and Cancer: An Overview. *Journal of Oncology* **2010**, *2010*, 1-11.
- (43) Anderson, J. M.; Van Itallie, C. M. Physiology and Function of the Tight Junction. *Cold Spring Harbor Perspectives in Biology* **2009**, *1* (2), 1-16.

- (44) O'Brown, N. M.; Pfau, S. J.; Gu, C. Bridging barriers: a comparative look at the blood-brain barrier across organisms. *Genes and Development* **2018**, *32*, 466-478.
- (45) Dias, M. C.; Coisne, C.; Lazarevic, I.; Baden, P.; Hata, M.; Iwamoto, N.; Francisco, D. M. F.; Vanlandewijck, M.; He, L.; Baier, F. A.; et al. Claudin-3-deficient C57BL/6J mice display intact brain barriers. *Scientific Reports* **2019**, *9* (203), 1-16.
- (46) Institute, N. C. *Drugs Approved for Brain Tumors*. Updated January 17, 2024. (accessed 2024 January 28, 2024).
- (47) Dotiwala, A. K.; McCausland, C.; Samra, N. S. *Anatomy, Head and Neck: Blood Brain Barrier*; StatPearls Publishing, 2023.
- (48) Loscher, W.; Potschka, H. Blood-brain barrier active efflux transporters: ATP-binding cassette gene family. *Neurotherapeutics* **2005**, *2*, 86-98.
- (49) Mittapalli, R. K.; Manda, V. K.; Adkins, C. E.; Geldenhuys, W. J.; Lockman, P. R. Exploiting nutrient transporters at the blood-brain barrier to improve brain distribution of small molecules. *Theranostics Delivery* **2010**, *1* (6), 775-784.
- (50) Ha, S. N.; Sheridan, R. P. Mini review in molecular modeling of P-glycoprotein (Pgp). *Current Topics in Medicinal Chemistry* **2007**, *7* (15).
- (51) Gibson, A. J.; Hossain, M. M.; Richardson, J. R.; Aleksunes, L. M. Inflammatory regulation of ATP binding cassette efflux transporter expression and function in microglia. *The Journal of Pharmacology and Experimental Therapeutics* **2012**, *343* (3), 650-660.
- (52) De Vivo, D. C.; Trifiletti, R. R.; Jacobson, R. I.; Ronen, G. M.; Behind, R. A.; Tarik, S. I. Defective Glucose Transport across the Blood-Brain Barrier as a Cause of Persistent Hypoglycorrhachia, Seizures, and Developmental Delay. *New England Journal of Medicine* **1991**, *325*, 703-709.
- (53) Cornford, E. M.; Hyman, S.; Swartz, B. E. The Human Brain GLUT1 Glucose Transporter: Ultrastructural Localization to the Blood-Brain Barrier Endothelia. *Journal of Cerebral Blood Flow and Metabolism* **1994**, *14*, 106-112.
- (54) Puris, E.; Fricker, G.; Gynther, M. Targeting Transporters for Drug Delivery to the Brain: Can We Do Better? *Pharmaceutical Research* **2022**, *39*, 1415-1455.
- (55) Fass, L. Imaging and cancer: A review. *Molecular Oncology* **2008**, *2* (2), 115-152.
- (56) Pomara, C.; Pascale, N.; Maglietta, F.; Neri, M.; Turillazzi, E. Use of contrast media in diagnostic imaging: medico-legal considerations. *Radiological Medicine* **2015**, *120* (9), 802-809.

- (57) Cai, W.; Gao, T.; Hong, H.; Sun, J. Applications of gold nanoparticles in cancer nanotechnology. *Nanotechnol Sci Appl* **2008**, *1*, 17-32. DOI: 10.2147/nsa.s3788 From NLM.
- (58) Joshi, B. P.; Hardie, J.; Farkas, M. E. Harnessing Biology to Deliver Therapeutic and Imaging Entities via Cell-Based Methods. *Chemistry (Weinheim an der Bergstrasse, Germany)* **2018**, *24*, 8717-8726. DOI: <https://doi.org/10.1002/chem.201706180>.
- (59) Murphy, D. E.; de Jong, O. G.; Brouwer, M.; al., e. Extracellular vesicle-based therapeutics: natural versus engineered targeting and trafficking. *Experimental and Molecular Medicine* **2019**, *51*, 1-12. DOI: <https://doi.org/10.1038/s12276-019-0223-5>.
- (60) Uthaman, S.; Huh, K. M.; Park, I. K. Tumor microenvironment-responsive nanoparticles for cancer theragnostic applications. *Biomater Res* **2018**, *22* (22). DOI: 10.1186/s40824-018-0132-z From NLM.
- (61) Wilhelm, S.; Tavares, A.; Dai, Q.; al., e.; Analysis of nanoparticle delivery to tumours. *Nat Rev Mater* **2016**, *1* (16014). DOI: <https://doi.org/10.1038/natrevmats.2016.14>.
- (62) Zhen, X.; Cheng, P.; Pu, K. Recent Advances in Cell Membrane-Camouflaged Nanoparticles for Cancer Phototherapy. *Small* **2019**, *15* (1). DOI: 10.1002/sml.201804105 From NLM.
- (63) Haumann, R.; Videira, J. C.; Kaspers, G. J. L.; al, e. Overview of Current Drug Delivery Methods Across the Blood–Brain Barrier for the Treatment of Primary Brain Tumors. *CNS Article* **2020**, *34*, 1121-1131. DOI: <https://doi.org/10.1007/s40263-020-00766-w>.
- (64) Thakor, A. S.; Jokerst, J. V.; Ghanouni, P.; Campbell, J. L.; Mittra, E.; Gambhir, S. S. Clinically Approved Nanoparticle Imaging Agents. *The Journal of Nuclear Medicine* **2016**, *57* (12), 1833-1837.
- (65) Thapa, B.; Diaz-Diestra, D.; Santiago-Medina, C.; Kumar, N.; Tu, K.; Beltran-Huarac, J. T₁- and T₂- weighted Magnetic Resonance Dual Contrast by Single Core Truncated Cubic Iron Oxide Nanoparticles with Abrupt Cellular Internalization and Immune Evasion. *ACS Applied Bio Materials* **2018**, *1* (1), 79-89.
- (66) Jeon, M.; Halbert, M. V.; Stephen, Z. R.; Zhang, M. Iron oxide nanoparticles as T₁ contrast agents for magnetic resonance imaging: fundamentals, challenges, applications, and prospectives. *Advanced Materials* **2020**, *33* (23), 1-18.
- (67) Dadfar, S. M.; Roemhild, K.; Drude, N. I.; von Stillfried, S.; Knuchel, R.; Kiessling, F.; Lammers, T. Iron Oxide Nanoparticles: Diagnostic, Therapeutic, and Theranostic Applications. *Advanced Drug Delivery Reviews* **2019**, *138*, 302-325.

- (68) Hadjipanayis, C. G.; Machaidze, R.; Kaluzova, M.; Wang, L.; Schuette, A. J.; Chen, H.; Wu, X.; Mao, H. EGFRvIII antibody-conjugated iron oxide nanoparticles for magnetic resonance imaging-guided convection-enhanced delivery and targeted therapy of glioblastoma. *Cancer Research* **2010**, *70* (15), 6303-6312.
- (69) Israel, L. L.; Galstyan, A.; Holler, E.; Ljubimova, J. Y. Magnetic iron oxide nanoparticles for imaging, targeting and treatment of primary and metastatic tumors of the brain. *Journal of Controlled Release* **2020**, *320*, 45-62.
- (70) Thi, T. T. H.; Suys, E. J. A.; Lee, J. S.; Nguyen, D. H.; Park, K. D.; Truong, N. P. Lipid-Based Nanoparticles in the Clinic and Clinical Trials: From Cancer Nanomedicine to COVID-19 Vaccines. *Vaccines* **2021**, *9* (4), 1-29.
- (71) Mehta, M.; Bui, T. A.; Yang, X.; Aksoy, Y.; Goldys, E. M.; Deng, W. Lipid-Based Nanoparticles for Drug/Gene Delivery: An Overview of the Production Techniques and Difficulties Encountered in Their Industrial Development. *ACS Materials* **2023**, *3* (6), 600-619.
- (72) Ashrafzadeh, M. S.; Akbazadeh, A.; Heydarinasab, A.; Ardjmand, M. In vivo Glioblastoma Therapy Using Liposomal Cisplatin. *International Journal of Nanomedicine* **2020**, *15*, 7035-7049.
- (73) Wu, S.-K.; Tsai, C.-L.; Huang, Y.; Hynynen, K. Focused Ultrasound and Microbubbles-Mediated Drug Delivery to Brain Tumor. *Pharmaceutics* **2021**, *13* (1), 1-15.
- (74) Nsairat, H.; Khater, D.; Sayed, U.; Odeh, F.; Bawab, A. A.; Alshaer, W. Liposomes: structure, composition, types, and clinical applications. *Heliyon* **2022**, *8* (5), 1-15.
- (75) Sirsi, S.; Borden, M. Microbubble Compositions, Properties and Biomedical Applications. *Bubble Science and Engineering Technology* **2009**, *1* (1-2), 3-17.
- (76) Akbarzadeh, A.; Rezaei-Sadabady, R.; Davaran, S.; Joo, S. W.; Zarghami, N.; Hanifehpour, Y.; Samiei, M.; Kouhi, M.; Nejati-Koshki, K. Liposome: classification, preparation, and applications. *Nanoscale Research Letters* **2013**, *8* (1), 1-9.
- (77) Sturm, L.; Ulrih, N. P. Basic Methods for Preparation of Liposomes and Studying Their Interactions with Different Compounds, with the Emphasis on Polyphenols. *International Journal of Molecular Sciences* **2021**, *22* (12), 1-20.
- (78) Zhang, H. Thin-Film Hydration Followed by Extrusion Method for Liposome Preparation. **2017**, *1522*, 17-22.
- (79) Du, G.; Sun, X. Ethanol Injection Method for Liposome Preparation. *Methods in Molecular Biology* **2023**, *2622*, 65-70.

- (80) Raju, R.; Abuwatfa, W. H.; Pitt, W. G.; Husseini, G. A. Liposomes for the Treatment of Brain Cancer - A Review. *Pharmaceuticals* **2023**, *16* (8), 1-35.
- (81) Duong, V.-A.; Nguyen, T.-T.-L.; Maeng, H.-J. Recent Advances in Intranasal Liposomes for Drug, Gene, and Vaccine Delivery. *Pharmaceutics* **2023**, *15* (1), 1-27.
- (82) Inglut, C. T.; Sorrin, A. J.; Kuruppu, T.; Vig, S.; Cicalo, J.; Ahmad, H.; Huang, H.-C. Immunological and Toxicological Considerations for the Design of Liposomes. *Nanomaterials* **2020**, *10* (2), 1-24.
- (83) Chen, H.; Zhang, S.; Fang, Q.; He, H.; Ren, J.; Sun, D.; Lai, J.; Ma, A.; Chen, Z.; Liu, L.; et al. Biomimetic Nanosensitizers Combined with Noninvasive Ultrasound Actuation to Reverse Drug Resistance and Sonodynamic-Enhanced Chemotherapy against Orthotopic Glioblastoma. *ACS Nano* **2023**, *17* (1), 421-436. DOI: 10.1021/acsnano.2c08861 From NLM.
- (84) Márquez, M. G.; Dotson, R.; Pias, S.; Frolova, L. V.; Tartis, M. S. Phospholipid prodrug conjugates of insoluble chemotherapeutic agents for ultrasound targeted drug delivery. *Nanotheranostics* **2020**, *4* (1), 40-56. DOI: 10.7150/ntno.37738 From NLM.
- (85) Roovers, S.; Sergers, T.; Lajoinie, G.; Deprez, J.; Versluis, M.; De Smedt, S. C.; Lentacker, I. The Role of Ultrasound-Driven Microbubble Dynamics in Drug Delivery: From Microbubble Fundamentals to Clinical Translation. *Langmuir* **2019**, *35* (31), 10173-10191.
- (86) Blomley, M. J. K.; Cooke, J. C.; Unger, E. C.; Monaghan, M. J.; Cosgrove, D. O. Microbubble contrast agents: a new era in ultrasound. *BMJ* **2001**, *322* (7296), 1222-1225.
- (87) Tsutsui, J. M.; Xie, F.; Porter, R. T. The use of micro bubbles to target drug delivery. *Cardiovascular Ultrasound* **2004**, *2* (23), 1-7.
- (88) Chomas, J. E.; Dayton, P.; Allen, J.; Morgan, K.; Ferrara, K. W. Mechanisms of contrast agent destruction. *IEEE Transactions on Ultrasonics, Ferroelectrics, and Frequency Control* **2001**, *48* (1), 232-248.
- (89) Chomas, J. E.; Dayton, P. A.; May, D. J.; Ferrara, K. W. Threshold of fragmentation for ultrasonic contrast agents. *Journal of Biomedical Optics* **2001**, *6* (2), 141-150.
- (90) Bamankar, S.; Londhe, V. Y. The Rise of Extracellular Vesicles as New Age Biomarkers in Cancer Diagnosis: Promises and Pitfalls. *Technology in Cancer Research and Treatment* **2023**, *22*.
- (91) Santavanond, J. P.; Rutter, S. F.; Atkin-Smith, G. K.; Poon, I. K. H. Apoptotic Bodies: Mechanism of Formation, Isolation and Functional Relevance. *Subcellular Biochemistry* **2021**, *97*, 61-88.

- (92) Zou, X.; Lei, Q.; Luo, X.; Yin, J.; Chen, S.; Hao, C.; Shiyu, L.; Ma, D. Advances in biological functions and applications of apoptotic vesicles. *Cell Communication and Signaling* **2023**, *21*, 1-24.
- (93) Pfeffer, C. M.; Singh, A. T. K. Apoptosis: A Target for Anticancer Therapy. *International Journal of Molecular Sciences* **2018**, *19* (2), 1-10.
- (94) Tricarico, C.; Clancy, J.; D'Souza-Schorey, C. Biology and biogenesis of shed microvesicles. *Small GTPases* **2017**, *8* (4), 220-232.
- (95) Skog, J.; Wurdinger, T.; van Rijn, S.; Meijer, D.; Gainche, L.; Sena-Esteves, M.; Curry Jr., W. T.; Carter, R. S.; Krichevsky, A. M.; Breakefield, X. O. Glioblastoma microvesicles transport RNA and protein that promote tumor growth and provide diagnostic biomarkers. *Nature Cell Biology* **2008**, *10* (12), 1470-1476.
- (96) Pegtel, D. M.; Peferoen, L.; Amor, S. Extracellular vesicles as modulators of cell-to-cell communication in the healthy and diseased brain. *Philosophical Transactions B* **2014**, *369* (1652), 1-9.
- (97) Ramos-Zaldivar, H. M.; Polakovicova, I.; Salas-Huenuleo, E.; Corvalan, A. H.; Kogan, M. J.; Yefi, C. P.; Andia, M. E. Extracellular vesicles through the blood-brain barrier: a review. *Fluids and Barriers of the CNS* **2022**, *19* (60), 1-15.
- (98) Choi, H.; Choi, K.; Kim, D. H.; Oh, B. K.; Yim, H.; Jo, S.; Choi, C. Strategies for Targeted Delivery of Exosomes to the Brain: Advantages and Challenges. *Pharmaceutics* **2022**, *14* (3). DOI: 10.3390/pharmaceutics14030672 From NLM.
- (99) Record, M.; Silvente-Poirot, S.; Poirot, M.; Wakelam, M. O. Extracellular vesicles: lipids as key components of their biogenesis and functions. *Journal of Lipid Research* **2018**, *59* (8), 1316-1324.
- (100) Bartheld, C. S.; Altick, A. L. Multivesicular bodies in neurons: Distribution, protein content, and trafficking functions. *Progress in Neurobiology* **2011**, *93* (3), 313-340.
- (101) Doyle, L. M.; Wang, M. Z. Overview of Extracellular Vesicles, Their Origin, Composition, Purpose, and Methods for Exosome Isolation and Analysis. *Cells* **2019**, *8* (7), 1-24.
- (102) Kalluri, R.; Lebleu, V. S. The biology, function, and biomedical application of exosomes. *Science* **2020**, *367* (6478), 1-15.
- (103) Banks, W. A.; Sharma, P.; Bullock, K. M.; Hansen, K. M.; Ludwig, N.; Whiteside, T. L. Transport of Extracellular Vesicles across the Blood-Brain Barrier: Brain Pharmacokinetics and Effects of Inflammation. *International Journal of Molecular Sciences* **2020**, *21* (12), 1-21.

(104) Heidarzadeh, M.; Gürsoy-Özdemir, Y.; Kaya, M.; Eslami Abriz, A.; Zarebkohan, A.; Rahbarghazi, R.; Sokullu, E. Exosomal delivery of therapeutic modulators through the blood-brain barrier; promise and pitfalls. *Cell Biosci* **2021**, *11* (142). DOI: 10.1186/s13578-021-00650-0 From NLM.

(105) Lane, R.; Simon, T.; Vintu, M.; al., e. Cell-derived extracellular vesicles can be used as a biomarker reservoir for glioblastoma tumor subtyping. *Communications Biology* **2019**, *2*. DOI: <https://doi.org/10.1038/s42003-019-0560-x>.

(106) Macedo-Pereira, A.; Martins, C.; Lima, J.; Sarmento, B. Digging the intercellular crosstalk via extracellular vesicles: May exosomes be the drug delivery solution for target glioblastoma? *J Control Release* **2023**, *358*, 98-115. DOI: 10.1016/j.jconrel.2023.04.038 From NLM.

(107) Raposo, G.; Stoorvogel, W. Extracellular vesicles: exosomes, microvesicles, and friends. *J Cell Biol* **2013**, *200* (4), 373-383. DOI: 10.1083/jcb.201211138 From NLM.

(108) Zhu, Q.; Ling, X.; Yang, Y.; Zhang, J.; Li, Q.; Niu, X.; Hu, G.; Chen, B.; Li, H.; Wang, Y.; et al. Embryonic Stem Cells-Derived Exosomes Endowed with Targeting Properties as Chemotherapeutics Delivery Vehicles for Glioblastoma Therapy. *Advanced Science* **2019**, *6* (6). DOI: <https://doi.org/10.1002/advs.201801899>.

(109) Li, C.; Qin, S.; Wen, Y.; Zhao, W.; Huang, Y.; Liu, J. Overcoming the blood-brain barrier: Exosomes as theranostic nano carriers for precision neuroimaging. *Journal of Controlled Release* **2022**, *349*, 902-916.

(110) Huda, M. N.; Nafiujjaman, M.; Deaguero, I. G.; Okonkwo, J.; Hill, M. L.; Kim, T.; Nurunnabi, M. Potential Use of Exosomes as Diagnostic Biomarkers and in Targeted Drug Delivery: Progress in Clinical and Preclinical Applications. *ACS Biomaterials Science & Engineering* **2021**, *14* (6), 2106-2149.

(111) Xu, J.; Zhang, J.; Zhang, Z.; Gao, Z.; Qi, Y.; Qiu, W.; Pan, Z.; Guo, Q.; Li, B.; Zhao, S.; et al. Hypoxic glioma-derived exosomes promote M2-like macrophage polarization by enhancing autophagy induction. *Cell Death and Disease* **2021**, *12* (4), 1-16.

(112) Zhang, M.; Hu, S.; Liu, L.; Dang, P.; Liu, Y.; Sun, Z.; Qiao, B.; Wang, C. Engineered exosomes from different sources for cancer-targeted therapy. *Signal Transduction and Targeted Therapy* **2023**, *8* (124), 1-20.

(113) Hood, J. L.; Scott, M. J.; Wickline, S. A. Maximizing exosome colloidal stability following electroporation. *Analytical Biochemistry* **2014**, *448* (1), 41-49.

(114) Dube, T.; Kumar, N.; Bishnoi, M.; Panda, J. J. Dual Blood-Brain Barrier-Glioma Targeting Peptide-Poly(levodopamine) Hybrid Nanoplatforms as Potential Near Infrared Phototheranostic

Agents in Glioblastoma. *Bioconjug Chem* **2021**, *32* (9), 2014-2031. DOI: 10.1021/acs.bioconjchem.1c00321 From NLM.

(115) Perera, V. S.; Chen, G.; Cai, Q.; Huang, S. D. Nanoparticles of gadolinium-incorporated Prussian blue with PEG coating as an effective oral MRI contrast agent for gastrointestinal tract imaging. **2016**, *141*, 2016-2022. DOI: <https://doi.org/10.1039/c5an01873k>.

(116) Kim, T.; Lemaster, J. E.; Chen, F.; Li, J.; Jokerst, J. V. Photoacoustic Imaging of Human Mesenchymal Stem Cells Labeled with Prussian Blue–Poly(L-lysine) Nanocomplexes. *ACS Nano* **2017**, *11*, 9022-9032. DOI: 10.1021/acs.nano.7b03519.

(117) Kalashnikova, I.; Chung, S.-J.; Nafiujjaman, M.; Hill, M. L.; Siziba, M. E.; Contag, C. H.; Kim, T. Ceria-based nanotheranostic agent for rheumatoid arthritis. *Theranostics* **2020**, *10* (26), 11863-11880.

(118) Gregory, J. V.; Kadiyala, P.; Doherty, R.; *al., e.* Systemic brain tumor delivery of synthetic protein nanoparticles for glioblastoma therapy. *Nature Communications* **2020**, *11*. DOI: <https://doi.org/10.1038/s41467-020-19225-7>.

(119) Zhang, D. Y.; Dmello, C.; Chen, L.; Arrieta, V. A.; Gonzalez-Buendia, E.; Kane, J. R.; Magnusson, L. P.; Baran, A. Ultrasound-mediated Delivery of Paclitaxel for Glioma: A Comparative Study of Distribution, Toxicity, and Efficacy of Albumin-bound Versus Cremophor Formulations. *Clinical Cancer Research* **2020**, *26*, 477-486. DOI: 10.1158/1078-0432.CCR-19-2182.

(120) Gregory, J. V.; Kadiyala, P.; Doherty, R.; Cadena, M.; Habeel, S.; Ruoslahti, E.; Powenstein, P. R.; Castro, M. G.; Lahann, J. Systemic brain tumor delivery of synthetic protein nanoparticles for glioblastoma therapy. *Nature Communications* **2020**, *11*, 1-15.

(121) Xu, F.; Lu, W.; Wu, H.; Fan, L.; Gao, X.; Jiang, X. Brain delivery and systemic effect of cationic albumin conjugated PLGA nanoparticles. *Journal of Drug Delivery* **2009**, *17* (6), 423-434.

(122) Gao, H.; Xiong, Y.; Zhang, S.; Yang, Z.; Cao, S.; Jiang, X. RGD and Interleukin-13 Peptide Functionalized Nanoparticles for Enhanced Glioblastoma Cells and Neovasculature Dual Targeting Delivery and Elevated Tumor Penetration. *Molecular Pharmaceutics* **2014**, *11*. DOI: 10.1021/mp400751g.

(123) Lingasamy, P.; Tobi, A.; Kurm, K.; Kopanchuk, S.; Sudakov, A.; Salumae, M.; Ratsep, T.; Asser, T.; Bjerkvig, R.; Teesalu, T. Tumor-penetrating peptide for systemic targeting of Tenascin-C. *Scientific Reports* **2020**, *10*, 1-13.

(124) Ayo, A.; Laakkonen, P. Peptide-Based Strategies for Targeted Tumor Treatment and Imaging. *Pharmaceutics* **2021**, *13* (4), 1-31.

- (125) Ruan, H.; Chen, X.; Xie, C.; Li, B.; Ying, M.; Liu, Y.; Zhang, M.; Zhang, X.; Zhan, C.; Lu, W.; et al. Stapled RGD Peptide Enables Glioma-Targeted Drug Delivery by Overcoming Multiple Barriers. *ACS Applied Materials & Interfaces* **2017**, *9*. DOI: 10.1021/acsami.7b03682.
- (126) Ruan, H.; Chen, X.; Xie, C.; Li, B.; Ying, M.; Liu, Y.; Zhang, M.; Zhang, X.; Zhan, C.; Lu, W.; et al. Stapled RGD Peptide Enables Glioma-Targeted Drug Delivery by Overcoming Multiple Barriers. *ACS Applied Material Interfaces* **2017**, *9* (21), 17745-17756.
- (127) Hou J; Diao Y; Li W; Yang Z; Zhang L; Chen Z; Y., W. RGD peptide conjugation results in enhanced antitumor activity of PD0325901 against glioblastoma by both tumor-targeting delivery and combination therapy. *International Journal of Pharmacy* **2016**. DOI: 10.1016/j.ijpharm.2016.04.017.
- (128) Hooper, G. W.; Ansari, S.; Johnson, J. M.; Ginat, D. T. Advances in the Radiological Evaluation of and Theranostics for Glioblastoma. *Cancer* **2023**, *15* (16), 1-13.
- (129) Dumont, M. F.; Yadavilli, S.; Sze, R. W.; Nazarian, J.; Fernandes, R. Manganese-containing Prussian blue nanoparticles for imaging of pediatric brain tumors. *Int J Nanomedicine* **2014**, *9*, 2581-2595. From NLM.
- (130) Kubelick, K. P.; Emelianov, S. Y. Prussian blue nanocubes as a multimodal contrast agent for image-guided stem cell therapy of the spinal cord. *Photoacoustics* **2019**, *18*. DOI: <https://doi.org/10.1016/j.pacs.2020.100166>.
- (131) Nagaraja, T. N.; Bartlett, S.; Farmer, K. G.; Cabral, G.; Knight, R. A.; Valadie, O. G.; Brown, S. L.; Ewing, J. R.; Lee, I. Y. Adaptation of laser interstitial thermal therapy for tumor ablation under MRI monitoring in a rat orthotopic model of glioblastoma. *Acta Neurochir (Wien)* **2021**, *163* (12), 3455-3463. DOI: 10.1007/s00701-021-05002-y From NLM.
- (132) Norouzi, M.; Yathindranath, V.; Thliveris, J. A.; *al., e.* Doxorubicin-loaded iron oxide nanoparticles for glioblastoma therapy: a combinational approach for enhanced delivery of nanoparticles. *Scientific Reports* **2020**, *10*. DOI: <https://doi.org/10.1038/s41598-020-68017-y>.
- (133) Rabbi, F.; Ramani, R. *Chapter 31 - Magnetic Resonance Imaging: Anesthetic Implications*; Elsevier 2017.
- (134) Grover, V. P. B.; Tognarelli, J. M.; Crossey, M. M. E.; Cox, I. J.; Taylor-Robinson, S. D.; McPhail, M. J. W. Magnetic Resonance Imaging: Principles and Techniques: Lessons for Clinicians. *Journal of Clinical and Experimental Hepatology* **2015**, *5* (3), 246-255.
- (135) Jaiswal, M.; Gandhi, A.; Purohit, D.; Mittal, R. S. Tiger hide appearance: Impaction and prolapse of brain parenchyma through burr holes after evacuation of bilateral chronic subdural hematoma: A rare case report. *Asian Journal of Neurosurgery* **2016**, *11* (3), 1-3.

- (136) Mehdorn, H. M.; Schwartz, F.; Dawns, S.; Hedderich, J.; Dorner, L.; Nabavi, A. High-field iMRI in glioblastoma surgery: improvement of resection radically and survival for the patient? *Acta Neurochir Suppl.* **2011**, *109*, 103-106.
- (137) Berger, A. Positron emission tomography. *BMJ* **2003**, *326* (7404), 1449.
- (138) Cai, W.; Chen, X. Multimodality molecular imaging of tumor angiogenesis. *J Nucl Med* **2008**, *49 Suppl 2*, 113s-128s. DOI: 10.2967/jnumed.107.045922 From NLM.
- (139) Verger, A.; Langen, K.-J. *Chapter 9 PET Imaging in Glioblastoma: Use in Clinical Practice*; Codon Publications, 2017.
- (140) Bolcaen, J.; Acou, M.; Descamps, B.; Kersemans, K.; Deblaere, K.; Vanhove, C.; Goethals, I. *Chapter 10 PET for Therapy Response Assessment in Glioblastoma*; Codon Publications, 2017.
- (141) Davis, F.; Il'yasova, D.; Rankin, K.; McCarthy, B.; Bigner, D. D. Medical Diagnostic Radiation Exposures and Risk of Gliomas. *Radiation Research* **2011**, *175* (6), 790-796.
- (142) Abd-Elghany, A. A.; Naji, A. A.; Alonazi, B.; Aldosary, H.; Alsufayan, M. A.; Alnasser, M.; Mohammad, E. A.; Mahmoud, M. Z. Radiological characteristics of glioblastoma multiforme using CT and MRI examination. *Journal of Radiation Research and Applied Sciences* **2019**, *12* (1), 289-293.
- (143) Marquardt, R. M.; Nafiujjaman, M.; Kim, T. H.; Chung, S.-J.; Hadrick, K.; Kim, T.; Jeong, J.-W. A Mouse Model of Endometriosis with Nanoparticle Labeling for In Vivo Photoacoustic Imaging. *Reproductive Sciences* **2022**, *29* (10), 2947-2959.
- (144) Nasri, D.; Manwar, R.; Kaushik, A.; Er, E. E.; Avanaki, K. Photoacoustic imaging for investigating tumor hypoxia: a strategic assessment. *Theranostics* **2023**, *13* (10), 3346-3367. DOI: doi:10.7150/thno.84253.
- (145) Qiu, T.; Lan, Y.; Gao, W.; Zhou, M.; Liu, S.; Huang, W.; Zeng, S.; Pathak, J. L.; Yang, B.; Zhang, J. Photoacoustic imaging as a highly efficient and precise imaging strategy for the evaluation of brain diseases. *Quantitative Imaging in Medicine and Surgery* **2021**, *11* (5), 2169-2186.
- (146) Li, M.-L.; Oh, J.-T.; Xie, X.; Ku, G.; Wang, W.; Li, C.; Lungu, G.; Stoica, G.; Wang, L. V. Simultaneous Molecular and Hypoxia Imaging of Brain Tumors In Vivo Using Spectroscopic Photoacoustic Tomography. *Proceedings of the IEEE* **2022**, *96* (3).
- (147) Liu, X.; Duan, Y.; Hu, D.; Wu, M.; Chen, C.; Ghode, P. B.; Magarajah, G.; Thakor, N.; Liu, X.; Liu, C.; et al. Targeted Photoacoustic Imaging of Brain Tumor Mediated by Neutrophils Engineered with Lipid-Based Molecular Probe. *ACS Materials Lett.* **2021**, *3* (9), 1284-1290.

- (148) Zhou, B.; Jiang, B.-P.; Sun, W.; Wei, F.-M.; He, Y.; Liang, H.; Shen, X.-C. Water-Dispersible Prussian Blue Hyaluronic Acid Nanocubes with Near-Infrared Photoinduced Singlet Oxygen Production and Photothermal Activities for Cancer Theranostics. *ACS Applied Materials & Interfaces* **2018**, *10*, 18036-18049. DOI: DOI: 10.1021/acsami.8b01387.
- (149) McCracken, D. J.; Schupper, A. J.; Lakomkin, N.; Malcolm, J.; Bray, D. P.; Hadjipanayis, C. G. Turning on the light for brain tumor surgery: A 5-aminolevulinic acid story. *Neuro-Oncology* **2022**, *24*, S52-S61.
- (150) Maragkos, G. A.; Schupper, A. J.; Lakomkin, N.; Sideras, P.; Price, G.; Baron, R.; Hamilton, T.; Haider, S.; Lee, I. Y.; Hadjipanayis, C. G.; et al. Fluorescence-Guided High-Grade Glioma Surgery More Than Four Hours After 5-Amn. *Frontiers in Neurology* **2021**, *21*, 1-7.
- (151) Gregucci, F.; Surge, A.; Carbonara, R.; Laera, L.; Ciliberti, M. P.; Gentile, A. M.; Caliandro, M.; Sasso, N.; Bonaparte, I.; Fanelli, V.; et al. Radiosurgery and Stereotactic Brain Radiotherapy with Systemic Therapy in Recurrent High-Grade Gliomas: Is It Feasible? Therapeutic Strategies in Recurrent High-Grade Gliomas. *Journal of Personalized Medicine* **2022**, *12* (8), 1-12.
- (152) Barisano, G.; Bergamaschi, S.; Acharya, J.; Rajamohan, A.; Gibbs, W.; Kim, P.; Zada, G.; Chang, E.; Law, M. Complications of Radiotherapy and Radiosurgery in the Brain and Spine. *Neurographics* **2011**, *8* (3), 167-187.
- (153) Lee, Y. W.; Cho, H. J.; Lee, W. H.; Sonntag, W. E. Whole Brain Radiation-Induced Cognitive Impairment: Pathophysiological Mechanisms and Therapeutic Targets. *Biomolecules and Therapeutics* **2012**, *20* (4), 357-370.
- (154) Feng, L.; Cheng, L.; Dong, Z.; Tao, D.; Barnhart, T. E.; Cai, W.; Chen, M.; Liu, Z. Theranostic Liposomes with Hypoxia-Activated Prodrug to Effectively Destruct Hypoxic Tumors Post-Photodynamic Therapy. *ACS Nano* **2017**, *11* (1), 927-937. DOI: 10.1021/acsnano.6b07525 From NLM.
- (155) Chen, H.-M.; Teng, H.-W. The Advantage of Bevacizumab in Treating Colorectal Brain Metastasis. *Journal of Cancer Research and Practice* **2014**, *1* (2), 146-151.
- (156) Bevacizumab. Bavacizumab, Ed.; DRUGBANK online, 2005.
- (157) Diseases, N. I. o. D. a. D. a. K. *LiverTox: Clinical and Research Information on Drug-Induced Liver Injury*; 2012 - [Updated 2017].
- (158) Falchook, G. S.; Long, G. V.; Kurzrock, R.; Kim, K. B.; Arkenau, T. H.; Brown, M. P.; Hamid, O.; Infante, J. R.; Millward, M.; Pavlick, A. C.; et al. Dabrafenib in patients with melanoma, untreated brain metastases, and other solid tumors: a phase 1 dose-escalation trial. *The Lancet* **2012**, *379* (9829), 1893-1901.

- (159) Dabrafenib Mesylate. National Library of Medicine: National Library of Medicine, 2009.
- (160) Trametinib Dimethyl Sulfoxide. Sulfoxide, T. D., Ed.; National Library of Medicine: National Library of Medicine, 2011.
- (161) Medicine, N. L. o. Temozolomide. Temozolomide, Ed.; National Library of Medicine: National Library of Medicine, 2005.
- (162) Liu, Y.; Bhattarai, P.; Dai, Z.; Chen, X. Photothermal therapy and photoacoustic imaging via nanotheranostics in fighting cancer. *Chem Soc Rev* **2019**, *48* (7), 2053-2108. DOI: 10.1039/c8cs00618k From NLM.
- (163) Jin, Z.; Nguyen, K. T.; Go, G.; Kang, B.; Min, H.-K.; Kim, S.-J.; Kim, Y.; Li, H.; Kim, C.-S.; Lee, S.; et al. Multifunctional Nanorobot System for Active Therapeutic Delivery and Synergistic Chemo-photothermal Therapy. *Nano Letters* **2019**, *19* (12), 8550-8564.
- (164) Bhatt, H. N.; Pena-Zacarias, J.; Beaven, E.; Zahid, M. I.; Ahmad, S. S.; Diwan, R.; Nurunnabi, M. Potential and Progress of 2D Materials in Photomedicine for Cancer Treatment. *ACS Applied Bio Materials* **2023**, *6* (2), 365-383.
- (165) Pang, S.; Kapur, A.; Zhou, K.; Anastasiadis, P.; Ballirano, N.; Kim, A. J.; Winkles, J. A.; Woodworth, G. F.; Huang, H. C. Nanoparticle-assisted, image-guided laser interstitial thermal therapy for cancer treatment. *Wiley Interdiscip Rev Nanomed Nanobiotechnol* **2022**, *14* (5). From NLM.
- (166) Nafiujjaman, M.; Chung, S.-J.; Kalashnikova, I.; Hill, M. L.; Homa, S.; George, J.; Contag, C. H.; Kim, T. Biodegradable Hollow Manganese Silicate Nanocomposites to Alleviate Tumor Hypoxia toward Enhanced Photodynamic Therapy. *ACS Applied Biomaterials* **2020**, *3* (11), 7989-7999. DOI: 10.1021/acsbm.0c01079.
- (167) Bhatt, H. N.; Diwan, R.; Borrego, E. A.; Alberto Martinez Perez, C.; Varela-Ramirez, A.; Kumar, R.; Aguilera, R. J.; Nurunnabi, M. A Photothermal Driven Chemotherapy for the Treatment of Metastatic Melanoma. *Journal of Controlled Release* **2023**, *361*, 314-333.
- (168) Xie, X.; Gao, W.; Hao, J.; Wu, J.; Cai, X.; Zheng, Y. Self-synergistic effect of Prussian blue nanoparticles for cancer therapy: driving photothermal therapy and reducing hyperthermia-induced side effects. *Journal of Nanobiotechnology* **2021**, *19* (126). DOI: <https://doi.org/10.1186/s12951-021-00819-2>.
- (169) Correia, J. H.; Rodrigues, J. A.; Pimenta, S.; Dong, T.; Yang, Z. Photodynamic Therapy Review: Principles, Photosensitizers, Applications, and Future Directions. *Pharmaceutics* **2021**, *13* (9), 1-16.
- (170) Medicine, N. L. o. *Clinicaltrials.gov*. (accessed 2024 January 28th, 2024).

- (171) Hill, M. L.; Chung, S.-J.; Woo, H.-J.; Park, C. R.; Hadrick, K.; Nafiujjaman, M.; Kumar, P. P.; Mwangi, L.; Parikh, R.; Kim, T. Exosome-Coated Prussian Blue Nanoparticles for Specific Targeting and Treatment of Glioblastoma. *ACS Applied Materials and Interfaces* **2024**, *16* (16), 20286-20301. DOI: 10.1021/acsami.4c02364.
- (172) Altagracia-Martinez, M.; Kravzov-Jinich, J.; Martinez-Nunez, J. M.; Rios-Castaneda, C.; Lopez-Naranjo, F. Prussian Blue as an antidote for radioactive thallium and cesium poisoning. *Orphan Drugs: Research and Reviews* **2012**, *2*, 13-21.
- (173) Hodorowicz, M.; Szklarzawicz, J.; Jurowska, A. The Role of Prussian Blue-Thallium and Potassium Similarities and Differences in Crystal Structures of Selected Cyanido Complexes of W, Fe and Mo. *Materials* **2022**, *15* (13), 1-15.
- (174) Dumont, M. F.; Hoffman, H. A.; Yoon, P. R. S.; Conklin, L. S.; Saha, S. R.; Paglione, J.; Sze, R. W.; Fernandes, R. Biofunctionalized Gadolinium-Containing Prussian Blue Nanoparticles as Multimodal Molecular Imaging Agents. *ACS Bioconjugate Chemistry* **2014**, *25* (1), 129-137.
- (175) Gautam, M.; Poudel, K.; Yong, C.; Kim, J. O. Prussian blue nanoparticles: Synthesis, surface modification, and application in cancer treatment. *International Journal of Pharmaceutics* **2018**, *549* (1-2), 31-49. DOI: 10.1016/j.ijpharm.2018.07.055.
- (176) Sholouhimehr, M. Prussian Blue Nanoparticles and its Analogues as New-Generation T1-Weighted MRI Contrast Agents for Cellular Imaging. Kent State University, 2010.
- (177) Zhang, W.; Hu, S.; Yin, J.-J.; He, W.; Lu, W.; Ma, M.; Gu, N.; Zhang, Y. Prussian Blue Nanoparticles as Multienzyme Mimetics and Reactive Oxygen Species Scavengers. *Journal of the American Chemical Society* **2016**, *138*, 5860-5865. DOI: <https://doi.org/10.1021/jacs.5b12070>.
- (178) Li, W.-P.; Su, C.-H.; Tsao, L.-C.; Chang, C.-T.; Hsu, Y.-P.; Yeh, C.-S. Controllable CO Release Following Near-Infrared Light-Induced Cleavage of Iron Carbonyl Derivatized Prussian Blue Nanoparticles for CO-Assisted Synergistic Treatment. *ACS Nano* **2016**, *10* (12), 11027-11036.
- (179) Qin, Z.; Li, Y.; Gu, N. Progress in Applications of Prussian Blue Nanoparticles in Biomedicine. *Advanced Healthcare Materials* **2018**, *7* (20). DOI: <https://doi.org/10.1002/adhm.201800347>.
- (180) Braun, J. D.; Lozada, I. B.; Kolodziej, C.; Burda, C.; Newman, K. M. E.; van Lierop, J.; Davis, R. L.; Herbert, D. E. Iron(II) coordination complexes with panchromatic absorption and nanosecond charge-transfer excited state lifetimes. *Nature Chemistry* **2019**, *11*, 1144-1150.
- (181) Chen, H.; Ikeda-Saito, M.; Shaik, S. Nature of the Fe-O₂ Bonding in Oxy-Meyoglobin: Effect of the Protein. *Journal of the American Chemical Society* **2008**, *130* (44), 14778-14790.

- (182) Jing, L.; Shao, S.; Wang, Y.; Yang, Y.; Yue, X.; Dai, Z. Hyaluronic Acid Modified Hollow Prussian Blue Nanoparticles Loading 10-hydroxycamptothecin for Targeting Thermochemotherapy of Cancer. *Theranostics* **2016**, *6*, 40-53. DOI: 10.7150/thno.13250.
- (183) Guichard, C.; Ho, A.-S. L.; Williams, H. Prussian Blue: Chemistry, Commerce, and Colour in Eighteenth-Century Paris. *Art History* **2023**, *46* (1), 154-186.
- (184) Morrison, J. O.; Chatham, N. J.; Perkins, B. H. *Manufacture of Iron Blue Pigments*. United States 1952.
- (185) Credo, R.; Burzcyk, L.; Schluter, E. *Process for the production of directly precipitated milori blue*. United Kingdom 1962.
- (186) Lim, C. Q. X.; Tan, Z.-K. Prussian White with Near-Maximum Specific Capacity in Sodium-Ion Batteries. *ACS Applied Energy Materials* **2021**, *4* (6), 6214-6220.
- (187) Li, F.; Ma, D.; Qian, J.; Yang, B.; Xu, Z.; Li, D.; Wu, Z.; Wang, J. One-step hydrothermal growth and electrochromic properties of highly stable Prussian green film and device. *Solar Energy Materials and Solar Cells* **2019**, *192*, 103-108.
- (188) IAEA. *The use of Prussian Blue to reduce radiocesium contamination of milk and meat produced on territories affected by the Chernobyl accident*. (IAEA), I. A. E. A., Ed.; IAEA: IAEA, Vienna, 1997.
- (189) Aaseth, J.; Nurchi, V. M.; Andersen, O. Medical Therapy of Patients Contaminated with Radioactive Cesium or Iodine. *Biomolecules* **2019**, *9* (12), 1-10.
- (190) Carniato, F.; Gatti, G.; Vittoni, C.; Katsev, A. M.; Guidotti, M.; Evangelisti, C.; Bisio, C. More Efficient Prussian Blue Nanoparticles for an Improved Caesium Decontamination from Aqueous Solutions and Biological Fluids. *Molecules* **2020**, *25* (15), 1-16.
- (191) *Prussian Blue*. 2005. (accessed 2024 January 27).
- (192) *Radiation Emergencies*. Services, D. o. H. a. H., Ed.; 2004; p 2.
- (193) Gao, X.; Wang, Q.; Cheng, C.; Lin, S.; Lin, T.; Liu, C.; Han, X. The Application of Prussian Blue Nanoparticles in Tumor Diagnosis and Treatment. *Sensors* **2020**, *20*, 6905. DOI: <https://doi.org/10.3390/s20236905>.
- (194) Hoffman, H. A.; Chakrabarti, L.; Dumont, M. F.; Sandler, A. D.; Fernandes, R. Prussian Blue Nanoparticles for Laser-Induced Photothermal Therapy of Tumors. *RSC Advances* **2014**, *4* (56), 29729-29734.

- (195) Liu R; Sang L; Wang T; Liu Y; Wang Z; Li J; D., W. Phase-change mesoporous Prussian blue nanoparticles for loading paclitaxel and chemo-photothermal therapy of cancer. *Colloids Surfaces B Biointerfaces* **2021**, 207. DOI: 10.1016/j.colsurfb.2021.112018.
- (196) Tao, Q.; He, G.; Ye, S.; Zhang, D.; Zhang, Z.; Qi, L.; Liu, R. Mn Doped Prussian Blue nanoparticles for T₁/T₂ MR imaging, PA imaging and Fenton reaction enhanced mild temperature photo thermal therapy of tumor. *Journal of Nanobiotechnology* **2022**, 20, 1-14.
- (197) Wang, H.; Shen, Y.; Chen, L.; Li, K.; Shi, Y.; Xu, Z.; Li, D.; Chen, H.; Wang, W.; Gao, L. Enhancing catalase-like activity of Prussian Blue nanozyme by gadolinium-doping for imaging-guided anti tumor amplification via photodynamic therapy and chemotherapy. *Materials Today Nano* **2023**, 22, 1-14.
- (198) Xu, Y.; Zhang, Y.; Cai, X.; Gao, W.; Tang, X.; Chen, Y.; Chen, J.; Chen, L.; Tian, Q.; Yang, S.; et al. Large-scale synthesis of mono disperse Prussian Blue nanoparticles for cancer theranostics via an "in situ modification" strategy. *International Journal of Nanomedicine* **2019**, 14, 271-288.
- (199) Huang, P.; Lin, J.; Li, W.; Rong, P.; Wang, Z.; Wang, S.; Wang, X.; Sun, X.; Aronova, M.; Niu, G.; et al. Biodegradable gold nanovesicles with an ultrastrong plasmonic coupling effect for photoacoustic imaging and photothermal therapy. *Angew Chem Int Ed Engl* **2013**, 52 (52), 13958-13964. DOI: 10.1002/anie.201308986 From NLM.
- (200) Li, L.; Nurunnabi; Nafiujjaman; Lee, Y. K.; Huh, K. M. GSH-mediated photoactivity of pheophorbide a-conjugated heparin/gold nanoparticle for photodynamic therapy. *J Control Release* **2013**, 171 (2), 241-250. DOI: 10.1016/j.jconrel.2013.07.002 From NLM.
- (201) Chen, J.; Gong, M.; Fan, Y.; Feng, J.; Han, L.; Xin, H. L.; Cao, M.; Zhang, Q.; Zhang, D.; Lei, D.; et al. Collective Plasmon Coupling in Gold Nanoparticle Clusters for Highly Efficient Photothermal Therapy. *ACS Nano* **2022**, 16 (1), 910-920.
- (202) Fu, G.; Liu, W.; Li, Y.; Jin, Y.; Jiang, L.; Liang, X.; Feng, S.; Dai, Z. Magnetic Prussian Blue Nanoparticles for Targeted Photothermal Therapy under Magnetic Resonance Imaging Guidance. *ACS Bioconjugate Chemistry* **2014**, 25 (9), 1655-1663.
- (203) Luo, L.; Qin, B.; Jiang, M.; Xie, L.; Luo, Z.; Gus, X.; Zhang, J.; Li, X.; Zhu, C.; Du, Y.; et al. Regulating immune memory and reversing tumor thermotolerance through a step-by-step starving-photothermal therapy. *Journal of Nanobiotechnology* **2021**, 19 (297), 1-18.
- (204) Melamed, J. R.; Edelstein, R. S.; Day, E. S. Elucidating the fundamental mechanisms of cell death triggered by photothermal therapy. *ACS Nano* **2015**, 9 (1), 6-11.
- (205) Lu, L.; Zhang, C.; Zou, B.; Wang, Y. Hollow Prussian Blue Nanospheres for Photothermal/Chemo-Synergistic Therapy. *International Journal of Nanomedicine* **2020**, 15, 5165-5177.

- (206) Cohen, S. R.; Plane, R. A. The Association of Ferrocyanide Ions with Various Cations. *ACS Journal of Physical Chemistry* **1957**, *61* (8), 1096-1100.
- (207) Wei, Y.; Zheng, M.; Zhu, W.; Pang, H. Hollow structures Prussian Blue, its analogs, and their derivatives: Synthesis and electrochemical energy-related applications. *Carbon Neutralization* **2023**, *2* (3), 271-299.
- (208) Rahman, M. Magnetic Resonance Imaging and Iron-oxide Nanoparticles in the era of Personalized Medicine. *Nanotheranostics* **2023**, *7* (4), 424-449.
- (209) Wahajuddin; Arora, S. Superparamagnetic iron oxide nanoparticles: magnetic nanoplatforms as drug carriers *International Journal of Nanomedicine* **2012**, *7*, 3445-3471.
- (210) Zhu, W.; Liu, K.; Sun, X.; Wang, X.; Li, Y.; Cheng, L.; Liu, Z. Mn²⁺-Doped Prussian Blue Nanotubes for Bimodal Imaging and Photothermal Therapy with Enhanced Performance. *ACS Applied Material Interfaces* **2015**, *7* (21), 11575-11582.
- (211) Pan, D.; Schmieder, A. H.; Wickline, S. A.; Lanza, G., M., Manganese-based MRI contrast agents: past, present, and future. *Tetrahedron* **2011**, *67* (44), 8431-8444.
- (212) Liang, X.; Deng, Z.; Jing, L.; Li, X.; Dai, Z.; Li, C.; Huang, M. Prussian Blue nanoparticles operate as a contrast agent for enhanced photoacoustic imaging. *Chemical Communications* **2013**, *94*, 11029-11031.
- (213) Cai, X.; Gao, W.; Zhang, L.; Ma, M.; Liu, T.; Du, W.; Zheng, Y.; Chen, H.; Shi, J. Enabling Prussian Blue with Tunable Localized Surface Plasmon Resonances: Simultaneously Enhanced Dual-Mode Imaging and Tumor Photothermal Therapy. *ACS Nano* **2016**, *10* (12), 11115-11126.
- (214) Dehaini, D.; Wei, X.; Fang, R. H.; Masson, S.; Angsantikul, P.; Luk, B. T.; Zhang, Y.; Ying, M.; Jiang, Y.; Kroll, A. V.; et al. Erythrocyte-Platelet Hybrid Membrane Coating for Enhanced Nanoparticle Functionalization. *Adv Mater* **2017**, *29* (16). DOI: 10.1002/adma.201606209 From NLM.
- (215) Fang, R. H.; Kroll, A. V.; Gao, W.; Zhang, L. Cell Membrane Coating Nanotechnology. *Adv Mater* **2018**, *30* (23). DOI: 10.1002/adma.201706759 From NLM.
- (216) Hu, C. M.; Zhang, L.; Aryal, S.; Cheung, C.; Fang, R. H. Erythrocyte membrane-camouflaged polymeric nanoparticles as a biomimetic delivery platform. *Proc Natl Acad Sci U S A* **2011**, *108* (27), 10980-10985. DOI: 10.1073/pnas.1106634108 From NLM.
- (217) Hu, C. M.; Fang, R. H.; Wang, K. C.; Luk, B. T.; Thamphiwatana, S.; Dehaini, D.; Nguyen, P.; Angsantikul, P.; Wen, C. H.; Kroll, A. V.; et al. Nanoparticle biointerfacing by platelet membrane cloaking. *Nature* **2015**, *526* (7571), 118-121. DOI: 10.1038/nature15373 From NLM.

- (218) Zhang, Q.; Dehaini, D.; Zhang, Y.; Zhou, J.; Chen, X.; Zhang, L.; Fang, R. H.; Gao, W. Neutrophil membrane-coated nanoparticles inhibit synovial inflammation and alleviate joint damage in inflammatory arthritis. *Nat Nanotechnol* **2018**, *13* (12), 1182-1190. DOI: 10.1038/s41565-018-0254-4 From NLM.
- (219) Hu, C.-M. J.; Fang, R. H.; Cops, J.; Luk, B. T.; Zhang, L. A biomimetic nano sponge that absorbs pore-forming toxins. *Nature Nanotechnology* **2013**, *8*, 336-340.
- (220) Zhang, F.; Zhuang, J.; Li, Z.; Gong, H.; de Avila, B. E.-F.; Duan, Y.; Zhang, Q.; Zhou, J.; Yin, L.; Kkarshalev, E.; et al. Nanoparticle-modified micro robots for in vivo antibiotic delivery to treat acute bacterial pneumonia. *Nature Materials* **2022**, *21*, 1324-1332.
- (221) Krishnan, N.; Fang, R. H.; Zhang, L. Cell membrane-coated nanoparticles for the treatment of cancer. *Clinical and Translational Medicine* **2023**, *13* (6), 1-3.
- (222) Liu, L.; Martikainen, M.-V.; Karlund, A.; Roponen, M.; Xu, W.; Hu, G.; Tasciotti, E.; Lehto, V.-P. Cell membrane coating integrity affects the internalization mechanism of biomimetic nanoparticles. *Nature Communications* **2021**, *12*, 1-12.
- (223) Nica, V.; Marino, A.; Pucci, C.; Sen, O.; Emanet, M.; De Pasquale, D.; Carmignani, A.; Petretto, A.; Bartolucci, M.; Lauciello, S.; et al. Cell-Membrane-Coated and Cell-Penetrating Peptide-Conjugated Trimagnetic Nanoparticles for Targeted Magnetic Hyperthermia of Prostate Cancer Cells. *ACS Applied Materials and Interfaces* **2023**, *15* (25), 30008-30028.
- (224) Ketch, N. A.; Ma, R.; Liu, Y.; Buch, S.; Hu, G. Extracellular Vesicle-Mediated Delivery of Ultrasmall Superparamagnetic Iron Oxide Nanoparticles to Mice Brain. *Frontiers in Pharmacology* **2022**, *13*, 1-9.
- (225) Nikoobakht, B.; El-Sayed, M. A. Preparation and Growth Mechanism of Gold Nanorods (NRs) Using Seed-Mediated Growth Method. *Chem. Mater.* **2003**, *15*, 1957-1962.
- (226) Ivics, Z.; Hackett, P. B.; Plasterk, R. H.; Izsvák, Z. Molecular reconstruction of Sleeping Beauty, a Tc1-like transposon from fish, and its transposition in human cells. *Cell* **1997**, *91* (4), 501-510. DOI: 10.1016/s0092-8674(00)80436-5 From NLM.
- (227) Zhuang, M.; Chen, X.; Du, D.; Shi, J.; Deng, M.; Long, Q.; Yin, X.; Wang, Y.; Rao, L. SPION decorated exosome delivery of TNF-alpha to cancer cell membranes through magnetism. *Nanoscale* **2020**, *12* (1), 173-188. DOI: DOI<https://doi.org/10.1039/C9NR05865F>.
- (228) Mulcahy, L. A.; Pink, R. C.; Carter, D. R. Routes and mechanisms of extracellular vesicle uptake. *J Extracell Vesicles* **2014**, *3*. From NLM.
- (229) Midekessa, G.; Godakumara, K.; Ord, J.; Viil, J.; Lättেকivi, F.; Dissanayake, K.; Kopanchuk, S.; Rinken, A.; Andronowska, A.; Bhattacharjee, S.; et al. Zeta Potential of Extracellular Vesicles:

Toward Understanding the Attributes that Determine Colloidal Stability. *ACS Omega* **2020**, *5* (27), 16701-16710. From NLM.

(230) Ma, M.; Liu, Z.; Gao, N.; Pi, Z.; Du, X.; Ren, J.; Qu, X. Self-Protecting Biomimetic Nanozyme for Selective and Synergistic Clearance of Peripheral Amyloid- β in an Alzheimer's Disease Model. *Journal of the American Chemical Society* **2020**, *142*, 21702-21711.

(231) Butterick, T. A.; Duffy, C. M.; Lee, R. E.; Billington, C. J.; Kotz, C. M.; Nixon, J. P. Use of a caspase multiplexing assay to determine apoptosis in a hypothalamic cell model. *J Vis Exp* **2014**, (86). DOI: 10.3791/51305 From NLM.

(232) Smith, M. H.; Fork, R. L.; Cole, S. T. Safe Delivery of Optical Power From Space. *Optics Express* **2001**, *8* (10), 537-546.

(233) Baumann, B. C.; Dorsey, J. F.; Benci, J. L.; Joh, D. Y.; Kao, G. D. Stereotactic Intracranial Implantation and In vivo Bioluminescent Imaging of Tumor Xenografts in a Mouse Model System of Glioblastoma Multiforme. *Journal of Visualized Experiments* **2012**, *25* (67). DOI: 10.3791/4089.

(234) Neuschmelting, V.; Harmsen, S.; Beziere, N.; Lockau, H.; Hsu, H.-T.; Huang, R.; Razansky, D.; Ntziachristos, B.; Kircher, M. F. Dual-Modality Surface-Enhanced Resonance Raman Scattering and Multispectral Optoacoustic Tomography Nanoparticle Approach for Brain Tumor Delineation. *Small* **2018**, *14* (23). DOI: <https://doi.org/10.1002/smll.201800740>.

(235) Chen, Y.; Wu, L.; Wang, Q.; Wu, M.; Xu, B.; Liu, X.; Liu, J. Toxicological Evaluation of Prussian Blue Nanoparticles After Short Exposure of Mice. *Human & Experimental Toxicology* **2016**, *35*, 1123-1132.

(236) Cormode, D. P.; Gao, L.; Koo, H. Emerging Biomedical Applications of Enzyme-Like Catalytic Nanomaterials. *Trends Biotechnol* **2018**, *36* (1), 15-29. DOI: 10.1016/j.tibtech.2017.09.006 From NLM.

(237) Ahmadi, S.; Rahimizadeh, K.; Shafiee, A.; Rabiee, N.; Slavish, I. Nanozymes and their emerging applications in biomedicine. *Process Biochemistry* **2023**, *131*, 154-174.

(238) Hou, M.; Wang, L.; Wang, Y.; Chen, Y.; Shi, J. Nanocatalytic Tumor Therapy by Single-Atom Catalysis. *ACS Nano* **2019**, *13* (2), 2643-2653.

(239) Xu, B.; Cui, Y.; Wang, W.; Li, S.; Lyu, C.; Wang, S.; Bao, W.; Wang, H.; Qin, M.; Liu, Z.; et al. Immunomodulation-Enhanced Nanozyme-Based Tumor Catalytic Therapy. *Advanced Materials* **2020**, *32* (33), 1-10.

(240) Wittmann, C.; Shockley, P.; Singh, S. K.; Pase, L.; Lieschke, G. J.; Grabher, C. Hydrogen Peroxide in Inflammation: Messenger, Guide, and Assassin. *Advances in Hematology* **2012**, 1-6.

- (241) Estelrich, J.; Busquets, M. A. Prussian Blue: A Nanozyme with Versatile Catalytic Properties. *International Journal of Molecular Sciences* **2021**, *22* (11), 1-16.
- (242) Sayin, V. I.; Ibrahim, M. X.; Larsson, E.; Nilsson, J. A.; Lindahl, P.; Bergo, M. O. Antioxidants Accelerate Lung Cancer Progression in Mice. *Science Translational Medicine* **2014**, *6* (221), 1-8.
- (243) Piskounova, E.; Agathocleous, M.; Murphy, M. M.; Hu, Z.; Huddleston, S. E.; Zhao, Z.; Leitch, A. M.; Johnson, T. M.; DeBerardinis, R. J.; Morrison, S. J. Oxidative stress inhibits distant metastasis by human melanoma cells. *Nature* **2015**, *527*, 186-191.
- (244) Beckhauser, T. F.; Francis-Oliveira, J.; De Pasquale, R. Reactive Oxygen Species: Physiological and Physiopathological Effects on Synaptic Plasticity. *Journal of Experimental Neuroscience* **2016**, *10*, 23-48.
- (245) Yang, S.; Lian, G. ROS and diseases: role in metabolism and energy supply. *Molecular and Cellular Biochemistry* **2020**, *467*, 1-12.
- (246) Sivak-Sears, N. R.; Schwartzbaum, J. A.; Mike, R.; Moghadassi, M.; Wrench, M. Case-Control Study of Use of Nonsteroidal Antiinflammatory Drugs and Glioblastoma Multiforme. *American Journal of Epidemiology* **2004**, *159* (12), 1131-1139.
- (247) Zhang, T.; Yang, X.; Liu, P.; Zhou, J.; Lou, J.; Wang, H.; Li, A.; Zhou, Y. Association between non steroidal anti-inflammatory drugs use and risk of central nervous system tumors: a dose-responsive meta analysis. *Oncotarget* **2017**, *8*, 102486-102498.
- (248) Gao, C.; Lyu, F.; Yin, Y. Encapsulated Metal Nanoparticles for Catalysis. *Chem Rev* **2021**, *121* (2), 834-881. DOI: 10.1021/acs.chemrev.0c00237 From NLM.
- (249) Jiang, D.; Ni, D.; Rosenkrans, Z. T.; Huang, P.; Yan, X.; Cai, W. Nanozyme: new horizons for responsive biomedical applications. *Chem Soc Rev* **2019**, *48* (14), 3683-3704. DOI: 10.1039/c8cs00718g From NLM.
- (250) Muz, B.; de la Puente, P.; Azab, F.; Azab, A. K. The role of hypoxia in cancer progression, angiogenesis, metastasis, and resistance to therapy. *Hypoxia* **2015**, *3*, 83-92.
- (251) Park, J. H.; Lee, H. K. Current Understanding of Hypoxia in Glioblastoma Multiforme and Its Response to Immunotherapy. *Cancers* **2022**, *14* (5), 1-20.
- (252) Monteiro, A. R.; Hill, R.; Pilkington, G. J.; Madureira, P. A. The Role of Hypoxia in Glioblastoma Invasion. *Cells* **2017**, *6* (4), 1-24.
- (253) Rich, L. J.; Seshadri, M. Photoacoustic monitoring of tumor and normal tissue response to radiation. *Scientific Reports* **2016**, *6*, 1-10.

- (254) Gomes, J. R. B.; Gomes, J. A. N. F.; Illas, F. Methoxy radical reaction to formaldehyde on clean and hydroxy radical-covered copper (111) surfaces: a density functional theory study. *Surface Science* **1999**, *443* (3), 165-176.
- (255) Aljama, H.; Yoo, J. S.; Norskov, J. K.; Abild-Pedersen, F.; Study, F. Methanol partial oxidation on Ag(111) from first principles. *Chem Cat Chem* **2016**, *8* (23).
- (256) Lehoczy, L. Purpald Reagent to Enhance Surface Plasmon Resonance Imaging Toward Sensing of Formaldehyde. Oklahoma State University, 2016.
- (257) Granger, E.; Boturyn, D.; Dumy, P. Tumor targeting with RGD peptide ligands-design of new molecular conjugates for imaging and therapy of cancers. *Anti-Cancer Agents in Medicinal Chemistry* **2007**, 552-558.
- (258) Wang, L.; Wang, N.; Zhang, W.; Cheng, X.; Yan, Z.; Shah, G.; Wang, X.; Wang, R.; Fu, C. Therapeutic peptides: current applications and future directions. *Signal Transduction and Targeted Therapy* **2022**, *7*, 1-27.
- (259) Sanati, M.; Afshari, A. R.; Aminyavari, S.; Kesharwani, P.; Jamialahmadi, T.; Sahebkar, A. RGD-engineered nanoparticles as an innovative drug delivery system in cancer therapy. *Journal of Drug Delivery Science and Technology* **2023**, *84*, 1-18.
- (260) Vogetseder, A.; Thies, S.; Ingold, B.; Roth, P.; Weller, M.; Schraml, P.; Goodman, S. L.; Moch, H. α v-Integrin isoform expression in primary human tumors and brain metastases. *International Journal of Cancer* **2013**, *133*, 2362-2371.
- (261) Valdembri, D.; Serini, G. The roles of integrins in cancer. *Faculty Reviews* **2021**, *10* (45).
- (262) Liu, Z.; Wang, F.; Chen, X. Integrin $\alpha_v\beta_3$ -Targeted Cancer Therapy. *Drug Development Research* **2010**, *69* (6), 329-339.
- (263) Neiberler, M.; Reuning, U.; Reichart, F.; Notni, J.; Wester, H.-J.; Schwaiger, M.; Weinmuller, M.; Rader, A.; Steiger, K.; Kessler, H. Exploring the Role of RGD-Recognizing Integrins in Cancer. *Cancers* **2017**, *9* (9), 1-33.
- (264) Reed, N. I.; Jo, H.; Chen, C.; Tsujino, K.; Arnold, T. D.; DeGrado, W. F.; Sheppard, D. The $\alpha_v\beta_1$ integrin plays a critical in vivo role in tissue fibrosis. *Science Translational Medicine* **2015**, *7* (288), 1-8.
- (265) Yokosaki, Y.; Nishimichi, N. New Therapeutic Targets for Hepatic Fibrosis in the Integrin Family, $\alpha_8\beta_1$ and $\alpha_{11}\beta_1$ Induced Specifically on Activated Stellate Cells. *International Journal of Molecular Sciences* **2021**, *22* (23), 1-18.

- (266) Zovein, A. C.; Luque, A.; Turlo, K. A.; Hofmann, J. J.; Yes, K. M.; Becker, M. S.; Fassler, R.; Mellman, I.; Lane, T. F.; Iruela-Arispe, M. L. β 1 Integrin Establishes Endothelial Cell Polarity and Arteriolar Lumen Formation via a Par3-Dependent Mechanism. *Developmental Cell* **2010**, *18*, 39-51.
- (267) Sloan, E. K.; Pouliot, N.; Stanley, K. L.; Chia, J.; Moseley, J. M.; Hards, D. K.; Anderson, R. L. Tumor-Specific expression of avb3 integral promotes spontaneous metastasis of great cancer to bone. *Breast Cancer Research* **2006**, *8* (2), 1-14.
- (268) Lee, S.-N.; Ahn, J.-S.; Lee, S. G.; Lee, H.-S.; Choi, A. M. K.; Yoon, J.-H. Integrins avb5 and avb6 Mediate IL-4-induced Collective Migration in Human Airway Epithelial Cells. *American Journal of Respiratory Cell and Molecular Biology* **2019**, *60* (4), 420-433.
- (269) Bandyopadhyay, A.; Raghavan, S. Defining the Role of Integrin avb6 in Cancer. *Current Drug Targets* **2009**, *10* (7), 645-652.
- (270) Meecham, A.; Cutmore, L. C.; Protopapa, P.; Rigby, L. G.; Marshall, J. F. Ligand-bound integral avb6 internalisation and trafficking. *Frontiers in Cell Developmental Biology* **2022**, *10*, 1-18.
- (271) Gianni, T.; Salvioli, S.; Chesnokova, L. S.; Hutt-Fletcher, L. M.; Campadelli-Fiume, G. avb6- and avb8-Integrins Serve As Interchangeable Receptors for HSV gH/gL to Promote Endocytosis and Activation of Membrane Fusion. *PLOS Pathogens* **2013**, *9* (12), 1-14.
- (272) Fenton, T. M.; Kelly, A.; Shuttleworth, E. E.; Smedley, C.; Atakilit, A.; Powrie, F.; Campbell, S.; Nishimura, S. L.; Sheppard, D.; Levison, S.; et al. Inflammatory cues enhance TGF β activation by distinct subsets of human intestinal dendritic cells via integral avb8. *Mucosal Immunology* **2017**, *10*, 624-634.
- (273) Schumacher, S.; Dedden, D.; Nunez, R. V.; Matoba, K.; Takagi, J.; Biertumpfel, C.; Mizuno, N. Structural insights into integral $\alpha_5\beta_1$ opening by fibronectin ligand. *Science Advances* **2021**, *7* (19), 1-17.
- (274) Muller, U.; Wang, D.; Dendra, S.; Meneses, J. J.; Pedersen, R. A.; Reichardt, L. F. Integrin $\alpha_8\beta_1$ Is Critically Important for Epithelial-Mesenchymal Interactions during Kidney Morphogenesis. *Cell* **1997**, *88* (5), 603-613.
- (275) Khalifeh-Soltani, A.; Gupta, D.; Ha, A.; Podolsky, M. J.; Datta, R.; Ataxia, K. The Mfge8- $\alpha_8\beta_1$ -PTEN pathway regulates airway smooth muscle contraction in allergic inflammation. *The FASEB Journal* **2018**, *32*, 5927-5936.
- (276) Lu, M.; Munger, J. S.; Steadele, M.; Busald, C.; Tellier, M.; Schnapp, L. M. Integrin $\alpha_8\beta_1$ mediates adhesion to LAP-TGF β 1. *Journal of Cell Science* **2002**, *1* (115), 4641-4648.

- (277) Bennett, J. S. Structure and function of the platelet integral $\alpha_{IIb}\beta_3$. *The Journal of Clinical Investigation* **2005**, *115* (12), 3363-3369.
- (278) Huang, J.; Li, X.; Shi, X.; Zhu, M.; Wang, J.; Huang, S.; Huang, X.; Wang, H.; Li, L.; Deng, H.; et al. Platelet integral $\alpha_{IIb}\beta_3$: signal transduction, regulation, and its therapeutic targeting. *Journal of Hematology and Oncology* **2019**, *12* (26), 1-22.
- (279) Parrasia, S.; Szabo, I.; Zoratti, M.; Biasutto, L. Peptides as Pharmacological Carriers to the Brain: Promises, Shortcomings and Challenges. *Molecular Pharmaceutics* **2022**, *19* (11), 3700-3729.
- (280) Weller, M.; Nabors, L. B.; Gorlia, T.; Leske, H.; Rushing, E.; Bady, P.; Hicking, C.; Perry, J.; Hong, Y.-K.; Roth, P.; et al. Cilengitide in newly diagnosed glioblastoma: biomarker expression and outcome. *Oncotarget* **2016**, *7* (12), 15018-15032.
- (281) Malric, L.; Monferran, S.; Gilhodes, J.; Boyrie, S.; Dahan, P.; Skuli, N.; Sesen, J.; Filleron, T.; Kowalski-Chauvel, A.; Moyal, E. C.-J.; et al. Interest of integrins targeting in glioblastoma according to tumor heterogeneity and cancer stem cell paradigm: an update. *Oncotarget* **2017**, *8* (49), 86947-86968.
- (282) Wu, P.-H.; Onodera, Y.; Ichikawa, Y.; Rankin, E. B.; Giaccia, A. J.; Watanabe, Y.; Qian, W.; Hashimoto, T.; Shirato, H.; Nam, J.-M. Targeting integrins with RGD-conjugated gold nanoparticles in radiotherapy decreases the invasive activity of breast cancer cells. *International Journal of Nanomedicine* **2017**, *14* (12), 5069-5085.
- (283) Han, H. S.; Choi, K. I. Advances in Nanomaterial-Mediated Photothermal Cancer Therapies: Toward Clinical Applications. *Biomedicines* **2021**, *9* (3). DOI: <https://doi.org/10.3390/biomedicines9030305>.
- (284) Overchuk, M.; Weersink, R. A.; Wilson, B. C.; Zheng, G. Photodynamic and Photothermal Therapies: Synergy Opportunities for Nanomedicine. *ACS Nano* **2023**, *17* (9), 7979-8003.
- (285) Jiang, Y.; Upputuri, P. K.; Xie, C.; Lyu, Y.; Zhang, L.; Xiong, Q.; Pramanik, M.; Pu, K. Broadband Absorbing Semiconducting Polymer Nanoparticles for Photoacoustic Imaging in Second Near-Infrared Window. *Nano Lett* **2017**, *17* (8), 4964-4969. DOI: 10.1021/acs.nanolett.7b02106 From NLM.
- (286) Zhang, Y.; Zhang, S.; Zhang, Z.; Ji, L.; Zhang, J.; Wang, Q.; Guo, T.; Ni, S.; Cai, R.; Mu, X.; et al. Recent Progress on NIR-II Photothermal Therapy. *Frontiers in Chemistry* **2021**, *9*, 1-26.
- (287) Fu, G.; Liu, W.; Li, Y.; Jin, Y.; Jiang, L.; Liang, X.; Feng, S.; Dai, Z. Magnetic Prussian Blue Nanoparticles for Targeted Photothermal Therapy under Magnetic Resonance Imaging Guidance. *ACS Bioconjugate Chemistry* **2014**, *25* (9), 1655-1663.

- (288) Lerner, E. C.; Edwards, R. M.; Wilkinson, D. S.; Fecci, P. E. Laser ablation: Heating up the anti-tumor response in the intracranial compartment. *Adv Drug Deliv Rev* **2022**, *185*. DOI: 10.1016/j.addr.2022.114311 From NLM.
- (289) Srinivasan, E. S.; Liu, Y.; Odion, R. A.; Chongsatthidkiet, P.; Wachsmuth, L. P.; Haskell-Mendoza, A. P.; Edwards, R. M.; Canning, A. J.; Willoughby, G.; Hinton, J.; et al. Gold Nanostars Obviate Limitations to Laser Interstitial Thermal Therapy (LITT) for the Treatment of Intracranial Tumors. *Clinical Cancer Research* **2023**, *29* (16), 3214-3224.
- (290) Kircher, M. F.; Zerda, A. d. I.; Jokerst, J. V.; Zavaleta, C. L.; Kempen, P. J.; Mitra, E.; Pitter, K.; Huang, R.; Campos, C.; Habte, F.; et al. A brain tumor molecular imaging strategy using a new triple-modality MRI-photoacoustic-Raman nanoparticle. *Nature Medicine* **2012**, *18*, 829-834.
- (291) Iyad, N.; Ahmad, M. S.; Alkhatib, S. G.; Hjouj, M. Gadolinium contrast agents- challenges and opportunities of a multidisciplinary approach: Literature Review. *European Journal of Radiology Open* **2023**, *11*, 1-10.
- (292) Tchounwou, P. B.; Yedjou, C. G.; Patella, A. K.; Sutton, D. J. *Heavy Metals Toxicity and the Environment*; Springer, Basel, **2012**.
- (293) Shen, Y.; Goerner, F. L.; Snyder, C.; Morelli, J. N.; Hao, D.; Hu, D.; Li, X.; Runge, V. M. T1 Relativities of Gadolinium-Based Magnetic Resonance Contrast Agents in Human Whole Blood at 1.5, 3, and 7T. *Investigative Radiology* **2015**, *50* (5), 330-338.
- (294) Kar, R.; Dhar, R.; Mukherjee, S.; Nag, S.; Gorai, S.; Mukerjee, N.; Mukherjee, D.; Vatsa, R.; Chandrakanth Jadhav, M.; Ghosh, A.; et al. Exosome-Based Smart Drug Delivery Tool for Cancer Theranostics. *ACS Biomater Sci Eng* **2023**, *9* (2), 577-594. From NLM.
- (295) Srivastava, A.; Rathore, S.; Munshi, A.; Ramesh, R. Organically derived exosomes as carriers of anticancer drugs and imaging agents for cancer treatment. *Semin Cancer Biol* **2022**, *86* (Pt 1), 80-100. DOI: 10.1016/j.semcancer.2022.02.020 From NLM.

APPENDIX

Notable Awards, Presentations, and Publications

Awards

- Outstanding Graduate Student Award – 2024 Michigan State University College of Engineering
- WMIC WIMIN Scholar Award – 2023 WMIC Annual Conference, Prague, Czech Republic, September 2023
- WMIC NIH Travel Award – 2023 WMIC Annual Conference, Prague, Czech Republic, September 2023
- 1st Place 5-minute Oral Presentation – 2023 Michigan State University Nanomedicine Symposium, June 2023
- Michigan State University Board of Trustees Oral Presentation – May 2023
- 1st Place 3-minute Thesis Competition – 2023 Michigan State University 3-Minute Thesis Competition, April 2023
- Dissertation Completion Fellowship – Michigan State University, January 2023
- Academic Achievement Withrow Fellowship Award – Michigan State University, September 2022

Presentations

1. **Hill, M.L.**, S-J. Chung, H-J. Woo, K. Hadrick, L. Mwangi, R. Parikh, and T. Kim (2023). “Biomimetic Phototheranostic Nanoparticles for Specific Targeting and Treatment of Glioblastoma.” 2023 Biomedical Engineering Society Annual Meeting. Seattle, Washington. Poster.
2. **Hill, M.L.**, S-J. Chung, H-J. Woo, K. Hadrick, L. Mwangi, R. Parikh, and T. Kim (2023). “Specific Targeting of Biomimetic Prussian Blue Nanoparticles using Photoacoustic Imaging for Early Glioblastoma Detection.” 2023 World Molecular Imaging Conference. Prague, Czech Republic. Oral Presentation.
3. **Hill, M.L.**, S-J. Chung, K. Hadrick, R. Parikh, L. Mwangi, H-J. Woo, and T. Kim (2023). “Phototheranostic Effects of Extracellular Vesicle-Coated Nanoparticles for Glioblastoma Treatment.” 2023 Michigan State University Nanomedicine Symposium. East Lansing, Michigan. Oral Presentation.

4. **Hill, M.L.**, S-J. Chung, K. Hadrack, R. Parikh, L. Mwangi, H-J. Woo, and T. Kim (2023). "Engineered Nanoparticles for Effective Brain Cancer Detection and Treatment." Michigan State University Board of Trustees Semester Meeting. East Lansing, Michigan. Oral Presentation.

Link to Presentation: <https://www.youtube.com/watch?v=993B9JBiTBA>

5. **Hill, M.L.** (2023). "Improving Brain Cancer Outcomes Using Engineering Nanoparticles." Midwestern Association of Graduate Schools Regional 3-Minute Thesis Competition. Chicago, Illinois. Oral Presentation.
6. **Hill, M.L.**, S-J. Chung, K. Hadrack, R. Parikh, H-J. Woo, and T. Kim (2022). "Phototheranostic Effects of Extracellular Vesicle Coated Nanoparticles for use in the Inhibition of Glioblastoma Development." American Chemical Society (ACS) Fall Conference. Chicago, Illinois. Oral Presentation.

Publications

1. **Hill, M.L.**, S-J. Chung, H-J. Woo, C. Park, K. Hadrack, M. Nafiujjaman, P.P. Kumar, L. Mwangi, R. Parikh, and T. Kim. Exosome-Coated Prussian Blue Nanoparticles for Specific Targeting and Treatment of Glioblastoma. *ACS Applied Materials and Interfaces (AMI)* **2024**, 16 (16), 20286-20301. DOI: 10.1021/acsami.4c02364.
2. Chung, S-J., K. Hadrack, M. Nafiujjaman, E.H. Apu, **M. L. Hill**, M. Nurunnabi, C.H. Contag, and T. Kim. Targeted Biodegradable Near-Infrared Fluorescent Nanoparticles for Colorectal Cancer Imaging. *ACS Bio Materials* **2024**. DOI: 10.1021/acsabm.4c00072.
3. Woo, H-J., S-J. Chung, **M.L. Hill**, K. Hadrack, and T. Kim. Europium-Doped Calcium Silicate Nanoparticles as High-Quantum Yield Red-Emitting Phosphors. *ACS Applied Nanomaterials* **2023**, 6 (11), 9884-9891.
4. Huda, M.N., M. Nafiujjaman, I.G. Deaguero, J. Okonkwo, **M.L. Hill**, T. Kim, and M. Nurunnabi. Potential Use of Exosomes as Diagnostic Biomarkers and in Targeted Drug Delivery: Progress in Clinical and Preclinical Applications. *ACS Biomaterials Science and Engineering* **2021**, 7 (6), 2106-2149.
5. Kalashnikova, I., S-J. Chung, M. Nafiujjaman, **M.L. Hill**, M. Siziba, C.H. Contag, and T. Kim. Ceria-Based Nanotheranostic Agents for Rheumatoid Arthritis Treatment. *Theranostics* **2020**, 10 (26), 11863-11880.
6. Nafiujjaman, M. S-J. Chung, I. Kalashnikova, **M.L. Hill**, S. Homa, J. George, C.H. Contag, and T. Kim/ Biodegradable Hollow Manganese Silicate Nanocomposites to Alleviate Tumor Hypoxia toward Enhanced Photodynamic Therapy. *ACS Applied BioMaterials* **2020**, 3 (11), 7989-7999.

7. Margulis, K., A. Honkala, I. Kalashnikova, S.E. Noll, **M. Hill**, R.N. Zare, and B.R. Smith. Nanoparticles Decorated with Granulocyte-Colony Stimulating Factor for Targeting Myeloid Cells. *Nanoscale* **2020**, 12, 2752-2763
8. Shuster, M.I., J. Mudge, **M. Hill**, K. James, G.A. DeFrancesco, M.P. Chadiarakou, and A. Sundararajan. Is p53 a Smoking Gun? How Mutational Signatures Forced Big Tobacco to Change. *National Center for Case Study Teaching in Science* **2019**.